Foamability of complex fluids : dynamic of bubble formation in yield stress fluids using confined geometries

Benoit Laborie

UNIVERSITÉ PARIS-EST

Thèse

Présentée pour obtenir le grade de

Docteur de l'université Paris-Est

Spécialité: Physique

Sujet portant sur:

Moussage des fluides complexes: dynamique de la formation des bulles dans des fluides à seuil en géométries confinées.
Foamability of complex fluids: dynamics of bubble formation in yield-stress fluids in confined geometries.

Présentée par:

Benoît LABORIE

le 1er octobre 2015 devant le jury composé de:

Mme.	Catherine	BARENTIN	Rapporteure
M.	Philippe	MARMOTTANT	Rapporteur
M.	Charles	BAROUD	Examinateur
M.	Piotr	GARSTECKI	Examinateur
Mme.	Anke	LINDNER	Présidente du jury
Mme.	Florence	ROUYER	co-encadrante
M.	Dan	ANGELESCU	co-directeur
Mme.	Élise	LORENCEAU	Directrice de thèse

Funding

This work has benefited from two French government grants managed by ANR within the frames of the national program Investments for the Future (ANR-11-LABX-022-01) and of the young researcher program (ANR-11-JS09-012-WOLF)

Nous étudions la formation de bulles dans un fluide à seuil (matériaux liquides si la contrainte appliquée est supérieure à la contrainte seuil, et solides autrement) au moyen de géométries millifluidiques (jonctions en T, “flow focusing“) constituées de canaux axisymetriques, et fabriquées par stéréolithographie. En tirant partie de la domination des effets capillaires par la contrainte seuil, nous produisons des bulles dans des fluides à seuil simples (émulsions concentrées, gels de carbopol). La formation des bulles est due au pincement du filament de gaz par l'écoulement de fluide à seuil à débit imposé. Il rappelle celui observé pour des fluides Newtoniens dans des géométries de “flow focusing“ 2D. Nous étudions les différents régimes de fonctionnement de ces systèmes lorsque le débit de fluide à seuil et la pression de gaz sont imposés. La production instationnaire de bulles est observée, et expliquée par la rétroaction provenant des variations de résistance hydrodynamique induites par la formation des bulles sur le débit de gaz. La déstabilisation finale se produit lorsque toutes les bulles coalescent. Ceci est du au transfert de fluides entre les ponts liquides séparant les bulles et les films fins situés près des parois solides. Aussi, nous étudions le dépôt de fluide à seuil dans un tube capillaire avec ou sans glissement aux parois. En effet, ce phénomène est courant lors de l'écoulement de fluide à seuil en milieu confiné sur des surfaces lisses. Les résultats peuvent être décrits par une loi d'échelle (contrainte interne équilibrant le gradient de pression capillaire) lorsqu'il n'y a pas de glissement aux parois. Dans le cas contraire nous montrons qu'il existe trois régimes dépendant de l'état de contrainte du système, et qu'ils fixent les formes de bulle observées en régime instationnaire. Finalement, différentes méthodes de régulations (pression, écoulement pulsés) nous permettent d'obtenir des régimes stationnaires. Ceux-ci sont caractérisés (fraction volumique de gaz, temps de formation de bulles), et permettent l'obtention de mousses de fluides à seuil. Ainsi, ouvrant potentiellement la voie à la production contrôlée de fluides à seuil aérés à grande échelle.

Mots clés : *fluides à seuil, bulles, rhéologie, confinement, millifluidique, rétroaction hydrodynamique, glissement, dépôt de film (Bretherton), mousses.*

We study the formation of bubbles inside yield-stress fluids using millifluidic geometries (T-junctions, flow-focusing devices) made of axisymmetric channels, and manufactured by stereolithography. We show that dispersing bubbles in simple yield-stress fluids (concentrated emulsions, and carbopol gels) is possible by taking advantage of the yield stress over the capillary stress, and due to the squeezing of the gas thread by the core of the yield-stress fluid flow at imposed flow rate. The observed behavior is reminiscent of the geometrical operating regime in 2D flow-focusing devices for Newtonian fluids. We investigate the different operating regimes that occur when the yield-stress fluid flow rate and the gas pressure are imposed. We report that, for these inlet conditions the production is unsteady, which comes from the hydrodynamic feedback induced by the formation of each bubble on the gas flow rate. The regime eventually breaks down when all bubbles coalesce. This is due to the transfer between the liquid plugs separating each bubble and the thin film located on the channel wall. Thus, we study the deposition of yield-stress fluid on the wall of capillary tubes. Indeed, this often occurs for yield-stress fluids flowing in confined geometries on smooth surfaces. The results with no-slip are well described by a classical scaling law (internal stresses balanced by capillary pressure gradient). When there is wall slip, we show that there are three regimes that depend on the stress state of the system, and set the bubbles' shape observed in unsteady regimes. Finally, different regulation methods (pressure, pulsated flows) allow to obtain steady regimes. They are characterized (gas volume fraction, bubble formation time) and we show that they allow to obtain yield-stress fluid foams. Thus, identifying pathways for potential steady-state controlled production of aerated yield-stress fluids at large scale.

Key words: *yield-stress fluids, bubbles, rheology, confinement, millifluidic, hydrodynamic feedback, wall slip, film deposition (Bretherton), foams.*

Il n'y a pas de RAT-PORC
ou en anglais : *Never enter an arsekicking contest with a porcupine.*
Terry Pratchett, in *Sourcery* (1988)

Remerciements (Acknowledgments)

Je souhaite tout d'abord remercier les membres du jury : les rapporteurs, Philippe Marmottant et Catherine Barentin, pour leur lecture attentive du manuscrit, ainsi que les examinateurs, Anke Lindner, Charles Baroud, et Piotr Garstecki, pour avoir accepté d'évaluer ce travail. Merci à vous tous pour vos remarques, suggestions, et encouragements.

Je tiens ensuite à remercier mes encadrants de thèse : Florence Rouyer, Dan Angelescu, et Élise Lorenceau. En premier lieu pour m'avoir laissé explorer ce sujet avec beaucoup de liberté, tout en ayant été là lorsque j'avais besoin de vous ! Merci. Ensuite, j'ai beaucoup appris à votre contact durant ces trois ans, aussi bien en terme de rigueur scientifique, de remise en question des résultats, d'astuciosité (ne pas hésiter à retourner le sujet, les expériences, les résultats, à 180° !), que sur la gestion d'une thèse (un looonnng projet) au jour le jour ! Je souhaitais aussi, mentionner spécialement Florence, qui, il me semble, m'a donné fortement gout aux expériences (le physique avec les mains ! comparé à tout le numérique que j'avais fait pendant mon cursus) lors du stage que j'ai effectué en première année de master. Encore merci à vous tous.

Enfin, je souhaiterais remercier ceux qui ont contribué à cette thèse d'un peu plus loin. D'abord Olivier, particulièrement pour les discussions sur la régulation de pression et la production stationnaire, mais aussi pour la blague du poisson dans le filet de badminton, et les conférences sur le pied de la mousse auxquelles j'ai pu assister. Je voudrais aussi remercier Philippe et Mathilde pour les discussions sur le dépôt de fluides à seuil qui m'ont beaucoup donné matière à réfléchir. Merci également, à Julie qui m'a permis de faire mes premiers pas en formulation des émulsions, et qui, avec Ilham, m'a fait découvrir le traitement de surface magique ; à Lucie qui m'a expliqué comment fabriquer "Ma première émulsion" (hum... j'ai noté "poêle à frire", est ce que tu sais à quelle pièce de l'émulsificateur ça peut correspondre ?) et qui m'a bien aidé en répondant à mes questions rhéologiques, tout ça avec beaucoup de patience, même en pleine rédaction ; Benjamin pour la géométrie ; Mathilde, encore, pour la préparation du carbopol et sa rhéologie ; mais aussi François et Marine pour un certain nombre de mesures rhéologiques ; enfin l'équipe technique (Pascal, David, Cédric, Laurent (le nouveau Yves)) pour tout ce qui a tourné autour de la stéréolithographie et leur bonne humeur ; et l'équipe administrative (Carmen, Sandrine, et Nathalie) qui m'ont bien aidé pour toutes les commandes, remboursement, et autres frais de conférences ; en dernier lieu, Xavier et François pour m'avoir accueilli dans l'équipe rhéophysique du laboratoire Navier il y a maintenant trois ans.

Maintenant, je voudrais aussi remercier particulièrement les doctorants avec qui j'ai passé une partie ou la totalité de ces trois ans et qui ont tous participé à cette thèse d'une manière ou d'une autre. Thibaud (toujours aussi sympa et présidentiable !), qui m'a ouvert la porte du laboratoire le premier jour alors qu'Élise avait oublié que je commençais. Adrien, grand koala devant l'éternel et la première personne sensée que j'ai rencontré : tu m'as presque redonné foi en l'humanité, merci ! Par contre je suis bien désolé de ne pas avoir pu être à ton mariage. Florian et ses rhums arrangés, dont le sens de l'hospitalité n'a d'égal que son manque d'organisation lors de son déménagement (ce petit voyage était vraiment très sympa !). Antoine, "à quoi tu joues ?", et artisan émérite. Claire et Manu : du glamour à Kepler. Michel W., les pauses thé de la rationalisation, super meat boy (alleeeez faut finir), la géographie, les insectes, et les discussions pseudo-philosophiques qui n'en finissent pas avec Florian avant le premier RER. Mathilde, dont le cerf est maintenant sur une étagère, et qui a supporté mon gout prononcé pour la provocation avec un flegme exemplaire. Après un tel entrainement tu es parée à toute éventualité. Sinon, les phares sont sur la manette gauche : une légende est en marche. Lucie, qui participa activement à la re-définition de la gougnaffe (ainsi qu'à l'article - au placard - sur diamètre et rayon). Ce qui devait être fait, car personne n'en avait parlé depuis Thalès et son fameux

Traité sur les gougnaffes mentionné seulement par le cousin au troisième degré de Pline le jeune sur son lit de mort. Ce qui devrait enfin permettre de corriger/compléter la définition :

> Gougnafe, subst., synon. de gougnafier. *On serait né fils d'un riche planteur à Cuba Havane par exemple, tout se serait passé bien gentiment, mais on est venu chez des gougnafes, dans un coin pourri sur toutes parts, alors faut pâtir pour la caste et c'est l'injustice qui vous broye* (CÉLINE, *Guignol's band*, Paris, Denoël, 1944, p. 29).
> Prononc. : []. Étymol. et Hist. 1899 « bon à rien » (s. réf. ds ESN.) ; av. 1901 (A. B[ruant] s. réf. ds BRUANT, 1901, p. 332, s.v. noctambule). **Orig. controversée.** À rapprocher de gougnafiasse « goinfre » (1891, RICHEPIN, Truandaille, p. 55 ds SAIN. Lang. par., p. 321). Dans SAIN., loc. cit., gougnafier est défini « paillard » et considéré, ainsi que gougnafiasse, comme dér. de gougne « prostituée » (gouine*). Pour ESN., s.v. gouillafe, gougnafier « bon à rien » et gougnafiasse « goinfre » sont des var. de gouillafe « goinfre » (goulafre*). Terminaison -afier prob. d'apr. d'autres mots comme p. ex. estafier* ou l'arg. grenaffier « fermier » (1800, P. LECLAIR, Hist. des brigands et assassins d'Orgères ds SAIN. Sources arg. t. 2, p. 92).

Et merci encore pour ta patience. Marine, clairvoyante la plupart du temps, fidèle co-référente du bad, pour sa contribution égale à la redéfinition de la gougnaffe, sa passion pour les bonnes histoires, les étiquettes de tripel karmeliet, dcdl, et le mémorable spin $\frac{1}{2}$! Jennifer et Caterpy, ainsi que leurs suppléants Juliette Fabienne Sufier et Gontrand A. Von Schmidtt Jr. pour leur sens de l'organisation, et leur agréabilité (la plupart du temps). Mais aussi pour sa superbe photo de vacances. François, toujours serviable, pour sa coolitude, et son engagement au bad. Michel B. pour son enthousiasme, wikipedia, les pâtes au coq (sauce au vin) et aux amandes, et parfois l'avant garde de l'avant garde. Avec toi je sais que le labo est entre de bonnes mains. Ilham et Yousra, beaucoup trop gentilles. Jules Pamplemousse, pour son absence de limites, et son ingénieux système de parachute lors de l'éjection des ordinateurs portables. Guillaume (et Fred'), la Picardie, les graines, le Ritz, le bad, et l'avant garde. Tu as tellement d'avance sur la tectonique des plaques avec ce Marseille-Agadir en passant par Beauvais. Benjamin et son langage fleuri, qui commença très fort avec le pousse seringue chantant, alla récupérer son slip à l'auto-école, le craqua plus d'une fois, et colla de nombreuses étiquettes. Ah, que de discussions sur la navigation. Ces trois ans furent forts en pommes. Rémy, qui j'espère continuera à danser la chenille encore longtemps. Mais aussi ceux que j'ai moins côtoyé, Mamadou et la phrase du jour, Alizée qui avait un problème à son vernis, Christelle qui a gagné au jeu de "bang", Romain, Simon, Louise, et Blandine qui se lance pour trois ans.

Dans le désordre le plus total je souhaiterais aussi remercier, Mr. Fer (saint patron de la manip'), Cindy-Sophie la girafe de petite vertu, Marc-Archibald le marcassin schizophrène, Bénédicte la plante en pot d'Élise, Louis-Léon-Léopold-Archibald III (Seigneur de la Forêt) qui défendit ses congénères contre une série d'agressions d'une rare violence, Corinne la limace, Edwige la brosse à dent de Benjamin, mon fritté de compagnie (N1), et l'homme taupe qui finalement n'est pas arrivé. Enfin merci à tout ceux qui ne sont pas venu et qui n'ont pas participé à cette thèse.

Merci à tous.

Contents

List of Figures

List of Tables

List of Symbols

Acronyms

CAD	Computer assisted design
FFT	Fast Fourier Transform
FF	Flow focusing
HB	Herschel-Bulkley
STL	Stereolithography
TJ	T-junction
YSF	Yield stress fluid

Continuum mechanics

$\underline{\underline{\tau}}$	Deviatoric part of the stress tensor
p	Pressure
G	Shear modulus
$\underline{\underline{D}}$	Shear strain tensor
$\underline{\underline{\epsilon}}$	Strain tensor
$\underline{\underline{\sigma}}$	Stress tensor

Dimensionless groups

Bi	Bingham number
Bo	Bond number
$\mathcal{Y}$	Compares the yield stress to the capillary and gravity stress
B	Compares the yield stress to the capillary stress
$Ca = \frac{\eta V}{\gamma}$	Newtonian capillary number
$\widehat{Ca} = \frac{k\left(\frac{V}{R}\right)^n}{\frac{T}{R}}$	Non-Newtonian capillary number
W	Weissenberg number

Flow properties

ℓ	Bubbles length
t_α, t_β, t_γ	duration of the stages of bubble formation
$W = \frac{v_b - v_m}{v_b}$	Excess velocity of bubbles with respect to the mean velocity of the flow
h_0	Final deposited thickness
Q_g	Gas flow rate
$h(x)$	Height of the film in the dynamic meniscus
Q	Imposed yield stress fluid flow rate
Ω	Junction volume (TJ or FF)
λ	Length of the dynamic meniscus
V	Magnitude of the typical velocity
t_b^{min}	Minimum time to form one bubble in TJ or FF geometries

P_b^{min} Necessary pressure to form the first bubble

ΔP Pressure gradient

f_{hb} Pressure/flow rate relation for an HB fluid

R_p Radius of the solid region during channel flow

ϕ_s Surface fraction of bubbles

t_b Time to form one bubble in TJ or FF geometries

$Q_{tot} = Q + Q_g$ Total flow rate

v_i Velocity along the axis i

ϕ_g Volume fraction of bubbles

τ_w Wall shear stress

ΔP_y yield pressure for channel flow

L_p YSF plugs' length

Materials properties

κ^{-1} Capillary length

L_y Capillary/yield stress length

κ_y^{-1} Capillary/yield stress/gravity length

ρ Density

ϕ droplets volume fraction for emulsions

η Shear viscosity

T Surface tension

τ_y, k, $n = \frac{1}{m}$ yield stress, consistency, flow index

h_c Yield-stress/gravity length

Rheology

γ_c critical yielding deformation

N_1, N_2 First and second normal stress differences

F_z Normal force

δ Phase angle

$\dot{\gamma}$ Shear rate

γ Shear strain

τ Shear stress

G', G'' Storage, and loss moduli

M Torque

Introduction

Dispersions of gas bubbles inside a liquid or a solid constitute a wide class of materials. They are commonly encountered in every day life or in industrial processes. For example, gas bubbles dispersion are found in gaseous drinks where they are desired. On the contrary, during glass (or metal) fining, they must be removed to enhance the quality of the final product. Gas bubbles dispersed in solids are found in various materials, such as aluminium foams, bread, pumice, or in volcanic or metallic slags.

Foams, made of a large number of gas bubbles (such that they are deformed by their neighbors) dispersed in a liquid, are also commonly used in everyday life. Examples include shampoo, shaving creams, dishwashing liquids, whipped cream, or firefighting foams. Besides these examples, foams are desirable in many industrial processes such as in the mining industry to retrieve minerals from slurry, in enhanced oil recovery [1], or for the production of aerated building materials [2].

The production of building materials is one of the more widespread examples of the production of so called aerated materials. This category also encompasses the fabrication of cosmetic, or food aerated products to name few. For civil engineering applications, the addition of gas bubbles leads to various improvements of the final product, such as: the use of less raw material, a greater thermal or/and acoustic insulation as well as a reduced weight. For food and cosmetic applications, an addition of bubbles allows to control the texture and shape at rest of materials, which are important commercial parameters [3]. More specifically, aerated complex materials are also used as templates for the production of metamaterials, showing particular acoustic properties due to their structure [4].

In all the industrial processes associated with the production of aerated materials the gas phase must be dispersed into a material having complex properties. For example, building materials such as concrete or plaster present a microstructure made of sand or gravel. Food products also exhibit lipid or protein aggregates as in mayonnaise, or milk in ice cream [5]. The presence of such microstructure confer complex (i.e more complex than for a simple liquid such as water) properties to the continuous phase: the material is often a complex fluid behaving in an intermediate way between simple liquids and elastic solids [6, 7]. Its microstructure is responsible for the material properties at the macroscopic scale (i.e. when deforming, or flowing). Among that class of materials, some behave like solids when the applied stress is lower than the critical stress (named *yield stress*), and like fluids otherwise. Lava and mud, dense snow, sewage sludges from wastewater treatment, mining slurries, drilling fluids from petroleum industry, glues, paint, fresh concrete, hair gel, whipped cream are examples of so called *yield-stress fluids* [3].

In most industrial processes, complex aerated materials are obtained by batch processing: a yield-stress fluid and a separately produced foam are mixed by mechanical means. Such methods provide little control over the stress state of the system and making high gas volume fraction difficult to obtain [8–10], with direct impact on the quality of the resulting material. Therefore, it raises the question of the production method of aerated yield-stress materials.

To produce dispersions of bubbles, or drops, of one fluid in another fluid the goal is always to break a large volume of the phase to disperse into smaller volumes (i.e. bubbles or droplets). Therefore, one must apply a stress that is sufficiently large to overcome interfacial stresses of the system due to surface tension. In this spirit, one method consists in injecting large bubbles, or a continuous stream of gas, into a pre-wetted porous medium constituted of interconnected channels. The individual channel possess a typical dimension of micrometric size, which promotes all the dynamics associated with interfaces and capillarity. In addition, these geometries are complex and often exhibit rapid change in cross-sectional area which allows the formation of bubbles under various flow conditions. At small

velocity (i.e. small shear rate) the formation of bubbles or droplets is governed by a balance between viscous forces and capillarity [11, 12]. When the velocity of the flow is large (i.e. large shear rate), gas compressibility leads to sudden acceleration of large bubbles when passing through small pores. In that case, the inertial force competes with the interfacial forces [11, 13, 14]. If the viscous force or the inertial force overcome the capillary force, both situations lead to the formation of bubbles or drops.

Still this method may not be satisfying to ensure a good control on bubble size. This can be due to the complex geometry of each pore and the dependency of preferential paths on the flow history, as well as physicochemical characteristics of the medium through changes in wettability. Besides, interactions between multiple drops or bubbles may take place during the flow, leading to coalescences, and therefore changing the hydrodynamic resistance of each path, and thus the overall dynamic of the flow [11, 14].

In addition, as highlighted for Newtonian fluids in small scale geometries, the formation of bubbles or drops is always driven by capillary effects, therefore the presence of a yield stress, and possibly of solid regions where the stress is below the yield stress, may intrinsically hinder the capillary break-up. Finally, if the pre-wetting fluid had a yield stress, we can mention the role of dead volumes (where the stress is below the yield stress), it corresponds to approximately 10 % of the fluid in a porous medium made of glass beads [15]. The presence of such dead regions increases the complexity of the flow and may also perturb the formation of bubbles or drops. This suggests the requirement for simpler geometry where the stress state is mostly known.

Microfluidics is a widely-used technology for performing diverse complex fluid manipulation, such as controlled droplet/bubbles transport or/and production [16, 17], production of complex materials [18], or cell manipulation [19], as well as for performing chemical reaction [20], and ultimately for medical diagnosis and drug delivery [19, 21, 22]. One of its main features is to allow the design of controlled geometry and the manufacturing of complex fluids at acceptable throughput with a highly accurate control on bubble size, and global flow rate. Recently, the production of monodisperse foams and emulsions as well as droplet manipulation and flow in microchannels has gained much interest, and knows a rapid expansion [16, 17, 20, 23]. Different simple geometries were develop to achieve this goal, the most popular being (i) T-junction [18, 24–27], (ii) flow-focusing geometry [28–34], and (iii) step emulsification [35–38]. Quite surprisingly, in spite of its popularity and the range of application that uses this technology, only a few literature reports of dispersions obtained in microfluidic systems using complex fluids or yield-stress fluids exist [39–46]. The classical flow focusing and T-junction geometries are shown on figure 1.

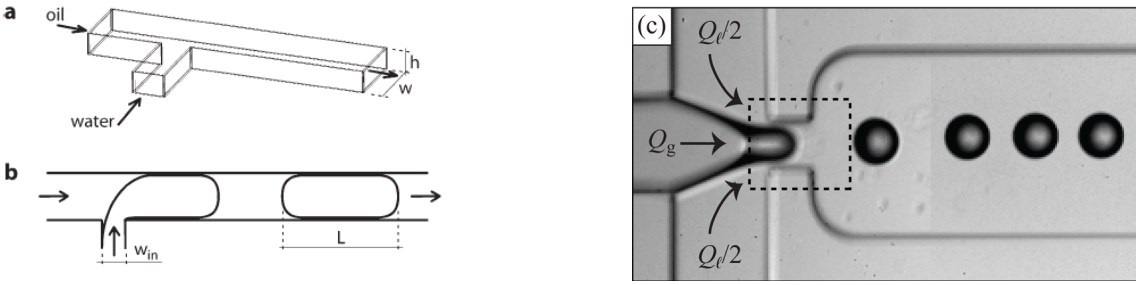

(a) Sketch of classical T-junction with channels of rectangular cross section and bubble formation. From [26].

(b) Picture of bubble production inside a classical flow-focusing device. From [28].

Figure 1 – Classical microfluidic geometries.

Different manufacturing processes of the afore-mentioned geometry are available, the main one being soft lithography [47–49], which often results in the fabrication of channels of rectangular or

square cross section. However, recently, stereolithography techniques were developed [50, 51] and allows to fabricate millifluidic devices with micrometric precision. First, it presents the advantage to allow the freeform design of devices with circular cross sections, which reduces the complexity of the flow. Then, to work at the millimeter scale, thus minimizing the pressure drop associated with the flow of complex fluids which is generally large, and therefore possibly require very high driving pressure that could damage micrometric geometries.

In this thesis we propose to **investigate the formation of gas bubbles inside yield-stress fluids using millifluidic T-junctions and flow-focusing devices**. We focus on three main topics: (i) bubble formation, (ii) the dynamics of the associated two phase flow, (iii) the characterization of steady regimes and the production of aerated yield-stress fluid foam.

In the first part of this manuscript we give a characterization of our system and of the situations encountered during two-phase flow in channels already filled with yield-stress fluids. The manuscript is organized as follows:

In the first chapter, we recall the basics of the continuum mechanics framework used to describe the behaviour of materials for elastic solids, Newtonian and non-Newtonian fluids. Then, the microstructure of the chosen model materials (i.e. carbopol gels and emulsions) is given, as well as the experimental production process of such materials. We finally discuss the influence of their microstructure on one of their most important properties for two-phase flow: surface tension. The second part of this chapter is dedicated to the rheology of emulsions, and carbopol gels. We first recall the measurement theory of the rheological characteristic of fluids using a parallel-plates rheometer. Then, we present the results of the measurements carried out on our materials to determine their rheological behavior.

In the second chapter, we first describe the stereolithography technique, and the different devices produced for this study. We pay particular attention to the surface roughness of such devices. In the second section, we recall the equations describing the motion of yield-stress fluids inside a straight circular channel with no-slip boundary conditions. In addition, we recall how a circular channel can be used to determine the rheology of the fluid (Mooney-Rabinowitsch rheometer). We then summarize the effects linked to a strong confinement of yield-stress fluids. Then, we give a review of the mechanisms leading to wall slip of yield-stress fluids and their effect on the measurement of the rheological parameters of the fluids. We describe the different solutions available to suppress wall slip (physically or chemically). Finally, we highlight how wall slip can simply be taken into account from in-situ capillary rheometry measurements. In the last part of this chapter we investigate the rheology of yield-stress fluid two-phase slug flow in circular channel using capillary rheometry. Different flow scenarii are suggested.

In the third chapter, we address the problem of the deposition of yield-stress fluid on the wall of circular channel (i.e. the analogous of the *Bretherton problem* for Newtonian fluids). The first part of this chapter is constituted of a review of the solutions (exact, and scaling laws) of the deposition problem for Newtonian, non-Newtonian, and particularly for yield-stress fluids. Then, we describe the experiments performed to investigate the deposition of yield-stress fluids on the wall of circular channels, both with and without wall slip. Steady and unsteady measurements of the film thickness are shown, and compared to typical dependencies found in literature. In the third part of this chapter, we first introduce the necessary dimensionless parameters, and discuss the literature models. Then, based on scaling arguments we derive an expression to describe the deposition with no-slip boundary conditions. Particular attention is paid to the stress state of the system to analyze and discuss the results obtained in slip regime. Finally, the results obtained in confined geometries are compared to

what is obtained in the geometry of a plate (the Landau-Levich-Derjaguin problem (LLD)). Similarly to what is done in a circular geometry, a scaling is proposed and discussed for the LLD problem with yield-stress fluids.

The second part of this manuscript is dedicated to the results of the bubble formation experiments and to the dynamics of the associated two-phase flow:

In the fourth chapter, we study the break-up mechanism leading to the formation of gas bubbles dispersed in yield-stress fluids using flow focusing and T-junction millifluidic devices. First, we give a review of the classical regime of bubble formation in flow-focusing and T-junction geometries for Newtonian fluids. Then, we detail the experiments performed in such geometries with yield-stress fluid driven at imposed flow rate and constant gas pressure. We report that bubble production is possible by taking advantage of the yield stress over the capillary stress. In the second section, the role of the hydrodynamic feedback induced by the unsteadiness of bubble production on the break-up mechanism is taken into account. Finally, we derive a limiting bubble frequency that holds for both steady and unsteady regimes, and is reminiscent of the geometry-driven operating regime in two dimensional flow-focusing devices for Newtonian fluids [31, 32].

In the fifth chapter, we investigate the dynamics of the unsteady operating regimes observed when the yield-stress fluid flow rate and the gas pressure are imposed. First, three different unsteady regimes are reported, and compared to what is observed for Newtonian fluids. The validity domains of these regimes are detailed on a pressure/flow-rate diagram. Next, we study the introduction of the first bubble produced inside the channel for both flow focusing and T-junction. The critical pressure necessary to form the first bubble is measured and compared to the pressure associated with the yield-stress fluid flow at imposed flow rate. Finally, we study the dynamics associated with the break down of the unsteady bubbling regime. We focus on the role of hydrodynamic feedback and yield-stress fluid film deposition. The whole process is correlated to the stress state of the system in slip regime. We also show that unsteady experiments can be used to retrieve a deposition law of the yield-stress fluids on the wall of the channels. This allows to further investigate the role of surface roughness on the deposition in slip regime.

In the last chapter of this manuscript, we propose and characterize different way to obtain steady regimes of bubble production. First, we recall the regimes obtained for different inlet conditions when the continuous phase is a Newtonian fluid, and the perturbations of the steady state that can occur. Then, we perform experiments at imposed yield-stress fluid flow rates and imposed gas flow rate, pressure, or for pulsated flow. The physical ingredients of each situation are discussed. Whenever obtained, steady regimes are described. We continue by performing the characterization of the steady regimes with pressure control, or pulsated flow, in term of volume fraction and bubble formation time. Finally, in the last part of this chapter we show that the production of yield stress fluid foams is possible using millifluic T-junction and flow-focusing geometries.

In the first annex we describe the roughness of the devices manufactured by stereolithography. In the second annex we report the different bubbles' shape that are observed and differ significantly from what is predicted from surface tension in a simple liquid. In the third annex we present different geometries designed for large scale production of yield-stress fluid foam. In the fourth annex we present preliminary results on the coarsening of gas bubbles inside yield-stress fluid in confined and unconfined geometries. In the last annex we provide the script used for the computation of the variation of bubbles' size based on the variation of hydrodynamic resistance in the outlet channel.

Part I

Single and two-phase yield-stress fluid flow in circular channels

1

Model Materials

This chapter is devoted to the materials used in this thesis. We start by presenting their constitutive law in the continuum mechanics framework for both liquid and solid state. We also describe their expression in simple shear. Then, the physico-chemical structure of the materials is detailed. Their microstructure is described as well as its effect on internal stresses of the material. Eventually, computation of rheometrical functions for a parallel-plate rheometer and results of rheometrical experiments are shown.

Contents

1.1 Constitutive equation

Materials consisting of a microstructure of small characteristic size compared to the chosen observation scale can be described in the framework of *continuum mechanics*. When a force, or a deformation is applied, the material departs from its equilibrium configuration. Therefore, the constituting molecules (or elements of the microstructure) of the materials are no more in their equilibrium state, and as a reaction to the solicitation, develop forces that tend to return the system to its state of lowest energy. These forces are called internal stresses [52].

Dividing the material into elementary volumes (V_c of typical size $a_c \simeq V_c^{\frac{1}{3}}$) large compared to the size of its molecules (or microstructure elements). If, (i) a_c is small compared to the typical size of the considered flow; and (ii) a_c is large compared to the mean free path of molecules, the material

can be described as a continuous medium. Then, the internal stresses of the material are described as follows: each elementary volume of the material applies an elementary force and an elementary torque on other elementary volumes. In each point M of the material the information on internal stresses is expressed in the form of a *stress tensor* denoted $\underline{\underline{\sigma}}(M)$, where σ_{ij} describes the i-th components of the surface force applied on the face of the tetrahedra perpendicular to the j-th axis, in the local base (x, y, z) (Fig. 1.1).

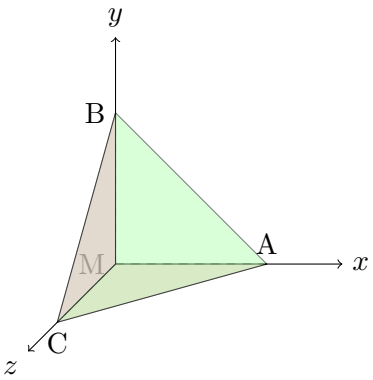

Figure 1.1 – Tetrahedra centered on the point M.

The stress tensor is real, symmetric, and represents a linear application that links, for a given state of internal stresses, the vector normal to the surface (denoted $\vec{n}$) and pointing inward, to the resulting force applied by the volume on that surface $\vec{F}$. Thus,

$$\int\int_S \underline{\underline{\sigma}} \cdot \vec{n} = \vec{F} \tag{1.1}$$

$\underline{\underline{\sigma}}$ contains the elastic stress and the viscous stress, and can be decomposed as the sum of a spherical part and a deviatoric part, such that the trace of the the deviatoric part is zero. This decomposition allows to separate two major kind of stresses: (i) normal stresses; (ii) tangential stresses.

$$\underline{\underline{\sigma}} = -p\underline{\underline{I}} + \underline{\underline{\tau}} \tag{1.2}$$

with:

- $\underline{\underline{I}}$ the unit tensor.
- $p = \dfrac{-tr(\underline{\underline{\sigma}})}{3}$ the isotropic (or spherical) part of the stress tensor. For a system inside an homogeneous pressure field (hydrostatic) the pressure acts with the same magnitude on all faces of the system, thus the force acting on the i-th surface is oriented along the inward normal and writes $-pn_i$. Identifying equation 1.1 with $-pn_i$ also results in a spherical tensor. The spherical part represent the homogeneous pressure which may induce volume change.
- $\underline{\underline{\tau}}$ the deviatoric part of the stress tensor which accounts for tangential stresses. The deviatoric part is non-isotropic and is responsible for deformations at constant volume, such as the shearing of elementary volumes.

The aim of the next paragraphs is to present the link between the stress tensor and the response of the system for the types of materials relevant to the work undertaken during this thesis. For each type

of material the description of their macroscopic response to a given solicitation, i.e. their constitutive law, is presented under the form of a specific equation linking stress and strain (resp. strain rate) for solid (resp. liquid) regime.

1.1.1 Linear elastic solid (solid regime)

For an isotropic elastic solid the behavior of the material is given by *Hooke's law*. It can be derived by expressing the free energy of a system as function of the strain tensor. Hooke's law is the constitutive equation for a solid undergoing deformations of small amplitude, and it links the stress tensor $\underline{\underline{\sigma}}$ to the strain tensor $\underline{\underline{\epsilon}}$:

$$\underline{\underline{\sigma}} = -\lambda \operatorname{tr}(\underline{\underline{\epsilon}})\underline{\underline{I}} + 2G\underline{\underline{\epsilon}} \tag{1.3}$$

with:

- $\underline{\underline{\epsilon}}$ the strain tensor, representing the deformation undergone by the elementary volumes of the material. Considering in a reference frame (Ox, Oy, Oz), a particular point of a material at position A of coordinates (x_0, y_0, z_0) at rest, which is displaced at a position B of coordinates $(x_0^{'}, y_0^{'}, z_0^{'})$ under a given solicitation, the displacement vector is thus given by $\vec{u} = \vec{OB} - \vec{OA}$. The strain tensor is built from the displacement of the system with respect to its initial state: the deformation of each component of $\vec{u}$ with respect to each direction of the reference frame. To avoid any dependency on motion of solid rotation, the strain tensor is symmetric by definition and each component is given by:

$$\epsilon_{ij} = \frac{1}{2}\left(\frac{\partial u_i}{\partial x_j} + \frac{\partial u_j}{\partial x_i}\right)$$

- λ the first *Lamé* coefficient or modulus of hydrostatic compression, and G the second *Lamé* coefficient also called shear modulus. G varies between few pascals for liquid foams and hundreds of GPa for the hardest metals [52]. Using general summation notation (sum over the index if it appears twice), the sum ϵ_{ii} represents the change of volume of a body. When the shape is changed and the volume is kept constant (i.e. $\epsilon_{ii} = 0$), the resulting deformation field is called *simple shear*.

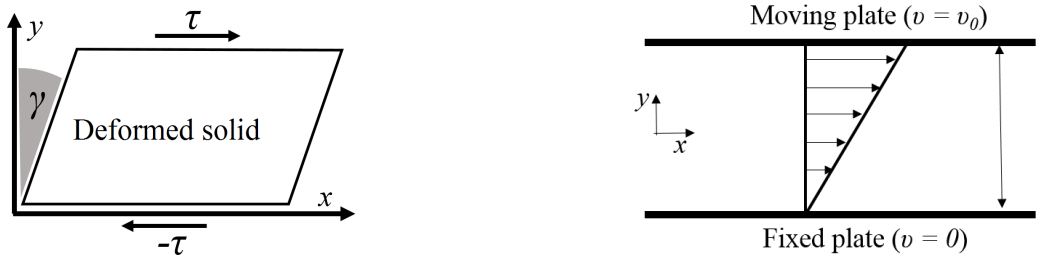

(a) Deformation of a solid during simple shear.

(b) Fluid confined between two plates separated by h, and entrained by the top plate at a velocity v_0.

Figure 1.2 – Schematic of simple shear for solid and fluid.

For simple shear (figure 1.2 (a)) in (x, y) plane the strain writes as $u_x = \gamma y$, and $u_y = u_z = 0$, thus the stress tensor reduces to:

$$\underline{\underline{\sigma}} = G \begin{pmatrix} 0 & \gamma & 0 \\ \gamma & 0 & 0 \\ 0 & 0 & 0 \end{pmatrix} \tag{1.4}$$

Finally, it reduces to a scalar relation between the shear stress ($\sigma_{xy} = \sigma_{yx} = \tau$) and the shear strain ($\gamma = 2\epsilon_{xy}$). Thus,

$$\tau = G\gamma \tag{1.5}$$

1.1.2 Newtonian fluids (liquid regime)

For a Newtonian fluid, the stress tensor is also decomposed into two parts: (i) normal stresses; (ii) tangential stresses. If an external force is applied to the system, it organizes into a flow with a velocity which depends on the considered point. The stress tensor is then decomposed into the hydrostatic part and the deviatoric part, with the deviatoric part depending on the shear strain rate [53]. Under the assumption of incompressibility, the stress tensor is written as:

$$\underline{\underline{\sigma}} = -p\underline{\underline{I}} + 2\eta\underline{\underline{D}} \tag{1.6}$$

- $\underline{\underline{I}}$ the unit tensor.
- $p = \dfrac{-tr(\underline{\underline{\sigma}})}{3}$ the isotropic (or spherical) part of the stress tensor which represents the hydrostatic pressure.
- $\underline{\underline{D}}$ the symmetric part of the strain rate tensor. Physically, it corresponds to the irreversible viscous transfer which occurs between volume of fluids that have different velocities, and accounts for internal friction into the fluid. This tensor must have a zero value if the fluid is at rest, and therefore depends only on the spatial variation of velocities. For small variations of velocities, it is supposed that it depends only on the first order derivative. The strain rate tensor is also symmetrical (i.e. independent of uniform rotation), thus each component is given by:

$$d_{ij} = \frac{1}{2}\left(\frac{\partial v_i}{\partial x_j} + \frac{\partial v_j}{\partial x_i}\right)$$

- η (Pa.s) the shear viscosity of the fluid (constant for a Newtonian fluid), accounting for the friction between different layers of fluid when flowing.

In the case of simple shear, for example when a fluid is confined between two flat parallel plates (two-dimensional flow) (see figure 1.2 (b)) in the (x, y) plane, the velocity has the following expression: $v_x = \dfrac{v_0}{h}y$ and $v_y = v_z = 0$, thus the stress tensor is re-written as:

$$\underline{\underline{\sigma}} = \begin{pmatrix} -p & \eta\frac{\partial v_x}{\partial y} & 0 \\ \eta\frac{\partial v_x}{\partial y} & -p & 0 \\ 0 & 0 & -p \end{pmatrix} = \begin{pmatrix} -p & \eta\frac{v_0}{h} & 0 \\ \eta\frac{v_0}{h} & -p & 0 \\ 0 & 0 & -p \end{pmatrix} \tag{1.7}$$

Thus for a Newtonian fluid in simple shear the internal stresses of the system are characterized by one scalar: $\tau \equiv \eta \frac{\partial v_x}{\partial y}$. Equation 1.7 reduces to:

$$\tau = \eta\dot{\gamma} = \eta\frac{\partial v_x}{\partial y} \tag{1.8}$$

with $\dot{\gamma} = \frac{v_0}{h}$.

Equation 1.8 is very general and is commonly used to define what is a Newtonian fluid. For non-Newtonian fluids, the relation between the velocity gradient and the stress is a priori unknown. Therefore, it is necessary to rewrite equation 1.7 in terms of the deviatoric part of the stress tensor $\underline{\underline{\tau}} = \underline{\underline{\sigma}} + p\underline{\underline{I}}$ which corresponds to the general expression of the internal stresses of the material, thus leading to equation 1.9 :

$$\underline{\underline{\sigma}} = \begin{pmatrix} -p+\tau_{xx} & \tau_{xy} & 0 \\ \tau_{xy} & -p+2\tau_{yy} & 0 \\ 0 & 0 & -p+2\tau_{zz} \end{pmatrix} \tag{1.9}$$

The flow is characterized by 3 quantities built from non-zero components of the stress tensor. From equation 1.9 it reduces to:

- the shear stress $\tau = \tau_{xy}$
- the first difference of normal stresses, noted $N_1 = \tau_{yy} - \tau_{xx}$
- the second difference of normal stresses, noted $N_2 = \tau_{yy} - \tau_{zz}$

1.1.2.1 Flowing fluids

Considering any fluid flow, it is always possible to write the momentum conservation on a volume of fluid $\mathcal{V}$ moving with its constitutive particles. Applying the second Newton's law of motion to a volume of fluid, i.e. equating the temporal variation of momentum to the sum of the forces exerted on the volume (i.e. surface forces from the stress tensor, and volume forces) [54], produces the following local equation:

$$\rho\left(\frac{\partial v_i}{\partial t} + v_j v_{i,j}\right) = \sigma_{ij,j} + \rho f_i \tag{1.10}$$

Equation 1.10 is written in general index notation (with $v_{i,j} = \frac{\partial v_i}{\partial x_j}$), ρ standing for the density of the fluid, v_i the i-th component of its velocity, and f_i the i-th component of the volume forces. Equation 1.10 expresses the momentum conservation and reduces to the Navier-Stokes equation in the case of a Newtonian fluid. The left member of the equation represents the inertial term, which is non-linear and comes from the temporal derivative of the momentum of the considered volume of fluid. In the following we assume that the flow is steady and that this term is small compared to the term arises from internal stresses of the material (i.e. viscous stresses for a Newtonian fluid). Under this assumption, equation 1.10 reduces to the *Stokes' equation*:

$$0 = -\vec{\text{grad}}(p) + \eta\Delta\vec{v} + \rho\vec{g} \tag{1.11}$$

For a fluid of unknown constitutive law, equation 1.11 becomes:

$$0 = -\vec{\text{grad}}(p) + \text{div}(\underline{\underline{\tau}}) + \rho\vec{g} \tag{1.12}$$

1.1.3 Fluid/fluid interfaces

Many systems, such as the ones studied during this thesis are two-phase systems. When the two phases are immiscible, the system is characterized by the presence of stable interfaces which may deform and change the whole dynamic of the flow. Here, we consider gas/liquid interfaces, or liquid/liquid interfaces.

Fluid interfaces (such as soap films) exhibit a behavior characteristic of elastic membranes under tension (fig. 1.3 from [55]): the soap film pulls the thread, forcing it to arrange into circular arcs. The normal force per unit length applied to the thread is called surface tension.

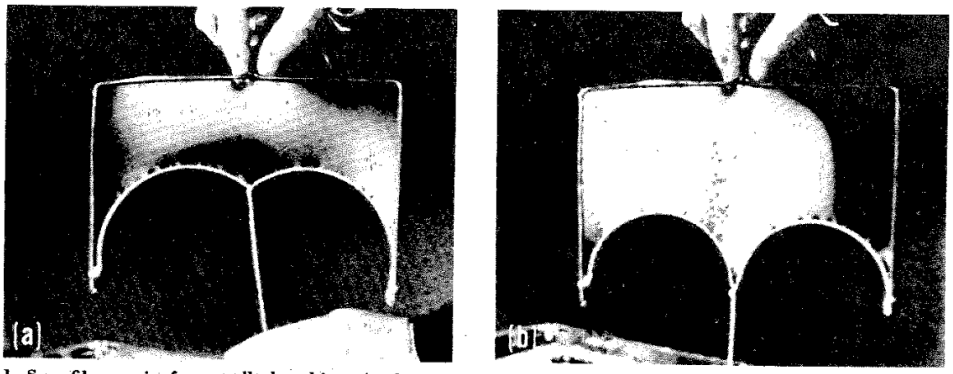

1. Soap film on wire frame pulls thread into circular arcs. The film can be enlarged by doing work, by drawing the string down. This pulls more molecules onto the surface to make it larger.

Figure 1.3 – Liquid soap film experiment, from [55].

1.1.3.1 Definition of surface tension

For Newtonian fluids the surface tension is well defined and arises from lack of cohesive interactions of the molecules located at the interface. To compensate, the molecules adjust their position to minimize the surface. The liquid takes the form of a sphere when no other forces are involved. The surface tension can be expressed through the work necessary to increase the liquid surface of one unity:

$$\delta W = T dS \tag{1.13}$$

with δW the elementary quantity of work necessary to increase the surface of the area of the surface element dS, T the surface tension, expressed in N/m. $T = 0.023$ N/m for ethanol; $T = 0.072$ N/m for water; $T = 0.485$ N/m for mercury [56].

1.1.3.2 Laplace pressure

For curved interfaces such as drops or bubbles, there is a pressure jump at the interface which accounts for the energy necessary to deform the interface with respect to the plane case. This pressure jump is

called *Laplace pressure*. It can be derived by considering the total work undergone by an interface during any deformation [53], and is expressed as:

$$\Delta p_\gamma = T\left(\frac{1}{R_1} + \frac{1}{R_2}\right) \tag{1.14}$$

With, R_1 and R_2 the two principal radii of curvature of the interface, and T the surface tension. The pressure is always higher on the concave side of the interface.

1.1.3.3 Fluid interfaces under gravity

When an interface is subjected to gravity its shape may differ from what is predicted by surface tension only. Figure 1.4 shows drops of mercury on a flat glass plate: the largest drop is flattened by gravity and therefore not spherical, whereas the smallest has a shape that is close to a sphere. The transition between these two regimes occurs when surface tension balances the gravity stress acting on the drop. Denoting κ^{-1} the critical length corresponding to the transition between these regimes, the balance between the hydrostatic pressure (ρ being the density of the fluid) and the surface tension forces leads to:

$$\rho g \kappa^{-1} = \frac{T}{\kappa^{-1}}$$
$$\kappa^{-1} = \sqrt{\frac{T}{\rho g}}$$

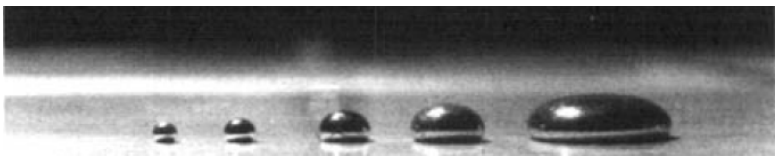

Figure 1.4 – Deformation of mercury drops of different sizes under the action of gravity. The smallest drop has a diameter close to 2 mm. The mercury does not spread on glass. From [54].

κ^{-1} is the capillary length, its value is around 2 mm for most liquids. Finally, to determine whether the effect of gravity are large compared to surface tension, we use the *Bond* number which compares the gravity stress to the capillary stress, or equivalently the capillary length to the characteristic length (R) of the problem: $Bo = \left(\frac{R}{\kappa^{-1}}\right)^2 = \frac{\rho g R}{T R^{-1}}$. For $R \gg \kappa^{-1} \Leftrightarrow Bo \gg 1$ gravity dominates, whereas for $R \ll \kappa^{-1} \Leftrightarrow Bo \ll 1$ capillarity dominates.

1.1.3.4 Surface active agents (surfactants)

The magnitude T of surface tension forces may vary depending on various parameters such as temperature, or bulk phase pressure. Surface tension value and interface properties are also drastically modified by the addition of surface active agent (*surfactant*) [56–58]. These surfactant molecules, such as polymers, amphiphilic molecules, proteins, or small particles, are adsorbed at a fluid interface and may change its properties [58].

The value of surface tension (T) depends on the surfactant concentration c in volume (figure. 1.5). This process can be described by *Gibbs' adsorption law* [57]. At high concentration, the surface tension value stops to decrease and reaches a plateau, which defines a concentration threshold. For amphiphilic molecules, this threshold corresponds to the point where all interfaces are covered by a monolayer of

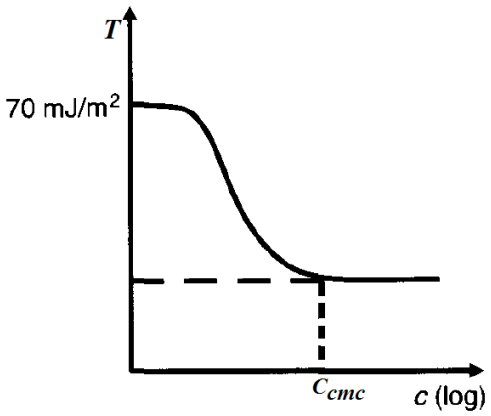

Figure 1.5 – Typical variation of surface tension T as function of the surfactant concentration, adapted from [56].

surfactant molecules, and micellar structures, made by assembly of surfactant molecules, start to form spontaneously in the bulk [56, 57]. This concentration is called the *critical micellar concentration* and denoted *cmc*. For sodium dodecyl sulfate in water its value is 8.10^{-3} mol/L [57].

An adsorbed monolayer of surfactant molecules also confers complex rheological properties to interfaces [58]. Depending of the nature of the molecules, it may add further elasticity to interfaces, modify their tangential forces and also increase the viscosity of the continuous phase in dispersion of droplets or bubbles inside another liquid [58, 59].

Finally, when interfaces are created, such as during a bubble formation process, surfactant molecules initially in the bulk take some time to be adsorbed at the new interface. Therefore, if the rate of production of interfaces is faster than the adsorption time (i.e. a diffusive process) of surfactant, surface tension becomes a dynamical property of the system [57].

1.1.4 Non-Newtonian fluids

Many fluids possess a microstructure of intermediate scale between the size of their molecules and the macroscopic scale, such as small droplets, particles of various shapes, or entangled polymers. Most of them do not obey Newton's law (eq. 1.8) and therefore are called non-Newtonian. They exhibit a non linear relationship between shear rate and shear stress, formally noted $\tau = f(\dot{\gamma})$. Figure (1.6) and table (1.1) detail the most common types of complex fluids encountered, and their 1-D constitutive law in shear geometry. The Newtonian case is also shown for sake of comparison. For 3-D tensorial expressions see [6, 7].

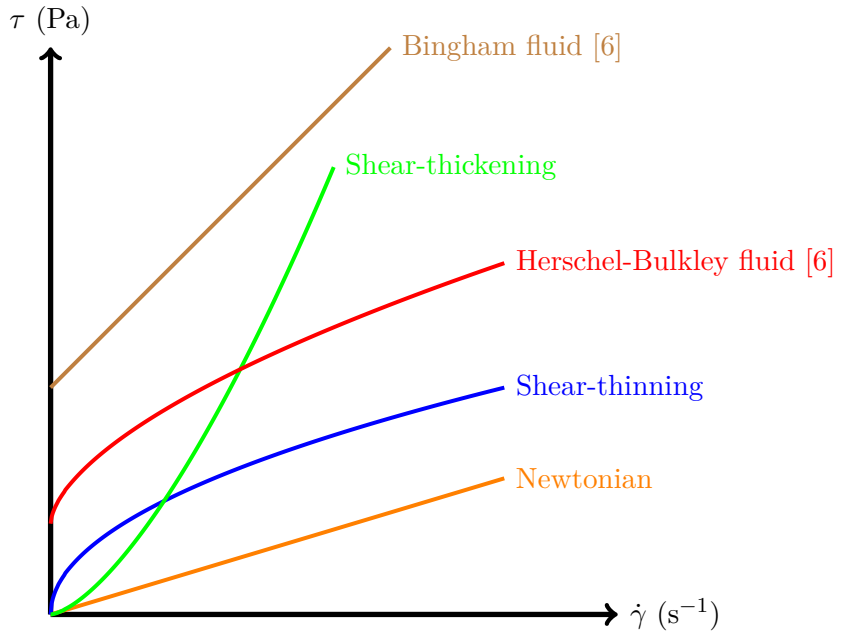

Figure 1.6 – $\tau = f(\dot{\gamma})$ for the most common behavior of materials

Constitutive law	$\tau = f(\dot{\gamma})$	Examples
Newtonian	$\tau = \eta\dot{\gamma}$	water, air
Shear-thinning	$\tau = k\dot{\gamma}^n$, with $n < 1$	blood, paints, glues
Shear-thickening	$\tau = k\dot{\gamma}^n$, with $n > 1$	Corn starch dissolved in water (Maizena)
Bingham fluid [6]	$\tau = \tau_y + k\dot{\gamma}$	some dense suspensions of particles mud from petroleum industry toothpaste, mayonnaise
Herschel-Bulkley [6]	$\begin{cases} \dot{\gamma} = 0 & \text{if } \tau < \tau_y \\ \tau = \tau_y + k\dot{\gamma}^n & \text{if } \tau > \tau_y \end{cases}$	some lava flows, ketchup emulsions, some hair gels (polymers)

Table 1.1 – Tabular summarizing the behavior of the most common type of fluids, with: τ_y (Pa) the yield-stress, when the applied stress is below the yield-stress the material behave like an elastic solid, and like fluid otherwise; k (Pa.s^n) the consistency index, which can be used to define an effective viscosity: $\eta_{eff} = k\dot{\gamma}^{n-1}$ (Pa.s); n the flow behavior index.

1.1.4.1 Yield-stress Fluids

Among the types of constitutive law presented in figure 1.1, two of them (Bingham and Herschel-Bulkley fluids [6]) exhibit a parameter named yield stress (τ_y). This parameter accounts for the self-organization of the microstructure of the fluid at low level of applied stress. If the elements of the microstructure are concentrated enough they may create a contact network which is able to handle stresses through elastic deformations. However, if the level of applied stress overcomes the yield stress then the microstructure of the material begins to disorganize or rupture and the contact network progressively breaks down. Thus, the material starts to flow.

Consequently, considering a yield-stress fluid, equation (1.5) holds for $\gamma < \gamma_c$, with γ_c the critical deformation corresponding to the beginning of yielding and flow such as $\gamma_c \simeq \frac{\tau_y}{G}$. However for $\gamma > \gamma_c$ or $\tau > \tau_y$ a constitutive law for fluid behavior is needed, as given in figure 1.1.

In this thesis, we use two model fluids: a carbopol gel and an emulsion, both behaving like Herschel-Bulkley fluids. In the following, we first present their microstructure and the preparation procedure, then we give their rheological characterization.

1.2 Microstructure of the model yield-stress fluids

Two model yield-stress fluids presenting different microstructure but the same constitutive law are used:

- ➤ an oil-in-water emulsion, constituted of oil droplets dispersed in an aqueous phase.
- ➤ a 980 carbopol gel, constituted of small *blobs* of cross-linked weakly-bounded polymer chains.

These two materials are known to exhibit viscoelastic properties and not to be thixotropic materials: for constant applied shear rate, their viscosity does not depend on the time. Thixothropy is generally due to a slow destructuration of the material under a given solicitation [6], but is not observed for carbopol gel and emulsions. Therefore Carbopol gels and oil-in-water emulsions are regarded as good model of simple yield-stress fluids, and their behavior is well described by the Herschel-Bulkley model [60–64].

1.2.1 Emulsion

1.2.1.1 Generalities

Emulsions, constituted of a dispersion of small droplets of one phase in another immiscible phase, are often encountered in our daily life through common products such as vinaigrette. Emulsions exhibit different behavior depending on their concentration of droplets. For low concentration of droplets ($\phi \ll 1$, with ϕ the droplet volume fraction) droplets are independent of each other and emulsions exhibit mostly the property of their continuous phase when flowing. This is called the dilute regime. However when droplets are strongly concentrated they start to be deformed by the contact (through a thin film of continuous phase) of their neighbors. This happens when $0.64 \leq \phi$, where 0.64 corresponds to the value of the random close packing for monodisperse spherical particles without cohesive forces [65]. At this point the system of droplets is able to handle stresses without flowing, through the elastic deformation of the contact network. This elasticity also arises from the deformation of the interface of each individual droplet which are able to store more energy under stress. The system behaves like a soft elastic solid. However past a critical deformation γ_c (or stress τ_y), the contact network breaks apart and the emulsion starts to flow [6, 7, 61]. In other words, concentrated emulsions are yield-stress fluids.

Emulsions are examples of non-equilibrium thermodynamic systems, therefore their production requires an initial amount of energy stored into the droplets interfaces. Consequently, as the system is let to rest it tends to destabilize in order to recover its state of minimum energy (minimum surface area): two separate immiscible phases [57, 61]. Therefore, emulsions must be stabilized to slow down this natural aging process. This is done by adding surfactant molecules that are adsorbed at the interface of droplets [56, 57]. In this way, it is in principle possible to stabilize emulsions for months or even for years. For a surfactant concentration $c > c_{cmc}$ (critical micellar concentration), micelles form in the continuous phase. When the distance between two droplets is less than the effective radius of a micelle, micelles are excluded from the area between the droplets. Thus it creates an osmotic pressure, driven by the concentration of micelles in the continuous phase, which tends to form aggregates of droplets (called flocs) [66]. This depletion mechanism resulting in an aggregation of droplets is called flocculation.

However, emulsions are still prone to aging. Molecules of a fluid inclusion can diffuse through the droplet interface. The driving force of this process is the *Laplace pressure*: molecules from small fluid inclusions diffuse with a larger flux than molecules from large fluid inclusions. Larger droplets get larger, and smaller droplets get smaller until they disappear. Thus (i) the mean size of drops (or bubbles) increases, (ii) the number of drops (or bubbles) decreases. This classical process is one of the most significant aging phenomenon and is called *Ostwald coarsening*. It occurs in the same way for liquid foams [67]. Thus, emulsions with a narrow droplet distribution tend to be more stable in time.

The preparation of such concentrated emulsion is detailed in the following sections.

1.2.1.2 Production

As previously mentioned, it is necessary to bring an initial amount of energy to the system which must be transferred to the droplet interfaces. This is usually done by the simultaneous mechanical shearing of the two phases. The dispersion of one phase into droplets occurs if the viscous stress is large enough to overcome the capillary stress. The comparison between the viscous stress and the capillary stress is usually depicted under the form of a non-dimensional number: the capillary number, denoted Ca. Its expression is given by considering the order of magnitude of the stresses at play.

- The order of magnitude of the capillary stress is given by $\frac{T}{a}$ for an object of typical size a.
- The order of magnitude of the viscous forces may be determined by considering the expression of the stress tensor (eq. 1.2). For a Newtonian fluid under simple shear flow, where the typical velocity is V around an object of size a, a will also set the typical size of variations of the velocity gradients of the flow around the object, thus eq. 1.8 allows to determine that $\tau \sim \frac{\eta V}{a}$.

The capillary number is then defined as the ratio of the order of magnitude of the viscous forces to the capillary forces, thus:

$$Ca = \frac{\eta V}{T} \tag{1.15}$$

For $Ca \gg 1$ the capillary forces may be neglected, whereas for $Ca \ll 1$ the viscous forces may be neglected.

The dispersion of one phase into another has been first studied by Taylor [68] by placing a drop of one liquid into an extensional flow (or into a simple shear flow) of another liquid. These two flows are well defined and allow to consider that the dominant stress acting on the drop is due to the viscous force. The break-up results from the balance between the tendency of the system to minimize its surface area, thus resisting any extension or shear, and the viscous stresses of the flow.

Assuming an ellipsoidal shape for drops under deformation (major axis a_e, minor axis b_e), and that break-up occurs when the deformation ($\epsilon_T = \frac{a_e - b_e}{a_e + b_e}$) is of order $\frac{1}{2}$, Taylor derived the final radius of droplets: $R_d = \frac{TCa_{crit}}{\eta_c \dot{\gamma}}$ which depends on the ratio of surface tension to viscous forces, (η_c being the viscosity of the continuous phase, and T the surface tension). Ca_{crit}, the critical capillary number for break-up to occur, is computed from the pressure jump between the inside and the outside of the drop [69] and depends on its deformation. It has been demonstrated later that Ca_{crit} depends itself on the viscosity ratio between the two phases [70]. Practically, it is interesting to note that the radius of resulting droplets depends on the shear rate $\dot{\gamma}$. To obtain a monodisperse emulsion, it is then necessary to apply to the system a shear that is as homogeneous as possible.

In this spirit, our emulsions were produced using a *Couette Emulsifier* (figure 1.7, manufactured by the company TSR [71]) which consists of:

- a classical Couette cell, with fixed outer cylinder (r = 40mm) and a rotating inner cylinder. The gap between the two cylinders is 143 μm. This is in principle small enough to provide an homogeneous shear rate throughout the gap. It is possible to vary the shear rate in the cell between 90 s^{-1} and 17000 s^{-1}
- a syringe pushed at constant speed to fill the Couette cell with the initial mixture.

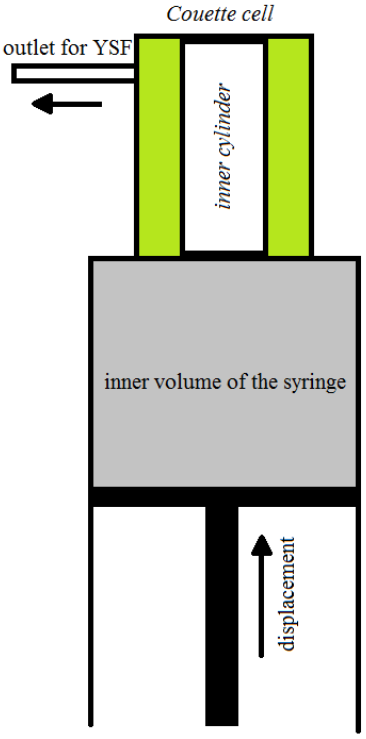

Figure 1.7 – Sketch of the Couette emulsifier.

However this emulsifier does not allow to produce emulsions from simple liquids. The initial mixture injected into the cell must have visco-elastic properties [72]. To match this requirement a gross emulsions, mixed by hand, is produced and then injected into the Couette cell. The droplet diameter obtained after the whole process (i.e. hand-mixing + Couette emulsifier) lies in the range 1 μm - 10 μm (Fig. 1.8).

The rotation speed of the inner cylinder is varied between 600 rot/min, and 500 rot/min, thus allowing to modify the shear rate and the size of the resulting droplets. The injection velocity is always set at its maximum value $\sim$ 0.5 cm/min.

1.2.1.3 Formulation

Our emulsions are prepared from:

- Silicone oil (Sigma-Aldrich) for the dispersed phase, of viscosity 20 mPa.s or 350 mPa.s. The volume fraction of oil is varied between 90 and 92 %.
- Glycerol-water (50-50, or 53-47 wt. %) mixture for the continuous phase. The glycerol (Sigma-Aldrich) quantity is adjusted to obtain an index-matched final material which is almost transparent. The quantity of each phases necessary to obtain a matched material can be theoretically computed

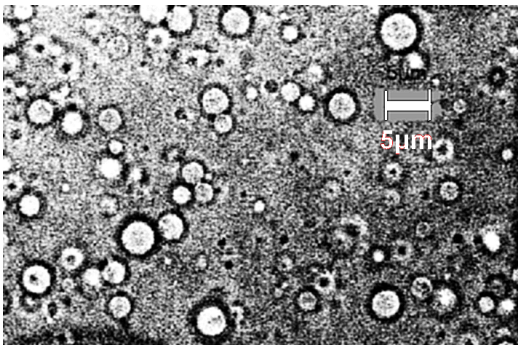

Figure 1.8 – Image (after image processing) of oil droplets from typical emulsion and obtained by optical microscopy. The white scale stands for 5 μm.

using the *Lorentz-Lorenz equation* [73]. However, due to variation of structural properties of chemicals depending on manufacturers, our emulsions are index-matched by fine-tuning the quantity of glycerol in the continuous phase.

➤ To stabilize the emulsion we add TrimethylAmonium Bromid (TTAB) from Sigma-Aldrich. These molecules possess a hydrophilic head (ammonium) and a hydrophobic tail. 3 wt. % of the aqueous phase are used: this is enough to stabilize the emulsion but not enough to induce flocculation that may change the rheological behaviour of the emulsion through short range attractive forces [66, 73, 74].

It is also interesting to note how the emulsions composition affects the values of the parameters of the Herschel-Bulkley model parameters ([74], and figure 1.2):

➤ The viscosity of the dispersed phase has almost no influence on the parameters.

➤ The larger the viscosity of the continuous phase, the larger the value of the consistency k.

➤ The larger the surface tension T between the two liquid phases the larger the yield-stress τ_y.

➤ The larger the volume fraction of droplets ϕ, the larger the yield-stress τ_y.

1.2.2 Carbopol

1.2.2.1 Generalities

Carbopol gels are constituted of cross-linked (by means of ionic interactions) polyacrylic acid (PAA) resins. When mixed with water, the PAA resins, which looks like a white powder, gives a solution of acid pH that must be neutralized with a base to obtain a gel. The neutralization generates ionic repulsions between the polymer chains which adopt an extended, cross linked configuration [63]. These weak interactions, characteristic of a physical gel, may be broken when the gel is forced to flow, and reform when the gel is let to rest. However, the exact organization of the chains is not exactly known. It seems that polymers arranges in almost spherical blobs swelling in water like sponges [60, 63, 75] until the osmotic pressure inside the blob balances the pressure inside the solvent [76]. The size of the micro-structure of individual sponges seem to depend on the carbopol manufacturer. It is roughly of the order 100 μm [60]. According to [63] it should be between 2 μm and 20 μm. This is of the same order of magnitude as the size of oil droplets presented in the previous section.

Above a critical concentration the blobs may start to be deformed by the contact of their neighbours, giving rise to a contact network that is able to handle stresses without flowing. Just as in the emulsion

case it can break-apart if the applied stress is sufficiently large, and then the gel starts to flow, and behaves like a yield-stress fluid.

We only used carbopol gels at sufficiently high concentration (typically 1 wt. %), for the material to develop a significant yield stress. However at this high concentration all the polymer may not be dissolved in the aqueous phase. It manifests as very small shiny particles dispersed in the gel. In the next section we show that this phenomenon does not change the rheological properties of the gel. Finally, the value of the yield stress tends to a finite value as the concentration of polymer is increased [63].

1.2.2.2 Production and formulation

Our Carbopol is prepared from U980-Cooper polymer. The carpobol powder is dispersed in water at the desired concentration. The mixing is performed by a mortar mixer, a planetary mixer which provides an homogeneous mixing throughout the sample. This mixture is sheared during 24 hours at 90 rot/min. Then a base (NaOH at 1 mol/L) is introduced to neutralize the solution, thus the carboxylate groups ionize, creating ionic repulsions. Once the NaOH is introduced mixing continues for 24 hours. This ensures that the system has mostly reached its equilibrium. However reactions may slowly advance during the week following the end of the mixing, and so do the rheological properties of the gel. Therefore, when a carbopol gel is prepared it is let at rest during 3 weeks after the mixing, thus ensuring that the system is at equilibrium.

1.2.3 Surface tension measurement for yield-stress fluids

The surface tension of Newtonian fluids can be measured easily (for example using *Du Nouy ring*, *Wilhelmy plate*, or pendant drop method [54]), however for yield-stress fluids surface tension measurements may be modified by the microstructure of the fluid.

1.2.3.1 Yield-stress fluids

Measuring the surface tension of yield-stress fluid is quite a recent and open topic. While elements constituting the microstructure of the fluids are fully surrounded by liquid, it seems reasonable to expect that the value of the surface tension is the one of the continuous phase [3, 77]. However for more concentrated systems, that is in the limit of a very thin liquid layer around inclusions, measurements may be modified by [78]:

- The microstructure of the fluid [79].
- The necessary role of viscous force that deform the inclusions. This may appear when pulling a plate outside of a liquid bath, and more generally when creating any interface [77, 78].

However such considerations are beyond the scope of this manuscript. Here, we assume that the surface tension of yield-stress fluids is the surface tension of their continuous phase. This is at least verified (within 10 %) for carbopol gels whatever their yield-stress [77] and should also be verified for emulsions [2].

Concerning the surface tension measurements of carbopol gels, it can also be underline that *Gutfinger and Tallmadge* [80] use highly concentrated carbopol gel and measure their surface tension. For highly concentrated carbopol solutions (i.e. that may present a yield stress even if they do not mention either the presence or absence of such property) they find the same surface tension value as in [77].

Finally, providing that the rate of interface formation is slow, we will not take into account surfactant motion but only static surface tension [56].

1.3 Macroscopic characterisation of model yield-stress fluids: shear rheometry, drag flow

The determination of the constitutive law of non-Newtonian materials has become possible through the progressive development of rheological instrumentation [81]. In this section we present the techniques used to measure the 1-D constitutive law of yield-stress fluids described in the previous section. Different geometries are available: (i) concentric cylinders (i.e. Couette cell); (ii) rotating vane; (iii) cone and plate; (iv) parallel plates. All these systems possess their own advantages and disadvantages.

1.3.1 Suitable geometry

For rheometrical measurements, the choice of the geometry is determined by the nature of both the measurement that one would perform and the investigated material.

The majority of the yield-stress fluids used in this thesis are highly concentrated and so exhibit wall slip on smooth surfaces (see chapter 2 for more details). Thus, it is necessary to use a rough geometry, that is either covered with sandpaper or grooved. In this way, the depletion layer is reduced by allowing the microstructure to occupy each individual groove. The simplest geometries that can be covered with sandpaper is the parallel-plates geometry. This geometry has also the advantage of requiring a very small amount of material compared to a Couette cell.

In addition, due to their high concentration in microstructure our yield-stress fluids are prone to exhibit edge failure during free-surface shear flows. It is therefore desirable to use a geometry with as little free surface as possible. The parallel-plate geometry matches this requirement and exhibits less free surface than the cone-plate geometry. However, in this geometry the shear-rate is not constant throughout the gap and depends on the radial position.

Last, when the yield-stress is large the material may exhibit shear banding. To avoid this phenomenon, it is advisable to use a gap as thin as possible [81]. With parallel-plates geometry the gap is easily tunable down to less than 1 mm. Finally, parallel-plates geometries present few inertial effects at high shear rates compared to a Couette cell.

All these characteristics make the parallel-plates geometry a very good match for our requirements. Therefore, in the following parts of this section, all measurements are performed with a parallel-plates geometry of diameter 40 mm, and gap size of 1 mm or 2 mm mounted on a Bohlin C-VOR rheometer. The following paragraphs detail the computation of $\tau_{\theta z}$, N_1, N_2 with plate-plate geometry, as well as the definition of linear visco-elastic functions.

1.3.2 Measurements theory

For computation in the parallel plates case we follow Macosko [81] (as sketched in figure 1.9) and assume: (i) a steady, laminar, isothermal flow; (ii) axisymmetric flow; (iii) negligible volume forces; (iv) flat edges.

In cylindrical coordinates (r, θ, z), with $0 \leq r \leq R$, Ω_r the angular velocity, and h the gap size as shown on Fig. 1.9, the expression of the velocity is $\vec{v} = v_\theta(r, z)\vec{\theta}$, with the following boundary conditions:

- ➤ the top plate is moving at the angular velocity Ω_r: $v_\theta(r, h) = \Omega_r r$
- ➤ the bottom plate is fixed: $v_\theta(r, 0) = 0$

These boundary conditions imply that $v_\theta(r, z) = \Omega_r r f(z)$, with f an unknown function depending on z only. At this point it is necessary to write the equation of motion on θ. Taking into account the previous assumptions equation 1.12 reduces to:

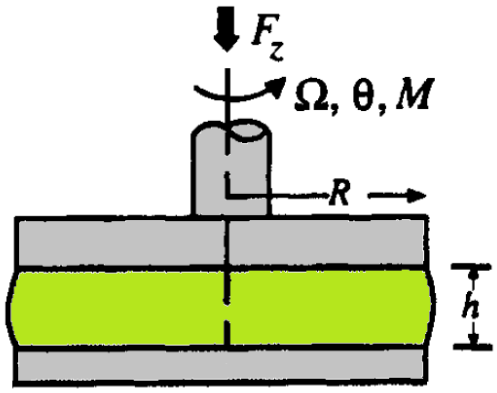

Figure 1.9 – Schematic of a parallel plate rheometer, adapted from [81].

$$\frac{\partial}{\partial z}(\tau_{\theta z}) = 0 \tag{1.16}$$

Finally considering a fluid behaving such as the stress is an unknown function of the velocity gradient: $\tau_{\theta z} = g(d_{\theta z})$ with $d_{\theta z} = \frac{1}{2}\left(v_{\theta,z} + v_{z,\theta}\right)$, replacing into equation 1.16 it leads to $\frac{\partial^2 v_\theta}{\partial z^2} g'(d_{\theta z}) = 0$. Therefore v_θ is linear with respect to z. Thus, the simplest velocity profiles satisfying the hypotheses is:

$$v_\theta = \frac{r\Omega_r z}{h} \tag{1.17}$$

1.3.2.1 Shear-stress

The shear rate is obtained by differentiating equation 1.17 with respect to z:

$$\dot{\gamma}(r) = \frac{\partial v_\theta}{\partial z} = \frac{r\Omega_r}{h} \tag{1.18}$$

To obtain an equation for the shear stress $\tau_{\theta z}$ as a function of measurable parameters it is necessary to write a torque balance on the upper plate of the geometry:

$$M = 2\pi \int_0^R r^2 \tau_{\theta z} dr \tag{1.19}$$

After a change of variable, such as $r = \frac{h\dot{\gamma}}{\Omega_r}$ and $\mathrm{d}r = \frac{R}{\dot{\gamma}(r=R)}\mathrm{d}\dot{\gamma}$ in equation 1.19, it leads to:

$$M = 2\pi R^3 \int_0^{\dot{\gamma}(r=R)} \left(\tau_{\theta z} \frac{1}{\dot{\gamma}(r=R)}\right)^3 \dot{\gamma}^2 \mathrm{d}\dot{\gamma} \tag{1.20}$$

Then, it is possible to obtain an expression of $\tau_{\theta z}$, by differentiation of equation 1.20 with respect to $\dot{\gamma}(r=R)$:

$$\tau_{\theta z} = \frac{M}{2\pi R^3}\left(3 + \frac{\mathrm{d}\ \ln(M)}{\mathrm{d}\ \ln(\dot{\gamma}(r=R))}\right) \tag{1.21}$$

Thus $\tau_{\theta z}$ is computed from a set of values of the torque M and $\dot{\gamma}(r = R)$, which is itself computed from the angular velocity (equation 1.18). However, conventional rheometers such as the one used during this thesis (Bohlin CVOR) are designed for measurement with non-Newtonian fluids, and use a common approximation of equation 1.21 to compute the shear stress:

$$\tau_{\theta z}(r = \frac{3}{4}R \simeq R) = \frac{3}{4}\frac{2M}{\pi R^3} \tag{1.22}$$

This expression is used during all computation done by the rheometer software. It produces a systematic error since the derivative (in eq. 1.21) is generally non-zero for measurements with non-Newtonian fluids [81, 82]. However, the correction needed to obtain the exact value of $\tau_{\theta z}$ is 10 % or 15 % and only changes the value of k for our carbopol gels and emulsions [82].

1.3.2.2 Normal-stress

With plate-plate geometry, it is also possible to obtain an equation for the normal stresses from the momentum balance on r where the inertial term has been neglected. Then, it is possible to make the normal stresses difference (denoted N_1, N_2) appear, and after integration to relate them to normal force F_z. This leads to:

$$F_z = -2\pi \int_0^R (N_2 - N_1) r dr \tag{1.23}$$

After a change of variable and a differentiation it is possible to write:

$$N_1 - N_2 = \frac{F_z}{\pi R^3}\left(2 + \frac{d\ \ln(F_z)}{d\ \ln(\dot{\gamma})(r = R)}\right) \tag{1.24}$$

N_1, and N_2 are the two normal stress differences. Their magnitude gives an idea of the stress normal to the shearing plane during a shear flow. It also manifests as strong source of non-linearity, leading for example to elastic recoil during drop impacts [83]. In confined flows it also may be accounted for the development of shear banding, as can be seen for foam flow in a Couette cell [84]. Finally, the normal stress difference is also known as the driving force of the *Weissenberg effect*: normal forces dominates centrifugal forces and the fluid rises in the direction perpendicular to the plane of motion [54].

Equation 1.24 does not provide the values of N_1 and N_2, but only their difference. Trying to measure the value of normal stress differences in various soft systems (such as yield-stress fluid) is a topic of current research and few measurements exists for emulsions and carbopol gels. However it has been recently observed that $N_2 \simeq -2N_1$ for soft glassy materials with thin films such as emulsions or carbopol gels [85, 86]. Thus, denoting the experimental observed value $\alpha_N = N_1 - N_2$, we assume that:

$$N_1 \simeq \frac{\alpha_N}{3} \tag{1.25}$$

$$N_2 \simeq -\frac{2}{3}\alpha_N \tag{1.26}$$

1.3.2.3 Viscoelasticity

Another usual way to probe the behavior of fluids is to impose sinusoidal oscillations of small amplitude (i.e. not deforming the microstructure of the fluid [87]): $\Omega(t) = \Omega_0 \cos(\omega_f t)$, with ω_f the oscillation frequency. Hence, the deformation is written as:

$$\gamma = \gamma_0 \sin(\omega_f t) \tag{1.27}$$

If $\gamma_0 \ll 1$ the assumption of small deformations is valid ($\tau \propto \gamma$). The shear stress should behave in the same way as the sinusoidal deformation:

$$\tau = \tau_0 \sin(\omega_f t + \delta) \tag{1.28}$$

Decomposing τ into two waves: one in-phase $\tau' \sin(\omega_f t)$, and one out of phase $\tau'' \cos(\omega_f t)$, and substituting with equation 1.27, equation 1.28 yields:

$$\tau = G'\gamma(t) + \frac{G''}{\omega_f}\dot{\gamma}(t) \tag{1.29}$$

or with complex notation:

$$G^* = G' + iG'' \tag{1.30}$$

with $\tan\delta = \dfrac{\tau''}{\tau'} = \dfrac{G''}{G'}$, and $G' = \dfrac{\tau'}{\gamma_0}$, $G'' = \dfrac{\tau''}{\gamma_0}$, with: δ is the phase angle, G' the storage (elastic) modulus, G'' the dissipative (viscous) modulus.

Two limit cases can be distinguished:

- The elastic solid: $G' = G$ and $G'' = 0$
- The viscous Newtonian fluids: $G' = 0$ and $G'' = \eta\omega_f$

For yield-stress fluids, it is thus clear that in solid regime $G' = G$ and that G'' must be low compared to G'. Yet, G'' should also be non-zero due to local rearrangements of the microstructure that involve viscous dissipation. However, in liquid regime there is no possibility to store energy through the contact network, thus implying that $G' < G''$. In the limit of very high shear rate, the contact network should have totally broken apart and G' should go to zero [54].

The value of each modulus is obtained from the measurements of γ, τ, and δ. Measurements of G' and G'' are shown in section 1.3.3.4 (Oscillatory measurements).

1.3.3 Rheometrical measurements

This section contains the results of the rheometrical measurements performed on emulsions and carbopol gels used for the bubble production experiments. Three kinds of measurements are carried out:

- Measurements at imposed shear-rate to determine the yield-stress (yield curves).
- Increasing/decreasing shear-rate ramp to obtain the constitutive law (rheograms), and normal stress differences.
- Oscillatory measurements to obtain the storage G' and loss G'' moduli.

1.3.3.1 Yield curves

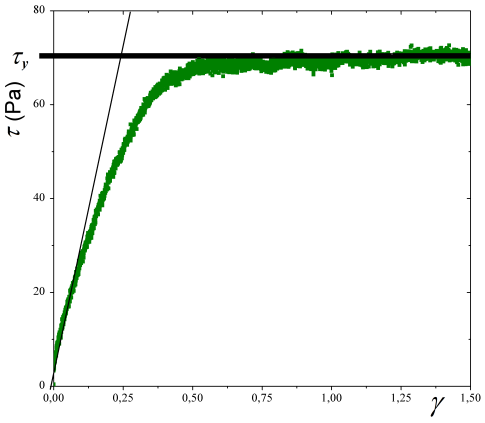

(a) Carbopol - 1 wt. % , $h = 1$ mm, 90 rot/min.

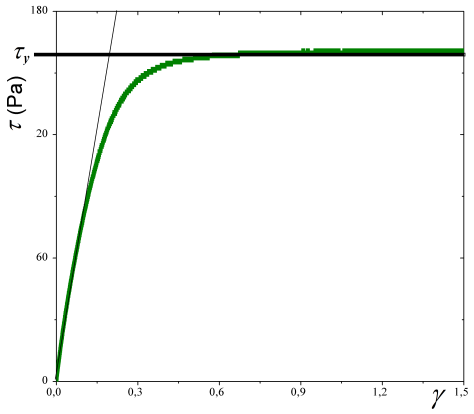

(b) Emulsion, glycerol-water: 53-47 wt. %, 3 wt. % aq. phase TTAB, 90 % oil volume fraction, 550rpm, $h = 1$ mm.

Figure 1.10 – Stress τ as a function of strain γ for carbopol gel, and emulsion.

Figure 1.10 shows stress-strain measurements for the determination of the yield stress. For both emulsion and carbol gel, the stress increases until a critical strain γ_c is attained, beyond which the linear deformation regime breaks down. This defines the end of the linear elastic regime. At some point the stress reaches a constant value that corresponds to the flow of the whole sample. This constant stress value is the yield stress. Once it is attained, the contact network is no more able to store elastic energy, and the material flows. Here, the value of the yield-stress is roughly 70 Pa for the carbopol, and 165 Pa for the emulsion. In addition, from the slope of the linear regime we can extract the value of the shear modulus G of the material which is 100 Pa for the carbopol gel, and 631 Pa for the emulsion. These values are typical of soft solids [6].

1.3.3.2 Rheogram

Figure 1.11 shows the flow curves (i.e. stress as a function of strain rate) for both the emulsion and the carbopol gel. The range of shear-rate investigated is smaller for emulsion. This is due to the high yield stress of this material which is prone to exhibit much more shear-banding than a material with a smaller yield stress. These curves are well fitted by the Herschel-Bulkley model. The extracted parameters from these two curves are summarized in the following table 1.2.

These parameters are consistent with measurements on carbopol gels [62, 78] and emulsions of equivalent composition [2, 74].

Finally, as mentioned in the section 1.2.2 the carbopol gel is prepared with 1 wt. % of polymer, and all the polymer may not be dissolved in water. However, this does not seem to affect the rheological behaviour of the gel which follows the classical Herschel-Bulkley law as seen on figure 1.11 (a).

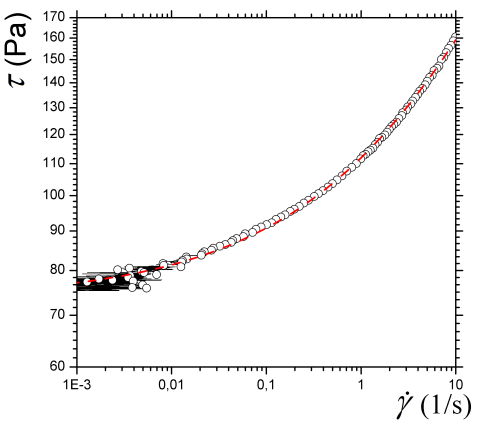

(a) Carbopol, $\tau_y = 75$ Pa.

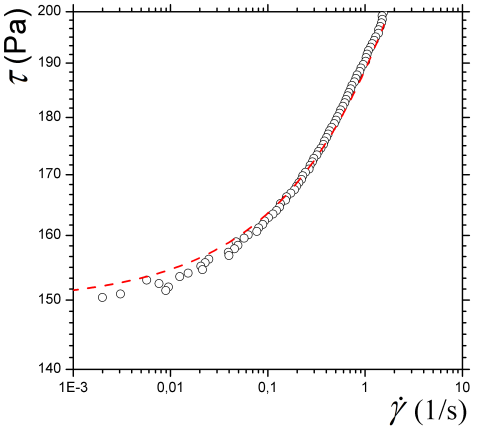

(b) Emulsion, $\tau_y = 100$ Pa.

Figure 1.11 – Stress τ as a function of strain rate $\dot{\gamma}$ for carbopol, and emulsion. Red dashed lines stand for the Hershel-Bulkley model fit.

Fluid	Composition	Ω (rot/min)	T (mN/m)	τ_y (Pa)	k (Pa.s^n)	n
Carbopol	C980, 1% w.t.	90	66	73.7	38.22	0.35
Carbopol	C980, 0.3% w.t.	90	66	22.5	11.2	0.35
	90% vol. V20 silicon oil					
Emulsion	3 % w.t aq. phase TTAB	550	35	149.35	39	0.45
	53-47% w.t. glycerol-water					
	92% vol. V350 silicon oil					
Emulsion	5 % w.t aq. phase TTAB	600	35	330	?	?
	50-50% w.t. glycerol-water					
	92% vol. V350 silicon oil					
Emulsion	5 % w.t aq. phase TTAB	550	35	265	∼100	0.5
	50-50% w.t. glycerol-water					
	92% vol. V350 silicon oil					
Emulsion	5 % w.t aq. phase TTAB	500	35	165	∼100	0.5
	50-50% w.t. glycerol-water					
	92% vol. V20 silicon oil					
Emulsion	3 % w.t aq. phase TTAB	500	35	100	∼70	0.5
	53-47% w.t. glycerol-water					

Table 1.2 – Summary of parameters of the Hershel-Bulkley model measured with parallel-plates geometry for emulsions and carbopol gels.

1.3.3.3 Normal stress

During the measurement of the flow curves (rheogram), the normal force F_z exerted by the fluid on the disc is also recorded. This allows to compute from equation 1.24 the first normal stress difference, $N_1 - N_2$ as function of $\dot{\gamma}$ for both carbopol gel and emulsion, as presented on figure 1.12.

As seen on figure 1.12, at low shear rate $N_1 - N_2$ tends to a finite value, whereas it increases at higher shear rate. This behavior is predicted by the classical model for the flow of soft glassy materials described in [85]. This model takes into account elastohydrodynamic interaction between the deformed inclusions of the microstructure and the lubrication that occurs through the thin films that takes place between the inclusions. This micromechanical model also predicts the exponent of the increase in

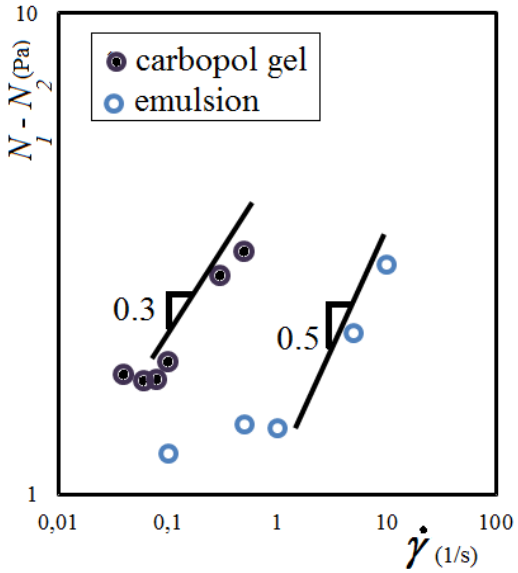

Figure 1.12 – $N_1 - N_2$ as a function of the applied shear rate for an emulsion and a carbopol gel.

normal stresses: for fluids with an Herschel-Bulkley flow index of 0.5 it yields $N_1 - N_2 \propto \dot{\gamma}^{0.5}$. This prediction agrees very well with the observed experimental behavior for our emulsion ($n = 0.5$).

Although this case is not developed in [85], the presented scaling suggests that for material exhibiting a flow index n which differs from 0.5, the relationship between the normal stresses and the shear rate might become: $N_1 - N_2 \propto \dot{\gamma}^n$. Therefore, for our carbopol gel with $n = 0.35$ the increase of $N_1 - N_2$ should follow a line of slope 0.35 in log-log plot. This result is in good agreement with the experimental data of figure 1.12.

By means of these measurements, we can estimate the order of magnitude of elastic effects during flows in confined geometries. This can be done by comparing the viscous stress to the normal stress, using the Weissenberg number $Wi = \dfrac{N_i}{k\dot{\gamma}^n}$ [88]. Since our emulsion and carbopol follow the micromechanical model for the flow of soft glassy material [85], we follow the experimental observation of [85] and assume that the normal stresses are linked: $N_2 \simeq -2N_1$. Thus, we determine N_1 and N_2 using equations 1.25, 1.26. Then, the corresponding Weissenberg numbers are defined as:

$$Wi_1 = \frac{N_1}{k\dot{\gamma}^n} \tag{1.31}$$

$$Wi_2 = \frac{|N_2|}{k\dot{\gamma}^n} \tag{1.32}$$

The value of N_1 and $|N_2|$ computed from equations 1.25, 1.26 are presented as functions of the applied shear rate on figures 1.13a and 1.13b. For both carbopol gel and emulsion, the computed value of N_1, N_2 are always less than 10 Pa. These values must be compared to the value of the viscous stress to estimate the effect of normal stresses during the flow.

The corresponding Weissenberg numbers are also plotted as function of the applied shear rate on figures 1.13c and 1.13d. For emulsion, the Weissenberg number seems to be larger at low shear rate, whereas for carbopol the low shear rates leads to low Weissenberg number. In spite of this difference we can note that $Wi < 0.1$, this suggests that, in our materials, normal stresses are always negligible compared to viscous stresses. This hypothesis, although based on rough measurements is in agreements with the results of experiments in confined geometry (see chapter 3).

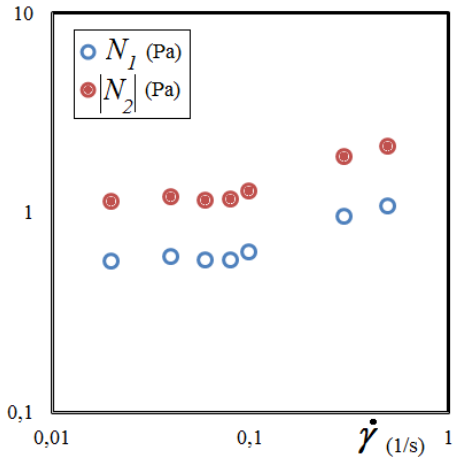

(a) First and second normal stress difference as function of the applied shear rate for carbopol gel.

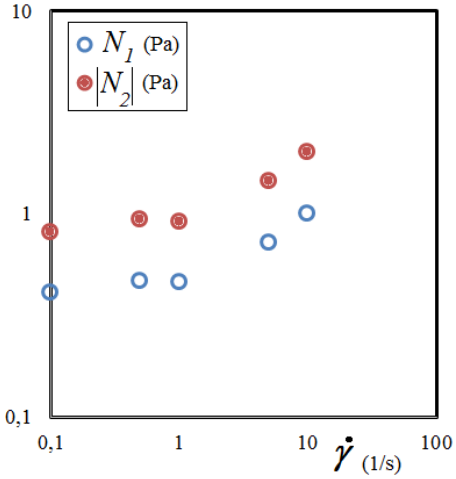

(b) First and second normal stress difference as function of the applied shear rate for emulsion.

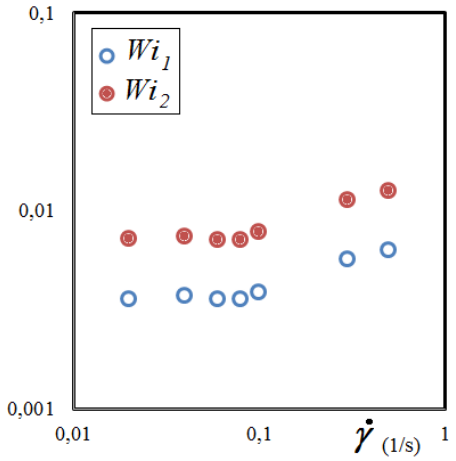

(c) Weissenberg numbers, built on the first and second normal stress difference as function of the applied shear rate for carbopol gel.

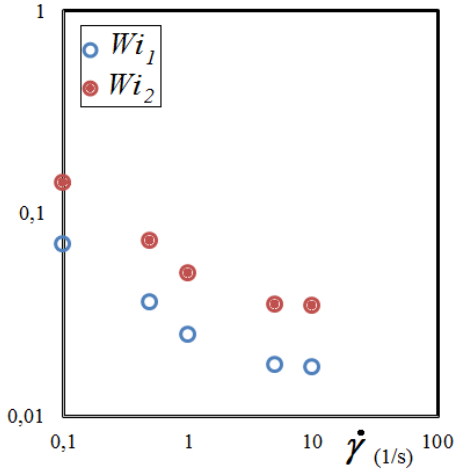

(d) Weissenberg numbers, built on the first and second normal stress difference as function of the applied shear rate for emulsion.

Figure 1.13 – Normal stresses in emulsion ($\tau_y = 100$ Pa) and carbopol gel ($\tau_y = 75$ Pa).

1.3.3.4 Oscillatory measurements

Figure 1.14 shows the values of the elastic modulus G' and the loss modulus G'' as a function of strain, determined by amplitude sweep.

The material is sheared back and forth at larger and larger strain, but at low frequency to avoid dynamic disturbances (i.e. edge failure, shear banding, or inertial perturbations). For both carbopol and emulsion the same typical behavior is observed:

- for $\gamma < \gamma_c$, $G' > G''$ which is typical of a solid regime where elastic storage of energy dominates with respect to hydrodynamic viscous energy loss.
- for $\gamma > \gamma_c$, $G'' > G'$ which shows that the contact network as broken apart and that energy loss becomes mostly viscous.

This behavior is typical of yield-stress fluids. Finally, it should be noted that for $\gamma > \gamma_c$, both

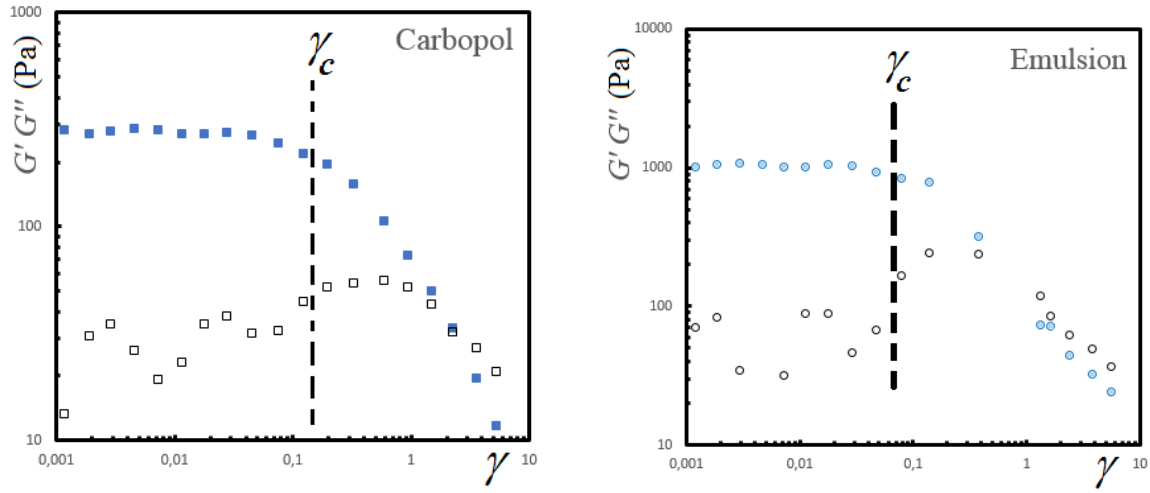

(a) Carbopol gel, $\tau_y = 75.$ Pa.

(b) Emulsion, $\tau_y = 100$ Pa.

Figure 1.14 – G' (blue - plain symbols) and G'' (black - empty symbols) as a function of strain γ for emulsion and carbopol gel at 0.05 Hz. With $h = 1$ mm, and plates of radius 2 cm.

moduli decrease rapidly as γ increases. This may be associated with the rapid breakdown of the material structure.

1.4 Conclusion

In this chapter we presented the general behavior of materials in the continuum mechanics framework, and the simplified equations related to shear flows. The two model yield-stress fluids used for the experiments are also presented. Their microstructure is described as well as their rheometrical behavior in shear flow.

Essential facts

- Emulsion and carbopol are choosen as model yield-stress fluids. Their rheological parameters can be easily varied.
- Their behaviour in shear flow is well represented by Herschel-Bulkley model.

$$\begin{cases} \dot{\gamma} = 0 & \text{if } \tau < \tau_y \\ \tau = \tau_y + k\dot{\gamma}^n & \text{if } \tau > \tau_y \end{cases} \tag{1.33}$$

- These materials exhibit normal stresses during shear flow, which may be neglected compared to viscous stresses.

2

Yield-stress fluid flow in circular channels

In this chapter, we describe the flow of yield-stress fluids in circular channel of millimetric radius. We first provide the solution of the equation of motion for a fluid flowing in a circular channel with no-slip boundary conditions and following the Herschel-Bulkley behavior (equation 1.33). The expression for the pressure drop relation is obtained from the expression of the velocity profiles. In a second part, the topic of wall slip is addressed. First, we recall the most recent results concerning wall slip of soft materials. Secondly, solutions to take wall slip into account during yield-stress fluid flow in circular channels are proposed. Finally, experimental results obtained using our system as a capillary rheometer are presented and compared to results obtained from parallel-plate rheometer. In the last part we consider the case of yield-stress fluid slug flow.

Contents

2.1 Microchannel: fabrication and characterization

The channels and millifluidic geometries used during this thesis were manufactured by stereolithography. In this section, we present the principle of this prototyping method, the material used for the fabrication of our channels, and the different geometries that were produced.

Stereolithography (STL) is a rapid prototyping technique that enables the fabrication of freeform parts with a precise geometry [50]. Beyond classical prototyping of small parts for industry or research, recently, STL has been used extensively for the fabrication of biomedical parts, such as implants [51].

The basic principle of STL is to polymerize successive layers of photo-polymers. This allows to produce parts with dimension of the order of a few centimeters and sub-millimetric resolution. The whole fabrication process can be summarized as follow:

- The design of any part begins by creating a file containing the information on the desired geometry. This can be easily achieved by using a computer assisted design (CAD) software. The part built during this thesis were originally designed using FreeCAD [1].

- The building process itself reduces to the controlled displacement of a laser on the surface of a bath of liquid photo-polymeric resin. If the laser communicates a sufficient amount of energy to the photo-polymer, it starts to reticulate by creating chemical bounds, therefore solidifying over a given depth. This depth must be large enough to allow the first layer to adhere to a support platform. Then, the platform is taken down of one step, once it is covered by the liquid polymer resin, the polymerization of the second layer starts. The process continues until the top of the part is reached, in this way, the whole part is built layer by layer.

  The laser is driven by the STL apparatus which divides the CAD file into slices of the desired resolution and builds the part. The fabrication of our devices is carried out with a vertical resolution of 50 μm, and a laser spot resolution of $\simeq 10\mu$m. Our devices were manufactured by U.S. company "FineLine Prototyping, Inc.".

The resin must be a liquid that solidify rapidly after exposition to a laser beam. Thus, most of the resin are photo-polymers that form a cross-linked network when sufficient luminous intensity is transmitted to them.

In order to obtain transparent devices, and be able to image the flow inside the microchannels, we have chosen transparent resin having similar look and feel to *Acrylonitrile butadiene styrene* (ABS), and sold under the name: "Watershed XC 11122", and manufactured by "Somos". This resin possess the advantages of transparency and resistance to water.

2.1.1 Geometries

Different geometries are manufactured, they are summarized in figure 2.1. Each geometry consists in a junction used to disperse the gas inside the yield-stress fluid, and an outlet channel to carry the bubbly yield-stress fluid out of the chip, where the material may eventually be retrieved. In the following, if nothing is specified, the cross-section of all channels on the chip are considered to have a circular cross section and the same radius.

2.1.1.1 Junctions

Two main different junctions were manufactured: (i) T-junction, and (ii) flow-focusing devices. These two classical microfluidic geometries are presented on figure 2.1. Since these geometries are usually built by classical soft lithography [47–49], in most of the previous work the channels are rectangular.

[1] Licence GPL, http://www.freecadweb.org/index-fr.html

ID	Junction	Outlet channel length (cm)	Radius (mm)	details
TJ01	T-junction	10	0.5	straight channel
TJ02	T-junction	10	1	straight channel
TJ03	T-junction	10	2	straight channel
TJ04	T-junction	5	0.5	straight channel
TJ05	T-junction	5	1	straight channel
TJ06	T-junction	5	2	straight channel
FF01	flow focusing	10	1	2D flow focusing (2 inlets)
FF02	flow focusing	10	1	3D flow focusing (4 inlets)
JTP01	T-junction	10	1	Scale-up: 2 T-junctions
JTP01	T-junction	n/a	1	Scale-up: 16 T-junctions
JTS	T-junction	10	1	decentred final outlet
JTT	T-junction	10	n/a	triangular channel

Table 2.1 – Summary of the different microchannels manufactured

However, stereolithography enables the use of channels of almost circular cross-section (details of the cross section profile and roughness are discussed later). This has the advantage to reduce the complexity of the flow, particularly there are no corner flows in the straight channel parts. The CAD designs of the interior of a T-junction and a flow-focusing device are shown on figure 2.1.

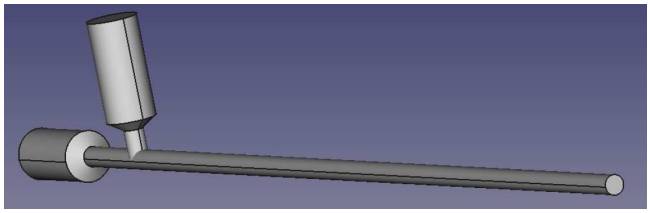

(a) T-junction.

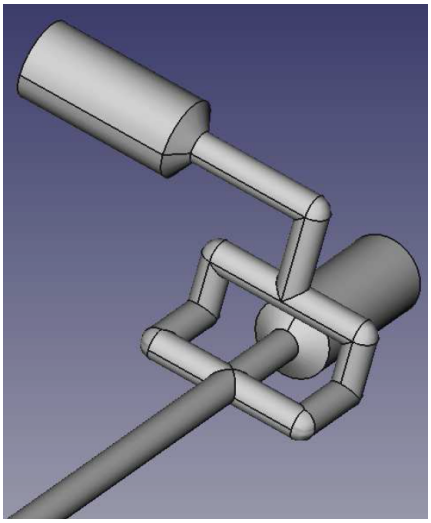

(b) Flow focusing.

Figure 2.1 – CAD drawing of the volume occupied by the inside of channels for different geometries (the radius of the channels is 1 mm).

2.1.1.2 Influence of the manufacturing process on the surface roughness

Geometries manufactured by STL technology are built layer by layer in a liquid photopolymer bath. Therefore, at the end of the fabrication of any channel (or more generally cavity), some polymer material remains inside the channel that must be washed. The washing is most likely performed by an operator and may affect slightly the surface roughness of the channel depending on the amount of resin that remains on the walls, especially for very small channels. The surface roughness is also dependent on the building process, particularly the size of the layers which determines the "pixelation"

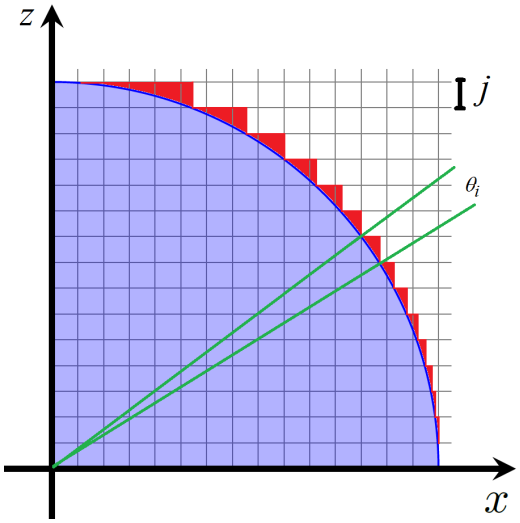

Figure 2.2 – Circle and sampling of the curve by a step j.

of the cavity profile along the building direction, thus imposing a given roughness. The part of the profile of a circular section is shown on figure 2.2. Since each layer have the same height j, it results in a discrete circle [89] which possess a slightly different area than the regular one. This area (in red on figure 2.2) can be computed by simple planar geometry arguments (detailed in annex on surface roughness), and is equal to $\simeq 5$ % of the total area of the regular circle, for $R = 1$ mm and $j = 50$ μm. The machine precision on the vertical direction being around 50 μm, the maximum roughness of the channel must be of this size.

2.2 Solving the equations of motion for YSF in a circular channel

First we consider the flow of yield-stress fluids behaving like an Herschel-Bulkley fluid (following equation 1.33) into a straight circular channel of length L and radius R. The pressure P_a is imposed at the channel inlet, and the ambient pressure is denoted P_b at the channel outlet (figure 2.3). We also assume a laminar flow with no inertial effects, and no-slip boundary conditions. Since the typical size of the channel is millimetric, the gravity stress is negligible with respect to the internal stresses of the fluid. The corresponding dimensionless number (denoted $\mathcal{G}$) compares the gravity stress $\rho_{ysf} g R$ on the typical vertical extension of the flow (R), to the internal stresses of the fluid: $\tau_y + k\dot{\gamma}^n$, where $\dot{\gamma}$ is a typical shear rate approximated by $\frac{V}{R}$. Dividing the gravity stress by the internal stresses of the fluids leads to:

$$\mathcal{G} = \frac{\rho_{ysf} g R^{n+1}}{\tau_y R^n + k V^n}$$

Wherein, V is the typical velocity of the flow, R is the typical size of the channel, ρ_{ysf} is density of the yield-stress fluid, and k, τ_y, n its rheological parameters given by the Herschel-Bulkley model. For $\rho_{ysf} = 1000$ kg/m^3, $R = 1$ mm, and typical emulsion with $k = 100$ Pa.s^n, $\tau_y = 300$ Pa, and $n = 0.5$, for a typical velocity $V = 1$ mm/s it yields $\mathcal{G} \simeq 0.025 \ll 1$. Thus confirming that the gravity stress can be neglected compared to the internal stresses of the fluid when flowing in a channel of radius 1 mm.

From axial symmetry, and translation invariance along z, the velocity writes as:

$$\vec{V} = v_z(r)\vec{z} \tag{2.1}$$

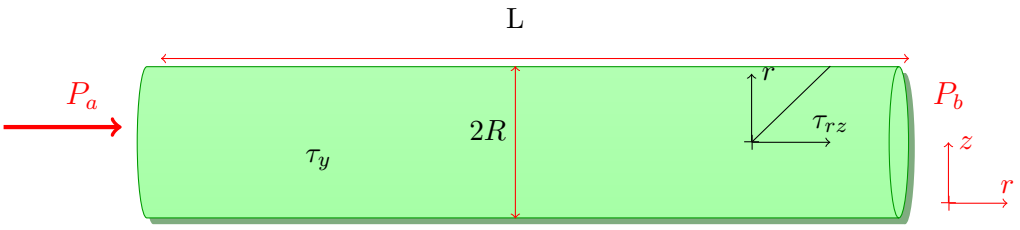

Figure 2.3 – Schematic of flow inside a circular channel.

Thus, neglecting gravity, for an incompressible fluid under Stokes' assumption the momentum balance on $\vec{z}$ in cylindrical coordinates (equation 1.12) reduces to:

$$-\frac{dp}{dz} + \frac{1}{r}\frac{\partial}{\partial r}(r\tau_{rz}) = 0 \tag{2.2}$$

Hence by integration,

$$\tau_{rz} = \frac{r}{2}\frac{dp}{dz} \tag{2.3}$$

From equation 2.2, the pressure drop is given by:

$$\frac{dp}{dz} = \frac{P_a - P_b}{L} = \frac{\Delta P}{L} \tag{2.4}$$

Hence the shear stress at the radial position r becomes,

$$\tau_{rz} = \frac{\Delta P}{L}\frac{r}{2} \tag{2.5}$$

and at the wall (i.e $r = R$),

$$\tau_w = \frac{\Delta P}{L}\frac{R}{2} \tag{2.6}$$

Finally, providing a constitutive law (i.e. that τ_{rz} is a function of $\dot{\gamma} = \dfrac{\partial v_z}{\partial r}$ only, i.e. $g(\tau_{rz}) = \dot{\gamma}$), and assuming $v_z(R) = 0$ equation 2.1 leads to the following equation for the velocity profile:

$$v_z(r) = -\int_r^R g\left(\frac{u}{2}\frac{dP}{dz}\right) \mathrm{d}u \tag{2.7}$$

It is also possible to obtain a general expression for the flow rate Q by integrating eq. 2.7 over the cross section of the tube:

$$Q = \int_0^{2\pi}\int_0^R v_z(r) r \mathrm{d}\theta \mathrm{d}r \tag{2.8}$$

Thus integrating by parts equation 2.7 gives the general expression for the flow rate:

$$Q = -\pi \int_0^R r^2 g\left(\frac{r}{2}\frac{dP}{dz}\right) \mathrm{d}r \tag{2.9}$$

Equation 2.7 is the most general expression of velocity profile and does not require any assumption on the rheological behavior of the fluid to be derived. However, to go further into the derivation of v_z, we need to assume a particular form for the function $g = f^{-1}$. In the following we use equation 1.33: the Herschel-Bulkley constitutive law to derive:

- the Mooney-Rabinowitsch equation (do not need an expression for f), which constitutes one way to determine the rheological behavior of fluids during their flow in the straight channels of our devices.
- the expression of the velocity profile.
- the pressure drop - flow rate relation.

2.2.1 Capillary rheometer: Mooney-Rabinowitsch formula

Channel flow at imposed pressure is useful for determining the rheological behavior of fluids. It can be achieved through the use of the Mooney-Rabinowitsch equation [54]. Starting from equation 2.9, and changing variable such that $\tau_{rz} = \tau_w \frac{r}{R}$, it can be rewritten in terms of τ_{rz} and τ_w (the wall shear stress) as:

$$Q = -\pi R^3 \int_0^{\tau_w} \frac{\tau_{rz}^2}{\tau_w^2}\dot{\gamma}\frac{1}{\tau_w}\mathrm{d}\tau_{rz} \tag{2.10}$$

Differentiating equation 2.10 with respect to τ_w gives the Mooney-Rabinowitsch equation (2.11, 2.12):

$$-\pi R^3 \dot{\gamma}_w = 3Q + \tau_w \frac{dQ}{d\tau_w} \tag{2.11}$$

or with $\mathrm{d}\ln(x) = \dfrac{dx}{x}$ and using equation 2.6,

$$\dot{\gamma}_w = -\frac{Q}{\pi R^3}\left[3 + \frac{\mathrm{d}\ln Q}{\mathrm{d}\ln \Delta P}\right] \tag{2.12}$$

Equations (2.12) or (2.11) are extremely convenient to compute the shear rate at the wall $\dot{\gamma}_w$, by evaluating the variation of flow rate for a given variation of pressure. Experimentally it is easily achieved by emptying at constant pressure a channel filled with the fluid of interest. The wall shear stress varies as the fluid is replaced by gas, and $\dot{\gamma}_w$ is computed from equation (2.11). In particular this method is applicable to determine the constitutive law of a yield-stress fluids. This principle has been recently used to determine the flow curves of complex fluids in microfluidic chips [90] or to investigate the flow of concentrated emulsions into microchannels [74].

In the following section, we describe the determination of the rheological parameters of yield-stress fluid with the Mooney-Rabinowitsch equation in the devices manufactured by STL.

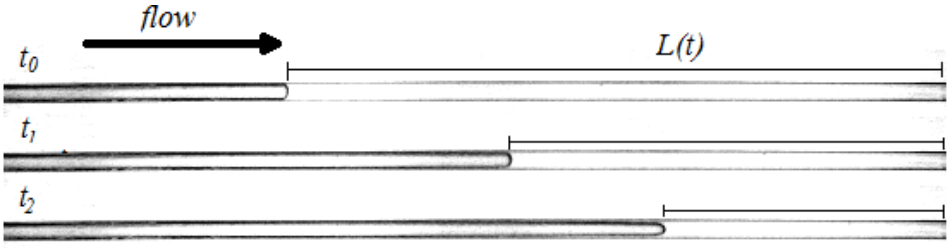

Figure 2.4 – Top view of a channel ($R = 1$ mm; $L = 10$ cm) filled with yield-stress fluid, and emptying at constant pressure, for three different times: $t_0 < t_1 < t_2$.

2.2.1.1 Data processing

Figures 2.4 shows the emptying of a capillary at constant pressure. During an experiment we measure:

- $L(t)$ the length of of the capillary filled with yield-stress fluid, which allows to compute τ_w (equation 2.6).
- The velocity of the rear meniscus, neglecting the deposited film of yield-stress fluid on the wall of the channel, it allows to compute the mean flow rate during the experiment ($Q = \frac{\mathrm{d}L}{\mathrm{d}t}\pi R^2$).

These two quantities are sufficient to determine $\dot{\gamma}_w$ by means of equation 2.12. However, due to the precision of the pressure controller (Fluigent MFCZ 0-2bar, 1mb) it is difficult to reach $\dot{\gamma}_w < 0.1$. In addition, at low velocities (i.e. low applied stresses) it is difficult to determine the derivative in equation 2.11 with an acceptable precision in a reasonable time, because of image acquisition limitation, and the resolution of acquired images. Thus results obtained with the Mooney-Rabinowitch equation are most of the time restricted to large value of $\dot{\gamma}_w$, typically $\dot{\gamma}_w > 0.1$. it is possible to obtain values for extremely high shear rates, typically $\dot{\gamma}_w \sim 1000$ s^{-1} without facing the problems of edge failures.

2.2.2 Velocity profile

For an Herschel-Bulkley fluid it is necessary to work out properly the integration boundaries for equation 2.7. To begin with, equation 2.5 shows that the shear stress depends linearly on the radial position inside the channel. Thus, two regions must be distinguished:

- a solid "plug-flow" region characterized by a constant velocity where $\tau_{rz} < \tau_y$
- a liquid region surrounding the plug, where $\tau_{rz} > \tau_y$

Therefore, this is interesting to express the radius of the solid region R_p. First, dividing equation 2.5 by equation 2.6 leads to:

$$\frac{\tau_w}{\tau_{rz}} = \frac{R}{r} \tag{2.13}$$

Hence, by evaluating eq. 2.13 at $r = R_p$ (implying that $\tau_{rz} = \tau_y$), it yields the following expression for R_p:

$$R_p = R\frac{\tau_y}{\tau_w} \tag{2.14}$$

or equivalently:

$$R_p = \frac{2L\tau_y}{\Delta P} \tag{2.15}$$

From symmetry argument the shear stress has zero value at the center of the channel. This suggests that an infinite stress must be applied to obtain a totally liquid profile velocity ($R_p = 0$). If $R_p > R$ no macroscopic flow is observed, it occurs for $0 \leq R_p < R$. In this regime equation 2.7 can be integrated between r and R for $\tau > \tau_y$, using equation 1.33 (the Herschel-Bulkley constitutive law):

$$v_z(r) = -\int_r^R \left(\frac{\frac{u}{2}\frac{\Delta P}{L} - \tau_y}{k} \right)^m \mathrm{d}u \tag{2.16}$$

wherein $m = \dfrac{1}{n}$. Hence, after integration [91]:

$$v_z(r) = \frac{R}{m+1} \left(\frac{\tau_w}{k}\right)^m \left(1 + \frac{R_p}{R}\right)^{m+1} \left[1 - \left(\frac{r - R_p}{R - R_p}\right)^{m+1}\right] \tag{2.17}$$

For $0 \leq r < R_p$ the velocity profile is flat and obtained by evaluating $v_z(r = R_p)$, it follows:

$$v_z(R_p) = v_{max} = R \left(\frac{\tau_w}{k}\right)^m \frac{(1 - \frac{R_p}{R})^{m+1}}{m+1} \tag{2.18}$$

Examples of such profiles are presented on figure 2.5.

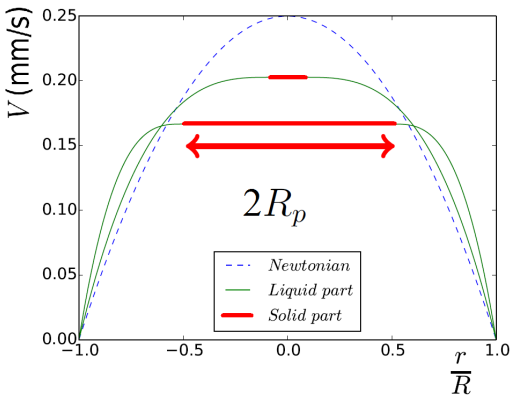

Figure 2.5 – Examples of velocity profiles for newtonian (dashed line) and Herschel-Bulkley flow inside a circular channel. Equation 2.18 is used for solid part (red) and equation 2.17 for the liquid part (green).

2.2.3 Pressure drop

Rewriting equation 2.8 using the expressions of the velocity profile (eq. 2.17, eq. 2.18) leads to the pressure-flow rate relationship for an Herschel-Bulkley fluid flowing in a circular channel:

$$Q = f_{hb}(\Delta P, L, R, \tau_0, k, n) = \begin{cases} 0 & \text{if } \tau_w < \tau_y \\ \frac{8\pi}{k^m}\left(\frac{L}{\Delta P}\right)^3 (\tau_w - \tau_y)^{1+m} \left[\frac{(\tau_w - \tau_y)^2}{3+m} + 2\frac{\tau_w(\tau_w - \tau_y)}{2+m} + \frac{\tau_y^2}{1+m}\right] & \text{if } \tau_w > \tau_y \end{cases} \tag{2.19}$$

Equation 2.19 is plotted on figure 2.6 for different values of the rheological (τ_y, k, n) and geometrical parameters (R, L).

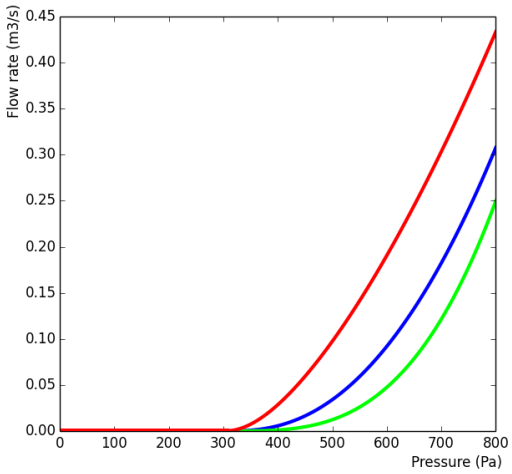

Figure 2.6 – $Q = f_{hb}(\Delta P)$ for $R = 1$ mm, L =10 cm; and blue: τ_y =25 Pa, k =25 Pa.s^n, n =0.5; green τ_y =25 Pa, k =25 Pa.s^n, n =0.35; red τ_y =15 Pa, k =25 Pa.s^n, n =0.75

It is interesting to note that it exists a yield pressure (denoted ΔP_y) below which no macroscopic flow is observed. Its expression can be obtained by rewriting equation 2.5 for $r = R$, and $\tau_{rz} = \tau_y$ the stress to overcome on all the channel wall to make the material flow. Hence,

$$\Delta P_y = 2\frac{L}{R}\tau_y \tag{2.20}$$

2.3 Flow confinement

The afore mentioned description of the flow of an Herschel-Bulkley fluid is valid at the macroscopic scale, that is for channel radii larger than the size of the microstructure of the fluid. We now give a brief summary of the effects that may occur when this condition is invalidated, and are useful to discuss the results presented in the following chapters. It has been shown that, when a yield-stress fluid is confined (i.e. the size of the system approaches the size of the microstructure of the fluid), its rheology becomes dependent on the confinement and on the boundary conditions [74, 82, 92–97].

These effects are explained by considering the rearrangements of the microstructure that occur during the flow, and called *plastic events*. These events dissipate energy by propagating elastic stresses to other area of the material. For example, as a result of the flow heterogeneities any inclusion may be increasingly deformed by the contact of its neighbors. Therefore as its interfacial energy increases, it is also more likely to escape the cage formed by the neighbors to recover a more spherical shape. Doing so it increases the stress on its new neighbors, which in turn are more likely to escape their cages. Such behavior is non-local, and may be triggered by external stimulation, for example when boundary effects become dominant [97]. Practically, strong effects due to plastic rearrangement have been observed to appear for a confinement of $\simeq 40$ [92], defined as the ratio of the smallest size of the system over the typical size of the microstructure. In the following, our smallest channels possess a diameter of 500μm, for a typical size of the microstructure of 6 μm, it yields a confinement of $\simeq 80$, thus plastic events should not modify drastically the dynamic of the flow.

2.4 Wall slip

2.4.1 Generalities

When surfaces in contact with yield-stress fluids are smooth, flows may exhibit behavior that are quite different of the one expected by considering their bulk rheology (determined on rough surfaces). In particular, modifications of the velocity profile due to surface effects may affect the measurements of the rheological parameters of the fluid. In the case of yield-stress fluid, such modifications of the flow profile are due to an apparent slip of the material along smooth surfaces, itself due to a lubrication layer that develops near the wall [98]. For example, during channel flow with smooth channel walls, there is an apparent velocity at the channel wall, denoted v_s, and called slip velocity, the whole dynamic being called *wall slip* (figure 2.7a). For a wall moving at v_0, $v_s < v_0$ the material does not stick to the wall, and the flow is generally slower than for no-slip boundary conditions. For a fixed wall (i.e. $v_0 = 0$), $v_s > 0$ the material flows for smaller applied stresses than what is predicted with no-slip boundary conditions [99]. Wall slip arises from the presence of a depletion layer where the concentration of the microstructure of the fluid is slightly lower than in the bulk, itself arising from various physical processes (table 2.2).

Static effects	Dynamic effects
Steric	hydrodynamic forces
electrostatic forces	shear rate gradients
physico-chemical interactions	

Table 2.2 – Summary of the principal phenomena leading to wall slip

The main physical phenomena giving rise to wall slip are summarized in figure 2.2 and categorized into two classes: *static effects* that manifests even when the material is at rest, and *dynamic effects* that results mostly from the flow of the material near the surface. There is a brief description of their origin:

Steric effect. Considering a fluid having a microstructure of finite size (emulsion droplets, microgel blobs, micelles, flocs made of aggregates of droplets), because the inclusions cannot penetrate the solid wall, there exists a thin layer near the wall, of typical size of the microstructure, where inclusions can not take place. Therefore, this region must be filled with the continuous phase of the fluid. This results in a layer of continuous phase near the wall which has almost Newtonian flow properties [98].

Electrostatic forces. Considering a fluid that carries charges (ions), and charged surfaces, it may result in electrostatic interactions between the surface and the liquid. In addition, *Van der Waals* forces between the solid and liquid can contribute to these forces [100]. If the two have the same charge, the inclusion-wall interaction is repulsive and therefore are separated by a thin layer of solvent. However if the interaction is attractive, slippage may also occur but from dynamical effects thus resulting in a stick-slip motion [76, 101]. Emulsions naturally carry surface charges due to the presence of surfactant in the bulk and at the surface of droplets. Depending on their chemical structure polymer microgel may also have surface charges.

Physico-chemical interactions. A signature of physico-chemical interactions between solids and liquids manifests through the wetting phenomenon [100]. Depending on the affinity of the considered fluid and solid couple, a drop of liquid will either spread on the solid surface (*wetting case*), or stay under the form of a drop having a finite angle of contact (θ) between the solid and the liquid ($\theta > 90°$: *non-wetting case*) [56, 57]. Thus, in a two phase system, if the continuous

phase wets the surface, it spontaneously generates a thin liquid film close to it, leading to total wall slip. In the *non-wetting case* inclusions are more likely to be in contact with the wall, which may reduce wall slip [76, 102, 103].

Hydrodynamic forces. Hydrodynamic forces exerted by the continuous phase flow on the inclusions near the solid wall result in the concentration of inclusions at the center of the channel [76, 98]. As an inclusion moves along the solid wall, a high pressure develops inside the thin lubrication layer, thus producing a lift force. Similarly to the case of hydroplaning [104], this lift force pushes the inclusion away of the the wall thus increasing the size of the lubricated layer for repulsive surfaces, or overcoming short range attractive forces for attractive surfaces [76].

Shear rate gradients. Inhomogeneities in shear rate promote the migration of inclusions from high shear rate region where they may be highly deformed, to low shear rate regions. The slip layer being a confined high shear rate region, it automatically creates a shear rate gradient, that in turns enhance the migration of the inclusion away from the solid wall and the whole slippage dynamic [98].

2.4.2 Slippage of yield-stress fluids

Yield-stress fluids are particularly prone to exhibit wall slip due to steric effects. The finite size of their microstructure prevents an homogeneous distribution of their inclusions near plane solid surfaces. Assuming rigid spherical inclusions of diameter a, it exists a thin layer (of size $\frac{a}{2}$) near solid walls where the center of inclusions cannot take place, which results in a concentration gradient of inclusions [98]. However at equilibrium this gradient of concentration is balanced by an osmotic pressure resulting from the natural tendency of the inclusion network to pump liquid in order to recover a shape that is as spherical as possible [105, 106]. The concentration profile near the solid boundaries results in a balance between the osmotic pressure and the phenomena listed in table 2.2. In most cases, the concentration of inclusions is lower near the boundary than in the bulk, which implies that the area of lower concentration must be filled by the continuous liquid phase constituting the yield stress fluid, which results in a thin layer of liquid (fig. 2.7b), of typical size 1-10 μm [98]. Consequently there is no violation of the *no-slip* boundary condition at the wall, but the yield-stress fluid slips. Nonetheless the stress state of the system depends strongly on the flow of this layer. During channel flow, this thin layer of fluid experiences most of the shear stress, whereas far from the wall the bulk material experiences low stress and flows at constant velocity v_s like a plug. The slip velocity depends as a power law of the stress at the wall $v_s \propto \tau_w^p$. The value of p varies between 1 for repulsive or wetting surfaces, and 2 for for attractive or non-wetting surfaces [99, 101, 102].

The modification of the contact network of inclusions near solid walls through lubrication effect also changes drastically the rheology at low shear rates. This results in an apparent flow of yield-stress fluid for values of the imposed stress below the yield-stress (fig. 2.7c). Slip heterogeneities may also disturb the velocity profile over significant length scale, and even dominate the bulk flow in small systems (i.e. for channel of typical smallest length of tenth of micrometers [103]).

As explained in [107], the curve presented on fig. 2.7c may be divided into three regimes:

- for $\tau < \tau_y$ the whole flow is due to slip, and considering a circular channel of radius R, $\dot{\gamma}_{app} = \frac{v_s}{R}$.
- for large values of τ, wall slip tends to be negligible at least for cone-plate geometry. In other geometries discrepancies may subsist at high shear-rate [99].
- at intermediate stresses, that is for $\tau \sim \tau_y$ the flow, which is a combination of wall slip and bulk flow, is particularly difficult to analyze.

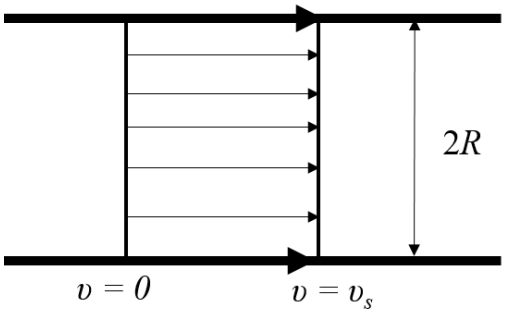

(a) Schematic of macroscopic flow at very low shear rates with wall slip inside a channel for yield-stress fluid.

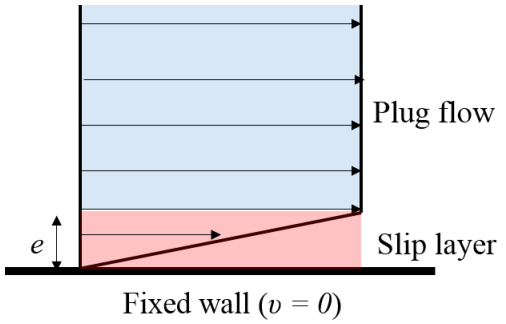

(b) Schematic of the velocity profile near the solid wall of the channel: the velocity gradient is localized into the slip layer.

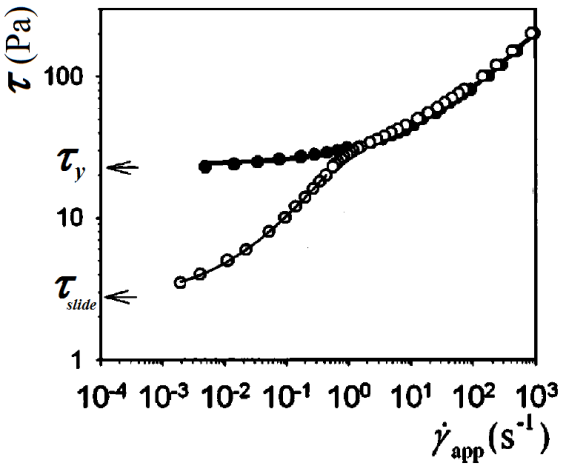

(c) Flow curves for microgel, with slip (empty symbols) and without slip (full symbols), adapted from [106].

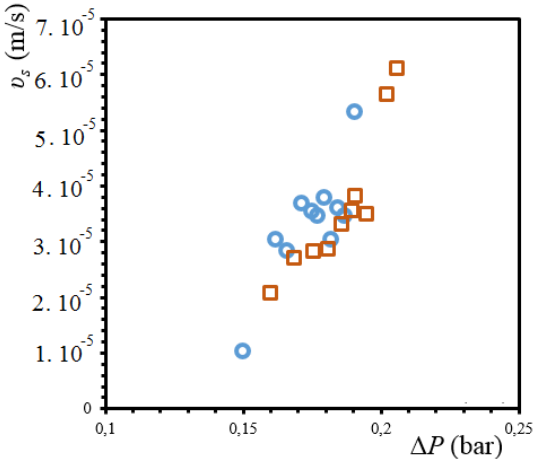

(d) Slip velocity v_s as function of applied pressure ΔP for an emulsion flowing in a circular channel of radius 1mm. Circles correspond to the velocity measure at the wall, squares to the velocity measured at the centerline of the channel.

Figure 2.7 – Wall slip in yield-stress fluids.

2.4.3 Slippage in channels manufactured by STL

The slip velocity corresponding to the first regime is plotted as a function of the applied pressure for an emulsion of yield stress $\sim$ 250 Pa on figure 2.7d. Small fluorescent particles (diameter: 6 μm) are added to the continuous phase of the emulsion to follow the streamlines during the flow. The velocity is plotted as a function of the applied pressure, but since the flow is extremely slow the length of the channel filled with yield-stress fluid during the experiment remains approximately constant, thus $\Delta P \propto \tau_w = \dfrac{\Delta P R}{2L}$. For a channel of radius 1 mm, and length 10 cm, the theoretical yield pressure to make the system flow is roughly 0.5 bar (no slip boundary conditions), however a flow is observed for pressure values as low as 0.15 bar. The flow velocity does not depend on the radial position, and exhibits the following behavior: $v_s \propto \tau_w \propto \Delta P$. This scaling is a classical feature of systems made of deformable inclusions flowing near smooth wetting solid surfaces [74, 97, 101, 102]. This result is compatible with the chemical nature of the continuous phase of the emulsion, which tends to wet the polymer resin surface.

Here we have shown that the use of this material in conjunction with emulsions results in wall slip.

Therefore, in the following paragraphs, we propose different techniques either to avoid wall slip, or to take its effect into account through the determination of effective rheological curves.

2.4.4 Avoiding wall slip

2.4.4.1 Surface roughness

The simplest way to suppress wall slip is to roughen the surface [108]. The roughness must be of large size compared to the size of the microstructure, thus suppressing the lift effect that may take place around a deformed inclusion flowing near the solid wall [106] and which tends to increase the inclusion concentration at the center of the channel. Roughness may also homogenize the concentration profile by letting the inclusions take place between valleys and peaks of the surface roughness [7]. However, this solution is extremely difficult to apply to channels with small dimensions.

2.4.4.2 Chemical surface treatment

Chemical treatments are another way to suppress wall slip. For carbopol gels it is possible to produce no-slip polymethylmethacrylate (PMMA) surfaces, or even glass surfaces with a suitable treatment using polyethylenimine (PEI) [109]. PEI is a cationic polymer which tends to attach to negatively charged surfaces, and to form complexes with carbopol polymers through ionic interactions, thus blocking wall slip of carbopol gels [109]. Using this experimental procedure we obtain no-slip boundary conditions for carbopol gel in glass capillaries (radius: 235, 513, 620, 702 μm).

No-slip treatment: experiments

The treatment is carried out as follows:

- A water-PEI solution at 0.2% w.t. is prepared and mixed until the PEI is completely dissolved ($\sim$ 5h).
- Clean glass capillaries are plunged into the PEI solution, for 24 hours.
- Glass capillaries are retrieved and dried, first by blowing air to expel the remaining PEI solution, and finally letting the remaining solution evaporate at ambient temperature ($\simeq 20°$C).

2.4.4.3 Comparison with bulk rheology

Figure 2.8a shows the Herschel-Bulkley fit of the data obtained by equation 2.11 in a treated glass capillary. The comparison between the rheological parameters obtained in parallel-plate rheometer with rough surfaces and the rheology obtained for treated glass capillaries are shown on figure 2.8b.

Although we only obtain data for $\dot{\gamma}_w > 1$ in the capillary rheometer case, and data for $\dot{\gamma}_w < 1$ in the parallel-plate rheometer case, the fitting parameters (figure 2.8b) are almost similar: within 5 % for the yield-stress, and 8 % for the consistency. This comparison validates the surface treatment which will be extensively used in chapter 3.

In this part we have shown that it is possible to avoid wall slip of carbopol gels inside glass capillaries by mean of chemical treatment, and that a general way to avoid wall slip of yield-stress fluids is to roughen the considered surface. However none of these solutions are applicable to emulsions inside STL manufactured polymer channels. Thus in that particular case wall slip nonetheless occurs ans it is necessary to take it into account, as described in the next paragraphs.

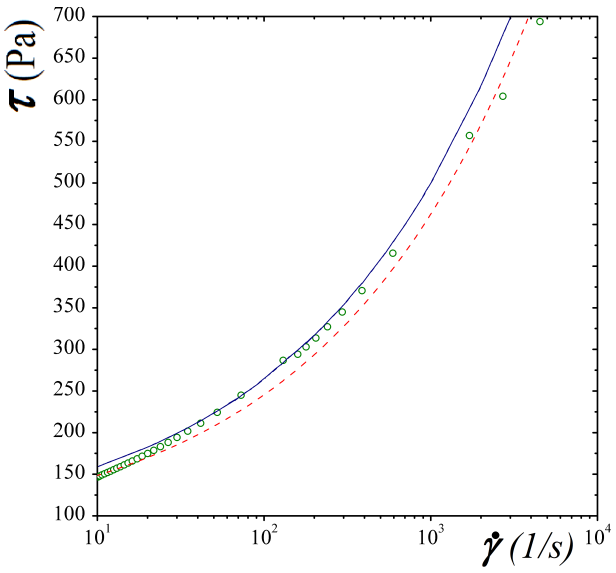

(a) Rheological data obtained from capillary rheometer computation ($R = 513$ μm) into a glass capillary treated with PEI. The red dashed line is the Herschel-Bulkley fit of the data. The blue plain line stands for the fit of the data obtained with plate-plate rheometer.

Rheometer	τ_y (Pa)	k (Pa.s^n)	n
Capillary (slip)	10.48	36.77	0.385
Capillary (no-slip)	70	34.97	0.35
Plate-plate (no-slip)	73.7	38.22	0.349

(b) Comparison of measured rheological parameters obtained for the same carbopol gel with different boundary conditions and geometries.

Figure 2.8 – Flow curve and comparison of no-slip treatment.

2.4.5 Taking wall slip into account: the capillary rheometer

To take wall slip into account during the flow inside channels with smooth surfaces, we try to determine the rheological behavior of the fluid when flowing in the channel of interest. One way of evaluating the rheological properties of the material during a channel flow is to use the channel as a capillary rheometer. In that case the Mooney-Rabinowitsch equation (2.12) allows to retrieve the rheological properties of the fluid. Therefore, we are able to predict the response of the material, even in the presence of slippage at the wall. However, with wall slip, the results given by the Mooney-Rabinowitsch formula are not intrinsic properties of the flow of the material (as with no-slip boundary conditions), but effective rheological parameters, which describe how the material responds to the applied stress on the considered surface and/or geometry.

We apply this method both for emulsion or carbopol gel flowing in glass capillaries and emulsions or carbopol flowing in STL manufactured channels. As an example, the difference between measured parameters inside a glass capillary ($R = 513\mu$m) in case of slip and no-slip are given in figure 2.8b. Analyzing this result it should be mentioned that:

- The apparent yield-stress is smaller than the bulk yield stress, which is characteristic of wall slip. Similar low yield stress was measured in the case of attractive surfaces, and sometimes called the *sliding yield stress*. This value is determined by the local dynamic of the flow inside the slip layer [101], and results in an equilibrium between attractive forces (i.e. osmotic pressure, proportional to the storage modulus [107, 110]) and hydrodynamic forces [101]. However, for non-attractive surfaces, the sliding stress is almost zero [101], which corresponds to the hypothesis of a purely Newtonian slip layer. It is also interesting to note that this yield stress is only related to the localized slip dynamics, thus an object (such as a bubble or drop) trapped inside the yield-stress fluid, although in slip regime, experiences stresses related to the flow of the bulk material, namely the bulk (or "true") yield stress of the material in addition to the viscous stresses.

➤ The consistency k, and n the flow index are not so different in the presence of slip. This similarity is explained as follows: these two parameters are dominant when describing the behavior of the fluid at high shear-rate, that is when the viscous stresses are large with respect to the yield stress and the velocity profile in the channel is mostly constituted of a liquid part ($\frac{R_p}{R} \ll 1$). Thus, at high shear rates, the material is mostly destructured, the bulk flow is predominant with respect to the flow into the slip layer, and the slip layer may become negligible [107].

Fitting parameters of the Herschel-Bulkley model, obtained by capillary rheometry in presence of slip, are presented in figure 2.3. Experimental data for emulsions and carbopol gels in channels manufactured by STL are represented on figure 2.9.

Fluid	Channel material	Radius (mm)	τ_y (Pa) no-slip (plate-plate)	τ_y (Pa) slip (capillary)	k (Pa.s^n) slip (capillary)	n
Emulsion	XC11122	1	100	9	78.5	0.5
Emulsion	XC11122	1	165	22	110	0.5
Emulsion	XC11122	1	250	58.84	123.94	0.5
Emulsion	glass	0.513	149.35	3.14	50.18	0.59
Carbopol	XC11122	1	75	31.58	67.76	0.35
Carbopol	XC11122	2	75	81.94	67.83	0.35
Carbopol	glass	0.513	75	10.48	36.77	0.385

Table 2.3 – Summary of the rheological parameters measured in presence of slip in various channels for different materials.

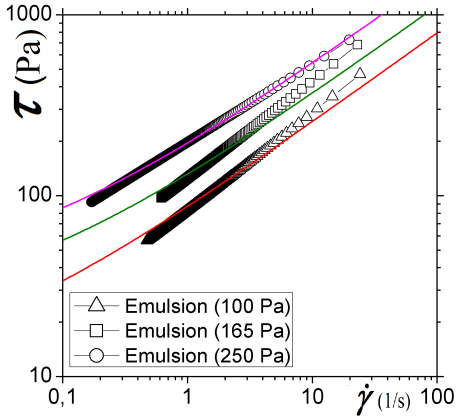

(a) Emulsions in channels made of XC11122 and radius of 1 mm. The plain lines stand for the Herschel-Bulkley fit of the data.

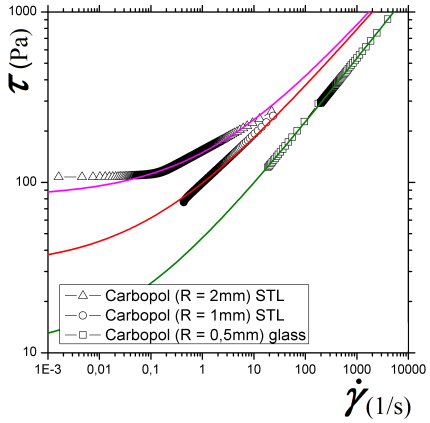

(b) Carbopol in different channels. The plain lines stand for the Herschel-Bulkley fit of the data.

Figure 2.9 – Data obtained by capillary rheometry, and corresponding Herschel-Bulkley fit.

For experiments in microchannels presented in this thesis, wall slip is accounted for by the method described above. Thus, for a given bubbling experiment, another one is performed with the same experimental set-up used as a capillary rheometer. Data presented in figure 2.3 are systematically used in chapter 5.

2.5 Two-phase flow: slug flow

The work undertaken during this thesis aims at producing yield-stress fluid foams. Therefore, it focuses largely on bubble production in yield-stress fluids and on the dynamics associated with the two-phase flows that occurs in the outlet channel prior to foam production. The aim of this section is to describe the rheology of a two-phase flow in a circular microchannel, for a yield-stress fluid continuous phase and a gas (air) dispersed phase. First of all, two cases of two-phase flows must be distinguished (see figure 2.10):

- bubbly flows: the radius of bubbles or droplets is smaller than the diameter of the channel. Multiple bubbles may flow side by side, and interact through hydrodynamic forces (figure 2.10a).
- slug flows: the radius of the bubbles or droplets is almost the radius of the channel, and thus one bubble occupy the majority of the cross section of the channel. These flows are made of bubbles surrounded by a liquid film, and separated from each other by plugs of yield-stress fluid (figure 2.10b).

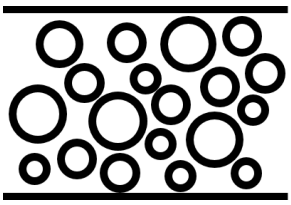

(a) Schematic of a bubbly flow.

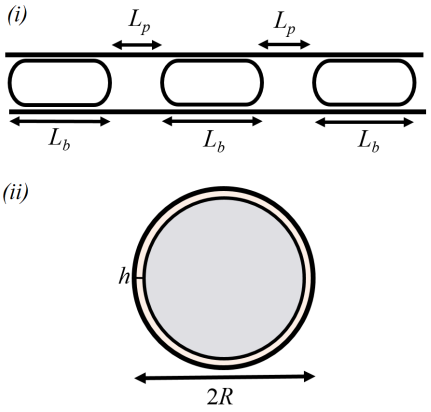

(b) (i) Schematic of a slug flow (ii) Schematic of the cross section of a slug flow inside a circular channel.

Figure 2.10 – Two types of two-phase flow.

The size of the objects (bubbles) produced with systems presented in chapter 4/5/6 is of order of the size of the channel. In this section, we therefore focus on the second category: slug flow. Since slug flows are common in microfluidic chips, they have been extensively investigated in the case of Newtonian fluids [16–18, 111–114]. These works mainly focus on: (i) pressure drop; (ii) lubrification films; (iii) flow field inside plugs.

2.5.1 Pressure drop and rheology

For a slug flow of Newtonian carrier phase the pressure drop comes from three distinct phenomena: (i) viscosity of the carrier fluid plugs; (ii) viscosity of the dispersed fluid drops; (iii) interfacial effects due the dynamic curvature of interfaces induced by the flow.

For a Newtonian fluid flowing in a circular channel, the pressure drop is linked to the flow rate by the following linear relation obtained for a Poiseuille flow (i.e. equation 2.19 with $\tau_y = 0$ and $n = 1$):

$$\Delta P = R_h Q \tag{2.21}$$

$$R_h = \frac{\eta L}{\pi R^4} \tag{2.22}$$

Wherein R_h is the hydrodynamic resistance. Since equation 2.21 is linear with respect to the flow rate (Q), and the pressure difference (ΔP), it is possible to sum the contributions of the pressure drop corresponding to different afore-mentioned physical process, providing that each of them depends linearly on the mean velocity, to obtain the total pressure drop due to a slug flow. In addition the expression of R_h (equation 2.22) being linear with respect to L, the length of an individual plug or bubble, we can consider the sum of the contribution of each individual bubble/plug as the total contribution of the viscous resistance of the flow. Neglecting the flow inside the thin film surrounding bubbles, and recirculations inside the liquid plugs, these two properties of the pressure/flow rate relation were used to derive simple expressions for the determination of the pressure drop in the case of slug flows in rectangular channels [115].

For a slug flow of Herschel-Bulkley carrier fluid, the pressure drop arises from the same physical phenomena. However, the modeling is much more complicated, because the pressure/flow rate relation $Q = f_{hb}(\Delta P)$ (eq. 2.19) is neither linear with respect to L, nor ΔP. This complexity makes the approach detailed above not applicable to derive a pressure/flow rate relation for an Herschel-Bulkley fluid. In addition, when considering the dissipation due to interfacial energy in a Newtonian fluid, it is assumed that the shape of the dynamic meniscus results in a balance between the viscous stress and the capillary stress [112]. Yet, for a yield-stress fluid flowing in a channel of typical radius 1 mm, the yield stress ($\sim$ 100 Pa) may compete with the capillary stress (for $T = 0.035$ mN/m it yields $\frac{T}{R} = 35$ Pa). Thus, bubbles' or drops' menisci may present shapes that depart significantly from the shape predicted by the afore-mentioned stress balance (figure 2.11). We will further discuss this point in chapter 3.

Finally, another complication of the problem arises from wall slip: what would be the pressure/flow rate relation in the presence of slip? To answer this question, it is interesting to point out that to express f_{hb} it is necessary to know the value of the rheological parameters of the material, and that the effect of wall slip on the flow can be taken into account by means of the capillary rheometer experiment, and the resulting effective rheological parameters. To simplify the problem further, a simple idea is to consider that due to the large viscosity of the yield-stress fluid the pressure drop due to the plugs is dominant with respect to pressure drop due to the deformation of bubbles interfaces and in the thin film, such that the only contribution to the pressure drop comes from the viscous flow inside the plugs. Thus, neglecting recirculations, the system is depicted as a set of plugs that do not interact with each other. In the following, the length of the plug i is denoted L_i. Since there are no interactions between the plugs, and in spite of the non linearity of equation 2.19, we also consider that this system is equivalent to a system of one plug of length $L_{eq} = \sum_i L_i$. These hypotheses are tested by means of two capillary rheometry experiments in a circular channel of radius 1 mm manufactured by STL:

- The reference experiment is performed with the channel completely filled with yield-stress fluid and no bubbles, as described on figure 2.4.
- The second experiment is a two-phase, slug flow rheometry, experiment. Bubbles of various sizes, but always with a radius $r_b \simeq R$, are injected one by one at the inlet of the channel with a syringe, which results in the picture presented in figure 2.11. At this point, the same experimental protocol as in the previous experiment, is followed. Data are also treated in the same way, providing that $L(t)$ is now replaced by $L_{eq}(t)$ in equation 2.11.

The results of these two experiments are plotted on figure 2.12. Although our hypothesis are rough with respect to the complexity of the flow, the difference between the reference experiment and the slug flow experiment is small. This suggests that the dominant physical ingredient during slug flow is the due to the viscous flow inside the plugs.

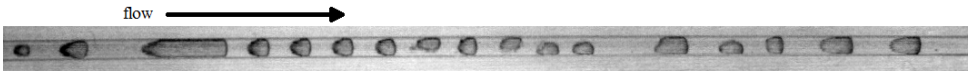

Figure 2.11 – Top view of a channel ($R = 1$ mm) filled with yield-stress fluid (carbopol, $\tau_y = 75Pa$) and bubbles.

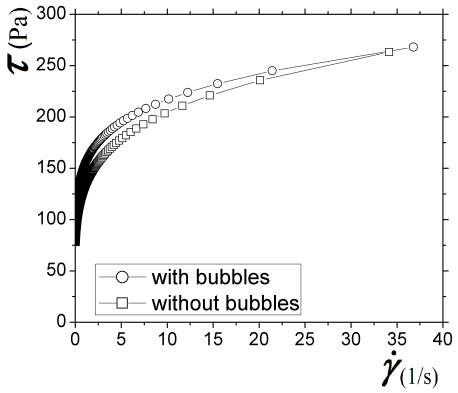

Figure 2.12 – Comparison of the apparent rheology of slug flow in a channel of radius $R = 1$ mm filled with yield-stress fluid (carbopol, $\tau_y = 75Pa$), and simple flow of yield-stress fluid in presence of slip.

This result validates that the apparent rheology of slug flows of yield-stress fluids can be obtained by capillary rheometry experiments. In addition, it is possible even for channels of diameter that is not too small (i.e. depending on a competition between the capillary stress and the yield stress), to approximate the pressure drop of a slug flow by the pressure drop of the sum of the plugs without departing too much from the apparent rheology of the flowing material, even in presence of wall slip.

2.5.2 Flow field in plugs

For Newtonian fluids, the flow field occurring in a slug flow is also well characterized [111–113, 116]. Due to the presence of a thin film of fluid the bubbles or droplets move at a larger velocity (denoted v_b) than the carrier fluid (denoted v_m). $W = \frac{v_b - v_m}{v_b}$, the excess velocity of bubbles with respect to the mean flow can be expressed by means of a mass balance between the flow inside the film and the global flow rate in the reference frame of the droplet, which leads to:

$$1 - W = \left(1 - \frac{h}{R}\right)^2 \tag{2.23}$$

$$W \propto \frac{h}{R} \text{ for } \frac{h}{R} \ll 1 \tag{2.24}$$

Equation 2.24 is the first order approximation of 2.23 and has been verified for circular channels [112, 117]. Because of this velocity difference and the presence of the interfaces, the flow is no longer uniform and the Poseuille profile is modified [16, 111]. Thus, as pointed out by Taylor, the flow exhibits vortices, both inside the plugs and inside the drops (figure 2.13). This occurs when the motion of bubbles is smaller than the maximum velocity of the Poiseuille flow: the fluid particle on the central streamline move faster than the bubbles and therefore must recirculate due to mass conservation. The modification induced by the velocity difference in the flow is well represented by the superposition of a Poiseuille flow and counter-rotative vortices both in the plugs and in the drops [16, 18, 116].

For an Herschel-Bulkley fluid, the velocity profile is split into two regions: a solid region where the stress is below the yield stress, and a liquid annulus surrounding the solid plug where the stress

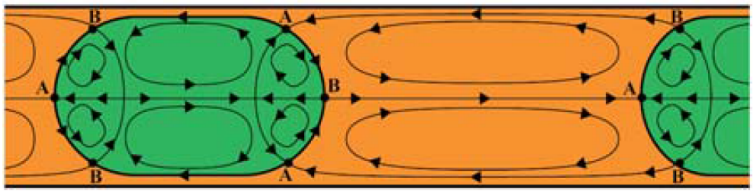

Figure 2.13 – Schematic of streamlines, in the reference frame of the droplet, of the counter-rotative vortices in a slug flow for inviscid drops, from [16].

is above the yield stress. In the limit case of a very thin liquid region, as in full slip for example, the macroscopic flow is a solid-plug flow, and providing that there is no fluid deposition on the wall of the channel and thus that the velocity of bubbles is equal to the velocity of the carrier fluid, the counter-rotative vortices disappear, and there should not be any relative motion of the fluid in the reference frame of the bubble.

Secondly, considering the case $\tau > \tau_y$, a naive idea consists in considering that the solid-plug at the center of channel blocks the recirculation in this part, and that the vortices might be confined in the liquid layer surrounding the solid core of the flow. However this approach neglects the effect of the microstructure of the fluid, which modify the local dynamics of the flow inside the plug through rearrangements (*plastic events*) [93]. Inside the droplets, the front and rear meniscus may become regions of stress-matching between the droplet and the solid plug, or the liquid layer surrounding it. One way to obtain more information on such flows could be to use particle image velocimetry.

In the last case, considering that $\tau \gg \tau_y$, the velocity profile is constituted of a liquid region that fills almost all the diameter of the channel, and is mostly Poiseuille-like. Thus, the flow scenario should be mostly the same as the one presented in the Newtonian case (figure 2.13).

2.6 Conclusion

In this chapter we detailed the characteristic of the flow of an Herschel-Bulkley fluid in a circular channel. We focus on velocity profiles, pressure drop/flow rate relationship, and determination of the constitutive law of the material from a flow at imposed pressure. Then, we described the phenomenon of wall slip, and propose a simple method to take it into account during the flow in circular channels. Finally we investigated the rheology of a two-phase flow of yield-stress fluid in circular channel by means of the capillary rheometer experiment. The study highlights the crucial role of the deposited film of material on the wall of the channel on the velocity profile and the whole dynamics of the flow, this point is further investigated in chapter 3.

Essential facts

- The description of the flow of an Herschel-Bulkley fluid with no-slip boundary conditions is given by equations 2.17, 2.18, 2.19.
- For a given fluid, wall slip is taken into account my measuring an effective law inside the considered channel geometry.
- A slug flow of yield-stress fluid is approximated by a channel flow of equivalent length corresponding the sum of the lenghts of the plugs.

3

Deposition of yield-stress fluid on the wall of circular channels

In this chapter we investigate the deposition of a yield-stress fluid on the wall of circular channels, when pushed by an air bubble. First, the treatment of this classical hydrodynamic problem (known as *Bretherton's problem*) is recalled. We then move to a review of the literature for the coating of non-Newtonian fluids in different geometries. Finally, we present the experiments performed in cylindrical geometry for yield-stress fluids. Particular attention is paid to the effect of wall slip. Where there is no slip at the channel wall, a scaling law is proposed and compared to the scaling obtained in other geometries.

Contents

3.1 Introduction

When an object, such as a plate or a fiber, is drawn out of a liquid bath, a thin liquid film remains on its surface. Similarly, when a long bubble moves into a tube preliminary filled with a fluid, a thin layer of liquid remains on the wall of the channel as the bubble displaces the fluid. This effect is commonly referred to as *deposition* or *coating*.

Historically, the study of the coating with non-Newtonian fluids was first motivated by the development of photographic industry which uses the coating of emulsions by means of moving rolls to obtain photographic paper with various properties [118, 119]. Since then, coating has widely been used in industrial processes to enhance, modify, or decorate the surface properties of the chosen substrate. Paints and lacquers are common example of coating used to prevent corrosion, for example in automobile industry. Coatings are also used to modify texture, optical, electric, or protective properties of substrates [120]. Most of the materials used in such processes behave like non-Newtonian fluids. Therefore, the prediction of the thickness of the deposited layer of yield-stress fluid is a question of industrial significance.

Solving the problem involves finding the parameters that drive the deposition of the fluid on the object, as well as the dependency of the coated layer thickness on those parameters. The first solution was obtained by Landau, Levich and Derjaguin (LLD) [53, 59, 118] for a withdrawn plate, and Bretherton [112] in the geometry of a circular channel.

The most common geometries for fluid coating are summarized on figure 3.1. It includes plates, fibers, rolls that entrain fluid from a bath, or coating of the inside of a tube. In chapter 2, we have highlighted the role of the thin film surrounding bubbles on the properties of two-phase slug flows. Since, these flow are used to achieve the production of foams, the study of the dynamic of the deposition of YSF films is of crucial importance for the production of controlled YSF foams, particularly through the knowledge of the dynamics of the associated two phase flow.

Thus, we focus particularly on the case of a circular channel, which has been extensively studied for Newtonian fluid [111, 112, 121]. Before addressing the topic of the coating of a yield-stress fluid, we recall the theory and its extension to less restrictive hypotheses.

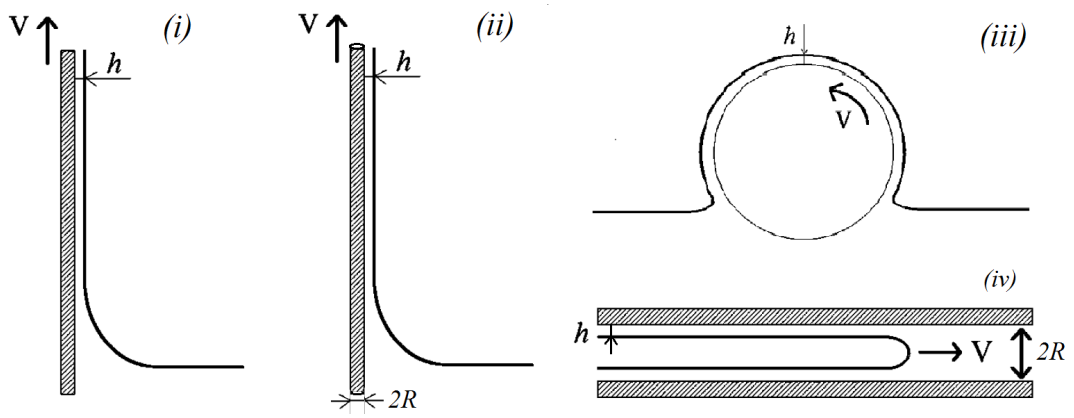

Figure 3.1 – Sketches of the most common configuration used for fluid coating: (*i*) coating of a plate drawn out of a bath; (*ii*) coating of a fiber; (*iii*) coating of a rotating roll; (*iv*) coating of the wall of a channel. Adapted from [122].

3.2 Literature review: Newtonian fluids

In this section, we recall the hypothesis and derivation of the coating problem inside a circular channel.

3.2.1 The Bretherton solution

We consider a cylindrical channel of radius R, filled with a Newtonian fluid of viscosity η and density ρ. An infinitely long gas bubble is pushed at constant velocity inside the channel: as it advances, a thin film of fluid remains on the channel wall. We assume that the size of the channel is small with respect to the capillary length $\kappa^{-1} = \sqrt{\frac{T}{\rho g}}$ so that $Bo = \frac{\rho g R^2}{T} \ll 1$ (see chapter 1). Therefore, gravity can be neglected and for a flow at low velocity described by Stokes' equation, the physical ingredients of the problem are the following:

- The viscous stress inside the thin film that tends to thicken the deposited fluid layer, to minimize the hydrodynamic resistance associated with such flow. Note that, in the mean flow that takes place in front of the bubble the viscous stress is of the order of $\eta\frac{\partial v}{\partial y} \sim \frac{\eta V}{R}$, whereas in the thin film it is of order $\frac{\eta V}{h_0}$.
- The capillary stress at the meniscus interface ($\frac{T}{R}$). The meniscus is deformed by the flow and the presence of the thin film, therefore it tends to retain liquid in order to recover its static shape.

The balance between the viscous stress of the mean flow and the capillary stress is expressed by the capillary number $Ca = \frac{\eta V}{T}$. Thus, since gravity and inertial effects are neglected, the solution of the problem must depend on this number only. The other parameter of interest is the thickness of the deposited layer (h_0), which must be made dimensionless. The natural length of the problem is the radius of the channel. Hence, denoting f_b an unknown function, we can guess that:

$$h_0 = R f_b(Ca)$$

In the following section we detail the derivation of f_b. Since the flow is considered to be slow, the film is considered to be thin. Therefore, to model the dynamic of the flow, it is possible to solve the equation of motion in the approximation of thin film (*lubrication*) in Cartesian coordinates (2D). Here, we follow the derivation as performed by Bretherton [112], a similar solution was derived by Reinelt using perturbation methods and matched asymptotic expansions [123, 124].

3.2.1.1 Description of the flow

First, to describe the flow close to the gas meniscus, it is useful to split it into three regions (figure 3.2):

- **Region *(a)***, where the interface has a spherical shape. The interface curvature in this region is $\mathcal{C}_a = \frac{2}{R - h_0}$. Indeed, since the film is thin ($\frac{h_0}{R} \ll 1$), it disturbs the meniscus shape over a length that is small, thus leading to $\mathcal{C}_a = \frac{2}{R}$.
- **Region *(b)***, where the deposited film has a constant thickness. There, the curvature of the interface is $\mathcal{C}_b = \frac{1}{R - h_0}$. Much interest in solving the lubrication problem lies in finding an expression for the film thickness (h_0) in this region as a function of the parameters of the problem.
- **Region *(c)***, the dynamic meniscus, is a transition region in between (b) and (a). There, the curvature of the interface is not constant, and progressively changes from $\mathcal{C}_a$ to $\mathcal{C}_b$. The length of this region is denoted λ. Due to the presence of the thin film, and the viscous stresses of the flow, the shape of the meniscus is different from its static shape (dashed curve on figure 3.2). Thus in

region *(c)*, the curve representing the position of the interface is denoted $h(x)$. Its curvature is given by the mathematical expression of the curvature for a plane curve (equation 3.1, where the superscript "prime" denotes the derivative with respect to x), the total curvature in this region is $\mathcal{C}_c = \mathcal{C}_\lambda + \dfrac{1}{R - h_0}$. The deposition of the film (and therefore its final thickness h_0) is assumed to be fully determined by the shape of this region.

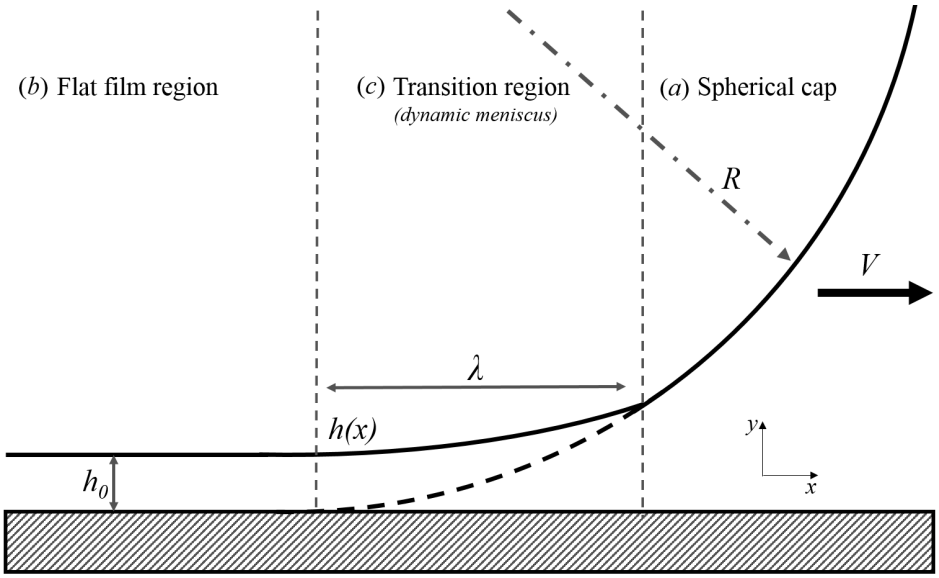

Figure 3.2 – Schematic of the advance of a gas meniscus into a viscous fluid near the wall of a channel.

$$\mathcal{C}_\lambda = \frac{h''}{(1 + (h')^2)^{\frac{3}{2}}} \tag{3.1}$$

3.2.1.2 Solution for the flow inside the dynamic meniscus

In the following, we solve the equations of motion in the region *(b)*. The first simplification of the problem, is to consider that since the film is thin, $h(x)$ is almost flat and varies slowly (i.e. $h' \ll 1$), and therefore that the lubrication approximation holds in region *(b)* and *(a)*. Thus:

$$\frac{h_0}{R} \ll 1 \qquad \frac{h(x)}{R} \ll 1 \tag{3.2}$$

$$\frac{h_0}{\lambda} \ll 1 \qquad \frac{h(x)}{\lambda} \ll 1 \tag{3.3}$$

Hence, equation 3.1 reduces to:

$$\mathcal{C}_\lambda = h'' \tag{3.4}$$

Furthermore, for a stationary flow under lubrication approximation (eq. 3.2, 3.3), the flow is described by Stokes' equation. This leads to equation 3.5, wherein p is the pressure across the liquid film, and v_x the axial velocity inside the liquid film.

$$\eta \frac{\partial^2 v_x}{\partial y^2} = \frac{\partial p}{\partial x} \tag{3.5}$$

In the dynamic meniscus the pressure gradient is locally imposed by the curvature of the interface. The total curvature is thus $\mathcal{C}_c = \mathcal{C}_\lambda + \dfrac{1}{R-h}$. Adjoining equation 3.2, the pressure p in the thin film becomes the sum of the pressure inside the bubble (p_0) minus the capillary pressure necessary to curve the interface (equation 3.6).

$$p \simeq p_0 - T\left(h'' + \frac{1}{R}\right) \tag{3.6}$$

Substituting equation 3.6 into equation 3.5, it yields:

$$\eta \frac{\partial^2 v_x}{\partial y^2} = -T h''' \tag{3.7}$$

First, equation 3.7 may be integrated twice with respect to y to obtain the velocity profile inside the film 3.8.

$$v_x = -h''' \frac{T}{\eta}\left(\frac{1}{2}y^2 - hy\right) \tag{3.8}$$

To solve equation 3.8 the boundary conditions are the following:

➤ No shear stress at the liquid/air interface:

$$\frac{\partial v_x}{\partial y} = 0 \qquad \text{for} \qquad y = h(x) \tag{3.9}$$

➤ Zero velocity at the solid wall:

$$v_x = 0 \qquad \text{for} \qquad y = 0 \tag{3.10}$$

Because of lubrication approximation the flow is considered to be two-dimensional, therefore the flow rate is expressed by unit circumference (Q_c), it is obtained by integrating equation 3.8 over the thickness of the film:

$$Q_c = \int_0^h v_x(y)\mathrm{d}y \tag{3.11}$$

$$= -\frac{T}{\eta} h''' \left[\frac{1}{6}y^3 - \frac{1}{2}hy^2\right]_0^h \tag{3.12}$$

$$= \frac{T}{\eta} h''' \frac{h^3}{3} \tag{3.13}$$

Since the motion is steady, and due to the film deposition, the total mean flow rate by unit circumference (Q_c) is also given by:

$$Q_c = V\left(h(x) - h_0\right) \tag{3.14}$$

Hence, equating equation 3.13 and equation 3.14 leads to:

$$3V\frac{h-h_0}{h^3} = \frac{T}{\eta}h''' \tag{3.15}$$

Changing variables such that: $H = \frac{h}{h_0}$, $Ca = \frac{\eta V}{T}$, and $X = \frac{x}{L_\lambda}$, with $L_\lambda = h_0 Ca^{\frac{-1}{3}}$, equation 3.15 reduces to the following dimensionless equation:

$$\frac{\mathrm{d}^3 H}{\mathrm{d}X^3} = 3\frac{H-1}{H^3} \tag{3.16}$$

First, it gives the order of magnitude of the different variables: the extension of the dynamic meniscus is L_λ, which depends on the capillary number, and its height is of order of the flat film h_0. Equation 3.15 also possesses three boundary conditions:

- $H \to 1$ for $X \to -\infty$
- $\frac{\mathrm{d}H}{\mathrm{d}X} \to 0$ for $X \to -\infty$
- $\frac{\mathrm{d}^2 H}{\mathrm{d}X^2} \to 0$ for $X \to -\infty$

These conditions correspond to the continuity of $h(x)$ with the flat film region and allow to solve equation 3.16 numerically. A consequence of equation 3.16 appears when looking at its limit for $H \sim 1$:

$$\frac{\mathrm{d}^3 H}{\mathrm{d}X^3} \to 0 \text{ for } H \to 1 \tag{3.17}$$

Equation 3.17 implies that the curvature of the interface H'' is constant when $h(x) = h_0$ (i.e at the junction of the thin film and the dynamic meniscus). Finding this numerical value is of particular interest because it allows the determination of the full profile by matching the curvature at the rear of the dynamic meniscus and at the front of the flat film region which finally leads to [112]:

$$\frac{h_0}{R} = 1.337 Ca^{\frac{2}{3}} \tag{3.18}$$

The derivation of equation 3.18 is rigorous but requires to solve thoroughly the flow inside the dynamic meniscus region under several hypotheses. This restricts the solvable cases to a small number, and requires to consider that lubrication approximation holds so that equations 3.2, 3.3 are valid. Note that, through equation 3.18, the afore-mentioned conditions automatically leads to $Ca \ll 1$ (i.e. that viscous stresses are small compared to interfacial stresses).

3.2.1.3 Comparison with experimental results

On figure 3.3, equation 3.18 is compared to the experimental results obtained by G.I. Taylor for glycerine in a circular channel [111].

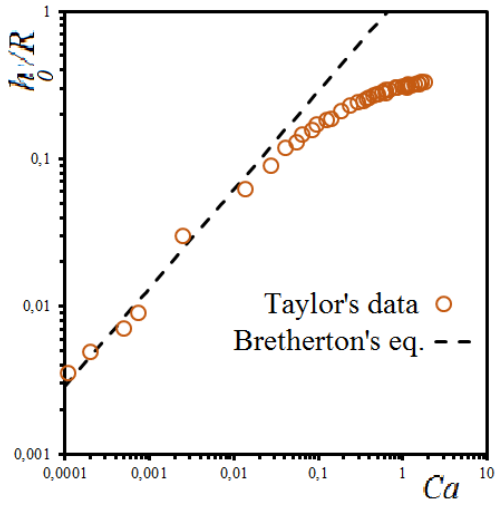

Figure 3.3 – Comparison between data of normalized film thickness as a function of the capillary number obtained by Taylor and equation 3.18.

As intended, equation 3.18 holds for small capillary numbers ($Ca \ll 1$), or equivalently small film thickness $\frac{h_0}{R} \ll 1$.

One alternate way to obtain the result of Bretherton (or Landau, Levich, Derjafuin (LLD)) is to use scaling arguments. Such reasoning not only allows to simplify the computation, but also to solve different variations of the problem involving a more complex flow profile than the original one. Examples include coating on textured surfaces, fiber drawn out of emulsion, or the coating at high velocities [121, 122, 125]. Thus, in the next section a scaling analysis of the coating problem inside a circular channel is presented.

3.2.2 Scaling analysis

Considering again a long bubble moving at a velocity V through a circular channel of radius R, filled with a liquid of viscosity η, a thin liquid film of thickness h_0 remains attached to the wall of the channel as the bubble advances (figure 3.1). In the following we summarize the arguments used by Bretherton to derive equation 3.18 under the form of scaling arguments [56].

For a flow verifying Stokes' assumption, the dominant stress associated with the flow and acting on the meniscus is the viscous stress which tends to thicken the liquid film in order to reduce the resistance associated to the flow in this region. The viscous stress is therefore considered to be the driving mechanism of the thin film deposition.

The second effect of the viscous stresses induced by the flow is to modify the shape of the bubble meniscus with respect to its static shape. This change of shape, in turns tends to create interfacial stresses for the meniscus to recover a shape of lower energy. This leads to a gradient of capillary pressure inside the meniscus, which in turn tends to retain liquid.

3.2.2.1 Order of magnitudes

To go further into the derivation, it is necessary to assume that similarly to equation 3.2, 3.3 the film is thin (i.e $\frac{h}{R} \ll 1$) and subsequently that the deformation of the meniscus is small and localized inside a transition region, where the curvature changes from the curvature of the static shape to the curvature of the flat film (figure 3.2).

Viscous stress: considering that the dynamic meniscus is flat enough, so that the typical size of variation of the velocity along y is h_0, the viscous stress is of order:

$$\eta \frac{\partial^2 v_x}{\partial y^2} \sim \frac{\eta V}{h_0^2} \tag{3.19}$$

Capillary stress: Considering that the meniscus is disturbed over a length λ, the capillary pressure gradient in region (b) is of order of the capillary stress divided by the characteristic length of the dynamic meniscus:

$$\frac{\partial p}{\partial x} \sim \frac{1}{\lambda}\frac{T}{R} \tag{3.20}$$

3.2.2.2 Solving the problem

Thus writing Navier-Stokes equation dimensionally leads to:

$$\frac{\eta V}{h_0^2} \sim \frac{1}{\lambda}\frac{T}{R} \tag{3.21}$$

However, since two unknowns (λ, h_0) appear in equation 3.21 it is necessary to add another equation to fully solve the problem. A usual way to determine λ, is to write the matching of curvatures between the static meniscus and the dynamic meniscus. As mentioned in the previous section, for a thin film, when the flow is slow and the approximation of lubrication is verified, the dynamic meniscus is almost flat, so that its length λ is large compared to its height. In addition, since the dynamic meniscus is almost flat and its shape varies slowly (i.e. $h' \ll 1$), its height is of order of the height of the thin deposited film (i.e. h_0). Therefore, considering the afore-mentioned orders of magnitude, equation 3.1 becomes:

$$\mathcal{C}_\lambda \sim \frac{h_0}{\lambda^2} \tag{3.22}$$

Matching the curvature given by equation 3.22 with the curvature of the static meniscus, it leads to:

$$\frac{1}{R} + \frac{h_0}{\lambda^2} \sim \frac{2}{R} \tag{3.23}$$

which produces an expression for λ, the size of the dynamic meniscus:

$$\lambda \sim \sqrt{h_0 R} \tag{3.24}$$

Now, injecting equation 3.24 into equation 3.21 yields:

$$\frac{h_0}{R} \sim Ca^{\frac{2}{3}} \tag{3.25}$$

Equation 3.25 is the same as equation 3.18 without the numerical factor. Furthermore, it is also possible to express the size of the dynamic meniscus by injecting equation 3.25 in 3.24. It leads to:

$$\frac{\lambda}{R} \sim Ca^{\frac{1}{3}} \Leftrightarrow \frac{\lambda}{h_0} \sim Ca^{-\frac{1}{3}} \tag{3.26}$$

Equation 3.26 is also consistent with the value of L_λ that appears to be the characteristic scale for x in equation 3.16. These results validate the scaling analysis for the case of a Newtonian fluid, for small value of the capillary number.

3.2.3 Effect of the interface curvature

The scaling analysis described in the previous section also allows to solve more complicated problems. For example, it is possible to consider inertial effects or larger dynamic meniscus [121]. In this section, assuming that Stokes' assumption still holds, we restrict ourselves to the second case. Therefore we consider that the thin film perturbs the static shape of the meniscus, so that its curvature is now given by equation 3.27. This hypothesis means that the considered film is thicker than in the classical case but that lubrication approximation still holds, and so that the results of this analysis must be valid for larger capillary numbers. We follow the derivation as performed in [121].

$$\mathcal{C}_a = \frac{2}{R - h_0} \tag{3.27}$$

Considering the above mentioned hypothesis, equation 3.21 becomes:

$$\frac{\eta V}{h_0^2} \sim \frac{1}{\lambda} \frac{T}{R - h_0} \tag{3.28}$$

as well as equation 3.23:

$$\frac{h_0}{\lambda^2} \sim \frac{1}{R - h_0} \tag{3.29}$$

Finally, injecting equation 3.29 into equation 3.28, it yields:

$$\frac{h_0}{R} \sim \frac{Ca^{\frac{2}{3}}}{1 + Ca^{\frac{2}{3}}} \tag{3.30}$$

However equation 3.30 does not provide a quantitative description of the deposition, therefore it is necessary to introduce a numerical coefficient to describe the data. Going back to equation 3.28 and introducing an unknown matching constant α_0, it can be rewritten as:

$$\frac{\eta V}{h_0^2} = \alpha_0 \frac{1}{\lambda} \frac{T}{R - h_0} \tag{3.31}$$

Hence, equation 3.30 becomes:

$$\frac{h_0}{R} = \frac{\alpha_m Ca^{\frac{2}{3}}}{1 + \alpha_m Ca^{\frac{2}{3}}} \tag{3.32}$$

wherein $\alpha_m = \alpha_0^{-\frac{2}{3}}$. Equations 3.32, 3.30 imply that the film thickness tends to a finite value as Ca increases. This conditions is required by the confined geometry: the film thickness cannot diverge.

3.2.3.1 Comparison with experimental results

Equation 3.32 is plotted on figure 3.4 and compared to the experimental results obtained by G.I. Taylor for glycerine in a circular channel [111] (empty symbols), and to *Bretherton's equation* (dashed line) for intermediate value of the capillary number. The dashed-dotted line represents equation 3.32 for $\alpha_m = 1.337$ (i.e. the value derived by Bretherton [112]). A convergence of the value of the film thickness for $Ca > 1$ capillary number is clearly seen, in addition, as expected by considering a thicker film, the scaling works slightly better for capillary numbers above 0.01. This correction is also similar to the one derived in [126] using perturbation theory in the case of the withdrawal of a cylinder from a liquid bath.

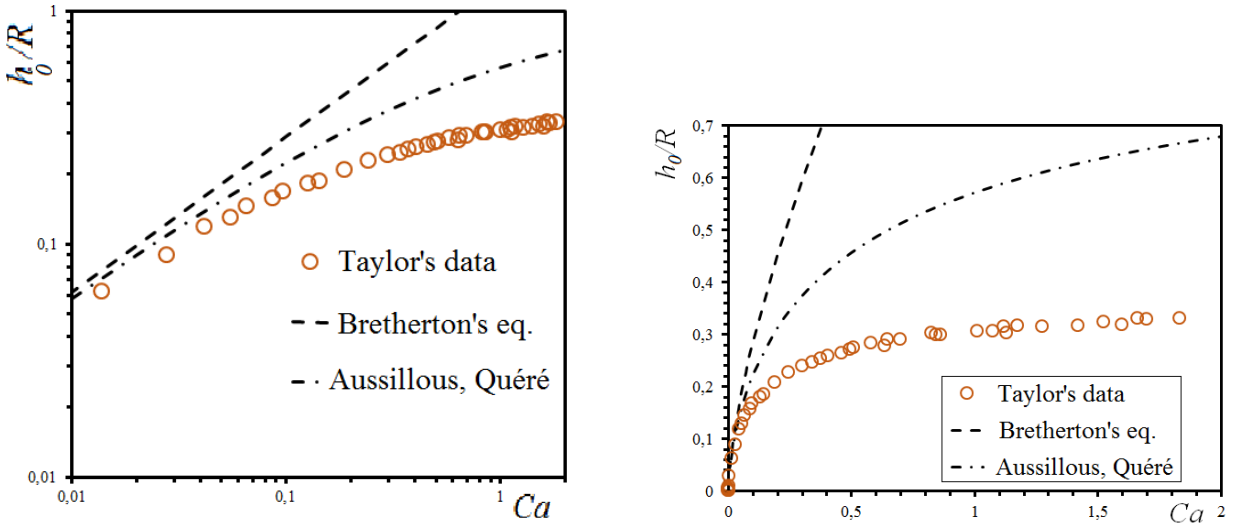

(a) Log-log scale.

(b) Linear scale.

Figure 3.4 – Comparison between the data of normalized film thickness as a function of the capillary number obtained by Taylor (empty symbols), and equation 3.30 (*Bretherton's equation*, dashed line) for $\alpha_m = 1.337$. The dashed-dotted line represents equation 3.32 for $\alpha_m = 1.337$ (i.e. the value derived by Bretherton [112]) [121].

3.2.3.2 Saturation value

The experimental results obtained by Taylor converge to a finite value of the film thickness ($\frac{h_0}{R} \simeq 0.35$), whereas equation 3.32 always converges to 1. However, the data can be described by an empirical fit similar to equation 3.32 [121], which thus incorporates the measured limiting value of h_0.

The saturation of the value of h_0 seems to be related to the structure of the flow inside the channel depending on the velocity [111, 127]. Taylor suggested that the flow does not exhibit vortices when the velocity of the bubble exceeds two times the mean velocity of the flow, that is the maximum velocity of the Poiseuille profile, because in that case, fluid particles on the central streamline must move toward the meniscus instead of away from it (figure 3.5)b.

Denoting v_b the velocity of a bubble, and v_m the mean velocity of the fluid, the excess velocity of bubbles ($W = \frac{v_b - v_m}{v_b}$) can be expressed as a function of the film thickness by equation 2.23 obtained through a mass balance on the moving bubble. For $v_b = v_{max} = 2v_m$, the excess velocity is $W = 0.5$ which corresponds to the limiting case mentioned above, it yields a corresponding film thickness of $1 - \frac{1}{\sqrt{2}} \simeq 0.29$ which roughly corresponds to the beginning of the saturation of the experimental data measured by Taylor (figure 3.4). Thus, he suggested that the saturation of the film thickness is due to

the structure of the flow which exhibit vortices when $W < 0.5$, and are not observed otherwise (figure 3.5)a.

The flow scenario was later confirmed by Saffman [123, 127], using matched asymptotic expansions and numerical simulations. These arguments suggest that when viscous stresses are large compared to interfacial stresses, the absence of vortices inside the flow leads to a saturation of the deposited thickness.

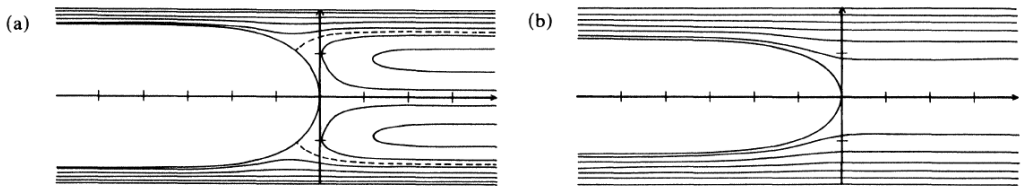

Figure 3.5 – Typical shape of the streamlines in the reference frame of the bubble computed numerically [123, 127]. (a) For $W < 0.5 \Leftrightarrow \frac{h_0}{R} < 1 - \frac{1}{\sqrt{2}}$; (b) for $W > 0.5 \Leftrightarrow \frac{h_0}{R} > 1 - \frac{1}{\sqrt{2}}$

3.2.4 The coating of a fiber with a dilute emulsion (capture model)

When drawing a fiber out a bath of a dilute emulsion with a droplet volume fraction $1 < \phi < 25$ %, it was found that, at very low velocity, the classical LLD (Landau-Levich-Derjaguin) law flailed to predict the film thickness which is almost constant [128]. The authors propose a capture model, considering that the fiber entrains all droplets in its vicinity (an annulus of spacing d, the droplet diameter), the equivalent thickness of continuous oil film, is given by:

$$h_0^* = \phi d \tag{3.33}$$

In our case, considering that this model is also valid for emulsions with higher volume fraction, estimating $d \simeq 5$ μm and $\phi \simeq 90$ % from chapter 1, it would lead to $h_0^* \sim 4.5$ μm.

3.3 Literature review: non-Newtonian fluids

The coating of the classical geometries (i.e. roll, plate, fiber, tube - figure 3.1) has been investigated for different types of non-Newtonian fluids. In this section, we give a brief review of the results obtained for Non-Newtonian fluids and particularly for yield-stress fluids.

3.3.1 Shear-thinning fluids

First, an analysis similar to the one developed by Bretherton for a Newtonian Fluid allows to determine the typical variation of the film thickness (h_0) coated on a plate drawn out of liquid bath as function of the withdrawal velocity V for power-law fluids [80].

$$h_0 \sim \left(\frac{kV^n}{T}\right)^{\frac{2}{2n+1}} \tag{3.34}$$

Wherein T is the surface tension, and the constitutive equation of the liquid is $\tau = k\dot{\gamma}^n$. Equation 3.34 is plotted on figure 3.6 for the Newtonian case ($n = 1$) and also for the flow indexes corresponding to our material: carbopol gels $n = 0.35$ and emulsions $n = 0.5$. In that case the predicted variation of deposited thickness is larger for a non-Newtonian fluid than for a Newtonian fluid.

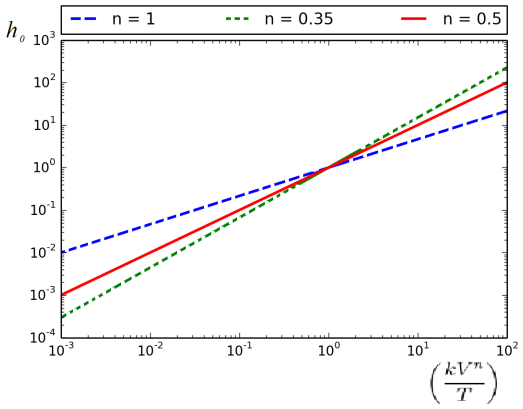

Figure 3.6 – Typical variation of the deposited film thickness as predicted by equation 3.34 as a function of $\frac{kV^n}{T}$.

The scaling predicted by equation 3.34 has later been tested when drawing a fiber out of a polymer solution [129], or plate at arbitrary angle [130]. Other studies focused on investigating the rise of long bubbles in inclined channels [131], or in horizontal microchannels [132], and derived similar expressions.

These studies highlights that, when the fluid is viscoelastic, normal stresses tend to modify the thickness of the deposited film [129, 132]. The larger the normal stresses, the larger the coated thickness. This increase is interpreted as a *Weissenberg effect* (see *normal stresses*, 1.3.3.3 in chapter 1). Such effect has also been reported to modify the *Saffman-Taylor instability* in *Hele-Shaw cell*, where the thin deposited film on the top and bottom plates plays an important role in the determination of the finger width [133, 134].

To try to take into account the normal stresses that develop in viscoelastic fluid during coating, other scaling than those presented in equation 3.34 were derived from matched asymptotic expansions analysis [88, 129]. The similarity between these scalings is that, when the normal stresses are considered to be large with respect to the viscous stresses, the coating thickness depends on the ratio of the normal stress (instead of the viscous stress) to the capillary stress.

3.3.2 Yield-stress fluids

Among non-Newtonian fluids, the coating of yield-stress fluids have received little considerations. Here, we summarize the different results related to the coating of yield-stress fluids in the classical geometries.

Regarding the older results obtained for coating of yield-stress fluids, it can be noted that Gutfinger and Tallmadge [80] used carbobol gels for their experiments. Even if they do not report the presence of a yield stress, the high concentrations that they use ($> 1\%$), and the typical surface tension value they find, suggest that their fluids may have one. However they do not take it into account in their analysis.

3.3.2.1 Matched asymptotic expansions in the geometry of a plate or a fiber

First, motivated by the development of photographic industry, Derjaguin [118] addressed the problem of the withdrawal of a plate, and a fiber, out of a bath of yield-stress fluid. Modeling the yield-stress fluid as a Bingham fluid (i.e $\tau = \tau_y + \eta\dot{\gamma}$), he attempted to fully solve the problem by the method of matched asymptotic expansions. However, he found no solution, and was obliged to consider two partial problems: (i) the problem of pure plastic material such that its stress is only defined by its yield stress; (ii) the problem involving the coating of a classical Newtonian liquid. Then he suggested that summing the thicknesses obtained separately for each problem would give the total coated thickness for a Bingham fluid. The coated thickness obtained from matched asymptotic expansion for a pure plastic material during the withdrawal of a plate or a fiber is given by equation 3.35.

$$\frac{h_0}{\ell_d} = \alpha_d B^2 \tag{3.35}$$

Wherein $B = \frac{\tau_y \ell_d}{T}$ is a non-dimensional number that compares the yield stress to the capillary stress. The characteristic length ℓ_d in equation 3.35 is a modified capillary length $\ell_d = \left(\frac{T}{(1-\cos(\theta))\rho g}\right)^{\frac{1}{2}}$ in the geometry of a plate (with θ the angle between the plate and the bath), and the fiber radius R for the withdrawal of a fiber. The values of the matching parameter α_d, and the characteristic length ℓ_d are summarized in table 3.1.

	ℓ_d	α_d
plate	$\left(\frac{T}{(1-\cos(\theta))\rho g}\right)^{\frac{1}{2}}$	13.0
fibre	R	1.62

Table 3.1 – Relevant parameters obtained by Derjaguin [118].

It must be noted that the previous analysis predicts that, as soon as the material presents a yield stress, a finite coated thickness exists and is independent on the velocity. Equation 3.35 is valid under lubrication approximation and when the yield stress is small compared to the capillary stress. Under these hypotheses the final thickness of the deposited film on a withdrawn plate is supposed to be given by equation 3.36.

$$\frac{h_0}{R} = 13.0B^2 + 1.34Ca^{\frac{2}{3}} \tag{3.36}$$

It is also possible to retrieve equation 3.35 by scaling arguments [122]. In the fiber case, considering that the deposition results from a balance between the capillary pressure gradient and the divergence of the stress tensor, for a pure plastic material it yields:

$$\frac{\tau_y}{h_0} \sim \frac{1}{\lambda}\frac{T}{R} \tag{3.37}$$

To find λ the characteristic size of the dynamic meniscus, one way is to write the matching of curvatures. As in the circular channel case, assuming that the film is flat enough, and providing that R is now the radius of curvature of the fiber, equation 3.23 remains unchanged and similarly leads to equation 3.24. Thus combining equation 3.37 and equation 3.24, the scaling law becomes:

$$\frac{h_0}{R} \sim B^2 \tag{3.38}$$

hence,

$$\frac{\lambda}{R} \sim B \tag{3.39}$$

From equation 3.39 it is clear that assuming $\frac{\lambda}{R} \ll 1$ is equivalent to say that the yield stress is small compared to the capillary stress.

3.3.2.2 The coating of a plate with an Herschel-Bulkley fluid

More recently Maillard and Coussot studied the withdrawal of a plate out of bath of yield-stress fluid (carbopol gels) at constant velocity [135, 136]. Their approach relies on the knowledge of the flow field inside the bath, so that they do not need to solve the full hydrodynamic problem by matched asymptotic expansions. They assume that, since the yield stress is at least of the order of the capillary stress, the viscous stress inside the layer is only balanced by gravity forces. Saying that the yield stress dominates the capillary stress also leads to the definition of a new length on which the results should depend; to satisfy the previous hypothesis, this new length scale is given by a balance between the gravity stress and the yield-stress: $h_c = \frac{\tau_y}{\rho g}$. Since surface tension is neglected, it implies that the complex dynamic associated with the meniscus is also neglected.

Therefore, writing the balance between the viscous stress inside the liquid layer entrained by the plate and the gravity stress, and assuming that the size of the coated layer is proportional to the size of the liquid layer inside the bath, they find that:

$$\frac{h_0}{h_c} \simeq 2a_0(1 + a_0^n Bi^{-1}) \tag{3.40}$$

In equation 3.40,

- $Bi^{-1} = \frac{k\left(\frac{V}{h_0}\right)^n}{\tau_y}$ the Bingham number where the typical shear rate is built on h_0, that compares the yield-stress to the viscous stress during the flow.
- a_0 is an empirical thinning factor that accounts for the separation of the liquid layer inside the bath into two parts: one part is coated on the plate, while the other part recirculates inside the bath. In the limit of vanishing velocities, $\frac{h_0}{h_c} \to 2a_0$.
- $h_c = \frac{\tau_y}{\rho g}$ is the length resulting from the balance between the yield stress and gravity stress length.

3.3.2.3 Coating experiments of a fiber with foams

Foams are constituted of a large number of gas bubbles separated by thin liquid films. The structure of foams is similar to the one of concentrated emulsions (described in chapter 1). Therefore, their properties and dynamic are also similar in many ways [65, 137]. Particularly, foams exhibit a yield stress. Thus, coating of foams is good example of the coating of yield-stress fluids.

Here we give an overview of the results obtained for the coating of a fiber with a foam. This problem was recently addressed experimentally [125, 138]. The authors drew a wire out of a container filled with foam at constant velocity. Their experimental results were divided into three regimes depending on the pulling velocity:

- at low velocities the fiber did not entrain the foam.
- above a critical velocity, the foam started to be coated on the fiber, but in a highly inhomogeneous fashion. Clusters of bubbles were attached to the fiber and separated by a constant distance for a given velocity.
- above another critical velocity (larger than the first one) the foam was entrained continuously, and the fiber was fully coated.

They proposed and dismissed different physical mechanisms that could possibly lead to such discontinuous coating behaviour: Rayleigh-Plateau instability, inertia, normal stresses, or the surface chemistry of the fiber. Finally, even if a detailed analysis of the physical process at play was not provided, the authors mention stick-slip motions, which highlight the possible role of wall slip during the coating process.

3.3.2.4 Bingham fluid in a circular channel

The coating of Bingham fluids with a small yield stress in a circular channel is investigated in [139]. The authors found that the deposited thickness quickly saturate to a finite value for $Ca > 1$, they validated their results by numerical simulations.

3.3.3 Conclusion

The theory of coating for Newtonian fluids is well established, and can be extended to more complex geometries by means of scaling laws. This allows to solve the majority of cases in the classical geometries. However, for non-Newtonian fluids, scaling laws were mostly developed for shear-thinning fluids. Finally, few works (experimental or theoretical) focused on yield-stress fluids (with or without wall slip), and to our knowledge, none of them on the coating of the wall of circular channels for an HB fluid with a large yield stress. This important problem for understanding the dynamics of two phase flow, is addressed in the next section.

3.4 Experiments for yield stress fluids

In this section we describe the experiments performed to investigate the analogous of the *Bretherton problem* with yield-stress fluids. We detail three measurement methods of the film thickness, which give similar results.

3.4.1 Experimental set-up

The experiments are performed using carbopol gels or oil-in-water emulsions. These materials, which are described in chapter 1, behave as simple yield-stress fluids. We use glass capillaries of circular cross section with different radii: 235, 513, 620, 702 μm. As detailed in chapter 2 (section 2.4.4.2), the surface of each of them can be treated to suppress wall slip of carbopol gels. Therefore, in the following, two types of experiment are performed: experiments with no-slip boundary conditions (using carbopol gels), and experiments with slip at the wall during the flow (using carbopol gels and emulsions).

3.4.1.1 Steady experiments

A capillary filled with yield-stress fluid is connected to an empty syringe mounted on an Harvard Apparatus syringe pump. The syringe pump is set on withdrawal mode at fixed flow rate (between 1 μl/min and 0.2 ml/min), such that the syringe pumps the yield-stress fluid initially inside the channel. Due to the deposition of the film on the wall, the meniscus must move faster than the mean flow rate imposed by the syringe pump. Therefore, we record a movie of the motion of the meniscus inside the capillary during the syringe filling using a CCD camera. Pictures of a typical experiment are presented in figure 3.7. The extracted position of the meniscus is plotted as a function of time on figure 3.8: as expected the dependency is linear and therefore the meniscus velocity is constant.

The velocity of the rear meniscus (V) is extracted from the movie and compared to the imposed flow rate of the syringe pump (Q_{sp}). Mass conservation yields:

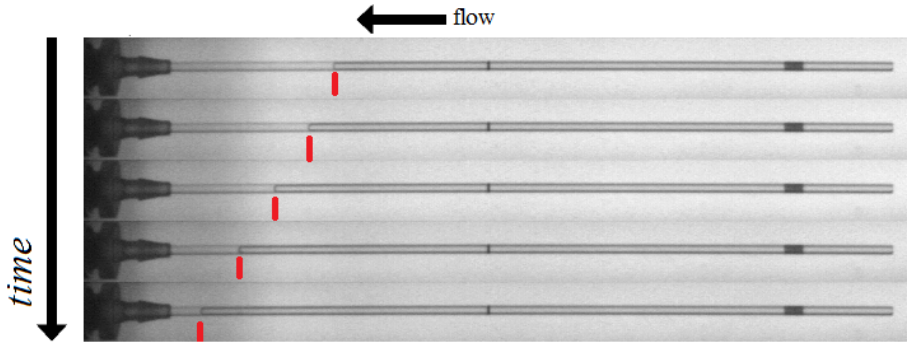

Figure 3.7 – Pictures of the emptying of a capillary at constant flow rate (0.1 ml/min) with $R = 513$ μm for carbopol gel ($\tau_y = 75$ Pa). Time increases from top to bottom, the red line on each image denotes the position of the meniscus.

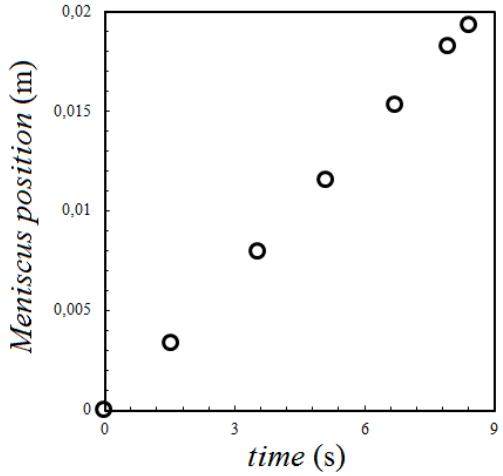

Figure 3.8 – Position of the meniscus as a function of time during steady experiment (0.1 ml/min, $R = 513$ μm).

$$Q_{sp} = V\pi(R - h_0)^2 \tag{3.41}$$

which leads to:

$$\frac{h_0}{R} = 1 - \sqrt{\frac{Q_{sp}}{\pi R^2 V}} \tag{3.42}$$

Values of the film thickness obtained as a function of the applied flow rate (Q_{sp}) are shown on figure 3.9.

Optical measurement

For an experiment with wall slip, we also estimate the thickness h_0 in the steady experiments using an optical microscope. The index mismatch between air and the yield-stress fluid allows us to obtain a mean value of h_0. The value obtained in steady experiment, and with optical measurement are compared in table 3.2.

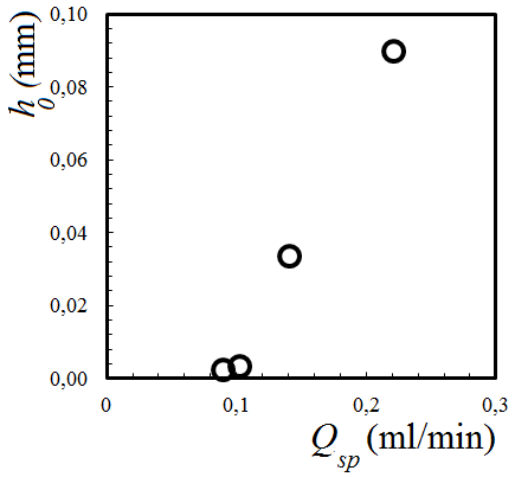

Figure 3.9 – Film thickness obtained from steady experiments for carbopol gel (τ_y = 75 Pa) in a channel of radius R = 513 μm) as function of the imposed flow rate.

	V (mm/s)	h_0 (mm)
steady experiment	2.85	0.033
optical measurement	2.85	0.056 ± 20 %

Table 3.2 – Comparison between optical measurement for carbopol gel (τ_y = 75 Pa) and steady experiment in a capillary of radius 513 μm.

3.4.1.2 Unsteady experiments

First, a drop (also called plug) of yield-stress fluid is placed inside a capillary using a syringe with a thin needle. The length of the plug is denoted (L) and its radius is always equal to the radius of the capillary (R). Then, the drop is pushed at constant pressure. The pressure is applied by means of a Fluigent pressure controller (MFCZ, 0-2bar, precision ± 1 mbar). Pictures of the experiments are recorded using a CCD camera at a maximum frame rate of 200 fps, as can be seen in figure 3.10.

As the plug advances inside the channel, it deposits a thin film of yield-stress fluid on the channel wall and thus its volume decreases. This leads to a drop in the viscous dissipation, and since the applied pressure is constant the plug accelerates. This scenario holds until the plug reaches a critical size and ruptures (last picture on figure 3.10).

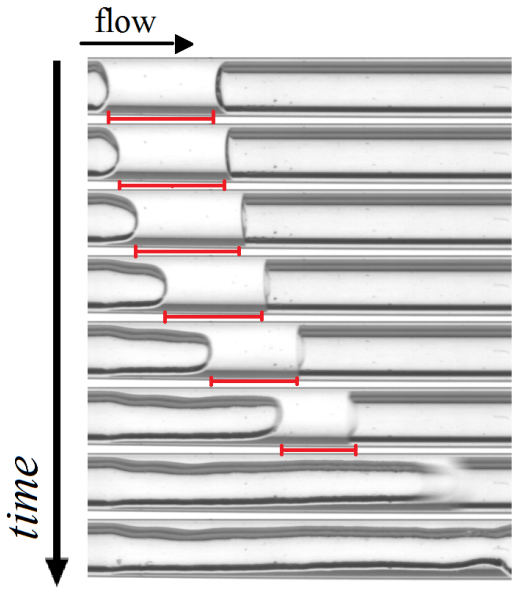

Figure 3.10 – Pictures of a plug pushed at constant pressure (25 mbar) inside a capillary with $R = 513$ μm. Time increases from top to bottom, the red line below each image stands for the measure of $L(t)$. Each image is separated by 0.33 s.

Measurement of the film thickness

We measure the length of the plug $L(t)$ as a function of the velocity of the rear meniscus ($V(t)$) of the plug. The velocity of the rear meniscus is the value of interest since it is this parameter that controls the deposition for a Newtonian fluid.

The film thickness is obtained from the measurements of $L(t)$, by assuming a uniform deposition along the channel wall. The deposited film is supposed to have the same thickness (h_0) everywhere on the surface of the capillary. Under this assumption, a mass balance between what is deposited during the time δt and the variation of the plug's length ($\delta L(t)$) during δt is expressed as:

$$\pi R^2 \delta L(t) = V(t)(\pi R^2 - \pi(R - h_0)^2)\delta t \tag{3.43}$$

which finally leads to:

$$\frac{h_0}{R} = 1 - \sqrt{1 - \frac{1}{V(t)}\frac{\mathrm{d}L}{\mathrm{d}t}} \tag{3.44}$$

Thus, knowing the velocity of the rear meniscus ($V(t)$) and the length of the plug (L), equation 3.44 allows to determine the deposited thickness (h_0). This method has the advantage to produce a full curve $h = f(V)$ with one experiment. Due to our set-up, the maximum measured value of V is close to 10 cm/s. Typical data of $L(t)$ and $V(t)$ are shown on figure 3.11a and 3.11b. Two regimes are seen, first the size decreases slowly while the velocity increases slowly too. However, at some point the decrease in size and the increase in velocity diverge. This non-linear effect is associated with the non linearity of the pressure / flow rate relationship for a yield-stress fluid (see chapter 2), and will be detailed in chapter 5.

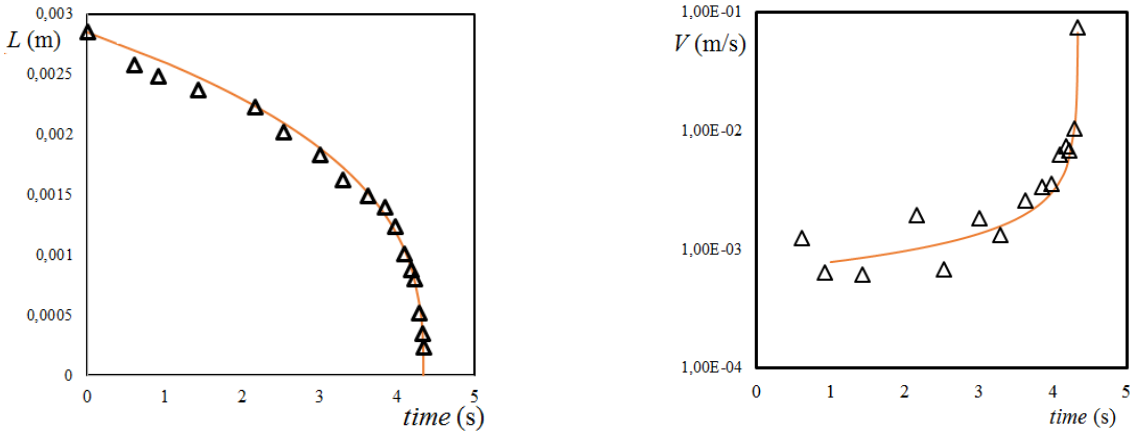

(a) Plug length.

(b) Velocity of the rear meniscus.

Figure 3.11 – Typical variations of the raw data for a carbopol plug ($\tau_y = 75$ Pa) inside a capillary of radius 702 μm pushed at 50 mbar. The orange lines are fitting functions used to obtain accurate values of the derivatives.

The results of such measurements are presented in the next paragraphs, first for no-slip boundary conditions, and secondly when there is slip at the wall. To ensure that these measurements are not affected by dynamical effects, the determination of the film thickness is compared to the afore mentioned steady measurements (i.e. at constant velocity).

Plug rupture

At the end of the experiment the plug of yield-stress fluid breaks due to its small length. Thus to avoid finite size effects on the measurements of the film thickness, we do not take into account the data obtained for plugs with: $L < 2R$.

3.4.2 Results for no-slip

In this section, we present the results obtained with carbopol gels ($\tau_y = 75$ Pa, $k = 35$ Pa.s^n, $n = 0.35$) and treated glass capillaries. Raw data of the film thickness as a function of the velocity obtained by unsteady measurements are presented on figure 3.12.

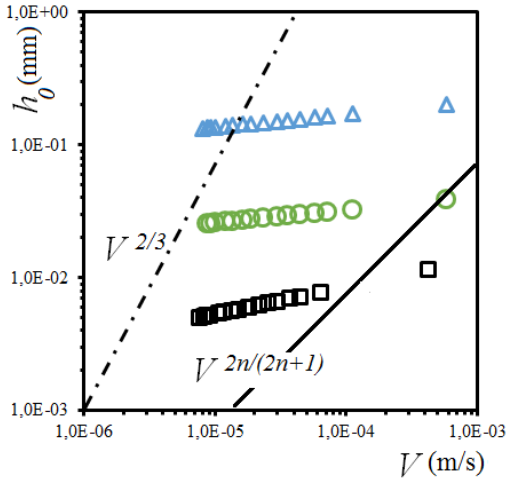

Figure 3.12 – Deposited film thickness as a function of the rear meniscus velocity for carbopol gel ($\tau_y = 75$ Pa, $k = 35$ Pa.s^n, $n = 0.35$) in different capillaries (□ 235 μm; ∘ 513 μm; △ 702 μm). Typical dependency for: Newtonian fluid in a circular channel (dashed-dotted line); shear-thinning fluid coated on a plate (plain line).

On figure 3.12, we observe that h_0 increases with V, yet in our experiments, this increase is much smaller than what is predicted for a Newtonian fluid in a circular channel (dashed-dotted line), or a shear-thinning fluid coated on a plate (plain line).

3.4.3 Results for slip

Slippage happens for carbopol gels when capillaries are not treated with PEI (see chapter two), or for emulsions flowing in any glass capillaries. In that case, the system exhibit two characteristic behaviors depending on the velocity.

3.4.3.1 Low velocities

At low velocity, in the unsteady experiments, the plug of yield-stress fluid does not decrease in size when pushed through the channel (figure 3.13).

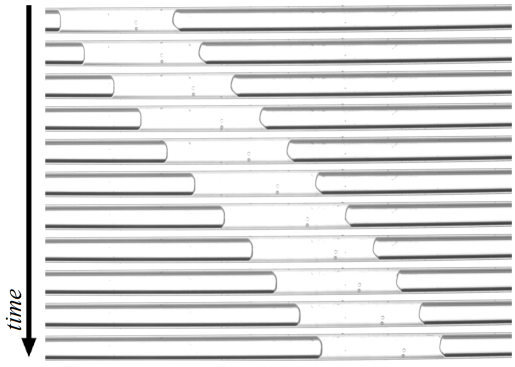

Figure 3.13 – Motion of a plug of emulsion pushed at 5 mbar inside a glass capillary ($R = 513$ μm), each picture from top to bottom is separated by 108 sec.

Pictures of a plug of emulsion pushed at 5 mbar (below the yield pressure associated with the flow of this plug with no-slip conditions) are shown on figure 3.13. At the end of the experiment the plug had traveled more than 7 cm without a measurable decrease in its size. Thus, in the following, we refer

to this regime as full slip. This happens for both emulsions and carbopol gels. We also report that in that case, the difference in velocity measured in steady experiments is not significant enough to produce convincing results. We then conclude that either the deposited thickness is so thin that we have attained the limit of resolution of our set-up (i.e. camera), or that there is not any yield-stress material deposited and the contact line is moving. We also tried interferometry measurements but probably due to the large size (compared to the radius of the capillaries) and low intensity of the laser spot we did not succeed in measuring the film thickness into our glass capillaries.

3.4.3.2 Transition

Above a critical velocity, the plug's length starts to decrease as the velocity increases. This is associated to the deposition of a yield-stress fluid film with a measurable thickness. Typical raw data are presented on figure 3.14 in log-log scale for emulsion and carbopol gel with wall slip.

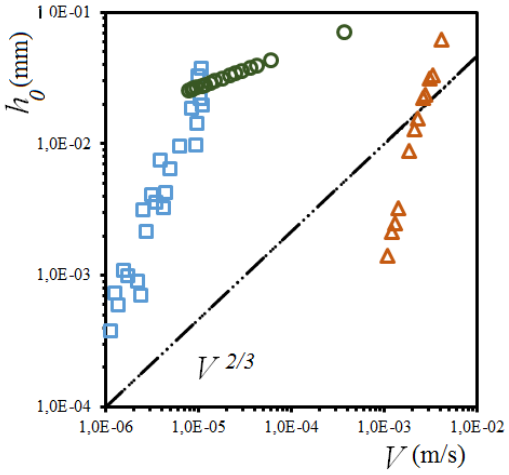

Figure 3.14 – Typical raw data of film thickness measurements as a function of the measured velocity for: □ emulsion $R = 235$ μm; ∘ carbopol gel (no-slip) $R = 235$ μm; △ carbopol gel (slip) $R = 513$ μm. The dashed-doted line stands for the typical variation of the deposited thickness with the velocity for a Newtonian fluid.

First, as can be seen on figure 3.14 the deposited thickness increases with the applied velocity for both slip and no-slip conditions. When there is wall slip the variation of the measured thickness is much sharper than what is predicted for a Newtonian fluid. The index of the power law obtained from experimental values when there is wall slip is between 2 and 3, whereas its value is close to 0.25 for no-slip boundary conditions.

3.4.3.3 High velocities

Experiments performed at large velocity, for plugs with $L > 2R$, are presented on figure 3.15a. As can be seen, when there is wall slip the film thickness tends to an almost finite value. This value seems to roughly correspond to the maximum measured value in unsteady experiments for no-slip boundary conditions (compare $h_0 = 0.07$ mm without slip, to the saturation value $h_0 = 0.09$ mm when there is wall slip).

When the applied stress is large compared to the yield stress, as discussed in chapter two, the effect of wall slip may become negligible compared to the bulk flow, thus we expect to recover the value of the film thickness obtained with no-slip boundary conditions. The results are shown on figure 3.15a. For carbopol in a channel of 513 μm the agreement with this assumption is relatively good. This further implies that the flow scenario may be the same as the one presented in the Newtonian

case. The saturation value seems also to be close to the last measured point for no-slip boundary conditions. This result is consistent with the assumption mentioned previously: the velocity profile with slip boundary conditions tends to the velocity profile with no-slip boundary conditions at large applied stresses (i.e. high velocities) compared to the yield stress.

3.4.3.4 Plug rupture

To avoid finite size effect we do not take data corresponding to plugs that have $L < 2R$ into account. On figure 3.15b both the circles and squares correspond to the same plug, however the circles stand for the measurements obtained when $L < 2R$. In that case the value of the deposited film thickness continues to increase until the plug ruptures. In that case, the film thickness may overcome the saturation value measured at high velocities. Example of such behavior is shown on figure 3.15b for emulsions.

We assume that this behavior is due to finite-size effects. Such effects might happen through an interaction between the front and rear menisci of the plug which may perturb the flow inside the rear meniscus which governs the deposition mechanism for a Newtonian fluid. Concerning this effect, it is worth noting that the experiments performed by Taylor correspond to an 'infinite' plug size [111], while Aussillous used plugs of 5 to 10 cm such that boundary effects are neglected [121].

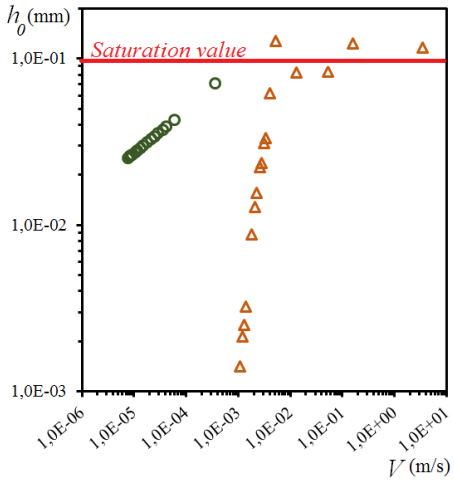

(a) Saturation: results for ∘ carbopol gel ($\tau_y = 75$ Pa, no-slip) $R = 513$ μm; △ carbopol gel (slip) $R = 513$ μm.

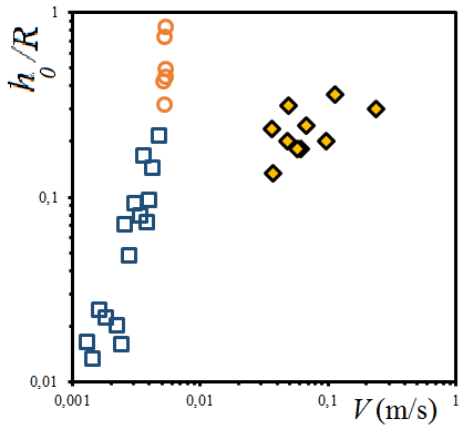

(b) $\frac{h}{R}$ as a function of velocity for emulsions ($\tau_y = 100$ Pa): ∘ short plug, i.e. $L < 2R$ for $R = 235$ μm; ⋄ long plug for $R = 513$ μm; □ long plug for $R = 235$ μm.

Figure 3.15 – Final stages of the deposition obtained by unsteady measurements.

3.4.3.5 Visualization

The afore-mentioned dynamics is visible on figure 3.16, showing a small carbopol plug pushed at constant pressure. On the first images, the plug advances without any measurable decrease in its size. In this regime, the menisci are almost flat due to the yield stress being larger than the capillary stress, and the absence of dynamical effects. Indeed, since there is wall slip and the velocity is extremely small, the whole flow is a plug flow, therefore the shape of the meniscus is only predicted by a balance between surface tension and the yield stress. At some point during this process (last image of figure 3.16), the meniscus recover a hemispherical shape, and a thin film on the wall of the channel is visible. This shows the beginning of the deposition process, and therefore suggests that the no-slip boundary

condition is recovered. Finally, note that, as the plug advances its velocity decreases. This observation is discussed later.

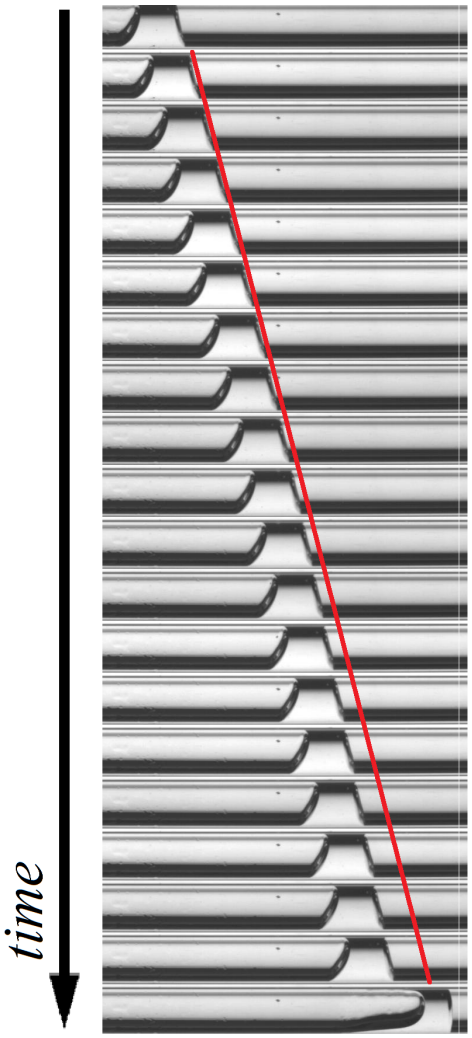

Figure 3.16 – Pictures (separated by 1.35 s) of a carbopol (τ_y = 75 Pa) plug pushed at constant pressure inside a circular capillary (R = 513 μm). Time increases from top to bottom. The red line shows the extrapolated position of the front meniscus of plug from the velocity of the four first images.

3.5 Models

In this section we try to describe the results detailed in the previous section mainly by means of scaling laws. First, we introduce the required parameters to characterize the flow. Then, we detail the different models of the literature and their implications. Finally, by analogy with the Newtonian case, we derive scaling law depending on these parameters.

3.5.1 Dimensionless numbers

Neglecting gravity (details in chapter 2), the two phase flow of yield-stress fluid in a capillary involves three main characteristic stresses:

- A characteristic stress associated with the solid plug flow at the center of the channel: the yield stress τ_y.

- A characteristic stress associated with the flow of the liquid layer experiencing a stress larger than the yield stress. This liquid layer surrounds the solid core during the flow. The viscous stresses in the Herschel-Bulkley model are given by $k\dot{\gamma}^n$, therefore to express the viscous stress, it is necessary to give a characteristic value of $\dot{\gamma}$ as a function of the parameters of the problem. The order of magnitude of the mean shear rate in a channel of radius R is given by $\dot{\gamma} = \frac{V}{R}$, so that the typical mean viscous stress is $k\left(\frac{V}{R}\right)^n$.
- A characteristic stress associated with *Laplace pressure* of gas/liquid interfaces. Since $\frac{h_0}{R} \ll 1$ this stress scales as $\dfrac{T}{R}$.

Using these characteristic stresses we define three dimensionless numbers.

Static case

First, to compare the yield stress to the capillary stress, following Derjaguin we define:

$$B = \frac{\tau_y R}{T} \tag{3.45}$$

B gives an information on the two-phase yield-stress fluid flow structure when at rest. When $B \ll 1$ the capillary stress is large compared to the yield stress, and interfaces of characteristic curvature R^{-1} are able to deform the material (and make it flow) to recover their shape of minimum energy. When $B \gg 1$ the yield stress is large compared to the capillary stress. As an example, the shape of the menisci may depart significantly from their equilibrium shape (i.e. spherical shape) predicted by surface tension in Newtonian fluid. This effect is clearly seen on the first images of figure 3.16. During slip, which is similar to the static case since the material does not yield at all, the menisci are almost flat. However, when the material starts to flow, the equilibrium shape (curvature $\sim R^{-1}$) is recovered (last image of figure 3.16).

Liquid regime

When the applied stress is large, the velocity profile of the yield stress fluid flow is mostly constituted of a liquid layer so that the yield stress does not modify the shape of interfaces. In this regime we can introduce a modified capillary number:

$$\widehat{Ca} = \frac{k\left(\frac{V}{R}\right)^n}{\frac{T}{R}} \tag{3.46}$$

It compares the mean viscous stress to the capillary stress, and reduces to the classical capillary number for $n = 1$.

Yielding process

When the applied stress is of the order of the yield stress or slightly larger, it is interesting to have information on the origin of the pressure drop during the flow. This can be achieved by defining the Bingham number, which compares the yield stress to the viscous stress.

$$Bi = \frac{\tau_y}{k\left(\frac{V}{R}\right)^n} \tag{3.47}$$

When $Bi \ll 1$, the viscous stresses dominate the flow, so that the velocity profile is mostly constituted of a liquid-like region. When $Bi \gg 1$ the velocity profile is mostly a plug flow with a constant velocity. This last situation approaches the case of full slip.

3.5.2 Discussion of literature models

In this section we discuss the models of the literature for the coating of yield-stress fluids.

3.5.2.1 The coating of a plate with an Herschel-Bulkley fluid

To compare the results obtained in [135] with what was obtained by Derjaguin, we can change variables so that the capillary length ($\kappa^{-1} = \sqrt{\frac{T}{\rho g}}$) becomes the characteristic length in equation 3.40. In this way we can introduce the surface tension and the capillary number. Hence,

$$\left(\frac{h_0}{\kappa^{-1}}\right)^{n+1} = 2a_0 \left[\mathcal{Y}\left(\frac{h_0}{\kappa^{-1}}\right)^{n} + a_0^n Ca\right] \tag{3.48}$$

wherein,

- $Ca = \dfrac{k\left(\dfrac{V}{\kappa^{-1}}\right)^n}{T\kappa}$ is a modified capillary number for shear thinning fluid.
- $\mathcal{Y} = \dfrac{\tau_y}{\sqrt{T\rho g}}$ is a non-dimensional number, analogous to the Ohnesorge number in its construction. It compares the yield stress to the capillary stress and the gravity stress. $\mathcal{Y}$ can also be interpreted as a comparison between the yield stress and the gravity stress, where the characteristic length in the gravity stress is set by the capillary forces (i.e. κ^{-1}).

A feature of equations 3.40, and 3.48, is that they reduce to the classical LLD law (in visco-gravitational regime) in the limit of a Newtonian fluid (i.e. $\tau_y = 0$ and $n = 1$):

$$\frac{h_0}{\kappa^{-1}} = \sqrt{2}a_0^2 Ca^{\frac{1}{2}} \tag{3.49}$$

Since the physical process described in equation 3.40 is fully driven by gravity, we expect that it does not hold in the circular channel case where gravity is negligible. Moreover, based on Derjaguin results, this suggest that $\sqrt{2}a_0^2 = 1$ which value corresponds to the matching parameter appearing in the hydrodynamic problem [59]. Thus, it would be possible to obtain its value even in the case of an Herschel-Bulkley fluid.

In the limit of vanishing velocities, equation 3.48 tends to $2a_0\mathcal{Y}$. Therefore, it predicts that the finite deposited thickness depends on the interplay between the gravity force, capillary force and the yield stress. This result should not be surprising since the stabilizing effect is the yield stress which tends to increase the size of the deposited layer and retains the material in its solid state, whereas the capillary stress and the gravity stress tend to make the material flow and compete with the yield stress, such that it may even happen that $\mathcal{Y} \to 0$.

$\mathcal{Y}$ can also be written as $\dfrac{\tau_y \kappa^{-1}}{T}$, which is exactly the same as B in equation 3.35. This suggests that, in the limit of vanishing velocities, the coated thickness is fully determined by an equilibrium between surface tension, gravity forces, and the yield stress. However, in equation 3.48 the dependency on the yield stress is weaker than predicted in equations 3.53 or 3.50.

Based on these considerations, we propose an alternate view of this problem in the last section of this chapter.

3.5.2.2 The coating of a Bingham fluid on a fiber or a plate

To go further into the exploration of Derjaguin results, it is possible to replace the stress τ_y in equation 3.37 by the total internal stresses for a Bingham fluid (i.e. $\tau_y \leftarrow \tau_y + \eta\dfrac{V}{h_0}$ wherein $\dfrac{V}{h_0}$ is the mean shear rate inside the film), thus it should be possible to recover the results of equation 3.36. However combining the modified equation 3.37 and as usual equation 3.24 leads to:

$$B\left(\frac{h_0}{R}\right) + Ca \sim \left(\frac{h_0}{R}\right)^{\frac{3}{2}} \tag{3.50}$$

or equivalently,

$$\left(\frac{h_0}{R}\right)^3 - \left(B\left(\frac{h_0}{R}\right) + Ca\right)^2 \sim 0 \tag{3.51}$$

On the contrary to what is found in equation 3.36 by superposition principle, there are coupling terms between the viscous stresses and the yield stress. Therefore there exists no simple expression of the film thickness in that case. However we can solve equation 3.51 by *Cardano's method*. Assuming that the Cardano's determinant is positive, which leads to a complicated condition on B and Ca:

$$27\left(B^4 - 2BCa\right)^3 + B^4\left(B^4 + 9BCa\right)^2 > 0 \tag{3.52}$$

then, equation 3.36 has one real solution given by:

$$\frac{h_0}{R} \sim \frac{B^2}{3} - \frac{2^{1/3}\left(-B^4 - 6BCa\right)}{3\mathcal{A}^{1/3}} + \frac{\mathcal{A}^{1/3}}{32^{1/3}} \tag{3.53}$$

where $\mathcal{A} = \left(2B^6 + 18B^3Ca + 27Ca^2 + 3\sqrt{3}\sqrt{4B^3Ca^3 + 27Ca^4}\right)$. As horrible as it is, equation 3.53 reduces to the classical LLD law for $B = 0$. In the limit of vanishing velocities ($Ca \to 0$), equation 3.53 reduces to $\dfrac{h}{R} \sim B^2$, and thus also predicts a finite deposited thickness due the presence of the yield stress. The exponent is the same as the one predicted by Derjaguin.

3.5.3 No-slip

In this section, we propose a model for the deposition of yield-stress fluid on the wall of circular channels with no-slip boundary conditions. Assuming that the deposition takes place according to the physical process described in the first part of this chapter (i.e. a balance between the internal stress of the material and the capillary pressure gradient), and that: (i) lubrication approximation holds; (ii) normal stresses are negligible compared to viscous stresses; we can write a scaling law for the deposition of an Herschel-Bulkley fluid flowing in a circular channel. Writing the Navier-Stokes equation dimensionally for an Hershel-Bulkley fluid, it produces:

$$\frac{\tau_y}{h_0} + \frac{k}{h_0}\left(\frac{V}{h_0}\right)^n \sim \frac{1}{\lambda}\frac{T}{R - h_0} \tag{3.54}$$

We keep the notations defined in the first part of this chapter. As usual, equation 3.54 has two unknowns h_0 and λ. To find λ we write the matching of curvature between the static meniscus and

the dynamic meniscus. Assuming that the dynamic meniscus is flat enough so that its y scale is h_0, equation 3.1 giving the curvature of the dynamic meniscus, written dimensionally reduces to:

$$\mathcal{C}_\lambda \sim \frac{\frac{h_0}{\lambda^2}}{\left[1+\left(\frac{h_0}{\lambda}\right)^2\right]^{\frac{3}{2}}} \tag{3.55}$$

However, contrary to the classical Bretherton problem, we do not assume that $\frac{h}{\lambda} \ll 1$, so that equation 3.55 cannot be assimilated to the second derivative of the interface profile. This attempts to make our results valid for larger value of the interface curvature, and thus of the film thickness. Therefore, the condition $\frac{\lambda}{R} \ll 1$ should also not be always verified. Based on the results of Derjaguin (equation 3.39), it also suggests that the yield stress can be of the order of the capillary stress. Therefore, the matching of curvatures between the static meniscus and the dynamic meniscus yields to:

$$\frac{1}{R-h_0} + \mathcal{C}_\lambda \sim \frac{2}{R-h_0} \tag{3.56}$$

With the previous definitions of the dimensionless numbers, and injecting equation 3.56 in equation 3.54 leads to:

$$\widehat{Ca} = \alpha \frac{\left(\frac{h_0}{R}\right)^{n+1}}{\frac{\lambda}{R}\left(1-\frac{h_0}{R}\right)} - B\left(\frac{h_0}{R}\right)^n \tag{3.57}$$

wherein α is the matching parameter that appears in front of viscous stresses when writing the exact form of equation 3.55. We can note that writing the full expression of the curvature in equation 3.56 makes λ appear in equation 3.57. This problem is constituted of two equations (3.56 and 3.57) which is sufficient to find the two unknown (λ, h_0). We propose to solve this problem by rewriting equation 3.56 after multiplying it by h_0. Hence,

$$\frac{h_0}{R-h_0} \sim \frac{\frac{h_0^2}{\lambda^2}}{\left[1+\left(\frac{h_0}{\lambda}\right)^2\right]^{\frac{3}{2}}} \tag{3.58}$$

recasting the right hand side of equation 3.58 as a function of $\frac{h_0}{\lambda}$:

$$f_{\mathcal{C}} = \frac{\left[1+\left(\frac{h_0}{\lambda}\right)^2\right]^{\frac{3}{2}}}{\frac{h_0^2}{\lambda^2}} \tag{3.59}$$

it finally leads to:

$$\frac{h_0}{R} \sim \frac{1}{1+f_{\mathcal{C}}(\frac{h_0}{\lambda})} \equiv g_{\mathcal{C}} \tag{3.60}$$

We denote the expression of $\frac{h_0}{R}$ obtained in equation 3.60 by $g_{\mathcal{C}}$. Thus, guessing a value for $\frac{h_0}{\lambda}$ gives a value for $\frac{h_0}{R} = g_{\mathcal{C}}(\frac{h_0}{\lambda})$. This allows to obtain a value for $\frac{\lambda}{R}$:

$$\frac{\lambda}{R} = \frac{h_0}{R}\frac{\lambda}{h_0} \tag{3.61}$$

Finally for a given value of $\frac{h_0}{\lambda}$, knowing the value of B we are able to compute the corresponding value of $\widehat{Ca}$ through equation 3.57. To obtain an analytical solution of equation 3.57, we can express it as a function of $\frac{h_0}{\lambda}$ only. Injecting equation 3.60 in equation 3.57, it produces:

$$\alpha\frac{\lambda}{h_0}g_{\mathcal{C}}^n\left(1-g_{\mathcal{C}}\right)^{-1} - \widehat{Ca}g_{\mathcal{C}}^{1-n} - Bg_{\mathcal{C}} = 0 \tag{3.62}$$

However, equation 3.62 is not easily solvable analytically.

3.5.3.1 The Newtonian limit

To validate equation 3.57, we first compare it to the results obtained by Taylor for a Newtonian fluid. Then, we set $B = 0$ and $n = 1$ in equation 3.57, which leads to:

$$Ca = \alpha\frac{\left(\frac{h_0}{R}\right)^2}{\frac{\lambda}{R}\left(1-\frac{h_0}{R}\right)} \tag{3.63}$$

For $\frac{h_0}{\lambda} \ll 1$ equation 3.56 reduces to $\lambda \sim \sqrt{h_0 R}$ (i.e. equation 3.24). Assuming that $\frac{h_0}{R} \ll 1$, and combining equation 3.63 with equation 3.24, leads to the classical Bretherton's law:

$$\frac{h_0}{R} \sim Ca^{\frac{2}{3}} \tag{3.64}$$

The computation with the expression of the full curvature (i.e. equation 3.63) is shown on figure 3.17 for $\alpha = 1.34$ (the value derived by Bretherton). Similar curves are found when considering the full curvature for the geometry of a plate or a fiber drawn out of a Newtonian fluid [128].

This scaling works very well until capillary numbers of order 0.8-1 are attained. This may be explained by the fact that at such velocities the deposited film attains a thickness that is not small enough compared to the radius of the tube for lubrication approximation to hold (i.e. for $0.25 \leq \frac{h_0}{R} \leq 0.3$). Therefore, it is not able to predict the saturation of the film thickness at large capillary numbers. The other drawback of this solution, is that there exists no simple analytical expression of the deposited film thickness when using the full expression of the curvature (equation 3.63).

3.5.3.2 Vanishing velocity

The other limit of equation 3.57 that we can investigate is the limit of vanishing velocity, so that $Ca \to 0$ (equation 3.65). In that case, adding that $\frac{h_0}{\lambda} \ll 1$ and $n = 1$ (i.e. Bingham fluid) gives a result similar to equation 3.38 that considers a pure plastic material with ($\frac{h_0}{R} \ll 1$ and $\lambda \sim \sqrt{h_0 R}$).

$$\frac{h_0}{\lambda\left(1-\frac{h_0}{R}\right)} \sim B \tag{3.65}$$

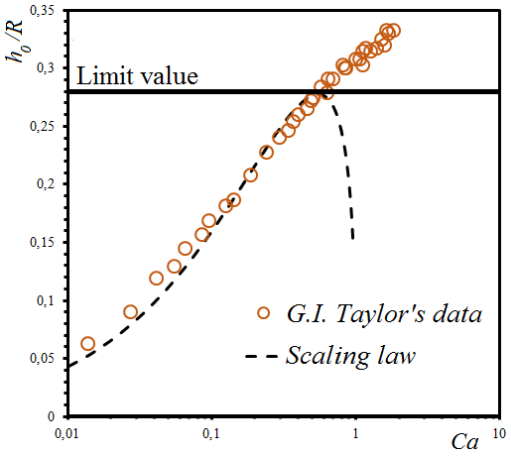

Figure 3.17 – Data of film thickness obtained by Taylor with glycerine. The dashed represent equation 3.63 with $n = 1$, $\tau_y = 0$, $\alpha = 1.34$. The horizontal line stands for the limit of validity of lubrication approximation.

Therefore, in the limit of vanishing velocities, the results depends only of the curvature of the interface and of the balance between Laplace pressure and the yield stress. The results obtained when considering the limits detailed above indicates that our scaling is consistent with the previous results from literature.

3.5.3.3 Comparison with experimental results

We can now move to the case of an Herschel-Bulkley fluid. The results are shown on figure 3.18 where the plain lines stand for equation 3.57 with $\alpha = 1.6$. The rheological characteristics of the fluid are determined using a plate-plate rheometer as detailed in chapter 2.

At low velocity, the scaling law works very well for capillary of radius 235 μm and 513 μm. We observe that the initial value of the film thickness increases with the radius of the channel, and that the model describes this behavior. The intersection of the model with the vertical axis depends on B, which itself depends of the Laplace pressure when crossing the meniscus interface. The Laplace pressure increases as the size of the channel decreases, therefore the smaller the channel, the more spherical the shape of the meniscus, and the smaller the value of B, and finally of the deposited film thickness.

For capillaries of radius 702 mum, the measured values of the film thickness are quite large, even at small velocities, so that lubrication approximation may not hold. The critical value for the break down of the scaling seems to be around $\dfrac{h_0}{R} \simeq 0.25$ which is consistent with the value found in the Newtonian case.

At high velocity, the film thickness seems to tend to a saturation value that is close to the one observed in the Newtonian case. This result could be expected since the rheological behavior of the fluid is taken into account into $\widehat{Ca}$. This point is discussed further in chapter 5.

3.5.4 Slip

To compare the result obtained with slip to results obtained with no-slip, we plot them as a function of the modified capillary number ($\widehat{Ca}$). As explained in chapter 2, the rheological parameters of the fluid are determined by capillary rheometry in a channel of same radius as the one used for the deposition experiments, so that the viscous stresses are apparent viscous stresses taking wall slip into account. The results for carbopol are presented on figure 3.19.

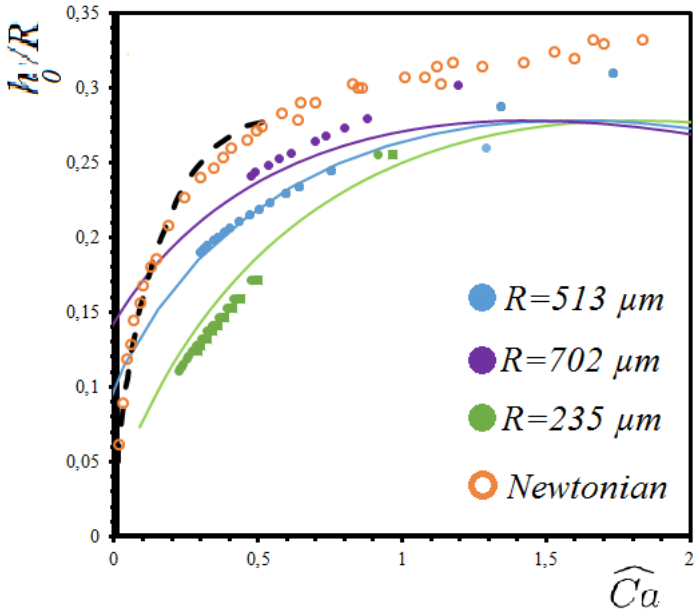

Figure 3.18 – Normalized film thickness, for carbopol gel ($\tau_y = 75$ Pa) as a function of the capillary number for different different radii of capillary tubes. The data for Newtonian fluid are also shown. Plain and dashed lines stand for the corresponding scaling law of each data set ($\alpha = 1.6$ for YSF and $\alpha = 1.34$ for Newtonian fluid).

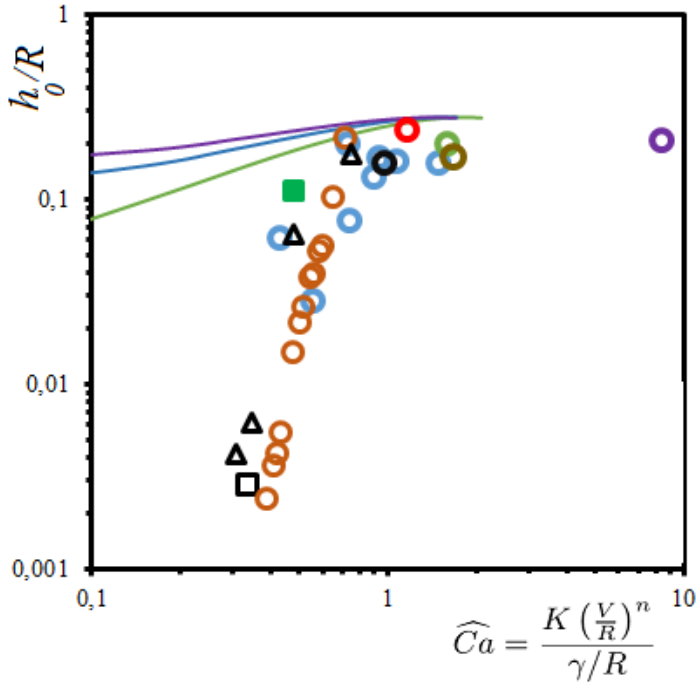

Figure 3.19 – Normalized film thickness as a function of the capillary number for different radii of capillary tubes obtained from: ∘ unsteady experiments ($\tau_y = 75$ Pa; $R = 235$, 513, 702, 620 μm); △ steady experiments ($\tau_y = 75$, $R = 513$ μm); □ optical measurement ($\tau_y = 75$, $R = 513$ μm). Every experiments are performed with carbopol gels ($\tau_y = 75$ Pa) The plain lines correspond to the scaling obtained with no-slip boundary conditions shown in figure 3.18.

First, all data collapse on the same curve with a relatively good agreement. At low capillary number, the measured values of the film thickness are much lower when there is slippage than what is predicted by the scaling law. However, as high capillary number the saturation value seems to be close in the two cases. This should be expected, since as the applied stress increases the material is destructured and yield stress is overcome, so that the material tends to flow as with no-slip boundary conditions. Finally, the breakdown of the scaling in slip regime is fully expected, this is one more time consistent with the assumption of negligible slip at high applied stresses.

3.5.4.1 The yield / viscous regime

To further interpret the results, we may note that the capillary number is the most relevant scaling when the profile is fully liquid (i.e. when the Bingham number $Bi \ll 1$). Thus, in slip regime, or during the yielding transition it should be more interesting to use the Bingham number as scaling parameter. There, the Bingham number is defined as the ratio of the true yield stress (not the sliding yield stress) of the material to the apparent viscous stresses in slip regime.

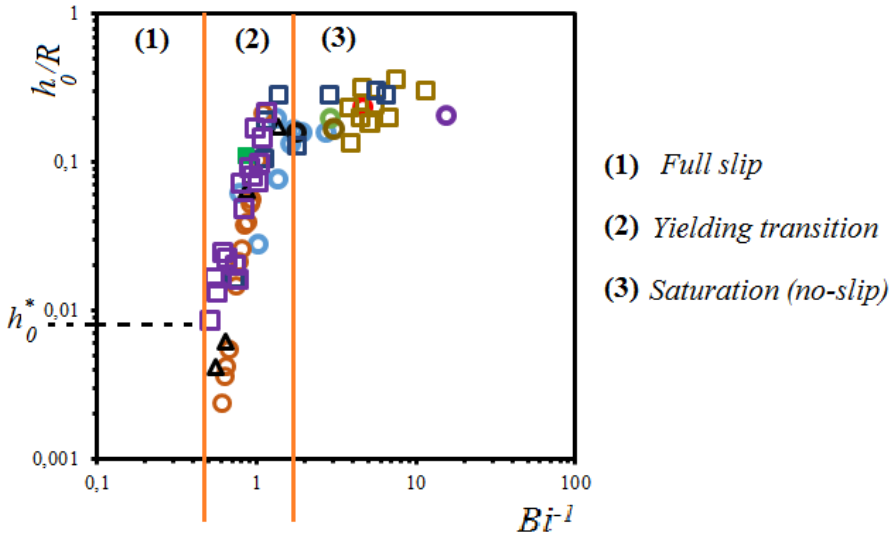

Figure 3.20 – Normalized film thickness as a function of the inverse of the Bingham number for different radii of capillary tubes obtained from: ∘ carbopol (unsteady, $\tau_y = 75$ Pa; $R = 235$, 513, 702, 620 μm); △ carbopol (steady, $\tau_y = 75$, $R = 513$ μm); □ emulsion (unsteady, $\tau_y = 100$, $R = 513$, 235 μm). Dashed line stands for the capture model for dilute emulsions (h_0^*).

The results are presented on figure 3.20 for both carbopol gels and emulsions. The three regimes discussed before are clearly visible. First at low velocity (i.e. large Bi), the film thickness is not measurable. This is the regime of full slip.

Then, there is a sharp transition. We can see that, especially during this transition, the collapse of data is better than when using the capillary number. Another remark is that the transition takes place around a Bingham number of approximately 1. A Bingham number around 1 corresponds to viscous stress at least of the order of the yield-stress. Considering the no-slip case, using the equations of chapter 2 (2.14), and assuming that the total stress at the wall $\tau_w = \tau_y + k\left(\frac{V}{R}\right)^n$, we find that:

$$Bi = 1 \Leftrightarrow \frac{R_p}{R} = \frac{1}{2} \tag{3.66}$$

Equation 3.66 shows that a Bingham number around 1 corresponds to a flow profile that is half liquid and half solid. This suggests that slip effect may start to decrease when the radius of the solid

region $R_p \simeq 0.5R$, and that the profile must be sufficiently liquefied to measure a deposited thickness. This also might be sufficient for capillarity to start playing a major role, which in turn triggers the deposition process.

The third regime, observed for small Bingham number, corresponds to the saturation when most of the flow profile is liquid. However the representation of the result as a function of the Bingham number does not give much information on this regime since it is mostly a viscous / capillary regime.

3.5.4.2 Discussion on low velocities

Going back to chapter 2, we know that full slip is favoured by wetting of the continuous phase on the solid surfaces in contact with yield-stress fluid. Therefore, the simplest physical picture we can suggest to explain the not-measurable deposition is the following: in glass capillaries there may be a deposited layer of solvent of very thin typical size ($< 1\mu$m), which leads to full slip of the plug. Nonetheless, it raises the issue of the size and thus of the constitution of the deposited layer for a yield-stress fluid. What happens when the size of deposited layer becomes of the order of the microstructure of the yield-stress fluid (no-slip) or even much smaller (slip)?

In addition, this regime cannot last for an infinite time. As the plug of emulsion advances inside the channel, it may deposit a thin film of continuous phase, therefore the concentration of inclusion must increase, so that they are more and more deformed. However, as it increases interfacial energy this process must stop at some point, and contact between the microstructure and the wall may happen, leading to no-slip boundary conditions and the start of the fluidization process (figure 3.16). This regime should also depend on the nature of the microstructure (i.e. deformability of the inclusions).

Finally, on figure 3.20, the thickness h_0^* stands for the thickness computed using the capture model for dilute emulsions. This model is discussed at the beginning of this section. The value of $\frac{h_0}{R}$ reported on figure 3.20 is computed for $R = 513$ μm, which corresponds to the data set represented by purple squares. The computed value of h_0^* seems to correspond to the first measurable value of the film thickness. This suggests that in slip regime, the first thickness deposited is set by the typical size of droplet and the volume fraction of the emulsion. The first value of the film thickness we measure is larger for emulsion than for carbopol gels, which might be attributed to the difference in size of their microstructure.

3.5.4.3 Discussion on the fluidization scenario

The sharp transition on figure 3.20 could be interpreted as a fast fluidization scenario: the material destructurates rapidly, and the velocity profile changes from a solid plug flow with a very thin lubrication layer to a Poiseuille-like flow as predicted by the classical equation of fluid mechanics. For both emulsions and carbopol, the data collapse on the same curve. Therefore, the fluidization scenario might be the same.

Furthermore, in that case, the fluidization scenario may involve stick-slip when the stress approaches the yield stress of the material [140]. A contact may be triggered locally (by heterogeneity of surface roughness for example, or a higher local concentration of the microstructure), so that the material may accumulate stresses which produce a fluidized zone. However, in our case we could not measure fluctuation in slip velocity due to a lack in the resolution needed to perform such fine measurements in our capillaries.

For a plug of carbopol pushed at constant pressure, the extrapolated position of the front meniscus of the plug obtained from the velocity of the first images is shown by the red line on figure 3.16. It suggests that, prior to fluidization the plug slows down during its full slip motion. This might be interpreted as a start of a transition from full a slip flow to a flow with no-slip boundary conditions. However on the investigated time scale no velocity fluctuations appears. As explained in the previous

section, we can suggest that it results from the deposition of thin film of continuous which may lead to a contact between the microstructure of the fluid and the wall.

3.5.4.4 Comparison with the coating of a fiber with foams

Indeed, the foam is a yield-stress fluid, as mentioned in chapter 2, it can exhibit wall-slip. Particularly, it may happen if there is a thin liquid film between the surface of the fiber and foam bubbles. In turn the size of this film may depend on surface chemistry or/and surface roughness, and change the boundary conditions and thus the flow behavior induced by the motion of the fiber.

If the fiber surface were rough and there were no-slip boundary conditions on the fiber, the presence of a yield stress would lead to a critical force dependent on the yield-stress. Below the critical value of this force the material must remain at rest and deform like an elastic solid, and above the critical value of this force the fiber can be displaced and foam should be continuously attached to it. However, for foams, such phenomenon is not mentioned [125, 138], and thus suggests that there is a slippage of the foam at the surface of the fiber during the experiments.

Thinking about wall slip, it seems reasonable to mention that at low velocity (i.e in full slip regime) the bubbles, or more generally the microstructure of a yield-stress fluid should not be entrained by the fiber, and that a thin continuous phase film may be entrained instead, especially if the size of the microstructure is of the order of the fiber radius.

At high velocity, considering that the slip layer and the material are fully destructured, the flow induced by the fiber should approach the bulk flow of the material with no-slip boundary conditions. Thus leading to an homogeneous coating of the fiber.

At intermediate velocities, which should correspond to applied stresses close to the yield stress, stick-slip motion cannot be excluded. Thus, some similarities with our observations in slip regime can be noted:

Low velocities. For foams, only continuous phase was found to be entrained. For emulsions, or carbopol gels, there is either no deposition or an extremely thin film of continuous phase that is deposited.

Yielding transition. For our fluids the transition to slip regime to the classical flow regime operates at a Bingham number around 1. However we do not observe discontinuous coating, or even stick slip motion, even if it might occur.

High velocities. In our case, as well as for foams, the coating is found to be continuous, such that wall slip may be negligible.

3.5.5 A scaling law for the withdrawal of a plate

In the previous section the scaling law for Herschel-Bulkley fluids were found to work well until the film thickness became too large and the subsequent break down of lubrication approximation. Here we show that the same reasoning agree with the literature results in the case of the withdrawal of a plate from a bath of yield-stress fluid at constant velocity [135, 136].

3.5.5.1 Static meniscus

First, writing the classical scaling equations require to match the curvatures of the dynamic meniscus with the curvature of the static meniscus to solve the coating problem. Therefore, considering the withdrawal of plate out of a bath raises the issue of the shape of the static meniscus under gravity. For Newtonian fluids, the equilibrium of a static meniscus (figure 3.21) translates into a pressure balance between the gravity stress and the capillary stress, at the interface (equation 3.67).

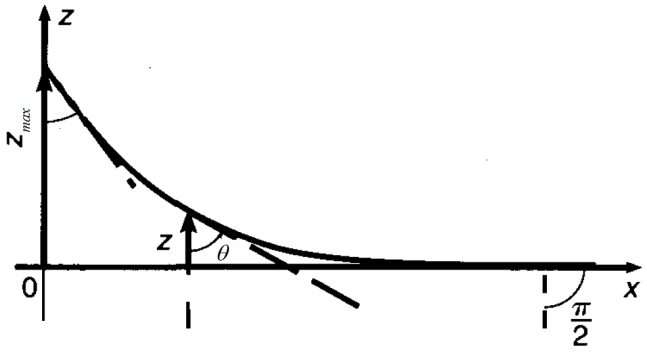

Figure 3.21 – Sketch of the meniscus on a plane wall for a Newtonian fluid. Adapted from [56].

$$P_0 + \frac{T}{R(z)} = P_0 - \rho g z \tag{3.67}$$

wherein z is the altitude of the considered point of the interface, and $R(z)$ its radius of curvature. Equation 3.67 becomes:

$$-\frac{R(z)}{\kappa^{-1}} = \frac{\kappa^{-1}}{z} \tag{3.68}$$

$\kappa^{-1} = \sqrt{\frac{T}{\rho g}}$ is the capillary length which results from an equilibrium between the hydrostatic pressure and the capillary stress. It appears to be the only scaling length for both the radius of curvature and the height of the meniscus in equation 3.68. We can also note that when $z = 0$, $R \to \infty$ which mean that the surface is flat.

For yield-stress fluids, the stress balance is modified by the yield stress so that gravity must balance both the yield stress and the surface tension. Then, equation 3.67 becomes:

$$P_0 + \frac{T}{R(z)} + \tau_y = P_0 - \rho g z \tag{3.69}$$

Note that, the yield stress is an unambiguous property of the material in shear flow only. In the case of the meniscus, the value of the limiting stress would be modified and generally be expressed as a *von Mises criterion* [141]. However, its magnitude should not be completely different of the yield stress. As an example the limiting shear stress is $\sqrt{3}\tau_y$ in extensional flow, so that the yield stress might be the right order of magnitude. This first difficulty indicates that, the scaling law approach requires an important preliminary work an the static meniscus shape when considering a yield stress fluid. Nonetheless, equation 3.69 is the simplest approximation of the meniscus shape we can think of, and finally equation 3.69 leads to,

$$-R(z) = \frac{L_y}{\frac{z}{h_c} + 1} \tag{3.70}$$

Here $L_y = \frac{T}{\tau_y}$ is a length that results from a balance between the yield stress and the capillary stress, and $h_c = \frac{\tau_y}{\rho g}$ results from a balance between the yield stress and the gravity stress. On the

contrary to the Newtonian case, equation 3.70 introduces two characteristic lengths, so that the scale of the meniscus is not easily definable, we can also note that when $z = 0$, $R = L_y$, so that the surface of the bath may not be flat. To take the three effects (i.e yield stress, capillary stress, gravity stress) into account we propose to define a length scale based on the balance between the gravity stress and the sum of the yield stress and the capillary stress. Denoting this length κ_y^{-1},

$$\rho g \kappa_y^{-1} \sim \tau_y + \frac{T}{\kappa_y^{-1}} \Leftrightarrow \kappa_y^{-2} - h_c \kappa_y^{-1} - \kappa^{-2} \sim 0 \tag{3.71}$$

Solving equation 3.71 gives:

$$\kappa_y^{-1} = \frac{h_c}{2}\left(1 + (1 + 4\mathcal{Y}^{-2})^{\frac{1}{2}})\right) \tag{3.72}$$

wherein $\mathcal{Y} = \frac{\tau_y}{\sqrt{\rho g T}}$. When the yield stress is large compared to other effects $\mathcal{Y} \gg 1$ and $\kappa_y^{-1} = h_c$, in the opposite case (i.e. $\mathcal{Y} \sim 0$) $\kappa_y^{-1} = \kappa^{-1}$. Even if we have no experimental validation of these results, in this section we assume that κ_y^{-1} is the characteristic length of the static meniscus when the considered fluid exhibits a yield stress. The values of previously defined length-scales are given in table 3.3 for different value of the yield stress and the surface tension of carbopol.

τ_y (Pa)	T (mN/m)	κ^{-1} (mm)	h_c (mm)	L_y (mm)	κ_y^{-1} (mm)
1	66	2.6	0.1	66	2.6
5	66	2.6	0.5	13.2	2.9
10	66	2.6	1	6.6	3.2
50	66	2.6	5.1	1.32	6.1
100	66	2.6	10.2	0.66	10.8

Table 3.3 – Values of the length-scales involved in the static meniscus shape for a yield-stress fluid.

3.5.5.2 Matching of curvature

Going back to the coating problem, similarly to what is done in the previous section in the geometry of a circular channel, we propose to write dimensionally the matching of curvature between the static and the dynamic meniscus, using κ_y^{-1}, it produces:

$$\frac{1}{\kappa_y^{-1}} \sim \frac{\frac{h_0}{\lambda^2}}{\left[1 + \left(\frac{h_0}{\lambda}\right)^2\right]^{\frac{3}{2}}} \tag{3.73}$$

Hence,

$$\frac{h_0}{\kappa_y^{-1}} \sim \left(f_C(\frac{h_0}{\lambda})\right)^{-1} = \frac{\frac{h_0^2}{\lambda^2}}{\left[1 + \left(\frac{h_0}{\lambda}\right)^2\right]^{\frac{3}{2}}} \tag{3.74}$$

3.5.5.3 Momentum balance

In the case of the withdrawal of plate, under lubrication approximation, the dimensional Navier-Stokes equations are:

$$\frac{\tau_y}{h_0} + \frac{k}{h_0}\left(\frac{V}{h_0}\right)^n \sim \frac{1}{\lambda}\frac{T}{\kappa_y^{-1}} + \rho g \tag{3.75}$$

Finally, choosing h_c as the length scale for building the dimensionless numbers, under dimensionless form equation 3.75 becomes:

$$Bi^{-1} \sim \left(\frac{h_0}{h_c}\right)^{n+1}\left(\frac{\kappa^{-2}}{\kappa_y^{-1}\lambda} + 1\right) - \left(\frac{h_0}{h_c}\right)^n \tag{3.76}$$

where $Bi = \frac{\tau_y}{k\left(\frac{V}{h_c}\right)^n}$. Or using h_0 instead of h_c to build the Bingham number:

$$\frac{h_0}{h_c} \sim \left(\frac{\kappa^{-2}}{\kappa_y^{-1}\lambda} + 1\right)^{-1}\left(1 + Bi^{-1}\right) \tag{3.77}$$

We can immediately note that this choice of length scale makes the inverse of the Bingham number appear in equation 3.76 and that equation 3.77 has a similar expression than the equation derived in [135] but also takes into account the flow inside the meniscus. Neglecting this effect, equation 3.75 becomes:

$$\frac{\tau_y}{h_0} + \frac{k}{h_0}\left(\frac{V}{h_0}\right)^n \sim \rho g \tag{3.78}$$

which leads to:

$$\frac{h_0}{h_c} \sim \left(1 + Bi^{-1}\right) \tag{3.79}$$

Equation 3.79 is similar to what is found in [135].

Finally, to fully solve the problem it is necessary to write the matched asymptotic expansions analysis. The regime described in equation 3.79 results from an interplay between the viscous stress, yield stress, and the gravity stress. As noted in "discussion of litterature models" section, for $n = 1$, and $\tau_y = 0$, it reduces to Derjaguin law, therefore it raises the question of the link between the capillary regime and the afore mentioned regime. This a difficult problem to solve especially concerning the asymptotic matching [128]. Therefore, as a first approximation we choose to introduce a constant as soon as a scaling law appear, i.e. in equations 3.74 (denoted β), and in 3.75 (denoted α), which corresponds to the simplest interpolation between the two regimes. This is consistent with what have been done and validated for Newtonian fluid [128]. This yields:

$$\frac{h_0}{h_c} = \alpha\left(1 + Bi^{-1}\right) \tag{3.80}$$

and,

$$Bi^{-1} = \alpha \left(\frac{h_0}{h_c}\right)^{n+1} \left(\beta \frac{\kappa^{-2}}{\kappa_y^{-1}\lambda} + 1\right) - \left(\frac{h_0}{h_c}\right)^{n} \tag{3.81}$$

Equation 3.80 also suggests that similarly to the Newtonian case, α may be derived by writing the expression of the flow rate inside the film [59, 118]. Finally, to obtain a solution of the problem, as in the circular channel case, using equation 3.74 we can compute $\frac{h_0}{\kappa_y^{-1}}$ for each value of $\frac{h_0}{\lambda}$, and finally obtain the corresponding value of the Bingham number. Equation 3.81 is plotted on figure 3.22a for $\beta = 0$ and $\alpha = 0.28$, and on figure 3.22b $\alpha = 0.28$ and $\beta = 0.1$ compared to the experimental results by Maillard [135].

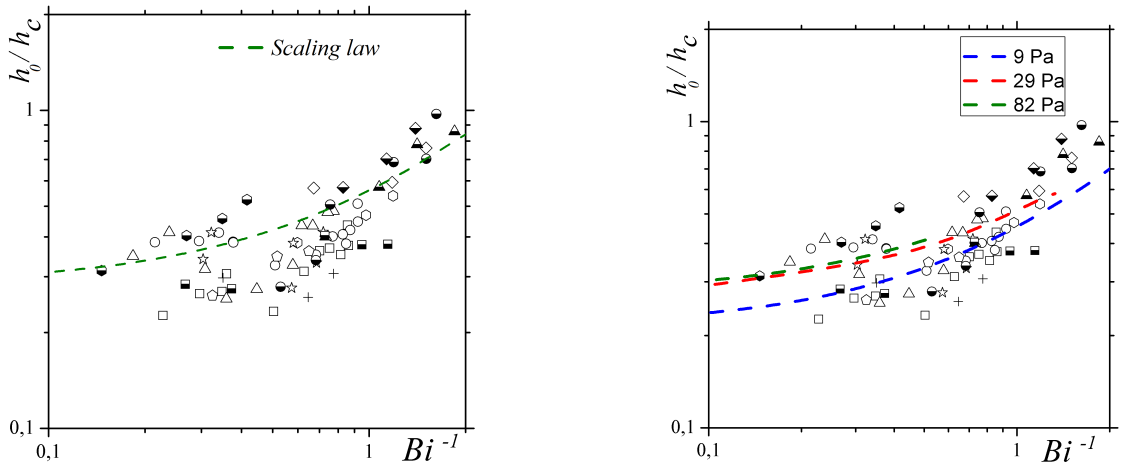

(a) Scaling for the gravitational regime ($\beta = 0$, $\alpha = 0.28$). (b) Scaling for the cross-over of the capillary and gravitational regime ($\beta = 0.1$, $\alpha = 0.28$).

Figure 3.22 – Comparison of the scaling plotted for different yield stresses and the same surface tension, with the experimental results of Maillard for different yield stress ($8 \leq \tau_y \leq 82$ Pa)[135].

The scaling compares qualitatively well to the experimental results until they break down, indeed at high velocity lubrication approximation does not hold any more. The larger the yield stress, the quicker the breakdown of the scaling law.

At low velocity (large Bingham number) equation 3.76 seems to tend to an almost constant value which depends on the yield stress. As the velocity increases, the growth rate of the scaling seems to be close to a power -1 of the Bingham number. These findings are consistent with the experimental results, suggesting that the hypothesis made above are applicable to the case of the coating of yield-stress fluids, even in complicated situation.

Another approach would be to consider, as in the Newtonian problem, that two regimes follow each other (i.e. visco-capillary and visco-gravity). However the results in each of them may depend on the ratio of yield stress to capillary stress. The real improvement of this approach would be to find proper values of the constant (α, β) in order to test the model quantitatively.

Comparing the results for the plate to what was found in a circular channel, we would expect to recover quite similar expressions in the case of negligible gravity. Thus leading to a regime dominated either by the yield stress or surface tension. This regime is expected to be observable at very slow velocities.

3.6 Conclusion

In this chapter, we investigate the deposition of yield-stress fluids on the wall of circular channels with or without wall slip. The film thickness, measured by different methods give similar results. When there is no slip at the wall, the deposition can be described by a scaling law, thus suggesting that the physics at play is well represented by a balance between the capillary pressure gradient and the internal stresses of the fluid. This type of reasoning also allows to describe the literature results in the case the withdrawal of a plate out of a bath of yield-stress fluid.

The slip regime is found to be much more complex, and different behavior can be distinguished depending on the value of velocity. These results are reminiscent and consistent with what is found in the case of foam entrainment on a fiber.

Essential facts

- The deposition with no-slip boundary conditions can be described by a scaling law balancing the capillary pressure gradient and the internal stress of the fluids.
- With wall slip, three regimes are observed independently of the considered fluid and depends on the Bingham number (Bi): (i) for $Bi > 1$, full slip; (ii) for $Bi \sim 1$ a sharp transition associated with the fluidization process; (iii) for $Bi < 1$, no slip regime.

Part II

Production of bubbles in yield-stress fluids using T-junction and flow focusing devices

4

Break-up mechanism

In this chapter we investigate the production of bubbles inside yield-stress fluids using millifluidic axisymmetric geometries. In the following, we first recall the operating regimes of T-junction and flow focusing devices when using Newtonian or non-Newtonian fluids as the continuous phase. Then, we move to the experiments and the corresponding scaling analysis. We detail our experimental set-up, and the associated results. We provide an explanation of the break up mechanism when the continuous phase is a yield-stress fluid and the dispersed phase is a gas. We pay particular attention to hydrodynamic feedback and its influence on bubble production. Finally we derive a simple expression for the limiting bubble production frequency in steady regimes. These results can also be found in [142].

Contents

4.1 Classical microfluidic geometries

Microfluidic is known to allow the design of controlled geometry and the manufacturing of complex fluids at acceptable throughput with a highly accurate control on bubble size and global flow rate. Recently the production of monodisperse foams and emulsions as well as droplet manipulation and flow in microchannels has gained much interest, and known a rapid expansion [16–18, 20, 23]. This has led to the development of different geometries for micro-bubbles or micro-droplets production: the simplest ones being: (i) T-junction [24–27], (ii) flow-focusing geometry [28–34], (iii) step emulsification [35–38] (see figure 1). More complex geometries are also designed and allow to produce fluids exhibiting an interlocked structure such as double emulsions, or vesicles to encapsulate drugs for targeted delivery [143–145]. Among those geometries some were developed in order to allow the mass production of

complex fluids through *parallelization* (or *scale-up*) consisting in multiple units of production (such as T-junction, or flow focusing units) linked in parallel [35, 146–148], as well as model porous media [149].

4.1.1 T-junctions

T-junctions possess different operating regimes depending on the confinement of the fluids, and inlet conditions [16, 25, 150]. Three regimes are identified:

The dripping regime. When the width of the channel used to inject the dispersed phase is small compared to the width of the other channel the situation is called *unconfined* (figure 4.1a). Assuming an analogy with the unbounded shear flow studied by Taylor [68], the break-up occurs when the viscous stresses of the continuous phase flow overcome the capillary stress that tends to resist the elongation of the emerging droplet. Different works focused on finding a scaling to predict the droplet size depending on the viscosity ratio of the two phases [151], or their interfacial tension [152]. The derivations are based on a force balance on the forming droplet. Keeping the same approach, the afore-mentioned effects, as well as the channels aspect ratio, were summarized into a single model to describe the break-up mechanism [150].

The squeezing regime. This regime, also referred to as *confined* break-up, is characterized by the blockage of the flow in the junction by the forming bubble (figure 4.1b). Thus, the bubble forces the continuous phase to flow through the thin liquid film that remains between the wall of the channel opposing the dispersed phase inlet and the bubble interface. This results in an increase in the pressure of the continuous phase upstream of the bubble, which in turn tends to force the break up by squeezing the gas thread. In this operating regime, a scaling law for the bubble length depending on the inlet conditions was derived [26, 31]. Since the channel is obstructed by the forming bubble, this regime of bubble or drop formation is mediated by the geometry. The time to form a bubbles is inversely proportional to the flow rate of the dispersed phase, and the size of the bubbles depends on the ratio of the flow rate of the dispersed phase to the continuous phase.

The jetting regime. A regular production of bubbles is not always observed: in some cases, the two phases flow side by side in the channel, this regime is called the jetting (or co-flow) regime [150]. This occurs when the pressure of one of the two phases is large compared to the other: either the dispersed phase meniscus may even not enter the junction, or the two fluids flow side by side.

4.1.2 Flow focusing

The other geometry we are interested in is the flow-focusing geometry. This geometry is constituted of three inlets, two of them facing each other and crossing perpendicularly the third, which is aligned with the outlet. The dispersed phase is injected through the center channel, whereas the continuous phase is injected through the side channels [28]. In addition, a small orifice is often placed downstream of the junction to reduce the size of the dispersed phase thread. most of the time the dispersed phase is pressure driven, whereas the continuous one is flow rate driven [18].

The break-up mechanism in flow-focusing geometry exhibits two different regimes depending on the value of capillary number [153]:

The squeezing regime. At low values of the capillary number flow-focusing devices operate in a regime that is qualitatively similar to the squeezing regime observed for T-junction. The dispersed phase thread obstructs the orifice, thus it restricts the flow of the continuous phase to the thin liquid film surrounding the dispersed phase thread [31]. This in turn, increases the pressure upstream of the forming bubble and forces the squeezing of the gas thread until the bubble

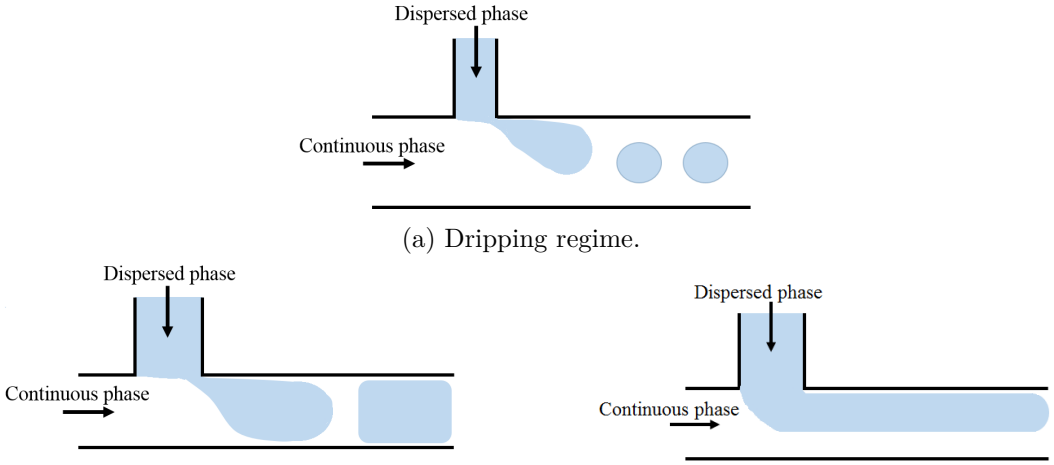

(a) Dripping regime.

(b) Squeezing regime.

(c) Jetting regime.

Figure 4.1 – Schematics of bubble production in a T-junction.

pinch-off is triggered (figure 4.2a). During this first part of the break-up mechanism the interface adjusts its shape to the slow thinning of the gas thread set by the imposed flow rate of the continuous phase which is guaranteed by the condition of small capillary number. The second part of the break up mechanism starts when the dispersed phase thread becomes axisymmetric. At this point the thread becomes unstable to *Rayleigh-Plateau instability* [1], and the final pinch off is governed by inertia and surface tension [32]. Denoting Ω the volume of the orifice and assuming that the dispersed phase is supplied at constant flow rate Q, the time to form a bubble is given at first order by:

$$t_b \simeq \frac{\Omega}{Q} \tag{4.1}$$

In this regime, when the gas pressure (ΔP) and the liquid flow rate (Q) are imposed, a scaling for the volume ($V_b^{(newt)}$) of produced bubbles is also derived [154]:

$$V_b^{(newt)} \propto \frac{\Delta P}{Q\eta} \tag{4.2}$$

The jetting regime. In this regime, a jet of dispersed phase extends even downstream of the orifice [155, 156] (figure 4.2b). This occurs when the flow is accelerated so that inertial forces are large compared to both viscous and surface tension forces. In that case the break-up mechanism is driven by a balance between the force applied by the fluid upstream of the growing bubble, and by the growing bubble on the fluid downstream.

[1] Responsible for the break up of a gas or liquid thread in a medium at rest [56]

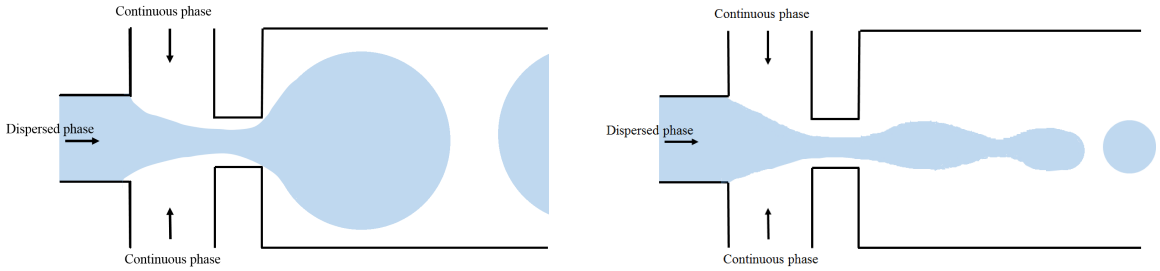

(a) Squeezing regime. (b) Jetting regime.

Figure 4.2 – Schematic of bubble production in a flow-focusing device.

4.1.3 Non-Newtonian fluids

Few studies combining microfluidic and bubble production in non-Newtonian fluids have been performed, the main ones focus on:

- the influence of the visco-elasticity on operating regimes, and rate of production of flow-focusing devices, either with visco-elastic [157] or shear thinning fluids [158];
- the flow dynamics of these fluids in micro channels [44];
- the break-up dynamics in shear thinning fluids for T-junctions [43] and flow-focusing devices [41, 42].

4.1.3.1 Yield-stress fluids

Among non-Newtonian fluids, bubble formation in yield-stress fluids have received relatively little consideration in spite of being at the heart of numerous industrial applications that requires the production of bubbly yield-stress fluids.

In all the interfacial processes described for Newtonian and non-Newtonian fluids (without a yield stress), the fragmentation of the dispersed phase in the continuous phase is always obtained through the capillary break-up of a thin liquid thread of the dispersed phase. The diameter of this thread diminishes due to the shear flow of the continuous phase in the confined geometry. Thus when the thread attains a critical size the *Laplace pressure* becomes the dominant driving force governing both the dynamics and the break-up of the thread [159–161]. This highlights that capillary effects are crucial ingredients in micro-bubble and micro-droplet production in microfluidic devices.

The existence of the *yield stress* (τ_y), a macroscopic property of the material, introduces a new stress scale in hydrodynamics problems. This implies that in every system *liquid behavior* and *elastic-solid behavior* may locally coexist, depending on the stress state of the material. Then the yield stress may compete with surface-tension driven processes and induce an intrinsic impediment for capillary break-up if the mean curvature of the interface is not sufficiently large. Thus the capillary stress may not overcome the yield stress, which can lead to a blockage of the break-up. Such antagonistic behavior showing a competition between yield stress and capillary stress have been recently observed in various systems:

- yield-stress fluid capillary rise: large yield stress inhibits surface tension effects and the final height depends weakly on the gap size [79].

- yield-stress fluid entrainment by a solid plate [135] which strongly differs from the Landau-Levich-Derjaguin theory for Newtonian fluids based on the key role of surface tension.
- control of interfacial instabilities using yield-stress fluids in multilayer flows [162].
- production of yield-stress fluids drops in air by gravity. The gravity stress has to overcome the yield stress for capillary break-up to occur [163, 164].
- *Saffman-Taylor instability* with yield-stress fluids for which larger wavelengths (i.e. when the yield stress dominates) are independent on the velocity [165].

Only a few studies combining microfluidic and yield-stress fluids are known to us, often motivated by applications related to ink-jet printing. The first is related to the framework of the formation of non-Newtonian drops in air [45], and investigates the pinch off a yield-stress fluid drops in air [166]. The second one, investigates the production of yield-stress fluid (carbopol $\tau_y < 10$ Pa) drops inside a Newtonian fluid using a flow-focusing device [167]. In this work the presence of a yield stress is shown to modify the break-up mechanism only at very low shear rate. This result might be expected since at low shear rates the velocity profile should mostly be constituted of a solid-like region, and thus the effect of the yield stress be more pronounced.

In the next sections, we study the formation of bubbles inside yield-stress fluids possessing a large yield stress, at least of the same order as the capillary stress, inside T-junctions and flow-focusing devices.

4.2 Experiments

To disperse gas bubbles inside yield stress fluids we used two of the classical microfluidic geometries: (i) T-junction; and (ii) flow focusing devices.

4.2.1 Set-up

As detailed in chapter 2, we use three-dimensional axisymmetric T-junctions and flow-focusing devices of radii: 0.5, 1, or 2 mm, manufactured by stereolithography (figure 4.3). All channels on a given chip have the same radius. As shown in chapter 1, we use two yield-stress fluids: oil-in-water emulsions and carbopol gels. The yield stress of emulsions is varied between 100 Pa and 300 Pa, and the carbopol has a yield stress of 75 Pa. We impose the yield-stress fluid flow rate (0.01 ml/min $\leq Q \leq$ 1.5 ml/min) with a syringe pump, and the gas pressure using a Fluigent pressure controller (MFCS-EZ, 0-2 bar). The whole experiments is recorded using a CCD camera (Marlin) at a maximum framerate of 100 fps.

The experiments are performed using the protocol detailed below:

- First, the outlet channel is filled with yield stress fluid at constant imposed flow rate.
- Then, the gas pressure is increased until it attains the critical value necessary to produce the first bubble [2].

The formation of multiple bubbles of increasing length ℓ is observed.

[2] This process is studied in details in chapter 5.

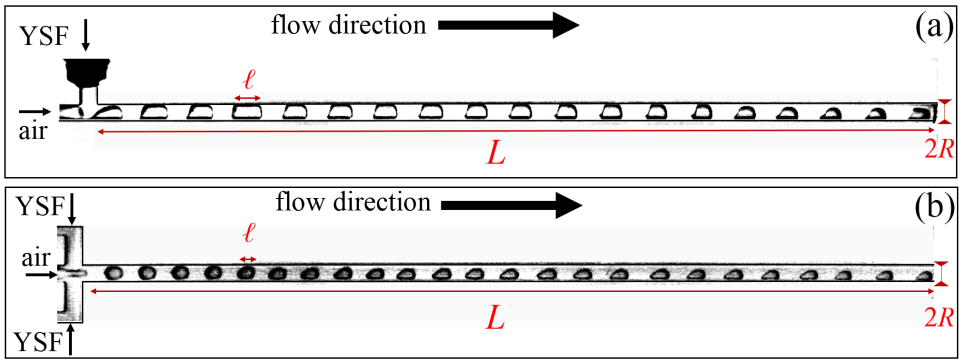

Figure 4.3 – Top view of different devices: (a) T-junction, (b) flow-focusing device; L is the outlet channel length, R the radius of all channels. Pictures taken with $R = 1$ mm and $L = 10$ cm.

4.2.2 Operating regime for the classical T-junction

For Newtonian fluids, the production of monodisperse bubbles down to low Ca has been reported when the gas is injected with either one or the other channel [168]. For yield-stress fluids, we were unable to produce bubbles using the classical T-junction set-up in some conditions.

- When the gas is injected through the side channel: at low shear rates, the formation of successive bubble seems to be relatively stable but unsteady. However, as soon as the shear rate slightly increases the gas thread tends to stay confined into the liquid layer of the yield-stress fluid flow (last images of figure 4.4a). As the shear rate increases, the gas thread either breaks up and coalesce very fast and the gas is not dispersed in the yield-stress fluid (figure 4.4b), or the system destabilizes quickly (only a few bubbles are produced before destabilization; figure 4.4a to be compared to figure 4.3b). Therefore, the break-up mechanism seems highly sensitive to the stress state of the system.

- When the gas is injected through the channel aligned with the outlet (set-up named "reverse T-junction"), the production is unsteady but regular. Multiple bubbles with increasing size are produced. At first order, their production does not seem to be altered by the shear rate associated with the yield-stress fluid flow (4.3b).

Therefore we have chosen to investigate bubble production inside the reverse T-junction.

4.3 Results

Unsteady bubble production. First, we report that for both geometries (TJ and FF devices) bubble production is unsteady. The length (ℓ) of successive bubbles becomes larger and larger until they coalesce and form a giant bubble that completely fills the tube. This breakdown of the bubbling regime occurs generally after the production of 10 to 50 bubbles. The destabilization process is mostly due to the variation of hydrodynamic resistance of the outlet channel. The hydrodynamic resistance decreases when a bubble is produced. Since the gas is driven at imposed pressure, the decrease of hydrodynamic resistance leads to an increase in the gas flow rate which turns into the production of larger and larger bubbles. This dynamics is also promoted by the yield-stress fluid deposition on the wall of the channel: as the velocity of the whole flow increases, the deposited film thickness increases and the size of the yield-stress fluid plugs that separate each bubble decreases. At some point the plugs reach a critical size and break-up. In this chapter we only observe the influence of the unsteady bubbling process on bubble formation, the process of destabilization is detailed in chapter 5.

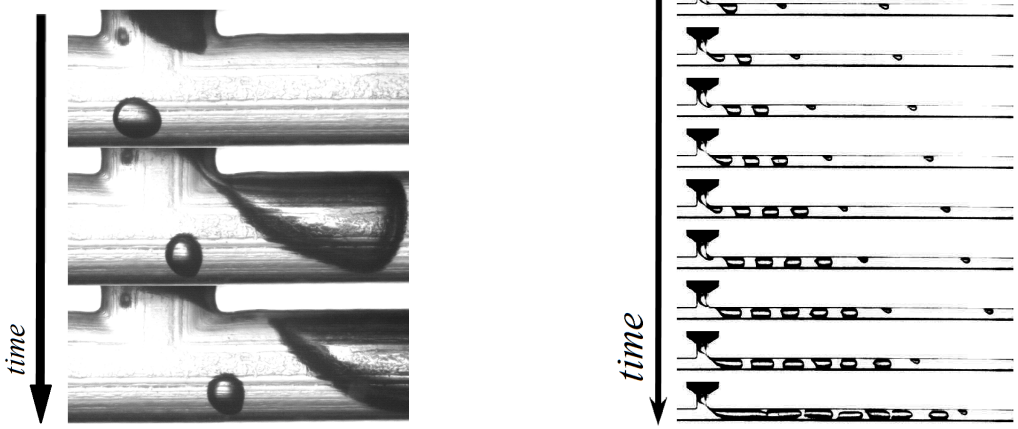

(a) Magnification of successive break-up and coalescence of the gas thread for an emulsion with $\tau_y = 300$ Pa. The channel has a radius of 1 mm, each image is separated by 0.2 s.

(b) Top view of bubble production with an emulsion $\tau_y = 160$ Pa. The channel has a radius of 1 mm, and each image is separated by 1.5 s.

Figure 4.4 – Bubble production in the classical T-junction device with yield-stress fluids.

Steady bubble production. Nonetheless, it is possible to achieve steady bubble production: either by decreasing the gas pressure of few millibars during the transient filling of the channel, until all bubbles have the same size, or using a peristaltic pump to supply the gas at constant volumetric flow rate. In this chapter, we present results obtained by the two above mentioned methods, which ensures that the break-up mechanism described in the next sections is not specific to the unsteady regime. The characterization of the steady operating regimes of the T-junction and flow-focusing devices is detailed in chapter 6.

4.3.1 Break-up dynamics

To quantify the break-up mechanism we follow the formation of a single bubble in the reverse T-junction. Note that similar observations can be done in the flow-focusing geometry. Different stages of the break-up mechanism are presented on figure 4.5. We can identify three main steps of respective duration t_α, t_β and t_γ.

1. For $0 < t < t_\alpha$ the gas meniscus advances in the T-junction until it reaches its maximum height. Due to the rather complex flow field that takes place there it advances faster near the bottom wall of the junction.

2. For $\leq t_\alpha < t < t_\alpha + t_\beta$ the gas meniscus height inside the junction decreases at nearly constant speed. It is squeezed by the perpendicular solid plug flow of yield-stress fluid which exhibits a flat region reminiscent of the velocity profile of yield-stress fluid flow in circular channel (highlighted in red).

3. At $t \simeq t_\alpha + t_\beta$ the solid core reaches the opposite wall of the junction and the gas thread breaks.

4. Finally for $t_\alpha + t_\beta < t < t_\alpha + t_\beta + t_\gamma$, the gas meniscus moves backward until it attains its initial position. Then, the junction is anew filled with yield-stress fluid and the bubble advances inside the outlet channel.

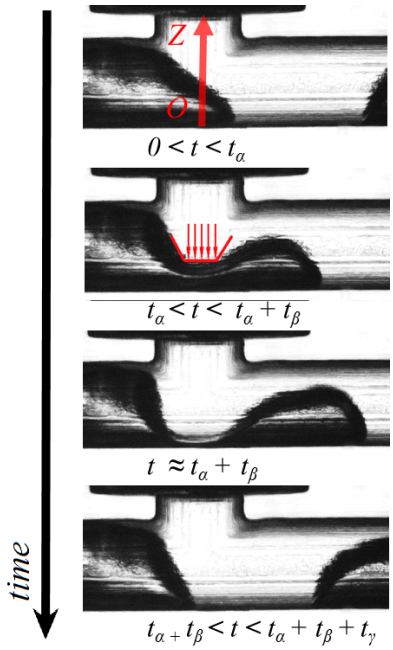

Figure 4.5 – Different steps of the break-up mechanism inside the T-junction ($R = 1$ mm), with emulsion ($\tau_y = 250$ Pa).

4.3.2 Temporal evolution

We visualize the evolution of t_α, t_β and t_γ by means of spatiotemporal diagrams. This allows to follow the temporal evolution of the grey levels along a particular line of a picture. The result is an image constituted of the concatenation of the grey level along the chosen line retrieved from each picture of the movie. We choose a line placed at the center of the junction and perpendicular to the outlet channel axis, as highlighted by the vertical red arrow on figure 4.5.

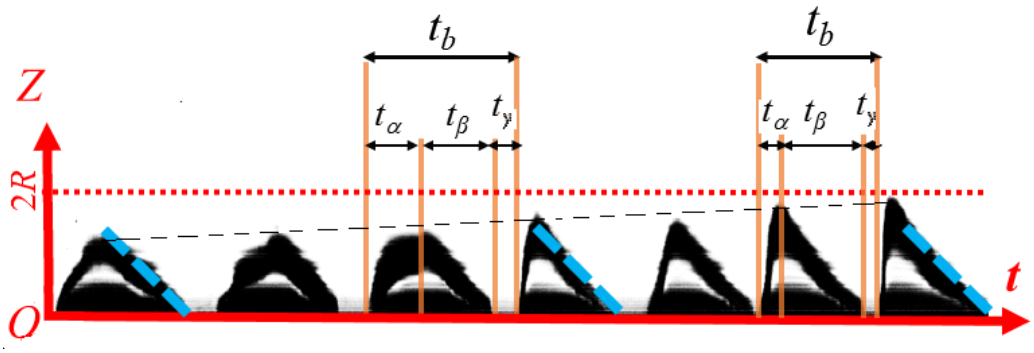

Figure 4.6 – Spatiotemporal diagram of the break up dynamic for a bubble train. The horizontal axis is time, while the vertical axis represents the (OZ) axis on the top picture of 4.5.

The resulting image presented on figure 4.6 shows the formation of seven successive bubbles. Each black and white pattern corresponds to the production of one bubble, and the upper limit of each pattern to the position of the air yield-stress fluid interface along the (OZ) axis. We can observe that:

1. The maximum height of the gas / yield-stress fluid interface increases with time until it reaches almost $2R$, the diameter of the tube.

2. t_α and t_γ progressively decrease with time. This suggests that at late time the bubble formation

is dominated by the time required by the solid core to move across the junction:

$$\lim_{t\to\infty} t_b = t_\beta \tag{4.3}$$

As mentioned previously the bubble production is unsteady due to the increase in gas flow rate that comes from the decrease in hydrodynamic resistance of the flow. This process creates hydrodynamic feedback that affects bubble formation [169, 170]: the increase in gas flow rate reduces the necessary time for the meniscus to enter the junction (t_α) and to go back to its initial position (t_γ). We can note that t_α, when the gas meniscus must counteract the yield-stress fluid flow, is always longer than t_γ.

In addition, as already mentioned, the produced bubbles are larger and larger due to the drop in hydrodynamic resistance associated with the production of each bubble. The correlation between the increase in bubble length and the decrease in the bubble formation time (t_b) is shown on figure 4.7. The vertical dashed line stands for the divergence of bubble time formation when the system is completely filled with gas due to the coalescence of the bubbles in the outlet channel. The horizontal line highlights the minimum value of the bubble formation time (t_b^{min}) which is attained when the longest bubbles are produced, that is for the highest velocity of the flow.

We can note that, the decrease in bubble formation time (t_b) suggests that the bubble size should decrease during an experiment. However, this decrease is not sufficient to counterbalance the increase in gas flow rate (Q_g) due to the flow resistance drop associated with bubbles production, so that the length of successive bubbles increases. The bubble formation stops after the coalescence of all bubbles due to the increase in deposition of yield stress fluid on the wall of the channels, itself due to the increase in velocity of the flow.

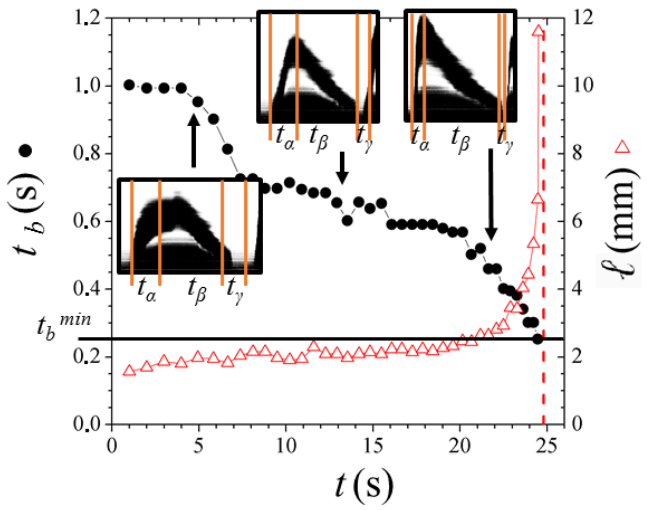

Figure 4.7 – Typical evolution of the time to form one bubble t_b and bubble length ℓ as a function of time, with corresponding pictures of the spatiotemporal diagram.

4.3.3 Minimum bubble formation time

To further investigate the parameters that control the value of t_b^{min}, we first report the bubble formation time for different imposed flow rate of yield-stress fluid (Q) using either flow-focusing (figure 4.8b) or T-junction device (figure 4.8a) for carbopol gel.

Figure 4.8 shows that for T-junction and flow focusing devices, either in steady or unsteady regime, t_b^{min} is always aligned along a line of slope -1 in log-log plot, suggesting a variation given by:

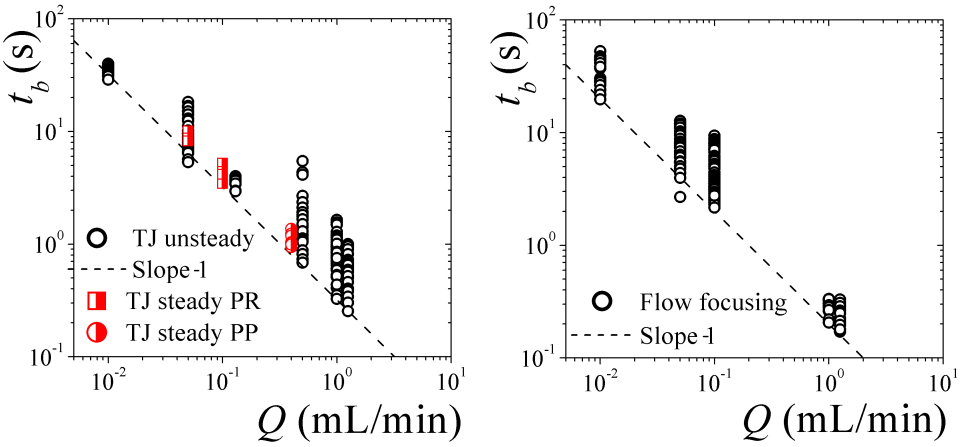

Figure 4.8 – t_b as function of the imposed yield-stress fluid flow rate in T-junction (left) and flow-focusing device (right) for carbopol ($\tau_y = 75$ Pa) with channels of radii 1 mm and length 10 cm. The half filled symbols stand for steady regimes obtained with pressure regulation (PR) or peristaltic pump (PP) (detailed in chapter 6).

$$t_b^{min} = \frac{\omega}{Q} \tag{4.4}$$

ω, has the dimension of a volume and thus can be interpreted as the volume of the intersection of the two crossing channels of the junction. These volumes are represented in figure 4.9.

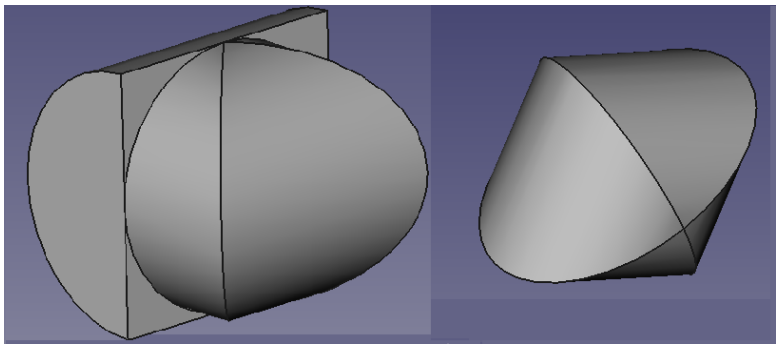

Figure 4.9 – CAD drawing of the volume of the intersection of two circular channels of same radii (i.e inner volume of the T-junction (left), and flow focusing device - right).

The volume of the intersection of two cylinders of radius R was calculated by Archimedes and can be easily computed by integration, it is given by $\Omega = \frac{16}{3}R^3$. Therefore, the volume of the intersection in the T-junction case is given by; one half this volume plus one half of the volume of a cylinder of radius R and length $2R$, hence: $\Omega = \frac{8}{3}R^3 + \pi R^3$. A comparison between Ω and ω is shown in table 4.1.

In the T-junction case, we find that $\Omega \simeq \omega$ (difference is less than 10 %). For the flow focusing geometry we find that $\omega = 0.6\Omega$.

The good correlation between the values of Ω and ω is consistent with the evolution observed on the spatiotemporal diagram. As the gas flow rate increases due the hydrodynamic flow resistance drop, $\lim_{t\to\infty} t_b = t_\beta = t_b^{min}$ the time required to squeeze the gas thread at constant imposed flow rate. Hence,

	R (mm)	ω (mm^3)	Ω (mm^3)
T-junction	1	14.91	13.80
T-junction	0.5	0.85	0.76
T-junction	2	50.2	46.4
Flow focusing	1	3.2	5.33

Table 4.1 – Comparison of the experimental and theoretical volumes.

$$t_b^{min} \simeq \frac{\Omega}{Q} \tag{4.5}$$

For the same channel radii, we find that the value of ω is significantly smaller in the case of the flow-focusing device than in the T-junction case. This suggests that for the same experimental conditions the bubble formation is at least 4.5 times faster in the flow-focusing device than in the T-junction. For flow-focusing devices, even if we can not explain the difference between the experimental value of ω and the predicted one in details, we observe that the gas thread that forms in the junction never fully fills the intersection volume. Due to the flow complexity and the unknown associated stress field in such junction we can only suggest that, as determined empirically this volume is equal to 0.6Ω.

Finally, to ensure the validity of equation 4.5, we have varied different parameters of the experiments over a wide range:

- two yield-stress fluids (carbopol with $\tau_y = 75$ Pa and emulsions with $\tau_y = 300$, 250, 100 Pa).
- T-junction with three different radii (0.5,1,2mm) and two different length (5,10cm), and flow flow focusing device $R = 1$ mm, $L = 10$ cm.
- between 6 to 15 flow rate values for each combination of the above mentioned parameters.

The measured value of t_b^{min} is plotted as a function of the theoretical value $\frac{\Omega}{Q}$ on figure 4.10.

An excellent agreement between the predicted and measured value is observed on almost 5 decades. This suggests that the break up mechanism of the gas thread by the filling of the junction volume at the imposed yield-stress fluid flow rate is very robust regardless of the flow complexity.

This break-up mechanism is analogous to the geometric break-up mechanism observed for Newtonian fluid in flow-focusing devices operating at small values of the capillary number [31, 32]. Since the final capillary pinch off is fast [32], the relevant time scale, in both cases, is the time to fill the junction (or the orifice) at the constant dispersed phase flow rate. In the case of yield-stress fluids, the extra confinement ensured by the orifice in classical flow-focusing geometries is not mandatory, since this is the solid-like region of the flow (where the stress is below τ_y) at the center of the channel, that provides the confinement down to the size where the capillary stress starts to drive the break-up. This allows the T-junction and the flow-focusing device to work the same way when the dispersed phase is a yield-stress fluid.

The measure of t_b^{min} also provides a theoretical limit for the frequency of bubble production in steady regimes. This point is discussed further in chapter 6.

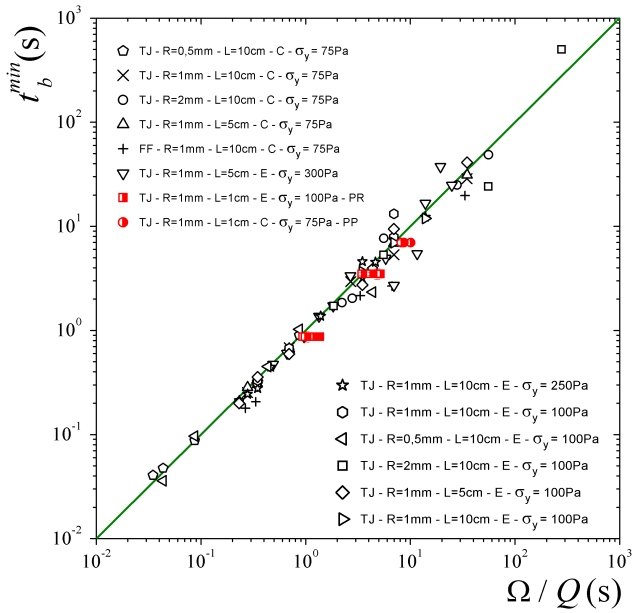

Figure 4.10 – t_b^{min} as a function of $\frac{\Omega}{Q}$ for T-junctions (TJ) and flow-focusing (FF) geometries. The different symbols are details in the inset. (E) stands for emulsion, (C) for carbopol, and (PR) and (PP) for pressure regulation and peristaltic pump (see chapter 6). The half filled symbols corresponds to steady regimes.

4.4 Conclusion

We have investigated the formation of bubbles inside yield-stress fluids using millifluidic axisymmetric T-junctions and flow-focusing geometries. We found that in both cases, when the gas is pressure-driven and the yield-stress fluid flow rate is imposed, the time to form a bubble is approximately given by the time needed to fill the volume of the junction at the yield-stress fluid flow rate [31, 32]. This regime is analogous to the squeezing regime observed for Newtonian fluids in flow-focusing devices. This is explained by the large value of the yield stress that inhibits the break up down to a critical size at which the capillary stress finally starts to drive the pinch off of the gas thread.

Essential facts

- ➤ Bubble formation occurs in the same way in flow-focusing and T-junction devices. This is reminiscent of the 2D operating regime of flow-focusing devices with Newtonian fluids.
- ➤ The minimum time to form a bubble is set by the geometry (proportional to the junction volume) and the imposed yield-stress fluid flow rate (inversly proportional to the imposed flow rate).

5

Unsteady operating regimes

In this chapter, we investigate the unsteady operating regimes of the millifluidic axisymmetric T-junction and flow-focusing devices. We first detail the different operating regimes that are observed when the gas is pressure-driven and the flow rate of yield-stress fluid is imposed, the results are presented under the form of a pressure/flow rate diagram. Then, we move to the analysis of the minimum pressure necessary to form the first bubble. Finally, we describe the process of destabilization that conducts to the break down of the bubbling regime and its link to yield-stress fluid deposition on the wall of the channel.

Contents

An important part of the characterization of microfluidic systems consists in determining the value of the imposed external parameters that lead to a given operating regime (i.e dripping, squeezing, or jetting for classical flow focusing, and T-junction devices). The aim of the following section is to provide this type of description for bubble production in yield-stress fluids using axisymmetric millifuidic T-junction and flow-focusing devices. We discuss the regime obtained when gas is pressure driven and the yield-stress fluid flow rate is imposed.

5.1 The three operating regimes

The experiments are performed as follows: the yield-stress fluid flow rate is set to a constant value between 0.01 ml/min and 1.5 ml/min. Once the channel is completely filled, the gas pressure is set to the desired constant value between 1 mbar and 2 bars. The evolution of the system under these conditions is recorded using a CCD camera (Marlin-080 B/C) at a maximum frame rate of 100 fps.

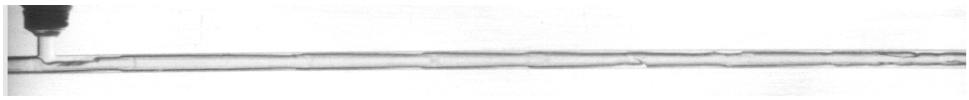

(a) High gas pressure: coflow, the gas thread is never fractioned.

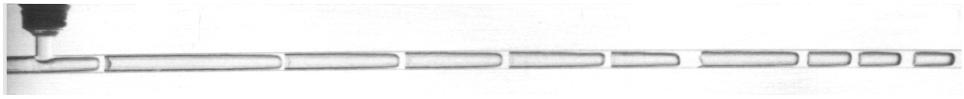

(b) Intermediate pressure: transitory bubbling regime (unsteady bubble production).

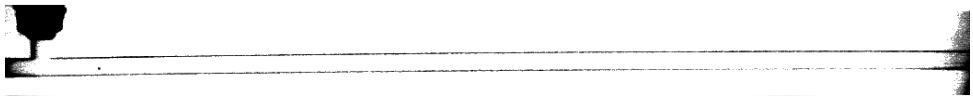

(c) Low pressure: no bubble production.

Figure 5.1 – Different operating regimes of the system when driven at constant pressure for gas, and imposed yield stress fluid flow rate, for an emulsion ($\tau_y = 100$ Pa) in a channel with $R = 1$ mm and $L = 10$ cm.

For given yield-stress fluid flow rate, three regimes are observed depending on the pressure values (figure 5.1).

- ➤ At high gas pressure (figure 5.1a), the gas phase is not fragmented by the yield-stress fluid; instead, an infinitely long gaseous thread fills all the length of the outlet channel leading to co-flow regime.
- ➤ At intermediate pressure (figure 5.1b), multiple bubbles are produced, albeit in a temporary, transitory regime. The size of successive bubbles increases until the plugs that separate each of them rupture and the system is completely filled with gas. This eventually leads, as in the case of high gas pressure, to a regime of co-flow.
- ➤ At low gas pressure (figure 5.1c), the gas interface cannot advance inside the junction. This occurs when the applied gas pressure is less than the minimum pressure necessary to overcome the stress associated with the yield-stress fluid flow. Therefore, no bubbles are produced. This also occurs for Newtonian fluids if the pressure difference between the two inlets is too large [150].

These three regimes are represented on a flow rate / pressure diagram (figure 5.2) for an emulsion of yield stress 300 Pa. The bubble production is possible inside a stripe at intermediate values of pressure/flow rate. In particular, the minimum bubbling pressure allows to probe the pressure imposed by the syringe pump to make the yield-stress fluid flow at a constant flow rate inside the chip.

In the following, we explain the origin of the value of this minimum pressure (P_b^{min}), thus allowing a detailed study of the bubbling process and dynamic of the unsteady regime.

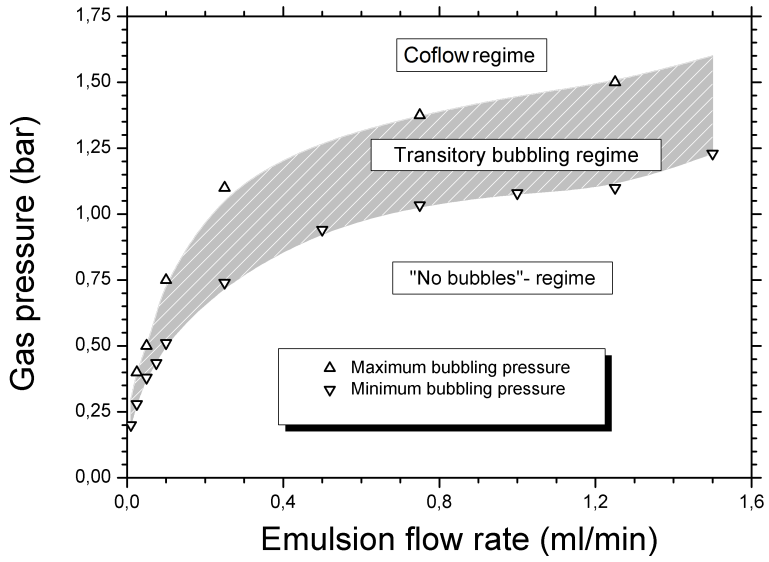

Figure 5.2 – Pressure / flow rate diagram for an emulsion with a yield stress $\tau_y = 300$ Pa for a T-junction with $R = 1$ mm and $L = 10$ cm.

5.2 Minimum bubbling pressure

To investigate the origin of the minimum bubbling pressure we vary different parameters of the system. We use two geometries (FF, TJ) with channels of different radii (0.5,1,2 mm) and length (5,10 cm), and two yield-stress fluids: a carbopol gel ($\tau_y = 75$ Pa) and emulsions ($\tau_y = 300$, 150, 100 Pa).

5.2.1 Results for the T-junction

5.2.1.1 Flow focusing vs. T-junction

Before going further into the description of the minimum bubbling pressure, we check that it does not depend strongly on the flow inside the junction by comparing the values obtained with carbopol ($\tau_y = 75$ Pa) in the T-junction (R= 1 mm, $L = 10$ cm) and in a flow-focusing device (R= 1 mm, $L = 10$ cm). The comparison is presented on figure 5.3.

The value of pressure obtained in both cases are in excellent agreement. This suggests that the flow geometry inside of the junction does not influence the minimum bubbling pressure. Therefore, in the following we only report results obtained for T-junction.

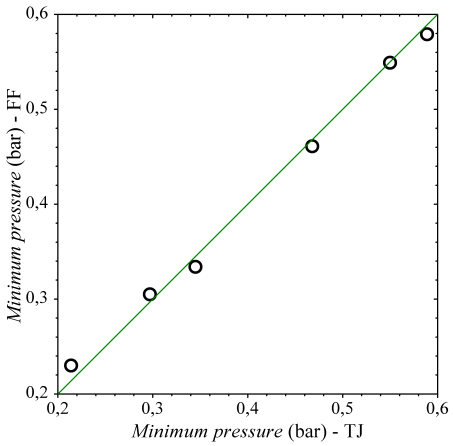

Figure 5.3 – Comparison of minimum bubbling pressure for T-junction (TJ) and flow focusing (FF) device with R= 1 mm, L = 10 cm, for carbopol (τ_y = 75 Pa). The plain line indicates $y = x$. The flow rate values are: 0.01, 0.05, 0.1, 0.5, 1, 1.5 ml/min.

5.2.1.2 Influence of the rheology, flow rate, and channel geometry

The value measured for the minimum bubbling pressure is reported as a function of the yield-stress fluid flow rate on figure 5.4a for emulsions, and on figure 5.4b for carbopol gels.

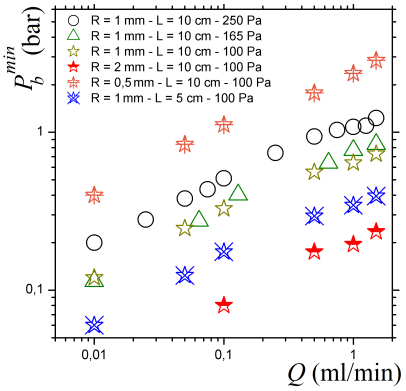

(a) For emulsions.

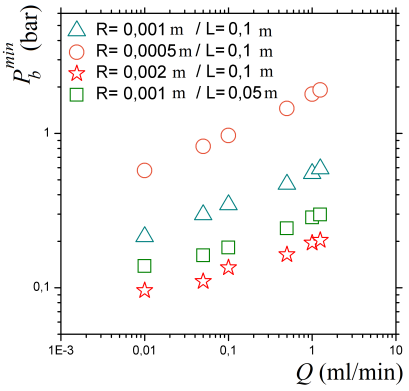

(b) For carbopol gels.

Figure 5.4 – Minimum bubbling pressure measured in different T-junctions, symbols are detailed in the inset.

These results show that the minimum bubbling pressure is both a function of the imposed flow rate, the rheological characteristics of the fluid, and the geometry of the channel. Its value also increases as a power law of the applied flow rate (exponent around 0.35). For Newtonian fluids, and very low flow rates, we expect the pressure necessary to produce the first bubble to be mostly the capillary pressure associated with the meniscus interface (i.e the Laplace pressure). This is also observed in flow-focusing devices with Newtonian fluids [114]. In our system, $32 \leq \frac{2T}{R} \leq 264$ Pa; these values are smaller than the yield pressure value measured here, which are typically larger than 1000 Pa, even for the smallest flow rates. Therefore, the minimum bubbling pressure cannot be accounted for by the curvature of the interface.

5.2.2 Computation of the minimum bubbling pressure

The minimum bubbling pressure only depends on the rheology of the fluid and the outlet channel dimensions. First, we compute the pressure necessary to overcome the one associated with the flow of yield stress fluid at constant flow rate in the outlet channel (of length L, and radius R).

The pressure drop in a circular channel filled with YSF is given by equation 2.19 (chapter 2). This expression, which only depends on the channel geometry, the applied pressure, and the rheology of the fluid, is compatible with the above mentioned observations. Therefore, for each considered outlet channel geometry (R,L), and yield-stress fluid (τ_y, k, n), we compute the associated pressure/flow rate relation. As detailed in chapter 2, the rheometrical parameters are obtained by capillary rheometry, which allows to take wall slip into account during our experiments. Thus, the yield stress used is a *sliding* yield stress (see chap. 2), and the value of the consistency (k) is an effective value modified by the presence of the slip layer.

The experimental data and the corresponding function are plotted on figure 5.5a for emulsions and for carbopol gel on figure 5.5b.

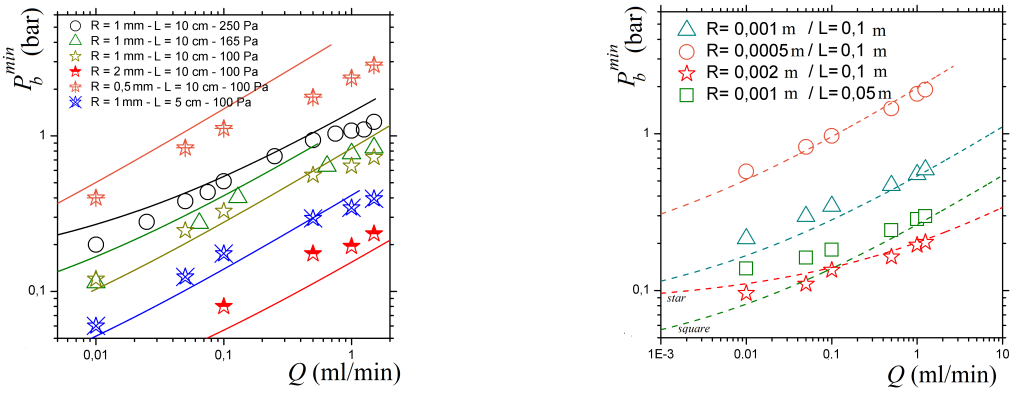

(a) For emulsions.

(b) For carbopol gels ($\tau_y = 75$ Pa).

Figure 5.5 – Minimum bubbling pressure measured in different T-junctions (symbols, detailed in the inset) and corresponding models (plain lines).

First, we observe that the agreement between the experimental data and the proposed model is reasonably good. Particularly, the slope predicted by the model is consistent with the experimental findings. However, we also observe discrepancies, which are more substantial for emulsions. Even if the curves are well ordered, there seems to be a constant breakdown of our prediction at high emulsion flow rate. For $Q > 0.5$ ml/min, the increase in the threshold bubbling pressure seems to be slower than what is predicted. This suggests that the observed pressure drop during the flow is less important than what is expected for a simple channel flow of yield-stress fluid with slip. This effect, which is not observed for carbopol gels, could be attributed to the difference in microstructure between the two fluids.

We can also underline that the results for carbopol gels are obtained with smaller yield stress than in the case of emulsions, thus it would be interesting to try the same experiments either with emulsions of smaller yield stress or/and carbopol gels of larger yield stress, to test the influence of the concentration of the microstructure, which in turn may strongly modify the slip dynamics. Finally, note that this discrepancy may be attributed to the slip dynamics that is not fully taken into account by means of the capillary rheometer method. Therefore, it needs to be explained by further investigations.

Another way to test this model is to rewrite equation 2.19 in dimensionless form. Denoting P_b^{min}

the minimum bubbling pressure, then factorizing equation 2.19 by τ_y and thus making $\tilde{P} = \frac{P_b^{min}}{\Delta P_y}$ (defined in chapter 2) appear, it yields:

$$\frac{Q}{Q_s} = \pi \tilde{P}^{-3} \left(\tilde{P} - 1\right)^{1+m} \left[\frac{\left(\tilde{P} - 1\right)^2}{3+m} + \frac{\tilde{P} - 1}{2+m} + \frac{1}{1+m} \right] \tag{5.1}$$

Equation 5.1 predicts that, if the applied pressure scales with the yield pressure necessary to make the yield-stress fluid flow, the flow rate scales with $Q_s = \left(\frac{\tau_y}{k}\right)^m R^3$; a typical flow rate that only depends on the rheology of the fluid ($(\frac{\tau_y}{k})^m$ is a typical shear rate) and the size of the channel.

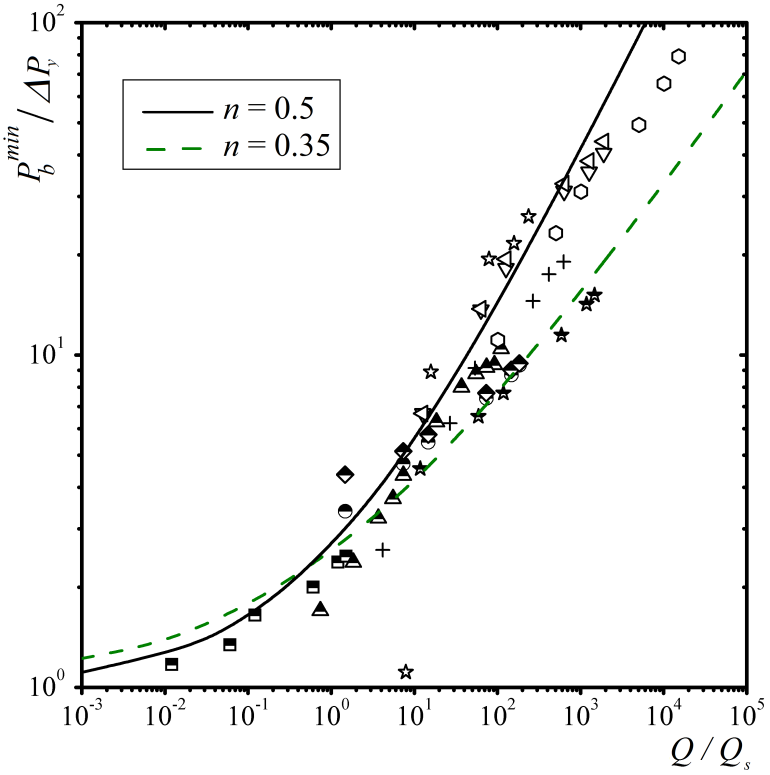

Figure 5.6 – Dimensionless critical pressure as a function of the dimensionless flow rate. The green dashed line stands for equation 5.1. The empty symbols correspond to experimental data obtained with emulsions ($\tau_y = 300$, 250, 165, 100 Pa; $n = 0.5$; $R = 0.5$, 1, 2 mm; $L = 10$, 5 cm), and the half-filled symbols to experimental data obtained with carbopol ($\tau_y = 75$ Pa; $n = 0.35$; $R = 0.5$, 1, 2 mm; $L = 10$, 5 cm).

Equation 5.1 is plotted on figure 5.6 with all data of minimum pressure shown previously for both carbopol gels and emulsions. The agreement between the equation 5.1 and the experiments is qualitatively good. Here also, we observe that the data obtained for emulsions correspond to large value of $\frac{Q}{Q_s}$, and systematically overshoot the value predicted by equation 5.1. This suggests that the capillary rheometry experiments are not sufficient to precisely determine the rheology of the fluid in this particular case.

5.3 Destabilization of bubble production

In the second part of this chapter we investigate the breakdown of the transitory bubbling regime when the yield-stress fluid flow rate and the gas pressure are imposed.

5.3.1 Comparison between Newtonian and non-Newtonian fluids

To emphasize whether the non-Newtonian character of the fluid is important, we compare pictures of the destabilization of bubble production, on figure 5.7a for carbopol gel ($\tau_y = 75$ Pa) and for a Newtonian fluid (silicone oil V100000; $\eta = 100$ Pa.s) on figure 5.7b.

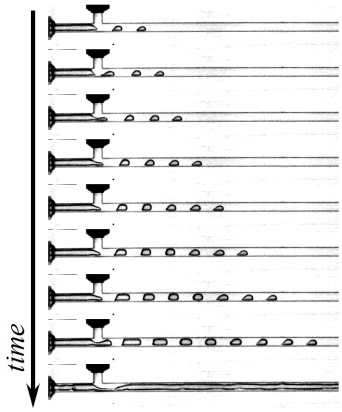

(a) For carbopol gels ($\tau_y = 75$ Pa). Pictures separated by 3.2 s.

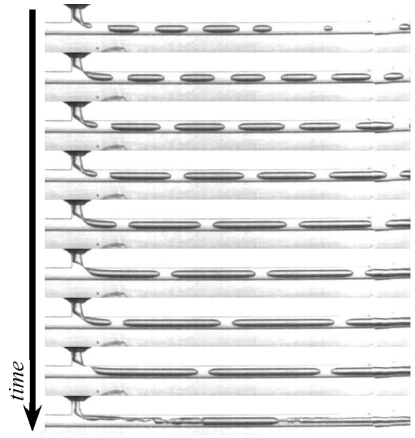

(b) For silicon oil, $\eta = 100$ Pa.s. Pictures separated by 0.9 s.

Figure 5.7 – Pictures of the temporal evolution of the unsteady regime until the breakdown of bubble production ($R = 1$ mm).

As already mentioned in chapter 4, we observe that the size of successive bubbles increases until the plugs of liquid separating each bubble reach a critical size and rupture (between picture 8 and 9 of figure 5.7a and 5.7b). Then, bubble production stops and the gas and liquid flow side by side (last image of figure 5.7a and 5.7b). This destabilization of the bubble train is not specific to non-Newtonian fluids. It occurs in a similar way for Newtonian fluids [170] when the viscosity contrast between the dispersed and the continuous phase is large, and the gas pressure is controlled (figure 5.7b). As proposed in [170], during this process we identify two main physical ingredients, the first being hydrodynamic resistance variations. The second being related to the decrease in size of YSF plugs separating each bubbles, which eventually leads to bubble coalescence. Theses two effects are detailed below:

- The hydrodynamic resistance of the channel decreases due to the formation of each bubble. Therefore, the gas flow rate increases since the flow is driven at constant pressure. Recalling that the time to form a bubble is nearly constant (see chapter 4), it leads to the production of larger and larger bubbles. Since the two-phase flow is partly pressure driven, the global flow rate and the mean velocity increase due to the hydrodynamic resistance drop.
- The second effect that leads to the breakdown of the bubbling regime is associated with the dynamics of the yield-stress fluid plugs that separates each bubble. As the flow accelerates due to the hydrodynamic resistance drop, the thickness of the yield-stress fluid film that surrounds each bubble increases (see chapter 3). Thus, due to volume conservation, the bubbles change their shape and become elongated. This leads to a transfer of fluid between the plugs and the thin

films, which results in a decrease in the plugs' size. This, in turn may trigger plugs rupture that leads to coalescence between successive bubbles, which decrease the hydrodynamic resistance of the channel and further promotes the destabilization mechanism. This process is shown by the arrows on images of figure 5.8).

Finally, at some point, the gas flow rate is so large that the front meniscus of the gas bubble that is produced (i.e. connected to the gas source: the forming bubble on figure 5.13) advances rapidly inside the channel. It breaks the first plug and accelerates due to the drop in hydrodynamic resistance. Then, it breaks the second plug, and so on until all bubbles coalesce (last images of figure 5.8).

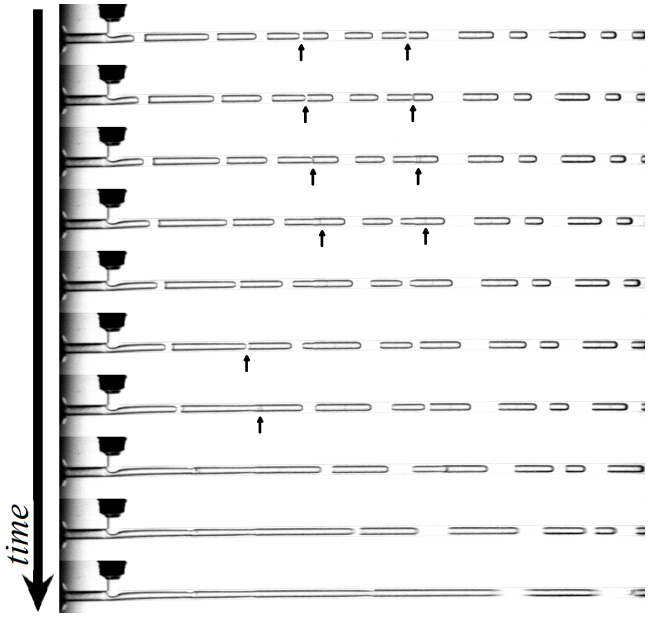

Figure 5.8 – Last stages of the destabilization of a bubble production. Each picture is separated by 0.0125 s, $R = 1$ mm.

5.3.2 Literature results and comments

The rupture of the plugs separating successive bubbles is sometimes studied in biomedical research in the context of lung closure under different pathological conditions [171]. This problem has been investigated experimentally for single plugs and trains of plugs [170], or numerically [172, 173] in the case of Newtonian fluids, and even for Bingham fluids in *Hele-Shaw cells* [174].

Most of these studies focused on computing the flow field inside the plugs, which is shown to exhibit counter-rotating vortices [172, 173], the stress profile [174], or on the rupture of the plugs depending on the presence of a pre-wetting film [173]. The physics at play during the destabilization of multiple plugs of Newtonian fluids flowing in a straight channel and pushed at constant pressure is attributed to [170]:

1. A decrease of the overall hydrodynamic resistance due to the decrease in plug size that first occurs in the front plug that encounters a non-wetted channel.

2. Interactions between successive plugs through lubrication effects and delay effects due the initial state of the system.

Comments

The destabilization of bubble production in our millifluidic devices is essentially due to the same physical ingredients which drive the rupture of a plug train of Newtonian fluid into a straight channel when pushed at constant pressure. This is due to hydrodynamic resistance variation and deposition of the fluid on the channel wall. Both of them are consequences of the pressure driving of the dispersed phase, and are enhanced by the large viscosity contrast between the gas and the yield-stress fluid.

5.3.3 Last stage of destabilization: plug rupture

The ultimate step of destabilization occurs when the gas flow rate, and therefore the flow velocity, is large. This implies that the stress applied on the plugs may be large compared to the yield stress, and the flow profile inside the channel is mostly Poiseuille-like. Thus, during this process which is mostly dominated by viscous and interfacial effects, the yield stress may not play a critical role. To further investigate the effect of the yield stress we observe the destabilization of a bubble train flowing slowly at the beginning of the experiment (i.e. so that the applied stress is not too large compared to the yield stress $Bi \leq 1$). The spatiotemporal evolution of such bubble train is shown on figure 5.9.

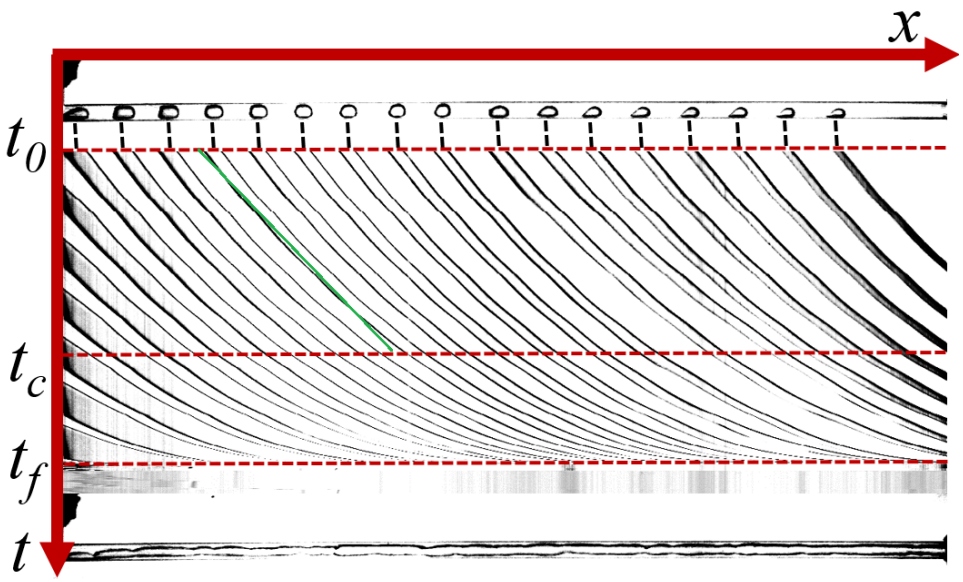

Figure 5.9 – Spatiotemporal diagram of the destabilization of a bubble train in emulsion ($\tau_y = 100$ Pa). The top picture corresponds to the initial state of the train, the last one to its final state ($R = 1$ mm).

First, we observe that, up to a critical time (t_c) the velocity varies slowly (i.e the trajectories on the spatiotemporal diagram (green line figure 5.9) are reasonably approximated by straight lines) and that the size of the plugs remains almost constant. At some point the variation in velocity becomes large and all plugs rupture in a very short time. We note that the decrease of plug size starts to be significant simultaneously for all plugs, at $t_c \simeq 36$ s. This suggests that the whole flow is affected at the same time.

To investigate further this regime, we measure the size of individual plugs as a function of time. The results are presented on figure 5.10.

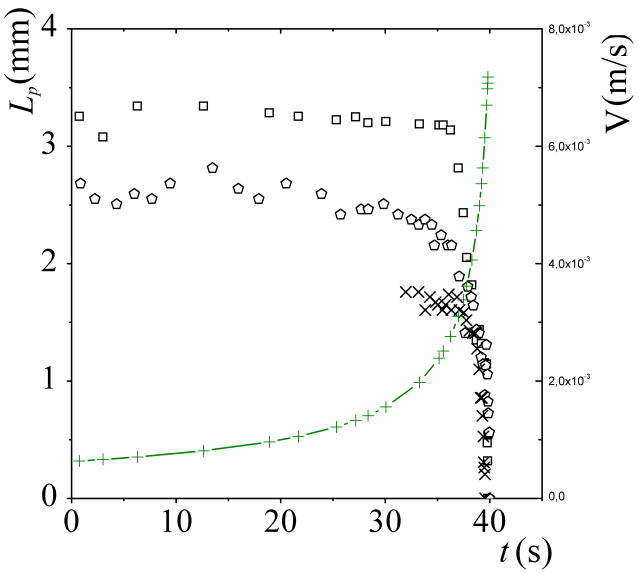

Figure 5.10 – Plug length (empty symbols) and bubble velocity (line) as a function of time during the destabilization of bubble production. Each data set corresponds to one plug of emulsion ($\tau_y = 100$ Pa) in a channel with $R = 1$ mm during the same experiment.

To relate this effect to the global characteristics of the flow we introduce the Bingham number that compares the yield stress of the material to the viscous stress during the flow, $Bi = \dfrac{\tau_y}{k\left(\frac{V}{R}\right)^n}$. In this expression, as explained in chapter 2, the viscous stress takes wall slip into account, and thus is an effective viscous stress and the yield stress is the yield stress of the bulk material (which must be overcome by interfacial stresses). The length of the plugs L_p normalized by their initial length L_0 are plotted on figure 5.11 as functions of the Bingham number.

We first emphasize that the data obtained for different plugs, of both carbopol gel and emulsion, reasonably collapse on a single curve. Two regimes are identified:

1. in the first regime the plug size does not varies significantly. This corresponds to values of the Bingham number larger than one (i.e. viscous stresses are small compared to the yield stress) and a flow profile mostly constituted of a solid-like region. Thus, we call this regime the solid regime. In this regime, we suggest that the plugs are stable due to wall slip, and the weak resulting deposition.

2. in the second regime, the plug size decreases rapidly until the plugs rupture. The rupture is observed to occur for $0.5 \leq Bi \leq 0.6$. This regime corresponds to values of the Bingham number smaller than one, i.e. to a mostly Poiseuille-like velocity profile. In chapter 3, we show that the deposition law (with slippage) exhibits a sharp increase in deposition for a Bingham number around one. This can be associated with the collapse of the plug size, which in turn may be triggered by the transition of the flow profile from mostly solid to mostly liquid. This suggests that the stress state of the system (which is strongly associated with wall slip) governs the plug rupture, and thus the whole dynamics of the flow.

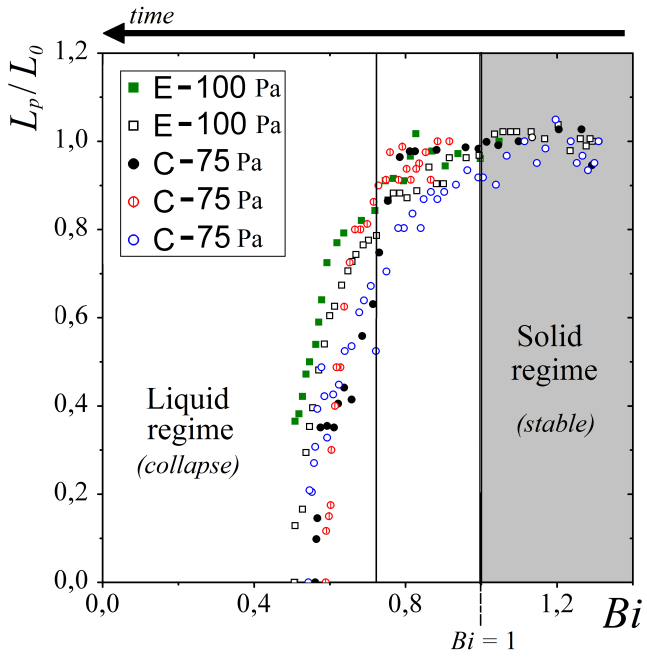

Figure 5.11 – Plug length normalized by the initial length of each plug as a function of the Bingham number during the destabilization of bubble production for carbopol gel (C) and emulsions (E) in a channel with $R = 1$ mm. The value of the yield stress is given in the inset. Each data set corresponds to one plug.

5.3.4 Numerical model of hydrodynamic resistance variation

To go one step further, we write a numerical model [1] of the destabilization of the bubble train. We consider the problem of the destabilization of the bubble production in T-junction of radius R and with an outlet channel of length L when the gas pressure (ΔP) and the yield-stress fluid flow rate (Q) are imposed. The fluid is an Herschel-Bulkley fluid ($\tau = \tau_y + k\dot{\gamma}^n$). We start with a simplified model, that shows that the initial destabilization of production is due to hydrodynamic resistance variation, and that it can be roughly decoupled from the deposition problem that must be taken into account only during the last stages. The method is designed as follows:

1. Computation of the initial parameters of the system: knowing the rheology, the geometry of the channel, and the imposed yield-stress fluid flow rate (Q), we compute the corresponding minimum pressure (P_b^{min}) to form a bubble using equation 2.19 that define f_{hb}.

$$P_b^{min} = f_{hb}^{-1}(Q, L) \tag{5.2}$$

2. If the imposed pressure $\Delta P > P_b^{min}$, the associated total flow rate is:

$$Q_{tot} = f_{hb}(\Delta P, L) \tag{5.3}$$

3. Hence, from mass conservation the gas flow rate is:

$$Q_g = Q_{tot} - Q \tag{5.4}$$

[1] an example of such script is given in annex E, written in python: https://www.python.org/

4. Then, assuming that the time to form a bubble (t_b) is constant and given by equation 4.5, the volume of the produced bubble is:

$$\omega_b = t_b Q_g \tag{5.5}$$

5. Assuming that the bubble has a slug shape and occupies the whole cross section of the tube (the thickness of the film is considered to be small compared the channel radius), its length (for bubble i) is given by:

$$\ell_i = \frac{\omega_b}{\pi R^2} \tag{5.6}$$

6. Indeed neglecting the thin film means that bubbles move at the average velocity of the flow and do not increase the dissipation, thus we assume that the new relevant length to compute the dissipation is $L - \ell_i$. Besides, note that the plugs separating each bubbles does not vary in size. At this point, it is necessary to go back to step (2), recompute the dissipation and the volume of the second bubble.

The computation of the simplified dynamics of the system can be achieved in this way. It is arbitrarily stopped when the produced bubble becomes longer than the tube, whereas in experiments the destabilization occurs earlier due to the deposition process. Therefore the destabilization times obtained numerically are much larger than what is observed experimentally. Typical results obtained for the volume of produced bubbles as a function of the time since the beginning of the simulation are shown on figure 5.12.

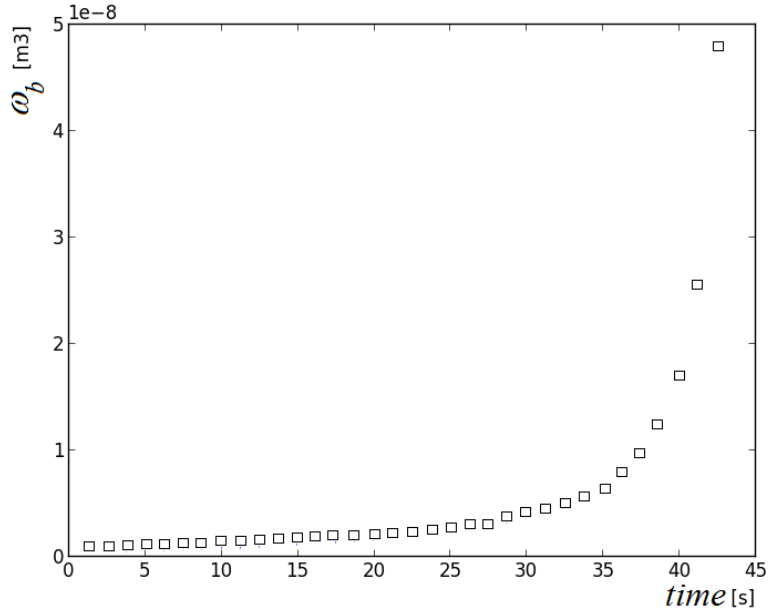

Figure 5.12 – Bubble volume as a function of the time since the beginning of the simulation, for $Q = 0.1$ ml/min and a channel of radius 1 mm and length 10 cm. The rheological parameters of the yield-stress fluid are: $\tau_y = 200$ Pa; $k = 100$ Pa.s^{-n}; $n = 0.5$.

Taking into account only one physical ingredient (the hydrodynamic resistance variation) is sufficient to produce an unstable behavior of the system. This simplified model should be especially relevant at the onset on bubbling when the flow is slow and deposition does not play a critical role into the dynamic of the system. As an outlook, it would be interesting to incorporate the deposition law

(derived in chapter 3) inside the model. This could be done by recomputing the size of the bubbles and of the plugs at each time step, and would possibly give more information on the last stages of the destabilization. Finally, we would also include the variation of the bubbles' volume due to gas compressibility as they advance in the channel (details on this phenomenon are given in annex on "Bubbles' shape").

5.4 Effects related to yield-stress fluid deposition

In this section, we further investigate the effects related to deposition of yield-stress fluid during the unsteady bubble production. First, we consider the shape of bubbles, and the change they undergo during an experiment. Then, we show that a deposition law, which is consistent with the results presented in chapter 3, can be retrieved from the unsteady experiments.

5.4.1 Bubbles' shape and position

We observe that, when the flow is sufficiently slow and the yield stress sufficiently large, bubbles are sometimes trapped near the wall of the channel (i.e. large value of the Bingham number ($Bi > 1$), corresponding to negligible dynamical effects). As can be seen on figure 5.9, this is especially striking for smaller bubbles. Similar deviation from straight trajectories in straight channels are observed for bubbles in visco-elastic fluids [175]. They are due to normal stresses and occurs after the bubble had traveled a finite distance from its formation point in the outlet channel. However, in our case, the bubbles are trapped at the wall immediately after their production (figures 4.5 or 5.7 for example) and stay close to it during their whole travel toward the exit. In addition, in chapter 1 we show that normal stresses are always small compared to viscous stresses. Therefore, we cannot attribute this effect to normal stresses.

Since bubble are formed close to the wall, we can reasonably assume that at low velocities they are trapped by the large yield stress just after the pinch off of the gas thread. Such bubble positions were observed during numerical simulations for bubble formation in Bingham fluids [39]. The authors attribute this effect to the large effective viscosity of the solid-like region at the center of the channel.

In flow-focusing devices, bubbles form at the center of the channel but almost always end up on one side of the channel (see figure 4.3b), whereas in visco-elastic fluids the bubbles have the same probability to end up on one or the other side of the channel [175]. However, due to the complexity of the flow profile with bubbles, in our case it is difficult to propose a physical mechanism responsible for the systematic deviation of bubbles' trajectory in flow-focusing device.

As in the Newtonian case, the bubbles' shape is also affected by the viscous stress during the flow. As they accelerate, the surrounding film thickens and the bubbles become more and more elongated due to volume conservation. This effect is particularly spectacular for yield-stress fluids since the bubbles initially adopt shapes that depart significantly from what is predicted by surface tension only. The shape of bubbles may change from non-axisymmetric and trapped at the wall (figure 5.13a - annex on bubbles' shape for more details on their initial shape) to axisymmetric and at the center of the channel (figure 5.13b).

To quantify this effect, we measure the diameter of bubbles inside the channel during the destabilization of bubble production. We plot the diameter of bubbles (D_b) inside the channel normalized by the channel diameter (D) as a function of the Bingham number. Thus, on figure 5.15 each point corresponds to one bubble at a Bingham number Bi with a diameter D_b. We follow the motion of each bubble from the junction to the outlet during the destabilization of bubble production. The measurement of D_b is sketched on figure 5.14.

On figure 5.15, the rolling mean data (green dots) are presented to clarify our point. At large values of Bi (i.e. for small velocities) the diameter of bubbles is small compared to the radius of the tube. As

(a) Picture of five bubbles at large Bingham number ($Bi > 1$).

(b) Picture of five bubbles at small Bingham number ($Bi < 1$).

Figure 5.13 – Bubbles shape depending on flow conditions in emulsion ($\tau_y = 100$ Pa), in a channel of radius 1 mm.

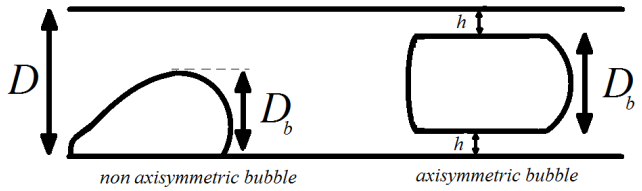

Figure 5.14 – Schematics of bubble shapes and the corresponding measure of the bubble diameter (D_b) in a channel of diameter $D = 2R$.

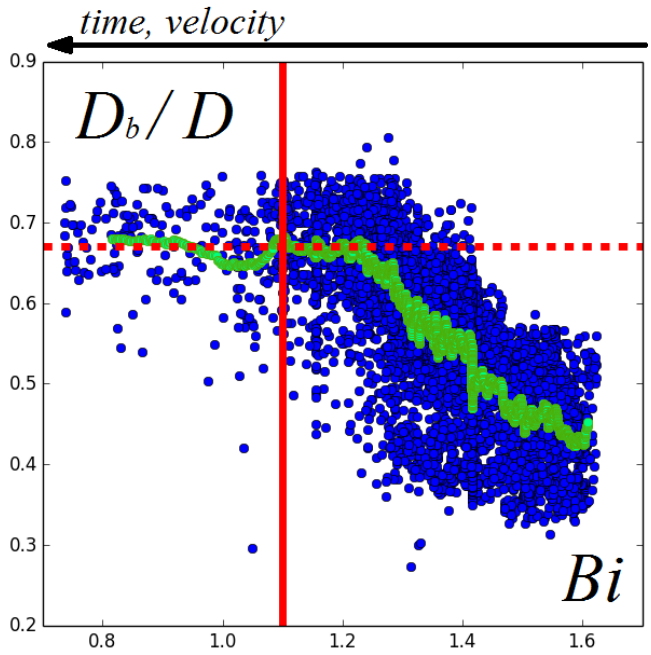

Figure 5.15 – Normalized diameter of bubbles during the unsteady regime as a function of the Bingham number for emulsion. The blue dots correspond to raw data, the green dots to the rolling average of the raw data for each pictures of the analyzed film. The vertical line highlights the shape transition; the horizontal dashed line the mean diameter of bubbles after the transition. The applied pressure is 343 mbar. The YSF is an emulsion with $\tau_y = 100$ Pa; $k = 78.5$ Pa.s^{-n}; $n = 0.5$. At the beginning of the experiment the tube is already filled with bubbles, and $\simeq 50$ bubbles are produced during the whole analysis.

the destabilization process is promoted by the decrease in hydrodynamic resistance, the size of bubbles increases and so does their velocity. However at some point (vertical line - $Bi \simeq 1.1$) the increase in bubble diameter slows down and even tends to an almost constant value $\simeq 0.7 D_b$ (horizontal dashed line).

As mentioned in chapter 3, the diameter of bubbles during flow in microchannels is linked to the

deposition of carrier fluid on the wall of the channel. Thus, as Bi decreases due to the increase in velocity of the flow, the deposited film thickness increases and the bubbles diameter decreases. For small Bingham numbers ($Bi < 1$), the bubbles diameter attains almost a constant value that roughly corresponds to the complementary of the saturation value of the film thickness at small Bingham number (see chapter 3): as can be seen if we compare the mean value from figure 5.15 $\langle \frac{h_0}{R} \rangle = 1 - 0.67 = 0.33$ to $0.1 \leq \frac{h_0}{R} \leq 0.3$ from figure 3.20. Also, note that once the Bingham number becomes smaller than one, most of the bubbles posses the average diameter corresponding to the saturation of the deposition law. This is also in agreement with the results from chapter 3, where the saturation value was found to be quickly attained when $Bi \sim 1$ (with wall slip).

As explained by Bretherton [112], the film thickness can be expressed as a function of the excess velocity of bubbles (see chapter 2). Taylor [111] suggested that the saturation of the deposition law (and thus of bubble diameter) to a constant value is due to the structure of the flow. When the bubbles moves faster than the maximum velocity of the velocity profile no recirculation occurs (since fluid particles on the central streamline move toward the front meniscus of bubbles), whereas counter-rotating vortices are observed in the opposite case (see chapter 2 and 3). Denoting v_b the velocity of a bubble, and v_m the mean velocity of the fluid, the excess velocity of bubbles ($W = \frac{v_b - v_m}{v_b}$) can be expressed as a function of the film thickness by equation 2.23.

Here, we try to extend this analysis to the case of an Herschel-Bulkley fluid. In the case of the Newtonian fluid, the maximum velocity of a Poiseuille flow is twice its mean velocity ($v_{max} = 2v_m$) leading to the straightforward value of $W = 0.5$ for the saturation. For an Herschel-Bulkley fluid, the relation between the maximum velocity of the profile and the mean velocity should be derived first. Recasting equations 2.18, and 2.19 divided by πR^2 yields:

$$v_m = v_{max} f_v \tag{5.7}$$

with,

$$f_v = \left(\frac{\tau_y}{\tau_w}\right)^2 \left[1 + \frac{1+m}{2+m}\left(\frac{\tau_w}{\tau_y} - 1\right) + \frac{1+m}{3+m}\left(\frac{\tau_w}{\tau_y} - 1\right)^2\right] \tag{5.8}$$

Note that, since the wall shear stress $\tau_w > \tau_y$, $f_v < 1$. f_v is a function of the applied stress, relation 5.7 is not as simple as in the Newtonian case. Therefore, to simplify the problem we assume that $\tau_w \gg \tau_y$. Indeed, in our case the saturation is observed when the flow velocity is large enough so that the applied stress is large compared to the yield stress, thus this condition must be fulfilled most of the time. This leads to:

$$\lim_{\tau_w \to +\infty} f_v = \left(1 + \frac{2}{1+m}\right)^{-1} \equiv f_v^l \tag{5.9}$$

This expression reduces to $v_{max} = 2v_m$ for Newtonian fluids (i.e. for $m = \frac{1}{n} = 1$. Thus, for $v_b = \frac{v_m}{f_v^l}$ at the saturation, we can rewrite W as:

$$W = 1 - f_v^l \tag{5.10}$$

and the film thickness is obtained from equation 2.23:

$$\frac{h_0}{R} = 1 - \sqrt{f_v^l} \tag{5.11}$$

Typical values of the film thickness and the excess velocity computed from equations 5.10, 5.11 are given in table 5.1. Considering the multiple hypotheses made, these values are in relatively good agreement with what was observed experimentally either when measuring the bubble diameter or the length of a plug pushed at constant velocity. Yet, we also observe that the computed values are systematically slightly larger than the measured one, it may be attributed to either not completely negligible slippage of the material at the wall, or the resolution of the measurements which does not allow to fully resolve the deposition at high velocity.

	n	$m = n^{-1}$	W	h_0/R (comp.)	h_0/R (meas.)
Newtonian	1	1	0.5	0.29	-
Carbopol	0.35	2.86	0.34	0.42	0.33
Emulsion	0.5	2	0.4	0.37	0.28

Table 5.1 – Summary of the saturation value computed for carbopol gel and emulsions.

We can also note that the computation predicts that the transition between the two flow fields depends only on the flow index n, and is shifted to lower value of the excess velocity of bubbles which corresponds to higher values of the film thickness. Finally, these results are consistent with the deposition mechanism, and clarify the shape transition undergone by bubbles during two-phase-flow when the carrier fluid exhibits a yield stress.

5.4.2 Retrieving a deposition law from multi-plugs experiments

In this section we show that it is possible to retrieve a deposition law from the measurement of the size of the plugs during the unsteady regime. We consider one plug that separates two consecutive bubbles. We measure the plug size and its velocity during an experiment (figure 5.10 for typical data). To obtain the deposition law, we first write a mass balance on the moving plug of length L_p. The cross sectional area of the tube is denoted $S_0 = \pi R^2$; the cross sectional area of bubbles is denoted $S^f(x,t)$ for the bubble placed at the front of the considered plug, and $S^r(x,t)$ for the bubble behind the considered plug (figure 5.16).

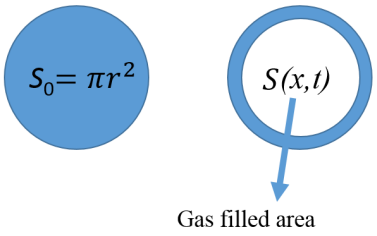

Figure 5.16 – Sketch of the cross sectional areas.

We first assume that all bubbles move at the same speed, so that $S^f(x,t) = S^f(t)$ and $S^r(x,t) = S^r(t)$. Secondly, we assume that the deposited film has an homogeneous thickness on all the circumference of the channel cross section: the cross sectional area occupied by the film is an annulus. Writing the variation of the plug volume during the time δt yields:

$$S_0 \delta L_p = \left[S_0 - S^f(t)\right] V(t) \delta t - \left[S_0 - S^r(t)\right] V(t) \tag{5.12}$$

Similarly to what is found for a train of plugs [170], the right-hand side of equation 5.12 corresponds to what is gained due to the film located in front of the plug minus what is deposited behind the plug. Equation 5.12 reduces to:

$$\frac{S_0}{V(t)}\frac{\mathrm{d}L_p}{\mathrm{d}t} = S^r - S^f \tag{5.13}$$

where,

$$S^r = \pi R^2 \left[1 - \left(1 - \frac{h_r}{R}\right)^2\right] \tag{5.14}$$

$$S^f = \pi R^2 \left[1 - \left(1 - \frac{h_f}{R}\right)^2\right] \tag{5.15}$$

The left-hand side of equation 5.13 is completely known since $V(t)$ and L_p are measured. To compute the film thickness, we further assume that what is deposited by the plug at t_i (corresponding to the i-th image) is what is retrieved at t_{i+1} (image $i+1$). Thus, if we know a particular pair (S^r, $V(t)$) we can iteratively compute all value of the film thickness during an experiment using equations 5.13, 5.15. The drawback of this method is that it is necessary to measure one value of the film thickness, which is difficult to perform precisely in our set-up. Since the computation is iterative the error is transmitted to all computed values of the film thickness. This even produces negative values of the film thickness. To be consistent, we choose to offset the curves with negative value, so that the maximum deposited film thickness is $\frac{h_0}{R} = 1$, which corresponds to the rupture of the plug (i.e. for $Bi \simeq 0.5$, figure 5.11). The results are shown on figure 5.17.

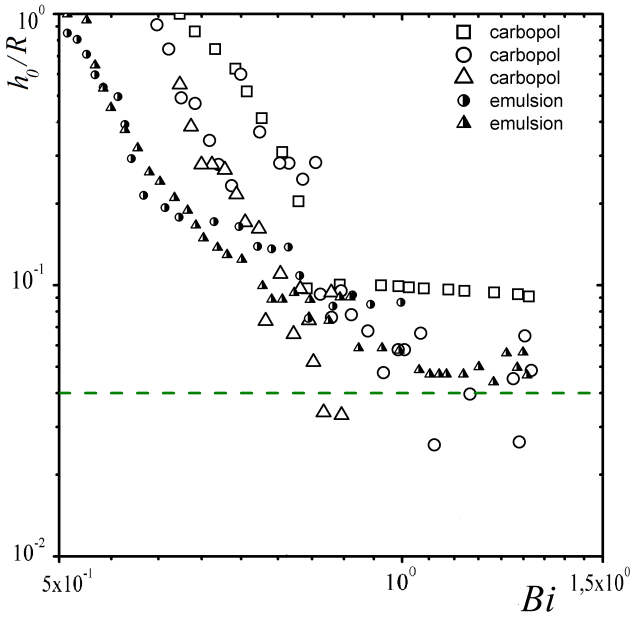

Figure 5.17 – Computed film thickness retrieved from unsteady multi-plugs experiments in STL manufactured channels ($R = 1$ mm) for different plugs of emulsions ($\tau_y = 100$ Pa) and carbopol ($\tau_y = 75$ Pa) as a function of the Bingham number. The dashed line stands for the limiting thickness imposed by surface roughness of STL devices.

First, we observe that the the deposited thickness saturates at small velocities (i.e. large Bingham). We assume that this is due to the roughness of the STL devices. As explained in chapter 2, due to

fabrication process the profile of the cross section is rather a discrete circle than a continuous one (figure 2.2). Thus, depositing a film which surface follow the associated roughness would require high surface energy compared to a circular one. This would lead to interfaces with typical radius of curvature of order of the vertical step size, and so cost at least 25 % more interfacial energy compared to the circular case. We can compute the necessary deposited quantity to fill the roughness with fluid, so that the film surface would be circular (detailed in annex on roughness of STL geometry). Therefore, if we denote A the area in red (i.e. the supplementary area associated with the roughness of the devices) on figure 2.2, and we compute an associated effective film thickness h_{eq} defined by:

$$A = \pi R^2 - \pi \left(R - h_{eq}\right)^2 \tag{5.16}$$

for $R = 1$ mm, and vertical step of 50 μm we find that $\dfrac{h_{eq}}{R} \simeq 0.04$. This value is represented by the green line on figure 5.17 and seems to roughly correspond to the limit of the deposited film thickness at large values of Bi. This suggests that the limiting film thickness at large Bi is only linked to the geometry of the devices. These results can be also be compared to what was found in chapter 3 for glass capillaries. The comparison is done on figure 5.18.

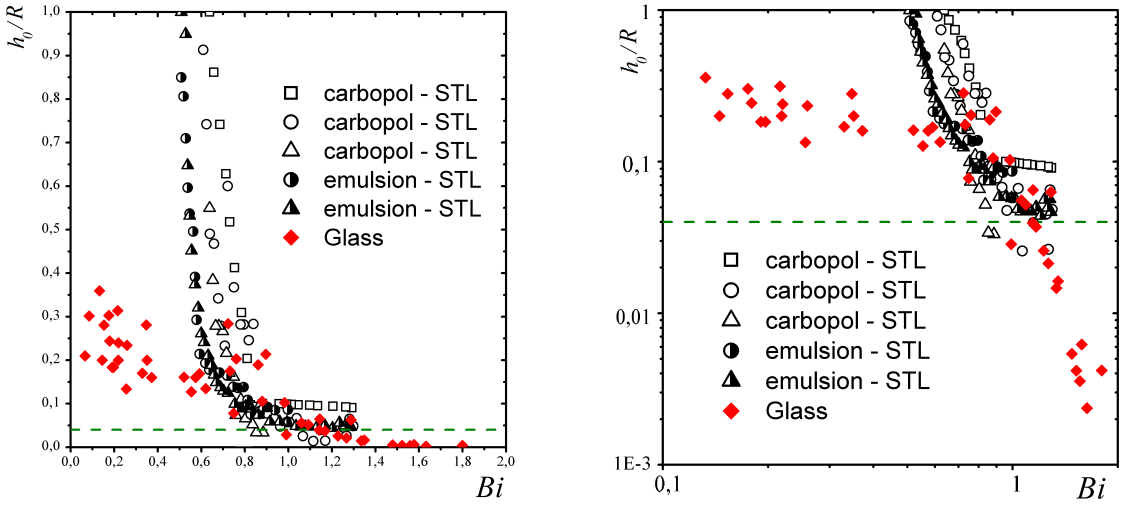

(a) Linear scale.

(b) Log-log scale.

Figure 5.18 – Comparison between film thickness obtained from unsteady bubbling experiments and single plug experiments. Multi-plugs experiments in STL channels ($R = 1$ mm): emulsion ($\tau_y = 100$ Pa); carbopol gel ($\tau_y = 75$ Pa). Single plug experiment in glass capillaries ($R = 235$, 513, 702 μm): emulsion ($\tau_y = 100$ Pa); carbopol gel ($\tau_y = 75$ Pa). The dashed line stands for the limiting thickness imposed by surface roughness of STL devices.

First, we observe that the results obtained with both methods are in relativity good agreement, especially for Bingham number around 1. However, on the contrary to what is found at large velocities (i.e small Bingham numbers) in chapter 3, the deposition law does not saturate to a value smaller than 1. This is due to the measurement method, which consists in following the plug size until its breakup, so that its size may even become smaller than the diameter of the channel, which case is not considered in chapter 3.

The other notable difference is the high Bi regime: the experiments performed in chapter 3 inside glass capillaries lead to significantly lower film thickness than what is found during unsteady bubbling experiments. This can be explained by considering the roughness of surfaces, which are only glass surfaces for experiments in chapter 3 (i.e. extremely smooth, possible roughness of the order of

few nanometers [176]). Thus, very thin film thickness can be deposited without requiring too much interfacial energy. This result can also be rephrased in term of the deposition law: the smoother the surface, the more important the wall slip, and the smaller the deposited thickness.

5.5 Conclusion

In this chapter, we investigate the unsteady regime of bubble production. First, we show that the pressure needed to form the first bubble is close to the pressure necessary to overcome the pressure associated with the imposed yield-stress fluid flow rate. Then, the destabilisation mechanism is found to exhibit two major phases each associated with different physical mechanisms. The first seems to be linked to the nature of the inlet conditions of the flow (pressure driven for dispersed phase) and the viscosity contrast between the two phases. The second stage is mostly driven by the deposition which leads to a decrease in the size yield-stress fluid plugs until they rupture. During this whole process, bubbles' shape change, which is also associated with the deposition law and the structure of the flow. The multi-plugs unsteady experiments are also used to recover data from the deposition law, and allow to gain an insight on the role of surface roughness on the deposition mechanism.

Essential facts

- The minimum pressure to form the first bubble corresponds to the pressure imposed by the yield-stress fluid flow at imposed flow rate.
- The unsteady regime is explained in terms of: (i) hydrodynamic resistance variation; (ii) yield-stress fluid deposition leading to plug rupture.
- The plug dynamics follows the dynamics of the film thickness.
- The deposition of yield-stress fluid is larger on rough surface than on smooth surface to compensate for the increase in interfacial energy associated with the roughness.

6

Steady regimes for yield-stress fluid foams production

In this chapter we discuss different pathways to obtain steady bubble production in yield-stress fluid in millifluidic geometries. We characterize the stability of each method in term of bubble formation time. The results are compared to the scaling law obtained in chapter 4. Finally, we show that these methods allow to produce yield-stress fluids foams, and thus are promising candidates for the large scale production of foamy yield-stress fluids. All experiments are performed with T-junctions, but the same observations could be made for flow focusing devices. In this chapter, we show that, despite the unsteady regimes analyzed in chapter 5, it is possible to reach steady states of bubble production when adapting the operating conditions. After briefly describing the steady states obtained for Newtonian fluids, we characterize the bubble formation process at imposed flow rate of the continuous phase, for different regulation methods of the dispersed phase in the case of yield stress fluid and gas.

Contents

6.1 Newtonian fluids

In this section, we give a brief review of the influence of the inlet conditions of each phase on bubble production for a Newtonian continuous phase.

6.1.1 Inlet conditions

To produce bubbles or drops with microfluidic devices, an important parameter is the choice of the feeding method of each phase [177]. Different possibilities are discussed below.

- Volume flow rate control of the continuous phase and pressure control of the dispersed phase. This case is more common for the production of bubbles in liquids [114, 154]. Indeed gas is compressible and a pressure control may limit the effects associated with compressibility (i.e. compliance effects) compared to a syringe pump for example.
- Volume flow rate control of the continuous phase and volume flow rate control of the dispersed phase. This is the most common case for the production of droplets in liquids because syringe pumps are easy to use and to implement. Moreover, for flow-focusing devices, even at large dispersed phase flow rate the droplets volume is found to be approximately constant [177]. Yet, using a syringe pump to control the flow rate may lead to pulsated flow due to the discrete steps of the motor. This effect can be counterbalanced by means of compliant tubing which damps the fluctuations in velocity [178].
- Pressure control of the continuous phase and pressure control of the dispersed phase. This set up is not commonly used. Contrary to the flow rate/flow rate case, in which the flow rate of the dispersed phase does not modify strongly the volume of the produced drop [177], the volume of the produced droplets depends strongly on pressure of the dispersed phase [177].

Finally, except for the pulsated flow induced by syringe pumps [179], the effect of the type of sources used to impose the inlet conditions is rarely discussed.

6.1.2 Toward the steady state

Depending on the inlet values of the imposed pressure or flow rate, a transitory regime of bubble production may occur before reaching the steady state.

First, in flow-focusing devices, when starting from a channel free of bubbles, the bubble size and formation frequency quickly stabilize to a constant value after oscillating [169]. Similarly, after each change in the inlet conditions, it is also necessary to wait for the system to recover a steady bubbling regime [154]. Such effects might even result in periodic complex flows exhibiting bubbles rearrangement and alternate structures [180].

After stabilization, the structure of the flow depends on the relative importance of the pressure in each phases. This leads to the production of monodisperse or bidisperse bubbles which can arrange in different fashion [114], or to complex periodic behaviors in more complicated geometries [181]. The destabilization only occurs when the two inlet pressures are too different from each other, which lead to no-bubble production, or to the co-flow of the two phases [150]. Literature results also underline that particular steady regimes of bubble production are harder to obtain when the viscosity contrast between the dispersed and continuous phase is large [182, 183].

Finally, to our knowledge, the destabilization of bubble production until the break down of the bubble formation regime is only described for pressure driven Newtonian trains of plugs [170].

6.2 Regulation

As we already mention, for very viscous fluids (or yield-stress fluids) and gas, the large contrast in viscosity between the dispersed and the continuous phase results in an instability of bubble production when the dispersed phase is driven at constant pressure, and the continuous phase flow rate is imposed. To counterbalance this effect we try different control methods of the dispersed phase (gas), which results are detailed in this section.

6.2.1 Flow-rate control

Since the destabilization of bubble production is both due to the effect of the high viscosity contrast between the phases and the pressure control, we first replace the later by a flow rate control. In this section we present the results obtained when the yield-stress fluid is driven at constant flow rate, and the gas flow rate is also controlled. First we consider the control of the gas flow rate with a syringe pump, and then with a mass flow controller.

6.2.1.1 Syringe pump

We use two Harvard Apparatus syringe pumps, for both gas and yield-stress fluid flow-rate control. They control the syringe piston speed to impose the target flow rate. In that case, a single operating regime is observed, independently of the ratio of the imposed flow rates. Pictures of an experiment are presented on figure 6.1. Qualitatively, we can immediately observe that there is no bubble production.

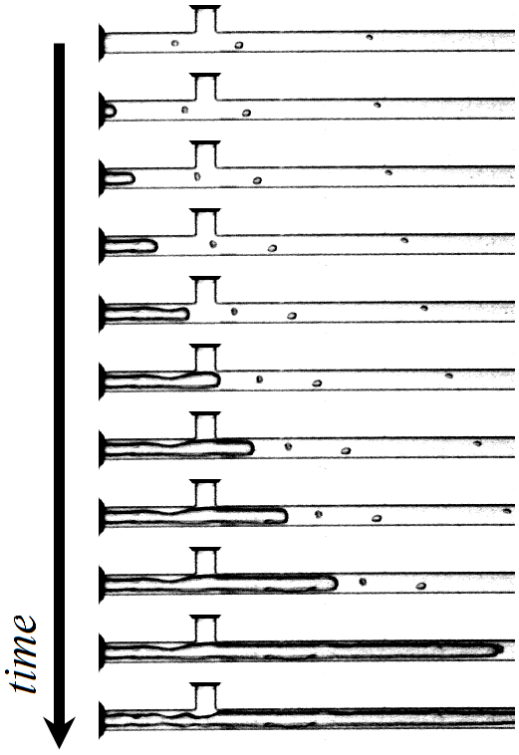

Figure 6.1 – Pictures of the regime observed when the yield-stress fluid ($Q = 0.2$ ml/min), and gas flow rate ($Q_g = 0.2$ ml/min) are imposed using syringe pumps, for a channel with $R = 1$ mm, and for a carbopol gel ($\tau_y = 75$ Pa).

As seen on the first image of figure 6.1, the system is initially completely filled with yield-stress fluid. During this first stage, the gas meniscus is pushed backward inside the inlet channel by the yield-stress fluid flow. Indeed, during this step the gas is compressed in the syringe, and pressure builds up inside the gas finger until it attains the critical value associated with the yield-stress fluid flow at imposed flow rate. At this point, the meniscus starts to move toward the exit of the outlet channel. Then, as the gas finger advances, the hydrodynamic resistance of the channel decreases, thus leading to an increase in the meniscus velocity. Finally since, the pressure inside the finger is large compared to the pressure necessary to form a bubble, and the hydrodynamic resistance decreases rapidly, the system ends up in co-flow (last image of figure 6.1). This occurs for both carbopol gels and emulsions. Therefore, due do gas compressibility, it is not possible to control the gas flow rate with a syringe

pump.

Modifying the ratio of the two imposed flow rates only changes the duration of the backward motion of the meniscus: the larger the target gas flow rate the faster the piston speed, and thus the shorter the time for the gas to be compressed and for the pressure to reach the critical pressure value associated with the yield-stress fluid flow. Finally, we emphasize that the response time of the system (and the duration of the regime) are lengthened by dead volumes (filled with gas) of the experimental set-up, for example the vanes connecting the syringe to the chip.

6.2.1.2 Mass flow controller

A well-suited method to control the gas flow rate consists in using a mass flow controller. We use a thermal mass flow controller (BRONKHORST France S.A.S.), which measures the thermal dissipation induced by the flow. It features heating elements, and thermal sensors to send the information to a control valve which adjusts the flow rate according to the target value. The yield-stress fluid flow rate is imposed using a syringe pump. Similarly to the previous case we observe a unique regime, with the production of few bubbles (figure 6.2).

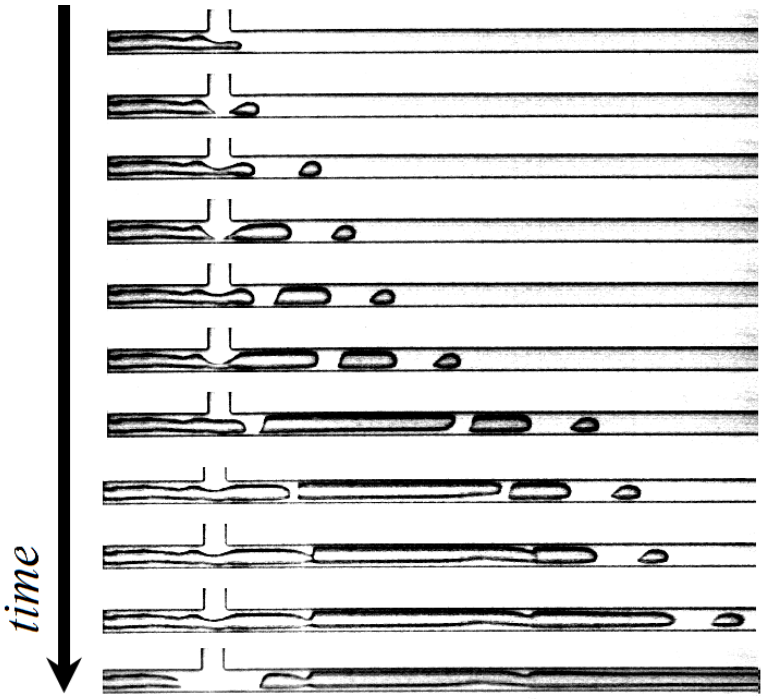

Figure 6.2 – Pictures of the regime observed when the yield-stress fluid volume flow rate ($Q = 0.1$ ml/min), and the gas mass flow rate ($Q_g = 0.2$ ml/min) are imposed, for a channel with $R = 1$ mm, an for a carbopol gel ($\tau_y = 75$ Pa).

As explained in the previous section, gas is compressible, and thus the pressure builds up inside the gas finger until it overcomes the necessary pressure to form the first bubble (first image on figure 6.2). Contrary to the previous case, the obtained pressure value allows to produce few bubbles. Each produced bubble decreases the hydrodynamic resistance of the outlet channel thus leading the production of larger and larger bubbles.

As the bubbles' volume increase, and they accelerate due to the hydrodynamic resistance drop, the plugs of yield-stress fluids separating consecutive bubble may rupture, thus leading to coalescences. When all bubbles have coalesced (last image on 6.2), the pressure inside the gas finger decreases below the critical pressure necessary to form a bubble, and the outlet channel is again filled with yield-stress

fluid. Finally, the pressure starts anew to build up inside the finger and the whole process restarts from the beginning. We can emphasize the role of dead volumes during this process. They are gas pockets which must be compressed before reaching the critical pressure associated with the yield-stress fluid flow. Due to the configuration of our device (particularly because of the volume between the controller and the junction) we always have quite large dead gas volumes. Therefore we cannot use the mass flow controller in optimal conditions.

As shown by the two previous examples, the flow rate control is difficult to achieve for gas, due to gas compressibility and the difficulty to have negligible dead volume in millimeter scale geometries, thus it is mostly unable to face the issue of the pressure increase/decrease associated with the rapid variations of hydrodynamic resistance inside the outlet channel due to bubble production which creates a complex feedback mechanism on the pressure inside the gas pockets. For flow rate control, achieving a steady bubble production would probably be possible by minimizing dead volumes and using non-return valves. We can also think of adapting the geometry (i.e. the length of the channel) in order to synchronize the different mentioned effects. Yet, we did not have enough time to test this idea during this thesis.

6.2.2 Pressure control

In this section we consider the system described in chapter 5 (i.e. imposed yield-stress fluid flow rate and imposed gas pressure). We have shown that the destabilization of bubble production when driven at constant pressure is due to a decrease in hydrodynamic resistance, and that a simple numerical model taking only this effect into account leads to a divergence in bubble size. However, this model can also be used to compute the theoretical pressure value to apply to the system to keep the size of the produced bubble constant.

6.2.2.1 Numerical model

Using the afore-mentioned model, it is possible to compute the theoretical value of the pressure adjustment needed to maintain the total flow rate constant (thus leading to steady bubble production). This can be easily achieved by imposing that the total flow rate is kept constant during the simulation and compute the corresponding pressure value at each time step, this yields the condition: $Q_{tot}^{(i)} = Q_{tot}^{(i+1)}$, where (i) and $(i+1)$ represent two successive time steps. An example of the computed pressure variation is shown on figure 6.3. However, it is difficult in practice to use such regulation curves which require very sensible pressure controller over a wide range of values.

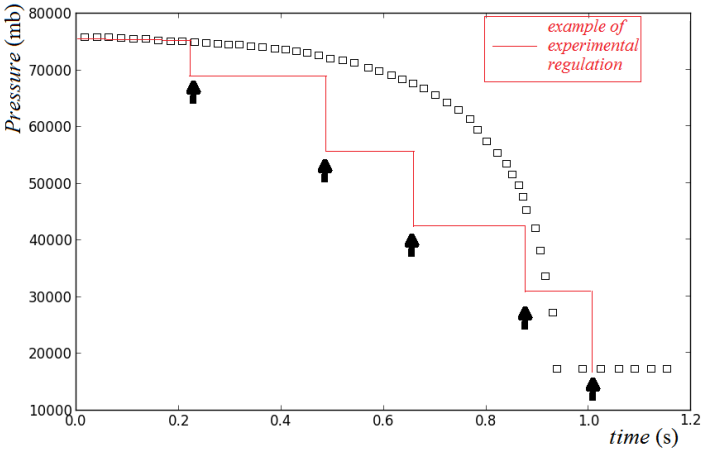

Figure 6.3 – Example of the computed pressure values (under the hypothesis detailed in chapter 5) necessary to keep the hydrodynamic resistance constant as bubbles are produced. $Q = 0.1$ ml/min, $\Delta P = 0.75$ bar, $\tau_y = 200$ Pa, $k = 79$ Pa.s^n, $n = 0.25$. The line shows an example of manual regulation.

6.2.2.2 Experiments

To test this principle, we the pressure in steps of a few millibars during the transient filling of the outlet channel with bubbles until their size become uniform. This process is shown on figure 6.4. At the beginning, the channel is completely filled with yield-stress fluid, then the pressure is progressively decreased to compensate for the hydrodynamic resistance drop associated with bubble production. Finally, iterating enough this process leads to an almost uniform bubble size, and therefore a constant flow rate and pressure drop. In this state, the system can produce bubbles without destabilizing for hours. However, the experimental values of the pressure are generally much smaller in experiments than what is predicted by the model. Besides the number of bubbles predicted by the model is generally much larger than what is observed.

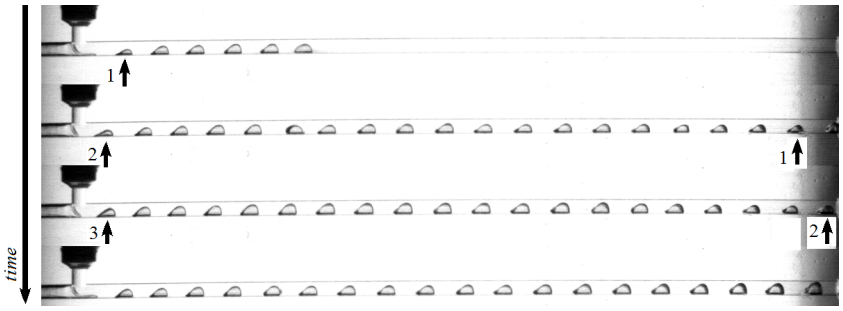

Figure 6.4 – Pictures of the transient filling and regulation process. For emulsion ($\tau_y = 100$ Pa) and a flow rate $Q = 0.05$ ml/min. The pressure is varied between $\Delta P = 235$ mbar (first image) ans 210 mbar (last image).

The black arrows on figures 6.4 and 6.3 points to the first produced bubbles after the pressure decrease. The different pressure drops before reaching the steady state are numbered (next to each arrow), and allow to follow the evolution of the corresponding bubble during the flow along the channel. As expected, when the pressure is decreased, the size of the next bubble is smaller than the preceding (arrow 1,2,3), but note that, as a bubble advances in the channel its sizes increases. This effect is associated with the large pressure drop associated with the flow and the decompression of the gas forming the bubbles (detailed in annex on bubbles' shape). The typical temporal evolution of bubble production once the steady regime is attained is shown on figure 6.5. During the steady regime, the size of successive bubbles, and the velocity of the whole two-phase flow are constant. The observation of straight lines (i.e. that the velocities of bubble are constant) on the spatiotemporal diagram of figure 6.5 shows the strong regularity of the this regime. These steady regimes of bubble production are analyzed in the next section.

Influence of the applied pressure

The yield-stress fluid flow rate is varied between 0.025 ml/min and 0.1 ml/min. For each flow rate the system is stabilized using the method described above. Once the regime is steady, the gas pressure is slightly increased. If the increase in pressure is sufficiently small (a few mbar) the system stabilizes again, and another steady state is reached. Pictures of steady states obtained for $Q = 0.1$ ml/min for different values of the gas pressure are shown on figure 6.6. For pressure between 339 and 341 mbar, bubbles are mostly trapped at the wall, whereas they exhibit an axisymmetric shape for higher pressure values.

Comments on bubbles' shape

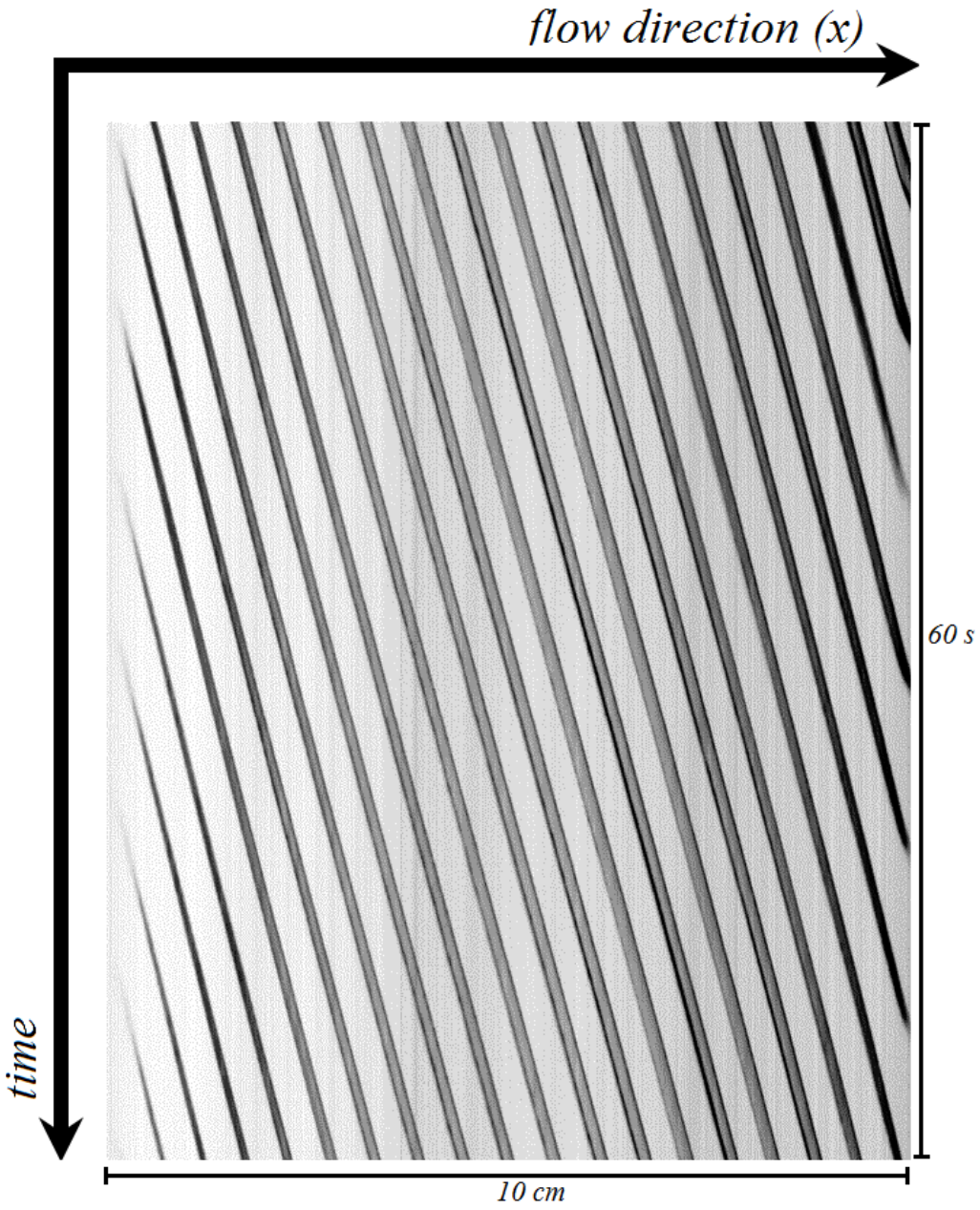

Figure 6.5 – Typical spatiotemporal diagram to illustrate the steadiness of bubble production during the steady regime when the gas is driven at constant pressure (210 mbar), for emulsion ($\tau_y = 100$ Pa) at a flow rate of $Q = 0.05$ ml/min in a channel of radius $R = 1$ mm. Dark and bright area corresponds to gas and yield stress fluid respectively.

This above mentioned effect is associated with the stress state of the material, as the flow accelerates the size of the liquid region where the stress is above the yield stress increases, which promotes the dynamics associated with surface tension, such as deposition (chapter 3). The Bingham number and mean velocity of the flow v_m corresponding to each image shown on figure 6.6 is given on table 6.1.

The value of the Bingham number computed during the experiments shown on figure 6.6 are always greater than 1. This is consistent with what was observed in unsteady regimes. Indeed as the velocity of the flow increases, the Bingham number decreases and bubbles' shape first become axisymmetric, and then elongates until the deposited film attains its limiting size when $Bi < 1$ (chapter 3). Also

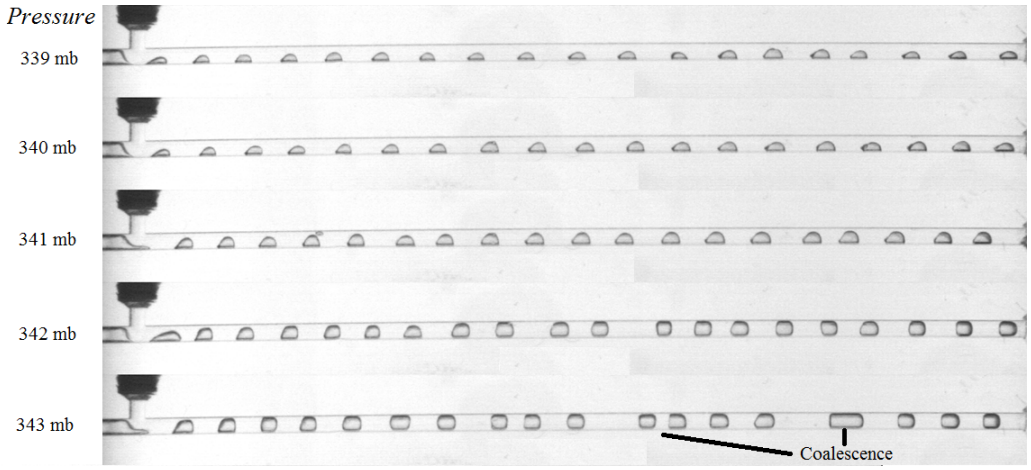

Figure 6.6 – Pictures of the steady states obtained at different pressure value for a yield-stress fluid flow rate $Q = 0.1$ ml/min. Emulsion ($\tau_y = 100$ Pa) is injected at a flow rate of $Q = 0.05$ ml/min in a channel of radius $R = 1$ mm.

Pressure (mbar)	v_m (mm/s)	Bi
339	0.792	1.482
340	0.797	1.487
341	0.92	1.38
342	1.08	1.27
343	1.13	1.24

Table 6.1 – Summary of the parameters associated with steady states presented on figure 6.6.

note that, for $Bi > 1$ the dynamics of the flow reduces to full slip. Therefore the viscous stress can be neglected with respect to the yield stress, and the shape of bubbles should be predicted by a balance between surface tension and the yield stress.

Comments on bubbles' dynamics

As qualitatively seen on figure 6.6, for the first three cases the bubble-to-bubble distance is almost constant. However, when the flow velocity is larger the distance between successive bubbles tends to change during the flow: some bubbles move faster than others. To quantify this effect, we plot the standard deviation of the bubble-to-bubble distance as a function of the mean velocity of the flow on figure 6.7.

The standard deviation increases rapidly with the velocity. We also report that the coalescence of bubbles is observed for the two larger pressure values. The increase in standard deviation, and coalescences, occurs when the Bingham number decreases to approach 1, corresponding to regimes that become less stable since the size of the sheared region increases, and the flow profile becomes more and more Poiseuille-like.

We also report that it is difficult to stabilize the flow at higher flow rate (i.e. $Q > 0.1$ ml/min) of yield -stress fluid, that is when the Bingham number approaches 1. Indeed, at large gas pressure (i.e. for $Bi < 1$), and flow rates, the break-up mechanism could be more perturbed by the interface dynamics, since the size of the solid-like region of the flow decreases when applied stress increases.

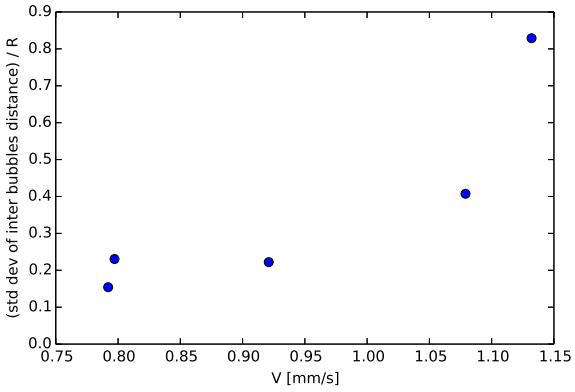

Figure 6.7 – Standard deviation of bubble-to-bubble distance normalized by the tube radius of the channel as a function of the whole flow mean velocity.

6.2.3 Pulsated flow

In this section we recall the most common method to obtain pulsated flows in microfluidics devices, and show that, for our set-up steady states can be achieved using a peristaltic pump.

6.2.3.1 Introduction

Another common type of flow encountered in microfluidic is pulsated flow. These are common when generating bubbles or droplets by external actuation [150]. Periodically-driven actuators can produce highly controlled resonance phenomena which leads to a wide range of behavior in microfluidic system [184].

One of the most common way to impose pulsated flows without requiring actuation and active control is to use a peristaltic pump. The principle of peristaltic pump lies on the periodic compression of a deformable tubing by an actuator. In most peristaltic pumps the actuators are rollers fixed to a rotating cylinder (figure 6.8a) which speed can be varied to achieve the desired flow rate.

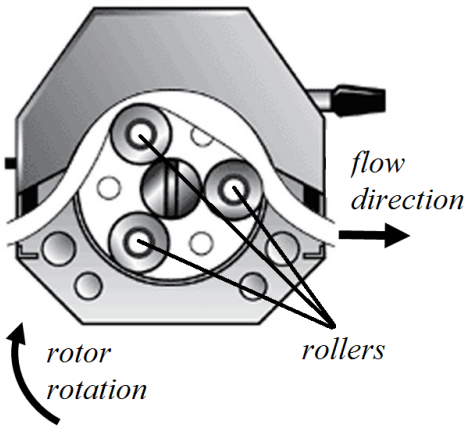

(a) Sketch of a peristaltic pump [1].

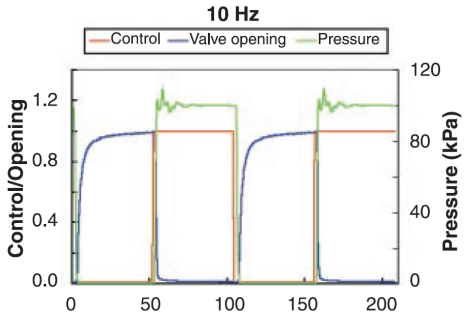

(b) Typical temporal evolution of the pressure applied by a peristaltic pump from [185].

Figure 6.8 – Characteristics of a peristaltic pump.

[1] adapted from http://www.coleparmer.com

Miniaturized peristaltic pumps are also common in microfluidic: such pumps can be manufactured by soft lithography and integrated on lab-on-chip devices [185]. The typical pressure applied by such peristaltic pumps is shown on figure 6.8b.

6.2.3.2 Experiments

In this section, we use a peristaltic pump (Cole-Parmer Masterflex 77202-60; tubing 13) to drive the gas, while the yield-stress fluid flow rate is imposed by a syringe pump. We report that steady regimes are achieved with this set-up for outlet channel length of 5 cm only. This is probably due to the operating pressure of the pump which may be too small for the large hydrodynamic resistance associated with longer channels. The start up of the steady regime is shown on figure 6.9.

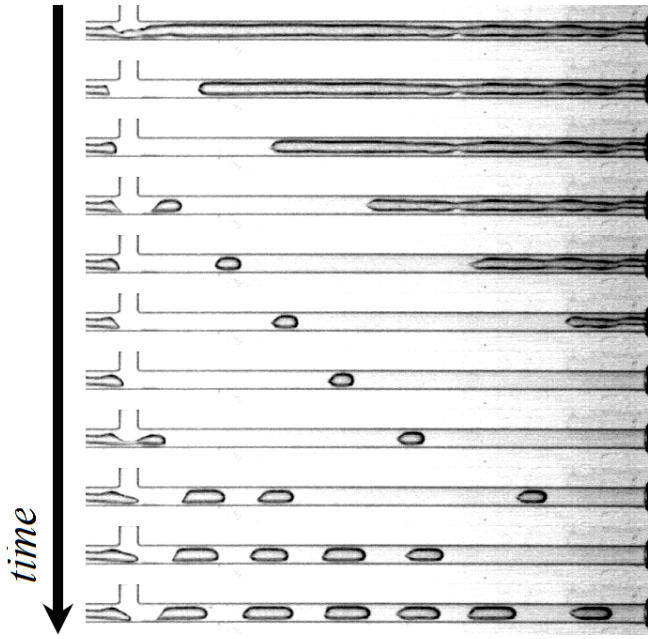

Figure 6.9 – Pictures of the transitory regime leading to steady bubble production for $Q = 0.4$ ml/min, and $Q_g = 0.3$ ml/min, for carbopol gel ($\tau_y = 75$ Pa) and a channel of radius 1 mm and length 5 cm.

The first image of figure 6.9 shows the initial state of the system: the gas and the yield-stress fluid flow side by side. Then, the yield-stress fluid starts to invade the channel and blocks the gas flow, indeed during this stage the pressure increases inside the gas finger. The pressure necessary to form a bubble is quickly overcome, and a bubble forms while the filling of the channel continues, which increases the hydrodynamic resistance of the system. In addition, due to the bubble production, the pressure decreases inside the gas finger and thus takes some time to increase again to the required value to produce the next bubble. At this point, a regular bubble production starts and a steady regime is quickly attained. During this transient filling by bubbles, it seems that for each bubble produced the decrease in pressure inside the gas thread compensates quickly the decrease in hydrodynamic resistance of the outlet channel.

Finally, note that the peristaltic pump also has a non-return mechanism (i.e. the tube pinching). Therefore, only a finite volume of gas is supplied at each revolution, and the system quickly self-regulates. These features may possibly counteracts the divergence effect and thus increases the stability of the steady regimes.

A spatiotemporal diagram of bubble production is shown on figure 6.10. The waves of the stripes are associated with the cycles of the peristaltic pump. We emphasize that the steady regimes obtained

with this set up are very stable.

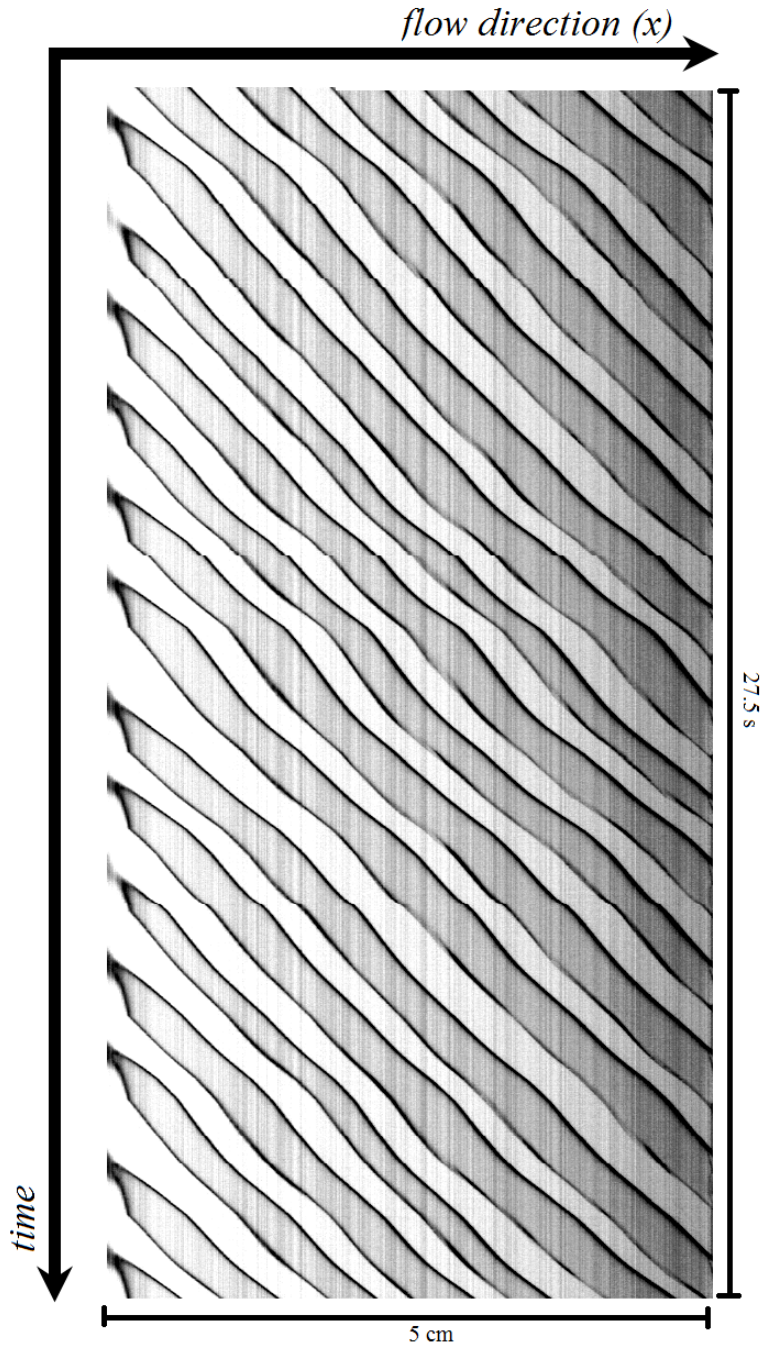

Figure 6.10 – Typical spatiotemporal diagram of bubble production during the steady regime when the gas is driven with a peristaltic pump at $Q_g = 0.35$ ml/min. Dark and bright area corresponds to gas and yield-stress fluid (carbopol $\tau_y = 75$ Pa) respectively.

6.3 Characterization of the steady states

In this section, we give a characterization of the steady state obtained either by pressure control or with a peristaltic pump. For both methods, we focus particularly on the attainable gas volume fractions, and production frequency.

6.3.1 Pressure control

We first characterize the steady regimes obtained by pressure regulation. The results presented in this section are most of the time obtained for emulsions, but same observations are true of carbopol gels.

6.3.1.1 Gas volume fraction

The apparent gas volume fraction is measured using a combination of manual thresholding and automatic detection [2]. Denoting $\mathcal{A}_b^{(i)}$ the area of the i-th bubble on an image, and n_b the total number of bubbles, we compute the surface fraction ϕ_s of gas:

$$\phi_s = \frac{1}{2LR} \sum_{i=1}^{n_b} \mathcal{A}_b^{(i)} \tag{6.1}$$

Wherein R is the radius of the channel, and L its length. For non axisymmetric bubbles equation 6.1 introduce an error on the volume fraction values, however this error is probably quite small for bubbles with heights of the order of the radius of the channel, as detailed in the annex concerning bubbles' shape. Therefore, we assimilate ϕ_s to the true gas volume fraction. The obtained values of ϕ_s are plotted, as a function of the applied pressure for different flow rate on figure 6.11. ϕ_s is extremely sensible to the applied pressure for the range of flow rate we have explored. In addition, when the gas pressure is imposed, we do not succeed in attaining gas volume fraction larger than 0.5.

Comparing carbopol gel to emulsion (for the same imposed flow rate), as seen on figure 6.11, the same volume fraction is attained for different values of the imposed pressure pressure. This difference is attributed to the yield stress, which is lower for the carbopol gel, and therefore the required pressure to drive the flow is also lower than for the emulsion.

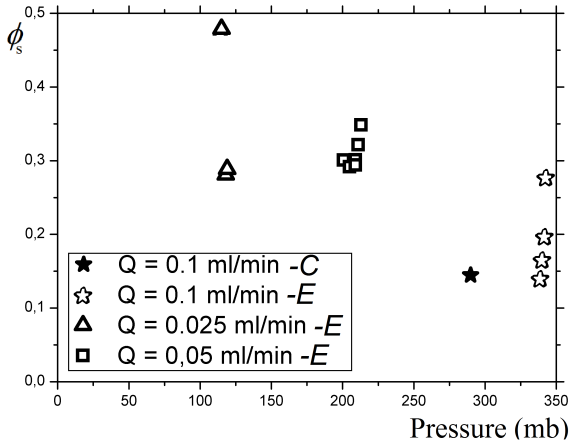

Figure 6.11 – ϕ_s as a function of the applied pressure for different values of the applied flow rate for emulsions (E, 100 Pa) and carbopol gel (C, 75 Pa), with $R = 1$ mm and $L = 10$ cm.

For the larger values of ϕ_s the hydrodynamic resistance of the channel is small compared to its value at lower ϕ_s, thus the flow becomes extremely sensible to perturbations and destabilizes easily. These perturbations may originates from multiple sources, such as pressure fluctuations, local inhomogeneity of the yield-stress fluid, and/or of the stress state of the system due to boundary conditions, and/or the approach of yielding [93, 95].

[2] Using ImageJ http://imagej.nih.gov/ij/

Volume fraction computation from mass conservation

We now compare the experimental results presented in the previous section to what is predicted by the mass conservation for a two-phase flow. Denoting Q_g the gas flow rate, Q the yield-stress fluid flow rate, and $Q_{tot} = Q + Q_g$ the total flow rate of the two-phase flow, the true gas volume fraction ϕ_g at the pressure ΔP is defined by:

$$\phi_g = \frac{Q_g}{Q_{tot}} = \frac{Q_g}{Q + Q_g} \tag{6.2}$$

which leads to:

$$Q_g = \frac{\phi_g Q}{1 - \phi_g} \tag{6.3}$$

Combining equations 6.2 and 6.3, we obtain the following expression for $Q_{tot} = v_m \pi R^2$, where v_m is the mean velocity of the flow:

$$v_m = \frac{Q}{\pi R^2} \frac{1}{1 - \phi_g} \tag{6.4}$$

Considering that $\phi_s \simeq \phi_g$, on figure 6.12, the experimental results of figure 6.11 are plotted as a function of Bi and compared to equation 6.4. The velocity v_m is measured independently of ϕ_s and used to build the Bingham number. Since we use STL manufactured devices, there is wall slip, and the Bingham number is built using the effective viscous stresses determined by capillary rheometry and the bulk yield stress of the material (see chapter 2).

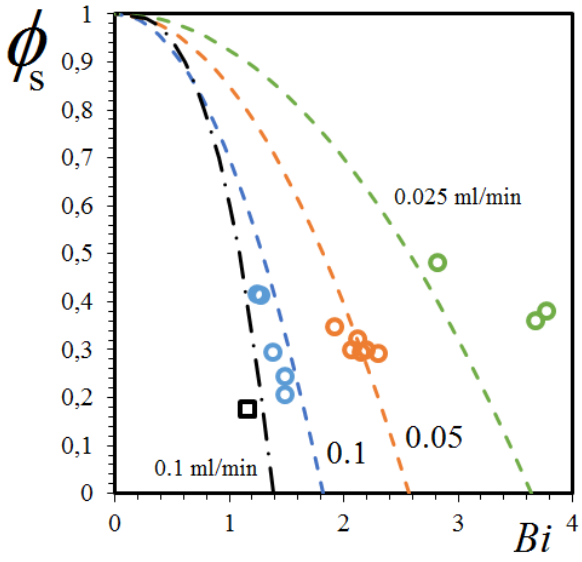

Figure 6.12 – Gas volume fraction as a function of the Bingham number built on v_m and computed from equation 6.4 for each value of the flow rate (dashed lines: emulsion; dashed-dotted line carbopol), and the experimental results of figure 6.11 (square: carbopol gel; circles: emulsions; channel with $R =$ 1 mm and $L = 10$ cm).

Except for $Q = 0.025$ ml/min, the agreement between the experimental results and the prediction from mass conservation are in good agreement. Interestingly, it predicts that for a given Bingham

number (but not the same rheometrical parameters), the gas volume fraction is not the same for two different fluids injected at the same flow rate. This result also shows that, the larger the yield-stress fluid flow rate, the steeper the curve linking the Bingham number to the gas volume fraction, which suggests that the system tends to become more and more sensible as the continuous phase flow rate is increased, and may explained the experimental difficulty encountered when trying to stabilize the system for $Q > 0.1$ ml/min.

6.3.1.2 Bubble formation time

In this section we characterize the bubble formation time during the steady regimes and compare it to the limit value derived in chapter 4. To quantify the break-up mechanism on a large amount of bubbles, two different methods are used. The first uses fast Fourier transform and allows to measure the different frequencies of the system. The second is a simple image processing technique that allows to obtain the break-up time for each produced bubbles.

Data processing

As in chapter 4, the first step consists in producing a spatiotemporal diagram of bubble production. Therefore we choose a line, as indicated by the dashed arrow (Z), taken perpendicular to the outlet channel and positioned at the middle of the junction on figure 6.13.

Figure 6.13 – An image taken during bubble formation in a steady state for $R = 1$ mm.

Then, we retrieve the grey level of each image constituting the movie along this particular line. The resulting pixels are stacked side by side to form a new image: the spatiotemporal diagram. A portion of the resulting spatiotemporal diagram is shown on figure 6.14 after post-treatment using predefined ImageJ binary operations and thresholding.

Figure 6.14 – Portion of a spatiotemporal diagram of bubble production (five bubbles). The cyan dashed line is used to obtain the signal values. Black and white area correspond to gas and yield-stress fluid respectively. The maximum height of the gas thread is 500 μm, each period lasts $\simeq 11.5$ s.

Finally to obtain the signal corresponding to bubble production and time to form a bubble t_b, we retrieve the value of the pixel of image 6.14 along a line positioned as close to the channel wall as possible. Since the gas meniscus advances asymmetrically inside the junction, this ensures the capture of the whole dynamic of the break-up process. An example of the retrieved values in case of pressure regulation is plotted on figure 6.15.

The signal shown on figure 6.15 is processed by FFT [3], or using a script to count the formation time of each bubble.

[3] Scipy, http://www.scipy.org/

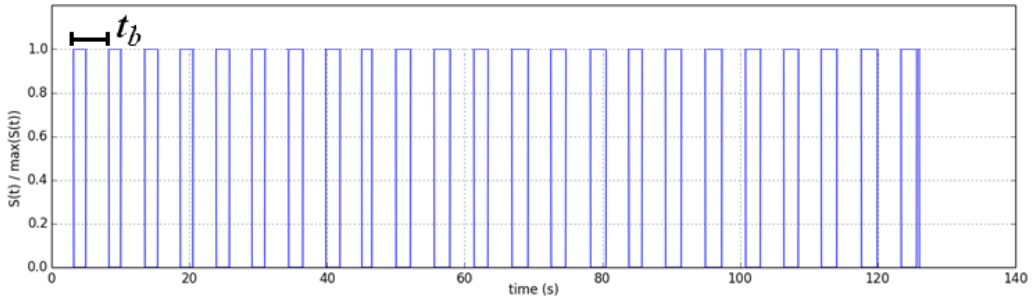

Figure 6.15 – Portion of a square wave obtained after the afore-mentioned processing for a steady flow at imposed pressure ($Q = 0.1$ ml/min, pressure 341 mbar). The value 1 corresponds to the the presence of yield-stress fluid inside the junction, and 0 to the presence of gas.

Discrete Fourier Transform

The frequency spectrum (obtained by FFT) of the signal shown on figure 6.15, is presented on figure 6.16.

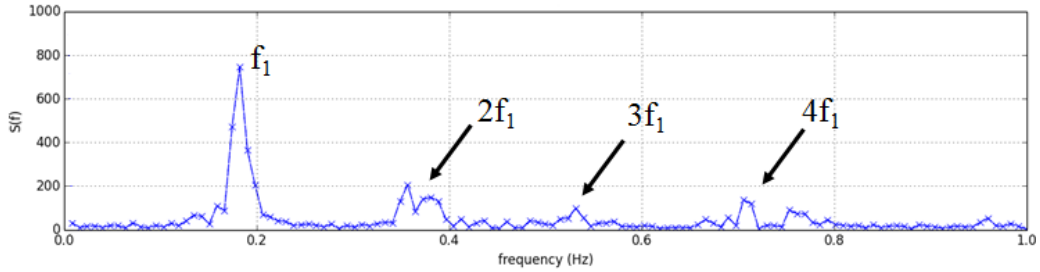

Figure 6.16 – Fourier transform of the signal shown on figure 6.15 by FFT. The first peak corresponds to the fundamental frequency (f_1), and the others to its harmonics.

The signal presented on figure 6.16 is typical of what is observed for pressure regulation: the frequency of bubble production is very well defined, and no other frequency appear. This suggests that, for the range of pressure/flow rate explored, the pressure controlled regimes are naturally well regulated albeit difficult to stabilize for $Bi < 1$.

Histograms

Another way to process the signal of figure 6.15 is to simply count the duration of each bubble formation events (t_b), and plot an histogram of the obtained time distribution. A typical distribution obtained from such treatments is shown on figure 6.17a. The time distribution are computed on few minutes of an experiment. Each distribution is fitted by a Gaussian function.

To further quantify the dispersion of data, the relative standard deviation $\%RSD = \frac{\sigma_{std}}{\bar{t_b}}$, where σ_{std} is the standard deviation of the Gaussian fit, and $\bar{t_b}$ its mean value, is summarized in figure 6.17b. For the investigated range of flow rates and pressure, $\%RSD < 10$. This result suggests that the break up mechanism in steady regime, is robust and not too much perturbed my the hydrodynamic feedback for moderate volume fraction. The results for $Q = 0.025$ ml/min, are not shown in figure 6.17b, because of their very poor stability. In such case, even if the regime is stable for tenth of minutes, the flow is so slow that it corresponds to the production of only few bubbles (i.e. not a sufficient number for a statistical treatment).

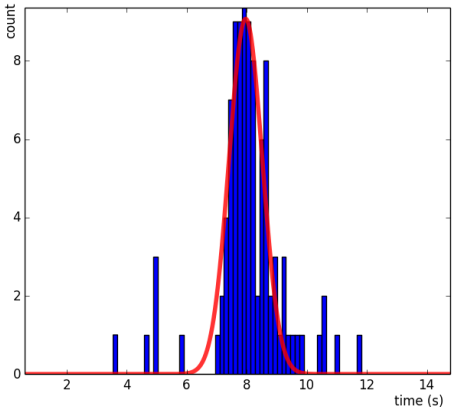

(a) Typical distribution of bubble formation time, and best Gaussian fit (red line) for $Q = 0.1$ ml/min and $\Delta P = 339$ mbar and a channel with $R = 1$ mm and $L = 10$ cm.

Q (ml/min)	Pressure (mbar)	$\%RSD$
0.1	339	8.3
0.1	340	5.8
0.1	341	2.3
0.1	342	3.5
0.1	343	3.1
0.05	205	4.0
0.05	209	4.6
0.05	211	4.9

(b) Summary of the relative standard deviation for steady states obtained for imposed gas pressure.

Figure 6.17 – Distribution of bubble formation time for emulsions $\tau_y = 100$ Pa in a T-junction with $R = 1$ mm and $L = 10$ cm.

Comparison

The mean of the Gaussian fit is compared to the fundamental frequency obtained by FFT on figure 6.18 for two different yield-stress fluid flow rates and several imposed pressure. The results obtained by the two methods are in excellent agreement, therefore in the following we use one value or the other indifferently.

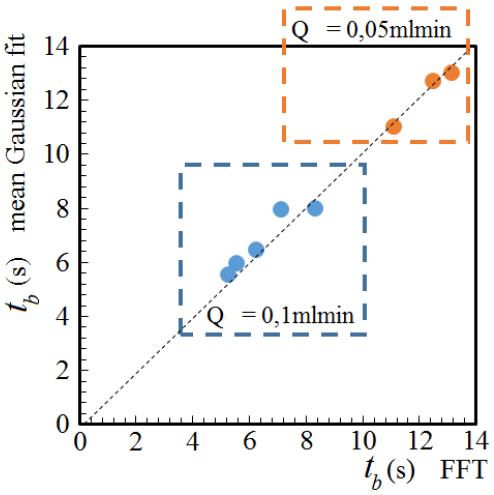

Figure 6.18 – Comparison of the bubble formation time computed by the two afore-mentioned method for two flow rates and different applied pressures. For emulsions ($\tau_y = 100$ Pa) in a T-junction with $R = 1$ mm, $L = 10$ cm.

Limiting bubble formation frequency

The data gathered from the distribution obtained at imposed pressure are compared to the limiting

bubble frequency $\frac{\Omega}{Q}$ derived in chapter 4, on figure 6.19 for two different imposed flow rates. The Gaussian distributions are normalized so that the area of each one is equal to 1. As expected, the measured bubble frequency is lower than $\frac{\Omega}{Q}$. Even if the curves are not perfectly well ordered, the limiting value is approached as the gas pressure is increased for a given value of the yield-stress fluid flow rate. This suggests that the explanation of the geometrical break-up of the bubbles monitored by the imposed flow rate of yield-stress fluid holds in steady regimes and provides the limit frequency of bubble production (see also figures 4.8, and 4.10 in chapter 4).

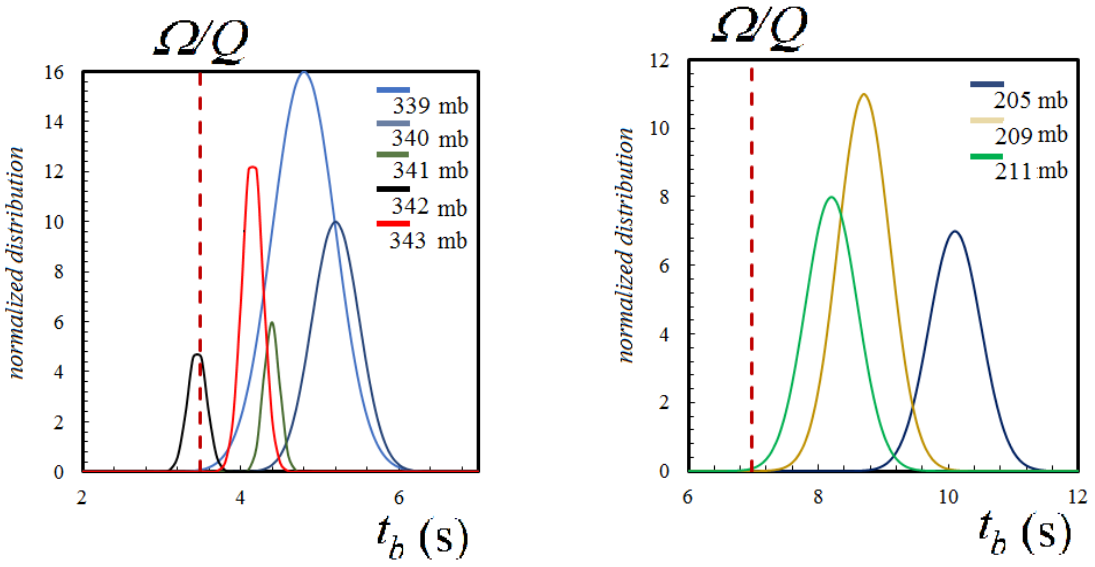

(a) For $Q = 0.1$ ml/min.

(b) For $Q = 0.05$ ml/min.

Figure 6.19 – Normalized distribution of bubble formation time and limiting value (vertical dashed lines) for emulsions ($\tau_y = 75$ Pa) for different values of the yield-stress fluid flow rate in a channel with $R = 1$ mm.

6.3.2 Pulsated flow

In this section, we analyze the results of steady regimes obtained when driving the gas with a peristaltic pump. Similarly to what is done in the previous section, we first present the obtained gas volume fraction, and then the frequencies of bubble formation. Pictures of the regime obtained for carbopol gels are presented on figure 6.20 for different values of Q_g. As seen on figure 6.20, bubbles are mostly axisymmetric, and their size varies reasonably.

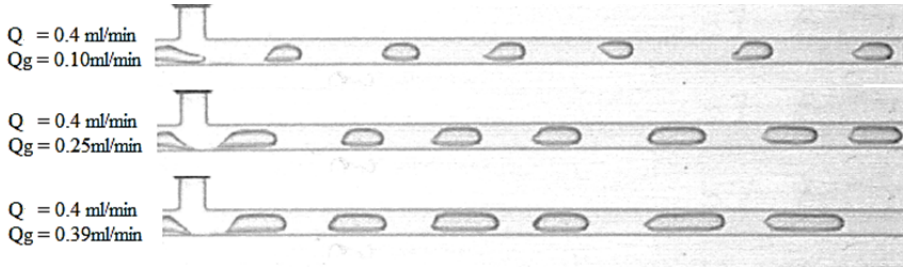

Figure 6.20 – Pictures of the steady regimes obtained with a peristaltic pump for carbopol gel ($\tau_y = 75$ Pa). The imposed flow rate are given on the left.

Typical picture of regimes obtained at $\frac{Q_g}{Q} > 1$ for emulsions are presented on figure 6.21. Since bubbles tend to coalesce in the channel, their size is quite polydisperse.

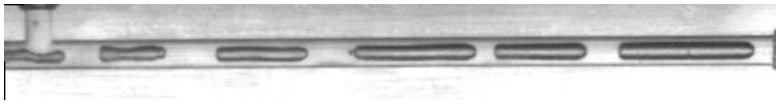

Figure 6.21 – Pictures of the steady regimes obtained with a peristaltic pump for emulsions and $\frac{Q_g}{Q} \simeq 3$.

The experiments presented in the next paragraphs are performed for a yield-stress fluid flow rate $Q = 0.4$ ml/min and different imposed gas flow rates (Q_g) between 0.1 ml/min and 0.39 ml/min for carbopol gels. For emulsions, experiments are performed for $Q < Q_g$, and $Q = 0.1$ ml/min. For these experiments, the Bingham number is typically less than 1, a regime which is not attained with pressure regulation. We report that, for both carbopol gel and emulsions, when $Q_g > Q$ the produced bubbles tend to coalesce during the channel flow, thus leading to the formation of polydisperse bubbles. The coalescence may be triggered by the pressure pulses of the pump. In addition, similarly to the pressure driven case, at large gas volume fraction the hydrodynamic resistance is lowered, thus the system is more sensible to pressure fluctuations, leading to coalescence. Despite its polydisperse character, this regime of bubble production is steady and leads to the formation yield-stress fluid foams (see last section of this chapter).

6.3.2.1 Gas volume fraction

The gas volume fraction is computed by assuming that the bubbles are axisymmetric. This seems reasonable on the basis of the shape observed on figures 6.20 and 6.21. This is mostly due to the large value of the yield-stress fluid flow rate that leads to typical values of $Bi < 1$ (minimum $Bi \simeq 0.7$). Indeed, as seen in chapter 3, when $Bi < 1$, the deposited film thickness tends to a constant value, and the bubbles become axisymmetric (see also chapter 5 for details on the shape transition). Therefore the gas volume fraction is given by:

$$\phi_g = \frac{1}{R^2 L} \sum_{i=1}^{n_b} R_i^2 L_i \tag{6.5}$$

wherein the index i corresponds to the i-th bubble inside the channel, and R and L the radius and length of the outlet channel. As in the previous section, we write mass conservation during the flow. Since the gas flow rate (Q_g) and the yield-stress fluid flow rate (Q) are imposed we can simply compute the theoretical volume fraction using equation 6.2. The experimental results for both carbopol gels and emulsions, and equation 6.2 are presented on figure 6.22. The error bars are between 15 and 20 % of the measured value of the volume fraction. These large values are due to the spatial resolution of the camera and correspond to an error of 2 pixels on the measurement of the bubbles' diameter.

The experiments are in good agreement with what is predicted by mass conservation for both carbopol gels and emulsions. Therefore, pulsated flow driven by a peristaltic pump allow to reach high gas volume fraction. These regimes are stable, but lead to polydisperse bubble production at large values of $\frac{Q_g}{Q}$. This effect may originates from the perturbations of the flow induced by the pressure pulses.

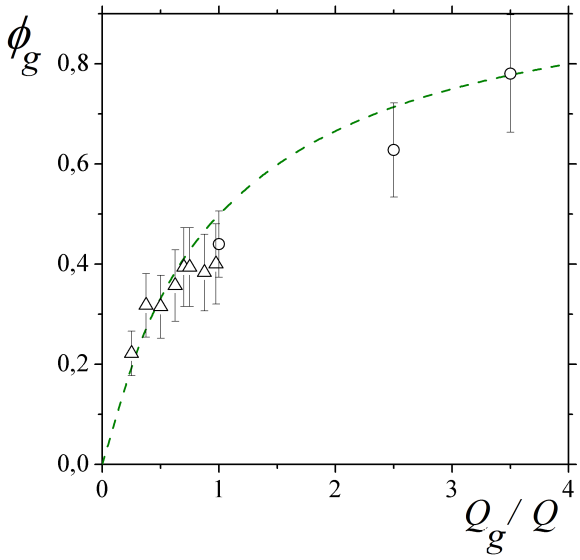

Figure 6.22 – Comparison between equation 6.2 (dashed line) and the experimental results for carbopol gels (triangles) and emulsions (circles).

6.3.2.2 Bubble formation time

As in the case of pressure control, we also analyze the formation time of each bubble, using both discrete Fourier transform and distributions.

Discrete Fourier Transform

The data are processed as explained in the previous section. A typical signal obtained when the gas is driven with peristaltic pump is shown on figure 6.23. As seen on figure 6.23 different frequencies appear. In the following, we show that the other frequencies than the one corresponding to the break-up mechanism are linked to the cycles of the pump.

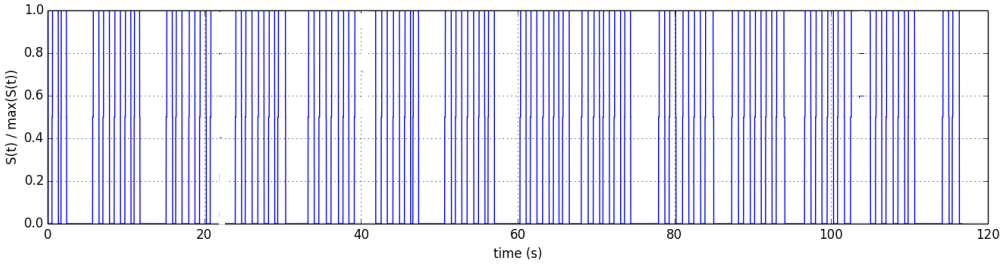

Figure 6.23 – Portion of a square wave obtained at imposed flow rate ($Q = 0.4$ ml/min, $Q_g = 0.1$ ml/min) for carbopol gel ($\tau_y = 75$ Pa). The value 1 corresponds to the the presence of yield-stress fluid inside the junction, and 0 to the presence of gas.

The typical frequency signal obtained from the square wave of figure 6.23 is shown on figure 6.24 in a semi-log graph. On all frequency signals we distinguish four (or three) different frequencies, denoted f_1^+, f_1^-, f_2 and f_3.

These different frequencies are plotted as a function of the gas flow rate for carbopol gel and $Q =$ 0.4 ml/min on figure 6.25.

As seen on figure 6.25, all these frequencies are below the limit frequency obtained in chapter 4.

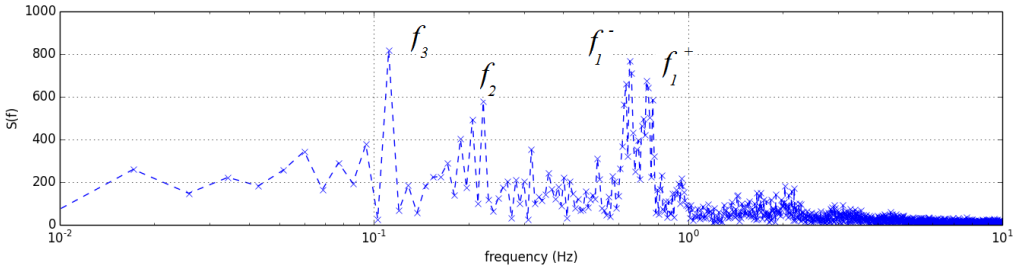

Figure 6.24 – Typical Fourier transform of the square waves with multiple frequencies. Different peaks appear ($Q = 0.4$ ml/min, $Q_g = 0.1$ ml/min).

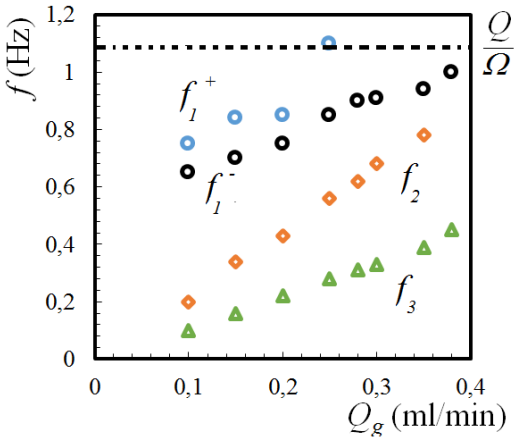

Figure 6.25 – Frequencies of the different peaks obtained by FFT processing as a function of the gas flow rate for carbopol gel ($\tau_y = 75$ Pa and $Q = 0.4$ ml/min). The horizontal line stands for limit frequency obtained in chapter 4.

We also note the following points: (i) $f_2 = 2f_3$, and both are proportional to the applied gas flow rate; (ii) f_1^+ and f_1^- also depends on the gas flow rate, but are not harmonics of each other, neither of f_2 or f_3. In addition f_1^+ increases rapidly until it reaches almost the limit frequency, then it seems to disappear of the frequency graphs. Also, the fact that these two frequencies are closer to the limit frequency than f_2, f_3 indicates that they are most likely the natural frequency of the system, whereas f_2 and f_3 are likely to be linked to the cycles of the pump. For our tubing with ($R = 400$ μm), the pump delivers 0.06 ml per complete rotation. The inner cylinder possess 4 rollers, therefore the volume between each of them is 0.02 ml. The theoretical frequency of the pump (f_p) for the values of the flow rate we have used is reported in table 6.2.

Q_g (ml/min)	f_p (Hz)
0.1	0.028
0.15	0.042
0.2	0.056
0.25	0.069
0.28	0.078
0.3	0.083
0.35	0.097
0.38	0.11

Table 6.2 – Theoretical frequency of the peristaltic pump.

f_3 is plotted as a function of the pump frequency (f_p) on figure 6.26. f_3 is 4 times larger than f_p. Since there are 4 rolls on the inner cylinder of the pump, the frequency of gas injection is $4f_p$, this shows that f_3 is the frequency of the injection of gas volumes by the peristaltic pump.

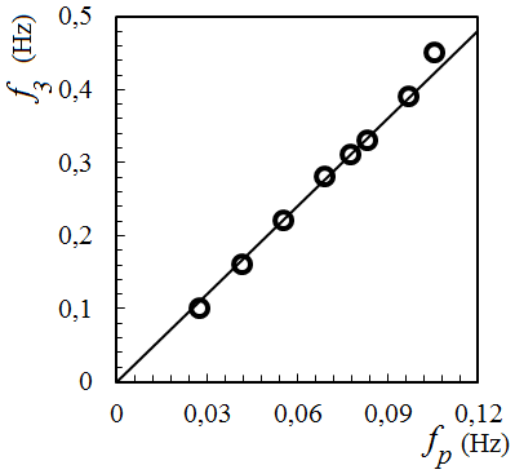

Figure 6.26 – f_3 as a function of f_p, the solid line indicate the line of equation $y = 4x$ for carbopol gel ($\tau_y = 75$ Pa) in a channel with $R = 1$ mm and $L = 5$ cm.

The fact that all frequencies depends on the gas flow rate confirms that a part of the time of bubble formation is linked to the motion of the meniscus interface. This was already observed in chapter 4, for imposed gas pressure.

Histograms

We also retrieved the distribution of bubble formation time by measuring each period on figure 6.23. A typical histogram obtained from such measurement is shown on figure 6.27. A very distinct peak corresponding to f_1^- appear. In addition, different smaller peaks (close to f_1^-) also appear, and a small tail is also visible at large times. As previously mentioned, except for f_1, all these frequencies are associated with the cycles of the pump. While not completely accurate, we also choose to represent this distribution by a Gaussian distribution, which is convenient way to model the data and allows to retrieve the mean and the standard deviation.

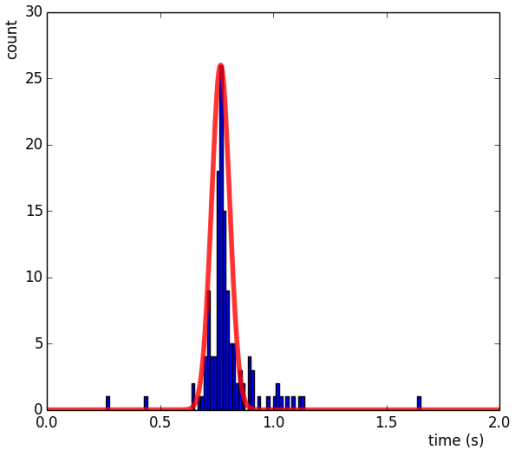

Figure 6.27 – Distribution of bubble formation time obtained for carbopol gel ($\tau_y = 75$ Pa) for $Q = 0.4$ ml/min and $Q_g = 0.15$ ml/min. The red line is the best Gaussian fit.

Comparison

The value of the mean of the fitted Gaussian function are compared to f_1^- and f_1^+ on figure 6.28. Both frequencies are close to the mean value, which confirms that they are related to the natural operating regime of the junction. However, the use of the peristaltic pump leads to two different frequencies for the lowest gas flow rates, albeit close to each other.

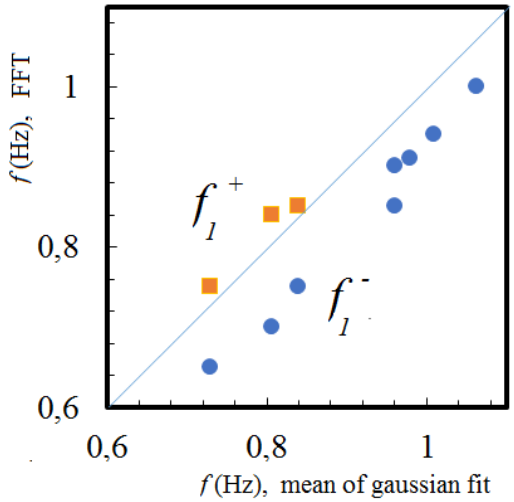

Figure 6.28 – Comparison between the frequency obtained from the mean value of the best Gaussian fit and f_1^- (circles) and f_1^+ (squares) for carbopol gel ($\tau_y = 75$ Pa) in a channel with $R = 1$ mm and $L = 5$ cm. The solid line indicates the slope $y = x$.

Limiting bubble production frequency

As already shown on figure 6.25, all frequencies are limited by $\frac{Q}{\omega}$. The normalized bubble formation time distributions are compared to this limiting bubble frequency on figure 6.29. This confirms that the limiting bubble frequency holds when the flow rates are large ($Bi < 1$), and for pulsated flows, which leads to steady states of bubble production.

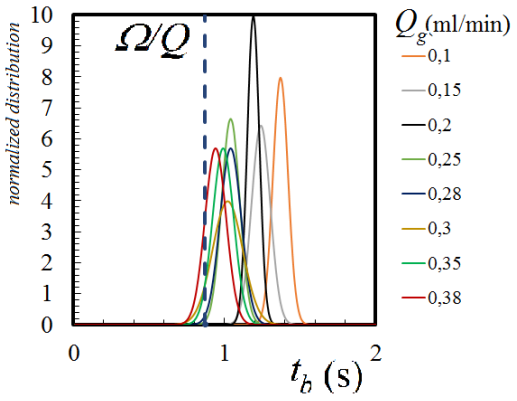

Figure 6.29 – Comparison between the normalized best Gaussian fit of the distribution for $Q = 0.4$ ml/min (carbopol gel with $\tau_y = 75$ Pa, in a channel with $R = 1$ mm and $L = 10$ cm), and the limiting bubble formation frequency.

6.4 Yield-stress fluid foams

As previously mentioned, using a peristaltic pump for $\frac{Q_g}{Q} > 1$ with emulsion allow the formation of yield-stress fluid foams. In this section, we report pictures of such foams, however their characterization remains to be done.

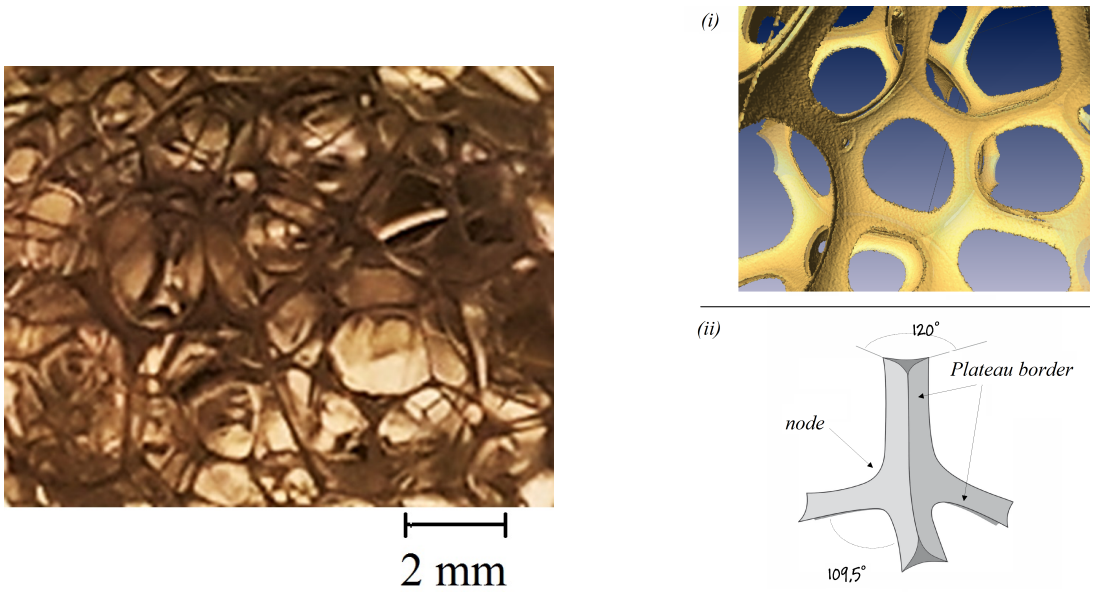

(a) Top view of the yield-stress fluid foam obtained with $Q = 0.1$ ml/min, and $Q_g = 0.25$ ml/min.

(b) Structure of a foam made of Newtonian fluid [67, 186].

Figure 6.30 – Comparison between a yield-stress fluid foam and a Newtonian foam.

The production of yield-stress fluid foams is only achieved for emulsions, this may be due to the absence of surfactant in the carbopol gel which prevents the stabilization of the thin soap films of the foam. A top view of the obtained foam with millimetric size bubbles is shown on figure 6.30a. Although our foam is quite polydisperse, we can distinguish the classical elements of foam structure: soap films, and Plateau borders which meet in four to form vertices in a Newtonian foam. A magnified picture of these elements for our emulsion foam is shown on figure 6.31. Figure 6.32 also shows a magnified picture of the emulsion foam, some structures seem irregular and of various sizes, which may be due to the yield-stress and the microstructure of the emulsions which may deform films, nodes, and plateau borders [2].

These results shows that the production of yield-stress fluid foams using millifluidic devices in a single step method is possible, thus opening routes for the scaled-up production of such foams (as introduced in annex on other geometries).

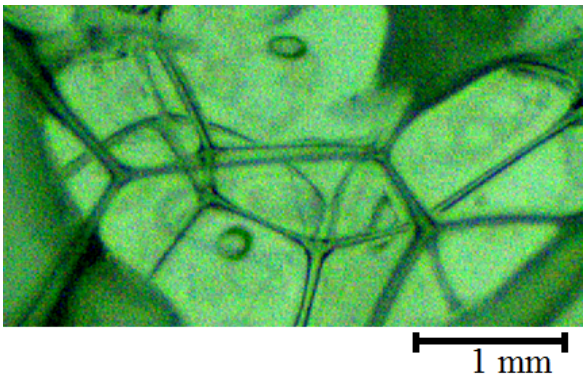

Figure 6.31 – Magnified top view of an emulsion foam obtained with $Q = 0.1$ ml/min, and $Q_g = 0.25$ ml/min.

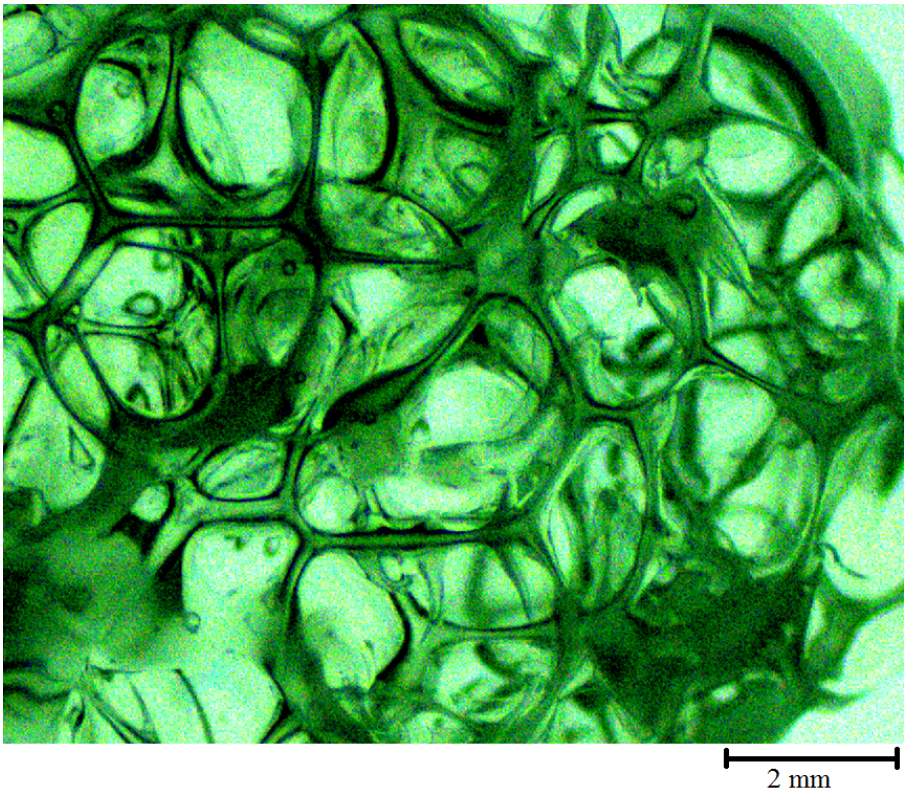

Figure 6.32 – Magnified top view of the yield-stress fluid foam obtained with $Q = 0.1$ ml/min, and $Q_g = 0.25$ ml/min.

6.5 Conclusion

In this chapter we have investigated different regulation methods leading to steady-state regimes of bubble production. The results are summarized in the following table along with the observed properties of the flow, as function of the Bingham number Bi (✓: observed; ✗: not observed).

In the case of pulsated flow, we manage to produce polydisperse yield-stress fluid foams. We have also shown that the limiting frequency of bubble production holds both for pressure driven flows and for pulsated flows. These results open potential routes for the production of monodisperse foams of yield-stress fluids in a single step method.

	Flow-rate control		Pressure control		Pulsated flow	
	$Bi > 1$	$Bi < 1$	$Bi > 1$	$Bi < 1$	$Bi > 1$	$Bi < 1$
Stability	✗	✗	✓	✗	✓	✓
Monodispersity	✗	✗	✓	✗	✗	✗
Foam production	✗	✗	✗	✗	✗	✓

Essential facts

- Steady regimes are obtained with pressure regulation and pulsated flows.
- When $Bi < 1$ and for large gas volume fraction, the production of yield-stress fluid foams is observed.

Conclusion & Outlooks

This study has focused on the introduction of gas bubbles inside yield-stress fluids. Three main problems were studied:

- The formation of bubbles using T-junction and flow-focusing devices.
- The dynamics associated with the resulting two-phase flow inside circular channels (unsteady and steady regimes).
- The thin film deposition on the wall of the channels.
- Pathways for finding optimal conditions of aerated YSF production.

First, the choice of model materials with a controlled size and physical properties, which behaves like simple yield-stress fluids, let us rule out complicated rheological effects, such as normal stresses, or thixotropy for the different studied processes. In addition, experiments carried out with carbopol and emulsion provide a way to compare the effect of the nature of the yield-stress fluid microstructure on the flow properties, but using only one constitutive law (Herschel-Bulkley). The use of stereolithography to manufacture several devices allows to use transparent channels of almost circular cross section. In addition, this method provides a lot flexibility in the manufacturing of the devices, which let us produce complex three-dimensional geometries.

In the first part, the conjunction of simple circular geometries and known yield-stress fluid properties let us determine the influence of wall slip during the flow in circular channels, and even to take it into account into the different models we derived. Since wall slip is a common perturbation of the flow of yield-stress fluid, for many industrial processes it may be easier to take it into account, than to modify surfaces either chemically or physically to suppress it. The first result we obtain concerns two-phase flows (slug flows) where the carrier fluid exhibit a yield stress and bubbles occupy the whole cross section of the channel. For the value of the yield stress we have investigated, we show that large bubbles do not contribute significantly to the rheology of the confined flow. From the macroscopic rheology point of view, this suggests that the two-phase flow is mostly equivalent to a single-phase flow of yield-stress fluid, as if the yield-stress fluid plugs flowed in a single block.

In addition to the behavior of the fluid, the first crucial process at play during two-phase flow is deposition. Thus, we studied the analogous of the Bretherton problem for yield-stress fluids. We used glass capillaries (i.e. with a negligible roughness) chemically treated to avoid wall slip. With no-slip boundary conditions, the deposition process can be described by considering the flow inside the dynamic meniscus and the classical scaling arguments proven for Newtonian fluids. Therefore, the deposited thickness depends on a balance between friction inside the thin film, associated with the internal stresses of the fluid, and the capillary pressure gradient that develops inside the meniscus. Although, there exists no simple analytical expression of the film thickness for a yield stress fluid, the results obtained with this approach are in good agreement with the experiments. However, the approach breaks down when lubrication approximation does not hold any more, which is anticipated by the modeling. Finally, since the viscous stress, the capillary stress, and the yield stress are taken into account, the Bingham number, that quantifies the stress state of the system, or the capillary number can both be used to describe the results.

The influence of wall slip on the deposition process is striking, and the slip regime is found to be much more complex. Three cases are identified depending on the stress state of the system. Here also,

the critical parameter is the Bingham number (Bi). When $Bi > 1$, the material is most likely in its solid state, and we are not able to measure the thickness of the deposited film. Therefore a combination of large yield stress and wall slip can lead to a screening of the dynamic associated with surface tension at low velocities. For emulsions, the first film thickness value we obtain corresponds to the thickness that is imposed by the quantity of droplets entrained in the vicinity of the wall. When Bi approaches 1, the deposited thickness increases dramatically, until reaching an almost constant value. This process is likely to be associated with a fast fluidization scenario. When no-slip boundary conditions are recovered, the thickness must be given by the afore-mentioned scaling law. Indeed, the deposited thickness increases until almost equating the predicted thickness for no slip boundary conditions, in agreement with what is observed. When $Bi < 1$, the material should mostly be liquid-like, and the deposited thickness tends to an almost constant value which, as suggested by Taylor and others, is imposed by the structure of the flow. This in turn, suggests that the flow of yield-stress fluid in a channel exhibits vortices in a certain velocity/applied stress domain. Since wall slip tends to become negligible at high shear rate, this thickness is close to what is measured for no slip boundary conditions. Finally, note that we never attain very large nor very small values of Bi, and that the investigated range is $0.5 < Bi < 10$. Even on such an interval the transitions are extremely sharp and localized between $0.9 < Bi < 1.1$. This suggests that the system is extremely sensible when close to the yielding transition. This feature is true of both carbopol gels and emulsions.

In a second part, we move to the study of bubble production using millifluidic three-dimensional T-junctions and flow-focusing devices. While the yield stress induces an intrinsic impediment of the classical break-up mechanism by competing with the capillary stress, we show that it is possible to take advantage of this picture to obtain a very robust break-up mechanism. We provide a detailed analysis of this break-up mechanism, and the time to form a bubble (t_b) is found to simply depend on the imposed yield-stress fluid flow rate and junction volume. The gas thread is confined between the channel wall and the solid-like region of the yield-stress fluid flow. We also highlight the role of hydrodynamic feedback and deposition on the break-up mechanism. As the hydrodynamic resistance decreases, the time associated with the motion of the gas interface inside the junction decreases and t_b tends to a limiting value equal to the time needed to fill the junction volume at the imposed dispersed phase flow rate. This value is shown to hold for both unsteady and steady regimes with different regulations. Furthermore, this scenario seems to be valid even for $Bi < 1$. For high flow rate we did not observe any crossover with a break-up which would be characteristic of Newtonian fluids. All these observations suggest that this break-up mechanism is very robust, even when there is strong feedback associated with bubbles' production.

The pressure necessary to form the first bubble is shown to depend on the pressure drop associated with the yield-stress fluid flow at imposed flow rate. The unsteady regimes, observed when the dispersed phase is driven at constant pressure, are explained in term of hydrodynamic feedback and yield-stress fluid deposition. The destabilization of bubbles production happens in two steps: (i) the drop in hydrodynamic resistance in the outlet channel leads to increase in the gas flow rate, and thus in the bubble size, which in turn decreases the hydrodynamic resistance again; (ii) the coalescence of successive bubbles due to deposition of yield-stress fluid on the wall of the channel. At this point the system starts to operate in co-flow. During the second stage, the measure of the distance between successive bubbles allows to retrieve a deposition law, and thus to test the effect of the surface roughness on the deposition mechanism. The results suggest that for the STL devices, the limiting deposited thickness is set by the roughness of the channel wall. The deposition law retrieved from multi-plug experiments compares well to what is found inside glass capillaries for a single plug of yield-stress fluid: in both cases we measure a sharp increase in the deposited thickness around $Bi \sim 1$. Finite size effects are shown to happen when the size of the plugs separating successive bubbles approaches

the diameter of the channel. Finally, we link the deposition of yield-stress fluids to the transition in bubble shapes observed during steady and unsteady experiments. Bubbles move from trapped at the wall when $Bi > 1$, to elongated, axisymmetric and positioned at the center of the channel when $Bi < 1$. The transition between the two shapes occurs when $Bi \sim 1$: indeed the shape of bubbles depends on the size of the deposited thickness, which itself depends on the Bingham number. Therefore, bubbles are forced to recover an axisymmetric shape only when the flow is close to a flow with no-slip boundary conditions, which occurs for $Bi > 1$ (i.e. for large film thickness), thus promoting the dynamic associated with surface tension and imposing the change in bubbles shape. Although the presence of bubbles increases the complexity of the flow, they also act as indicators of the stress state of the material, which is particularly difficult to determine when there is wall slip. Their change in shape is a signature of the predominant behavior of the material (i.e. solid-like, or liquid-like).

Finally, we propose and characterize different ways to control the instability of bubbles production observed with different gas regulation mechanisms. We find that flow rate control is not a good means to obtain steady regimes of bubble production. This is most likely due to gas compressibility, and the inability to control the pressure when it has overcome the pressure associated the yield-stress fluid flow. However, using pressure regulation or pulsated flows, we can control the unsteady regime and turn it into a steady bubble production. These regimes are shown to be less stable and/or monodisperse at smaller values of Bi. Nonetheless, using a peristaltic pump, we achieved the production of yield-stress fluid foams, albeit polydisperse, at theoretical gas volume fraction of $\simeq 90$ %.

As future developments, which unfortunately were not possible in this thesis due to limited time, we would emphasize the observation of flow fields with or without slip, in circular channels for two-phase flow; the measurements of the film thickness when $Bi > 1$ in slip regime; the determination of the shape of minimum energy of bubbles just after their formation or/and numerical simulation of bubble formation. Moreover, on the foam side, we would characterize the produced yield-stress fluids foams, improve their stability, or try to optimize the outlet channel geometry. Finally, we would think of scaled-up geometries to produce large quantity of yield-stress fluid foams at a higher throughput, as started in annex C. These results could find applications in several industrial processes dedicated to the production of yield-stress fluid aerated materials.

Appendices

A

Surface roughness of STL devices

With Benjamin Haffner.

In this annex we give elements of the derivation of the area associated with the roughness of stereolithography devices. Using the formula derived in this annex leads to a good estimate of the minimum deposited quantity of yield-stress fluid for multi-plug experiments at large Bingham number (chapter 5).

Contents

A.1 Surface roughness

As explained in chapter 2, the devices manufactured by stereolithography are built layer by layer, and therefore exhibit a visible roughness which depends on the vertical step of the SLA. The profile of the circular channel is then pixelated and resembles a discrete circle. The profile of a quarter of such circle is shown on figure A.1.

A.2 Limiting thickness

Here we give elements of the derivation of the area associated with the red zone on figure A.1. The thickness associated with this area limits the deposition process, due to the increase of interfacial energy associated with the deposition on the red steps compared to a circle. Indeed, the perimeter of the whole pixelated circle is $8R$, which is 27 % larger than $2\pi R$. The number of steps on $2R$ for j (50 μm) computed from the manufacturer date are given in table A.1.

A.2.1 Geometric derivation

Denoting θ_i the angle between the top and bottom position of the i-th step of height j on the circle, the area of the i-th single red portion is approximated by:

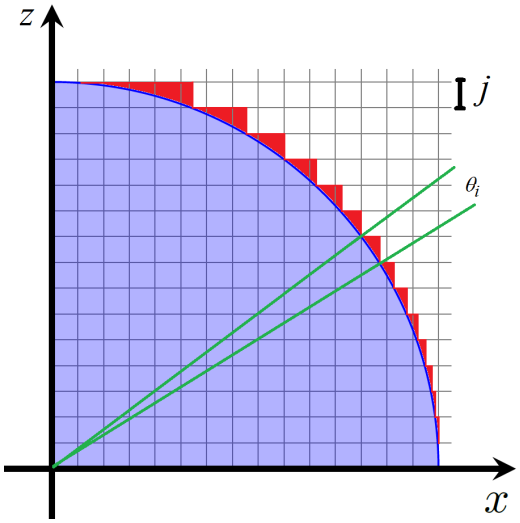

Figure A.1 – Circle and sampling of the curve by a step j.

Radius, R (mm)	number of steps per diameter i
0.5	20
1	40
2	80

Table A.1 – Number of steps for $j = 50$ μm.

$$\mathcal{A}_i = \frac{Rj}{2}\left[1 - \left(1 + \left(\frac{ij}{R}\right)^2\right)^{-\frac{1}{2}}\right] \tag{A.1}$$

Equation A.1, is only obtained by trigonometric arguments for a quarter circle. The total area of the red part is given by four times the sum of the elementary area $\mathcal{A}_i$, which leads to:

$$\mathcal{A} = 4\sum_{i=1}^{\frac{R}{j}} \mathcal{A}_i = 2Rj\sum_{i=1}^{\frac{R}{j}}\left[1 - \left(1 + \left(\frac{ij}{R}\right)^2\right)^{-\frac{1}{2}}\right] \tag{A.2}$$

For a circle of radius 1 mm and a step j of 50 μm, $\mathcal{A}$ obtained from equation A.2 is approximately 8 % of the total area of the circle.

A.2.2 Equivalent thickness

Since all deposited film thicknesses are computed as if the films were circular, we convert the area computed from equation A.2 into an equivalent annular thickness, which is written as:

$$\mathcal{A} = \pi R^2 - \pi\left(R - h_0\right)^2 \tag{A.3}$$

hence,

$$\frac{h_0}{R} = 1 - \sqrt{1 - \frac{\mathcal{A}}{\pi R^2}} \tag{A.4}$$

The value of the film thickness determined using equation A.4 agrees well with the experimental results of chapter 5 on figure 5.18.

B

Bubbles' shape

In this appendix we present experimental observations related to the shapes of the bubbles embedded in YSF. These shapes differ significantly from what would be predicted by surface tension effects in a Newtonian fluid. First we analyze the shape of bubbles produced in T-junction at large Bingham ($Bi > 1$), i.e. in the slip regime or equivalently when the yield stress is large compared to the viscous stress. A simplified empirical geometric shape is proposed to evaluate the true volume fraction of gas, and then compared to the surface fraction used in chapter 6. Then, we show the shape of bubbles obtained after an extensional flow. Finally, we investigate the decompression of gas bubbles inside the outlet channel.

Contents

B.1 Large Bingham number ($Bi > 1$)

A side view of a bubble train produced at large bingham number ($Bi \simeq 3$) is shown on figure B.1. Their shape differ significantly from what is predicted by surface tension. Besides, since bubbles are not axisymmetric, it is difficult to obtain an accurate measurement of the associated gas volume fraction, which might introduce systematic error on the results presented in chapter 6.

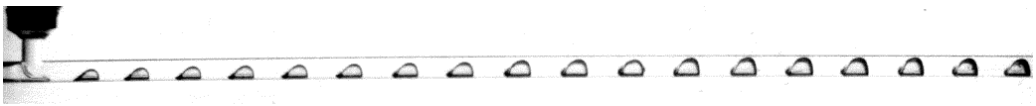

Figure B.1 – Top view of a bubble train at $Bi > 1$, $Q = 0.05$ ml/min and 205 mbar.

Similar bubble shape and positions (stuck to the wall) were obtained by numerical simulation for bubble production inside a T-junction when the carrier fluid is modeled as a Bingham fluid [39]. The authors report that bubbles deform to a flat ellipsoid due to extremely high equivalent viscosity of the solid-like region at the center of the channel. However, these numerical results do not show a sharp singularity at the rear of the bubbles. This may be associated with the large confinement they impose, which promotes interfacial stresses, or to the absence of wall slip that could enlarge the liquid region and therefore also promotes interfacial dynamics.

B.1.1 Experiments

To gain a more precise idea of the bubbles' shape, we use two cameras at the same time. One positioned at the top of the set up and the other on the side of the device facing the yield-stress fluid inlet. We then record bubble production for $Bi > 1$.

The top view is shown on figure B.2, and the side view on figure B.3.

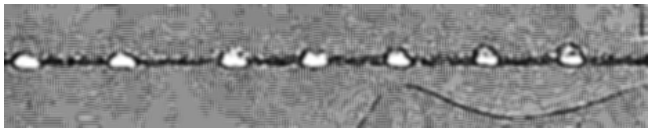

Figure B.2 – Top view of six bubbles produced in a T-junction ($R = 1$ mm; $L = 10$ cm) filled with carbopol ($\tau_y = 75$ Pa). We distinguish the egg-like shape of bubbles.

Figure B.3 – Side view of six bubbles produced in a T-junction ($R = 1$ mm; $L = 10$ cm) filled with carbopol ($\tau_y = 75$ Pa).

In both view the bubbles seem to have a similar egg-like shape. Therefore, we roughly approximate their shape by a *Kepler's egg* function [1]. The equation of this function is given by:

$$\left(x^2 + y^2\right)^2 = ax^3 \tag{B.1}$$

wherein a is the length of the longest axis, the shortest having a length $b \simeq 0.64a$. Its parametric equation (as a function of t) is given by equation B.2 which is plotted on figure B.4.

$$\begin{cases} x = \frac{a}{(1+t^2)^2} \\ y = tx \end{cases} \tag{B.2}$$

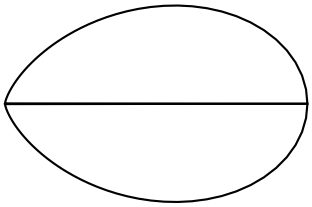

Figure B.4 – Kepler's egg curve for the approximation the cross section of a bubble at large Bingham number.

The volume Ω_o of the ovoid formed by rotating the Kepler's egg around its longest axis is given by:

$$\Omega_o = \frac{\pi}{15}a^3 \tag{B.3}$$

Therefore the local volume fraction occupied by a bubble having the shape of a Kepler's egg in a cylinder of same length, is given by:

[1] http://www.mathcurve.com/courbes2d/foliumsimple/foliumsimple.shtml

$$\phi_{g,l} = \frac{\Omega_o}{\pi R^2 a} = \frac{1}{15}\left(\frac{a}{R}\right)^2 \tag{B.4}$$

The typical length of our bubbles is $a \simeq 2R$, which leads to $\phi_{g,l} \simeq 0.26$. For the picture shown in figure B.2, the volume computation leads to $\phi_g \simeq 0.14$, while a surface fraction computation leads to $\phi_g \simeq 0.16$. This agreement, although based on rough observations, suggests that the error induced by surface fraction computation is small for non-axisymmetric bubbles.

B.2 Extensional (diverging) flow

Bubbles' shape strongly differing from what is predicted by surface tension are observed in diverging flows at large Bingham number. Bubbles in yield-stress fluid are first produced using a T-junction, then they are driven into a glass capillary which enters a larger channel where it is surrounded by a yield-stress fluid flow at the the same flow rate. A picture of such experiment is shown on figure B.5, a sketch of the set up and of the bubble shape is shown on figure B.6. When bubbles go from the small capillaries to the larger channel their shape change from axisymmetric to pancake like. This is presumably due to the stresses induced by the extensional flow.

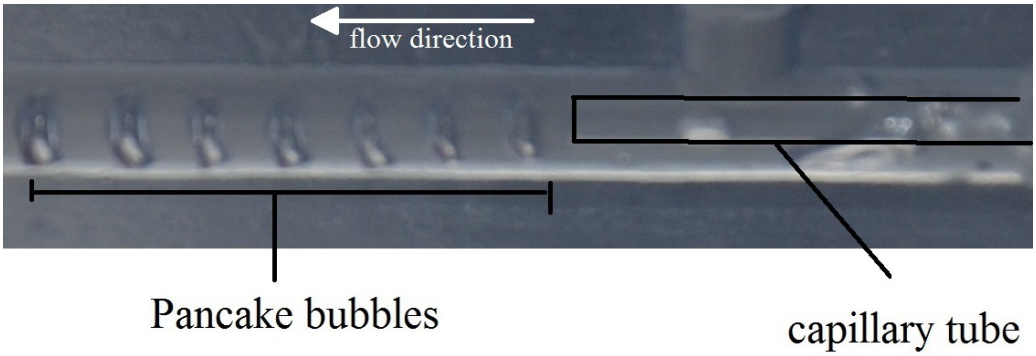

Figure B.5 – Picture of an experiment showing the shape of bubbles after passing in the extensional flow. The fluid is an emulsion ($\tau_y = 100$ Pa), the radius of the larger channel is 1 mm, and the capillary has a radius of 702 μm.

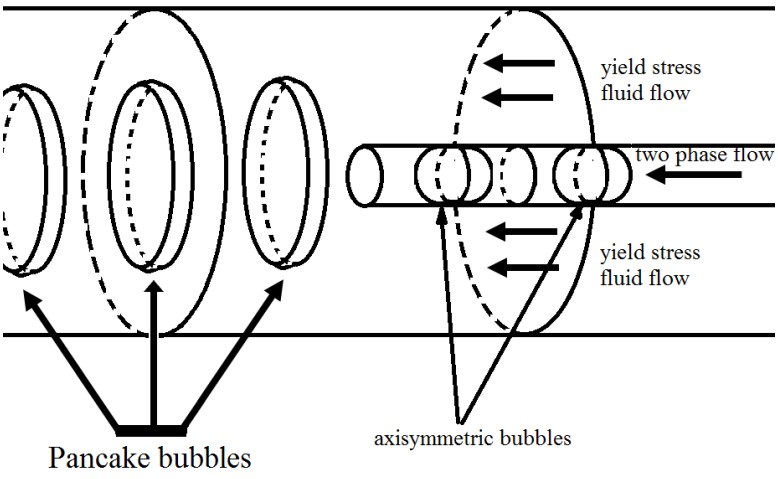

Figure B.6 – Sketch of the experiment.

B.3 Decompression of gas bubbles

During the flow in the outlet channel we observe that the volume of bubbles varies (figure B.7). Their size is smaller near the junction than close to the outlet. As in the Newtonian case for very long channels [187], this is associated with the decompression of the gas constituting the bubbles. Indeed the bubbles are produced at a larger pressure than the atmospheric pressure and inflate as they approaches the exit of the outlet channel and the value of the external pressure tends to the atmospheric pressure.

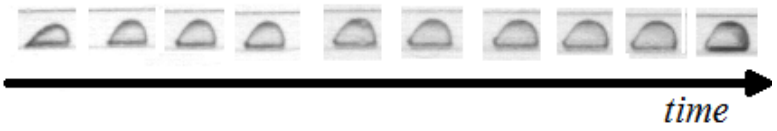

Figure B.7 – Time evolution of the shape of single bubble as it advances (from left: just after the junction; to right: just before the exit) in the outlet channel ($R = 1$ mm; $L = 10$ cm). For an applied pressure of 341 mbar, and an emulsion of yield stress $\tau_y = 100$ Pa.

To describe the decompression of the gas volume we can consider that the molecules of air undergo either an isothermal (constant temperature) or an adiabatic (without heat transfer) transformation. Considering an isothermal transformation for a perfect gas, leads to the *Boyle-Mariotte law*):

$$P_i V_i = P_f V_f \tag{B.5}$$

Where the index i denotes the initial state of the system, and f denotes the final state of the system. Considering a reversible adiabatic transformation for a prefect gas leads to the *Laplace* relation:

$$P_i V_i^{\gamma_l} = P_f V_f^{\gamma_l} \tag{B.6}$$

wherein $\gamma_l = \frac{C_p}{C_v}$ is the ratio of the heat capacity at constant pressure to the the heat capacity at constant volume (each of them expressed in J/K). For a diatomic perfect gas (such as 99 % of air), $\gamma_l = \frac{7}{5}$.

On figure B.7 the applied pressure is $P_{atm} + \Delta P$, with $\Delta P = 0.341$ bar and P_{atm} the atmospheric pressure (approximately 1 bar). The experimental and theoretical volume variations computed from equations B.5, B.6 are summarized on table B.1.

ΔP (mb)	$\frac{P_i}{P_f}$	$\frac{V_f}{V_i}$	$\left(\frac{V_f}{V_i}\right)^{\gamma_l}$
341	1.341	1.5	1.86

Table B.1 – Summary of the parameters of bubbles' decompression between the initial and final stage of figure B.7.

The decompression value given by $\frac{V_f}{V_i}$ (isothermal transformation) is closer to the value of the pressure ratio than what is predicted by considering an adiabatic transformation. Indeed, the hypothesis of an adiabatic process implies that the transformation undergone by the bubbles is fast enough to neglect heat transfer within the system. The characteristic diffusion time for heat in air, on a typical length (a) of 1 mm and a thermal diffusivity (d) of $\simeq 1.9\ 10^{-5}$ m^2/s, is $\frac{a^2}{d} \simeq 50$ ms, whereas on figure B.7 a bubbles travels from the inlet to the outlet in 1 min 20 s. Therefore, the heat transfer cannot be neglected. However, the room temperature remains approximately constant during the short time of

the experiment, which suggests the approximation of isothermal transformation. This may explain the better agreement of the pressure variation with the volume variation when considering an isothermal transformation. Moreover, we note that the measured decompression of the gas volume is slightly larger than what is predicted from the pressure variation, which result is also observed for Newtonian fluids [187].

C

Other geometries & scale-up

In this appendix we present some of the geometries that we design and not thoroughly investigate, especially the geometry linked to parallelization of bubbles production.

Contents

C.1 Flow focusing with five inlets

The results for the 3-inlets flow focusing geometry shows that bubble production is faster than in a T-junction by a factor 4.5 (see chapter 4). Therefore, it would be interesting to test what is the frequency obtained when the number of inlets is even larger. We design a flow-focusing geometry with 5 inlets: 4 four the yield stress fluids, and 1 for the gas. A sketch of the inner volume of the channels for the flow-focusing device with 5 inlets is shown on figure C.1.

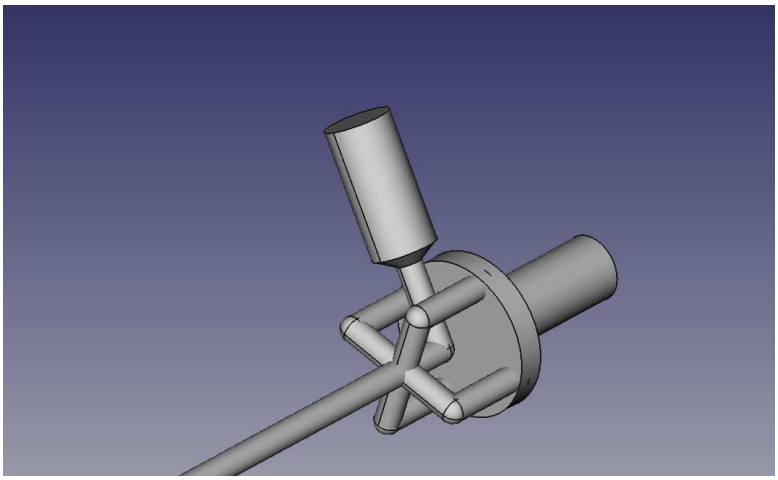

Figure C.1 – CAD drawing of the inner volume of the channels of a 5 inlet T-junction ($R = 1$ mm).

C.2 Parallelization

Scaled-up geometries are mentioned in chapter 4, and known to exhibit coupling between the different units of production. What would happen with yield-stress fluids? To answer this question, we design two different scaled-up devices, one with two T-junctions and the other with sixteen T-junctions.

C.2.1 2-channels T-junction

The CAD drawing of the inner volume of the device is shown on figure C.2.

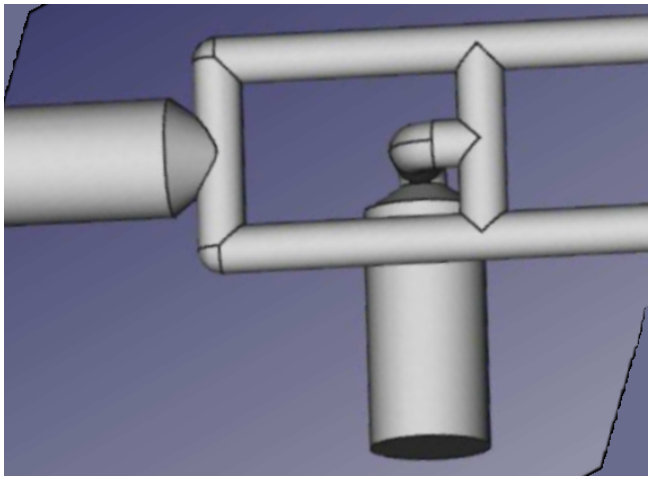

Figure C.2 – CAD drawing of the inner volume of the channels of 2-channels T-junction device ($R = 1$ mm).

C.2.1.1 Experiments

An experiment at imposed yield-stress fluid flow rate ($Q = 0.1$ ml/min) and imposed gas pressure ($\Delta P \simeq 300$ mbar) for the device shown in figure C.2. A top view of bubble production is shown on figure C.3. The instability of bubble production due to hydrodynamic resistance variation is also observed. The break-up mechanism also holds, and does not seem to be strongly perturbed by additional hydrodynamic feedback, however much work remain to be done to confirm this result.

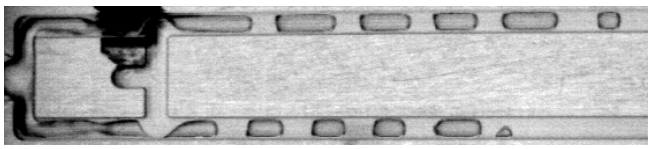

Figure C.3 – Top view of bubble production inside a 2-channels T-junction device ($R = 1$ mm, $L = 10$ cm) with carbopol gel ($\tau_y = 75$ Pa).

C.2.2 16-channels T-junction

As an example of larger possible scaled-up device, the inner volume of a scaled-up T-junction device with sixteen units of production is shown on figure C.4. The gas could be injected either by the top or bottom channels, and the yield stress fluid by the side channel.

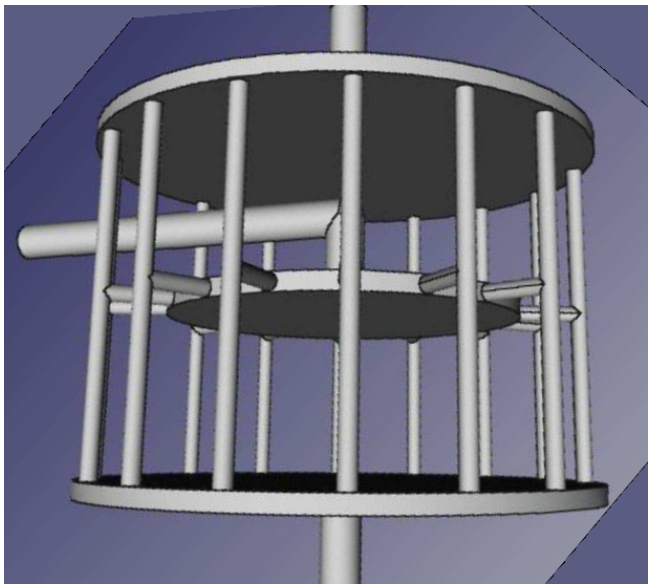

Figure C.4 – CAD drawing of the inner volume of the channels of a 16-channels T-junction device. The radius of the small vertical channels is 1 mm.

D

Preliminary results on coarsening

In this appendix we present two experiments illustrating the coarsening of gas bubbles inside yield-stress fluids. One case is confined and the other unconfined.

Contents

D.1 Introduction

For Newtonian fluids the dissolution of a gas bubble into the surrounding liquid is a diffusive process driven by the concentration gradient of the considered species and by the Laplace pressure. For a set of bubbles, as in a foam, the Laplace pressure between each bubbles must be taken into account. In both cases, the radius of small bubbles decreases until total disappearance while the mean radius of the remaining bubbles increases. For a single bubble, or for foams, the typical time dependency of the radius is $t^{\frac{1}{2}}$, with t the time from the beginning of the experiment [67, 188].

D.2 Unconfined coarsening

The first experiment consists in observing the change in bubble size in a bubbly yield-stress fluid placed in a small vessel having the shape of a rectangular parallelepiped (height 3 cm, square basis with side of length 1 cm). A picture of some bubbles is shown on figure D.1. The vessel is in contact with ambient atmosphere at its top. The bubbles shown on figure D.1 are positioned at the bottom of the vessel, and therefore should not empty into the atmosphere but rather into their other neighbors, and inside the interstitial liquid.

Since we do not have any information on the diffusion coefficients into the emulsion nor on its initial gas saturation, we measure the decrease in size of bubbles. We first report that large bubbles don't dissolve whereas small bubbles dissolve completely.

In addition, large bubbles initially having non-spherical shape tend to recover a more spherical shape. An example of such behavior is shown on figure D.2. A large bubbles is trapped close to the glass surface of the vessel and initially exhibit a shape with different curvatures. The area with the larger curvature disappear whereas the body of the bubble does not decrease in size. However, we lack sufficient experimental data to establish a rigorous criterion of bubbles' dissolution.

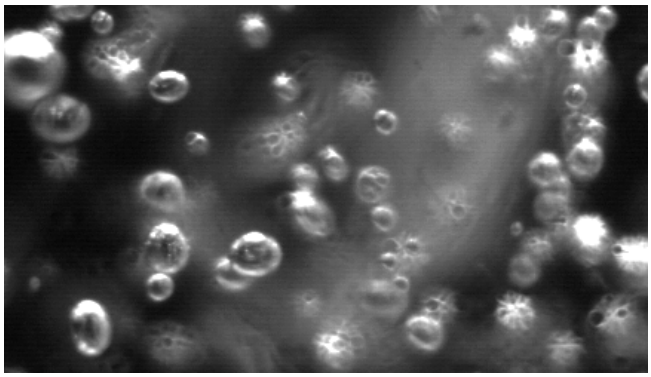

Figure D.1 – A set of bubbles trapped in yield-stress fluid, their typical size is 1 mm. The depth of field is small, therefore bubbles placed to far away appear blurred. For emulsion with $\tau_y = 100$ Pa.

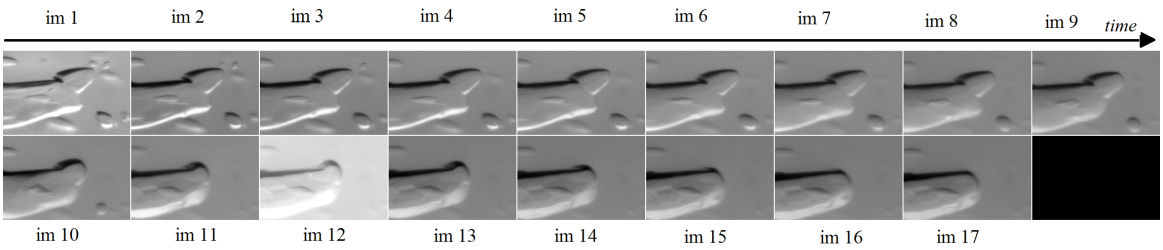

Figure D.2 – A set of bubbles trapped in yield stress fluid, the initial length of the larger bubble is 1.5 mm. For emulsion with $\tau_y = 100$ Pa. Each image is separated by 2 h 42 min.

The radius of bubbles is computed from their apparent surface area ($\mathcal{A}_b$) by:

$$R_{eq} = \sqrt{\frac{\mathcal{A}_b}{\pi}} \tag{D.1}$$

The typical variation of the equivalent radius computed using equation D.1 is shown on figure D.3. Its evolution is roughly represented by [188]:

$$R = R_0\sqrt{1 - \alpha t^2} \tag{D.2}$$

wherein α is a constant that depends on the diffusion coefficient and the saturation of the medium. Equation D.2 is plotted on figure D.3 for $\alpha = 7.10^{-7}$ s^{-2}. The results are reasonably well described by the theory developed for Newtonian fluids.

D.3 Confined coarsening

The other experiment consists in observing two bubbles close to each other inside a channel. A small bubble of initial radius 250 μm is positioned close to another of diameter 750 μm. They are separated by approximately 5 mm. A very large (infinite) bubble is positioned on the other side of the larger bubble. A picture taken during such experiment is shown on figure D.4.

The equivalent radius of the small bubble computed using equation D.1 is shown on figure D.5. The dependency seems mostly linear, and thus faster than in the unconfined geometry. The dependency on the radius is different from what is found in an unconfined geometry. Due to spatial resolution of the camera the measurement are noisy.

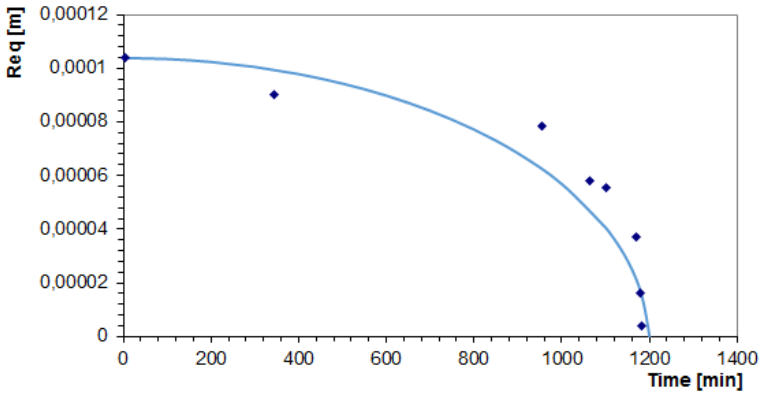

Figure D.3 – Evolution of the equivalent radius of a bubble during its dissolution. The continuous line stands for equation D.2 with $\alpha = 7.10^{-7}$ s^{-2}.

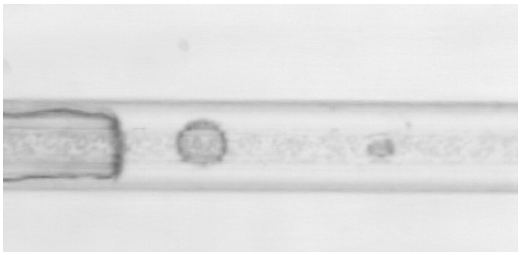

Figure D.4 – Picture during taken the dissolution of a small bubble inside a channel of radius 1 mm. For carbopol gel with $\tau_y = 75$ Pa.

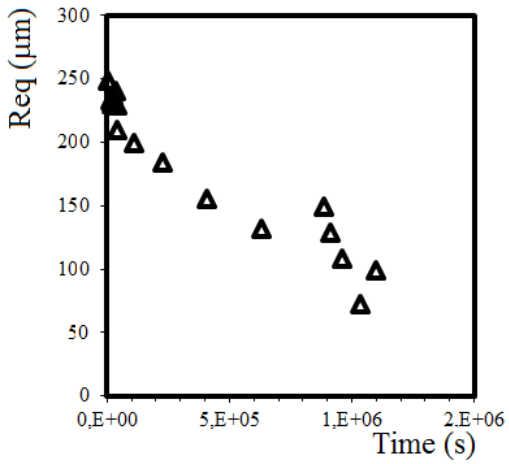

Figure D.5 – Evolution of the equivalent radius of a bubble during its dissolution in confined geometry for carbopol gel with $\tau_y = 75$ Pa.

D.4 Conclusion

The results obtained in the unconfined case seems to be close to what is observed for a single bubble in a Newtonian fluid. Comparing the confined coarsening to the unconfined coarsening, we find that the dynamic is faster in the confined case. However, literature results for elastic soft solid, or fluids with non-Newtonian rheology [189, 190] underline that the process can be either accelerated or decelerated, which could be consistent with our experimental results. Nonetheless, further work is needed to deepen

these preliminary results and suggestions.

E

Script for destabilization of bubble production

In this annex we provide the script used to compute the destabilization of bubble production.

E.1 Main program

```
# -*- coding: utf-8 -*-
"""
Created on Fri Nov 22 11:10:20 2013

@author: Benoit
"""

import mod_fluid_seuil_v4 as mfs
import math
import matplotlib.pyplot as plt

savepath='D:/Data_benoit/current_these/script_pyhton_fluide_seuil/res/'

#paramètres physique
r=0.001 #tube radius m
l=0.1 #tube length
tau0=250.0 #yield stress pa
k=79.0 #consistency Pa.s^n
n=0.39 #flow index

Qemin=1.0e-10 #imposed flow rate m3/s


Pfluid=[r,l,tau0,k,n,5.0]
#
#param0=mfs.calc_param0(Pfluid,Qe)
#
#print param0[:]
```

```
#structure of param0
#[0]: gas pressure
#[1]: YSF pressure
#[2]: total flow rate
#[3]: gas flow rate
#[4]: bubble formation time

vlbl=[] #list of bubbles' volume
ll=[] # list of the position of bubble fronts
lbl=[] # list of bubbles length
indl=[] # list of total number of bubbles
vtbl=[] # list of mean velocity value
tl=[] # list of simulation time
vcbl=[] # list total gas volume injected
qal=[] # ratio of YSF flow rate to gas flow rate



#qair=param0[2]
#tau=param0[3]
#p0air=param0[0]
#p0em=param0[1]


ni=1000.0
Qemax=1.0e-7
h=(Qemax-Qemin)/ni
print str(h)

tflist=[]
dplist=[]
qlist=[]


for ii in range(0,int(ni)):

    ind=0
    t=0.0
    vc=0.0
    vt=math.pi*r**2*l
    lc=l


    Qe=Qemin+ii*h

    param=mfs.calc_param0(Pfluid,Qe)

    qair=param[2]
```

```
        tau=param[3]
        p0air=param[0]
        p0em=param[1]

        while (((l-lc)/l)<1.0):

            ind+=1
            t+=tau

            vbulle=qair*tau

            vc+=vbulle

            lbulle=vbulle/(math.pi*r**2)

            lc-=lbulle

            Qc=mfs.relqp(p0air,tau0,r,lc,k,n)

            vitb=Qc/(math.pi*r**2)

            qair=Qc-Qe


            if (((l-lc)/l)<1.0):

        #         print str(qair/Qe)
                qal.append(qair/Qe)
                vcbl.append(vc/vt)
                vtbl.append(vitb)
                lbl.append(lbulle)
                vlbl.append(vbulle)
                ll.append(lc/l)
                indl.append(ind)
                tl.append(t)

        tflist.append(t)
        dplist.append(p0em+5.0)
        qlist.append(Qe)

plt.plot(tl,vlbl,"1")
plt.xlabel('Temps [s]')
plt.ylabel('Vb [m3]')
plt.savefig(savepath+'vb_vs_t_'+str(Qe)+'.png')

plt.plot()

for jj in range(0,len(tflist)):
```

```
    print tflist[jj]

for jj in range(0,len(tflist)):

    print dplist[jj]

for jj in range(0,len(tflist)):

    print qlist[jj]

plt.show()

print "Nombre de bulles= "+str(len(vlbl))

mfs.write_resfile(indl,tl,ll,lbl,vcbl,vtbl,vlbl, savepath,'hb_'+str(Qe))
```

E.2 Module

The file *mod-fluid-seuil-v4*:

```
 -*- coding: utf-8 -*-
"""
Created on Fri Nov 22 11:12:04 2013

@author: Benoit
"""

import math
from scipy.optimize import newton
#import matplotlib.pyplot as plt
import decimal

decimal.getcontext().prec = 24

#return a flow rate value for a given value of pressure

def relqp(p,tau0,r,l,k,n):

    p=decimal.Decimal(p)
    r=decimal.Decimal(r)
    l=decimal.Decimal(l)
    k=decimal.Decimal(k)
    tau0=decimal.Decimal(tau0)
    n=decimal.Decimal(n)

    tauw=p*r/(decimal.Decimal(2.0)*l)
    tauw=decimal.Decimal(tauw)

    if tauw>tau0:
```

```
            a=decimal.Decimal(8.0)*decimal.Decimal(math.pi)/k**(decimal.
                Decimal(1.0)/decimal.Decimal(n))*(l/p)**decimal.Decimal(3)
            b=(tauw-tau0)**(decimal.Decimal(1.0)+decimal.Decimal(1.0)/decimal
                .Decimal(n))
            c=((tauw-tau0)**decimal.Decimal(2))/(decimal.Decimal(3.0)+decimal
                .Decimal(1.0)/decimal.Decimal(n))
            d=decimal.Decimal(2.0)*(tauw-tau0)/(decimal.Decimal(2.0)+decimal.
                Decimal(1.0)/decimal.Decimal(n))
            e=tau0**decimal.Decimal(2)/(decimal.Decimal(1.0)+decimal.Decimal
                (1.0)/decimal.Decimal(n))
            f=c+d+e

            q=a*b*f

        else:
            q=0.0

        return float(q)

#function for inverting q=f(p)
#ie g(p)=q-f(p)

def opt_relqp(p,tau0,r,l,k,n,Q):


        p=decimal.Decimal(p)
        r=decimal.Decimal(r)
        l=decimal.Decimal(l)
        k=decimal.Decimal(k)
        tau0=decimal.Decimal(tau0)
        Q=decimal.Decimal(Q)
        n=decimal.Decimal(n)

        tauw=p*r/(decimal.Decimal(2.0)*l)
        tauw=decimal.Decimal(tauw)

        if tauw>tau0:

            a=decimal.Decimal(8.0)*decimal.Decimal(math.pi)/k**(decimal.
                Decimal(1.0)/decimal.Decimal(n))*(l/p)**decimal.Decimal(3.0)
            b=(tauw-tau0)**(decimal.Decimal(1.0)+decimal.Decimal(1.0)/decimal
                .Decimal(n))
            c=((tauw-tau0)**decimal.Decimal(2.0))/(decimal.Decimal(3.0)+
                decimal.Decimal(1.0)/decimal.Decimal(n))
            d=decimal.Decimal(2.0)*(tauw-tau0)/(decimal.Decimal(2.0)+decimal.
                Decimal(1.0)/decimal.Decimal(n))
            e=tau0**decimal.Decimal(2.0)/(decimal.Decimal(1.0)+decimal.
                Decimal(1.0)/decimal.Decimal(n))
            f=c+d+e
```

```
        res=Q-a*b*f

    else:
        res=Q

    return float(res)

#derivative of the inverse function g'(p)


def opt_der_relqp(p,tau0,r,l,k,n,Q):

    p=decimal.Decimal(p)
    r=decimal.Decimal(r)
    l=decimal.Decimal(l)
    k=decimal.Decimal(k)
    tau0=decimal.Decimal(tau0)
    n=decimal.Decimal(n)
    Q=decimal.Decimal(Q)

    tauw=p*r/(decimal.Decimal(2.0)*l)
    tauw=decimal.Decimal(tauw)
    a1=r/(decimal.Decimal(2.0)*l)

    if tauw>tau0:

        a=decimal.Decimal(8.0)*decimal.Decimal(math.pi)/k**(decimal.
            Decimal(1.0)/decimal.Decimal(n))*(l/p)**decimal.Decimal(3.0)
        b=(tauw-tau0)**(decimal.Decimal(1.0)/decimal.Decimal(n))
        c=decimal.Decimal(2.0)*a1*(tauw-tau0)
        d=decimal.Decimal(3.0)*((tauw-tau0)/p)-a1*(decimal.Decimal(1.0)+
            decimal.Decimal(1.0)/decimal.Decimal(n))
        f=(tauw-tau0)**(decimal.Decimal(2.0))/(decimal.Decimal(3.0)+
            decimal.Decimal(1.0)/decimal.Decimal(n))
        g=decimal.Decimal(2.0)*tau0*(tauw-tau0)/(decimal.Decimal(2.0)+
            decimal.Decimal(1.0)/decimal.Decimal(n))
        h=tau0**decimal.Decimal(2.0)/(decimal.Decimal(1.0)+decimal.
            Decimal(1.0)/decimal.Decimal(n))
        g1=g/(decimal.Decimal(2.0)*(tauw-tau0))
        f1=f/(tauw-tau0)

        e=decimal.Decimal(-1.0)*(a*b*((f1+g1)*c-d*(f+g+h)))

    else:
        e=0.0

    return float(e)
```

```
#compute the initial parameters of the system

def calc_param0(Pfluid,Qe):

    r=Pfluid[0]
    l=Pfluid[1]
    tau0=Pfluid[2]
    k=Pfluid[3]
    n=Pfluid[4]

    off=Pfluid[5]

    p0=((tau0*l*2.0)/r)+1000.0

    #search for the root of equation g(p)=0 by newton-rhapson method

    Pseuil=newton(opt_relqp,
                  p0,
                  fprime=opt_der_relqp,
                  args=(tau0,r,l,k,n,Qe),
                  maxiter=1000000, tol=0.0001)

    print "Pem= "+str(Pseuil*1.0e-5)+" bar"
    print "Pgaz= "+str((Pseuil+off)*1.0e-5)+" bar"

    Pair=Pseuil+off

    Qtot=relqp(Pair,tau0,r,l,k,n)

    Qair=Qtot-Qe


    #vol=2.0*r*(math.pi)*(alpha*r/2.0)**2
    vol=((16.0/3.0)*r**3)


    tfrac=vol/Qe

    param0=[Pair,Pseuil,Qair,tfrac]

    return param0


def write_resfile(a,b,c,d,e,f,g,savepath,label):

    svpt=savepath+'results_'+label+'.txt'

    with open(svpt, 'w') as fw:
```

```
        fw.write('Nb'+'\t'
        +'time [s]'+'\t'
        +'P rel 1ere bulle'+'\t'
        +'Lbulles [m]'+'\t'
        +'Vol cum [m3]'+'\t'
        +'Vit moy [m/s]'+'\t'
        +'Vol bulles [m3]'+'\n')

        for i in range(0,len(a)):

            fw.write(str(a[i])+'\t'
            +str(b[i])+'\t'
            +str(c[i])+'\t'
            +str(d[i])+'\t'
            +str(e[i])+'\t'
            +str(f[i])+'\t'
            +str(g[i])+'\n')

        print "Name of the file: ", fw.name

    fw.close
```

Bibliography

[1] N. Quennouz et al. “Microfluidic Study of Foams Flow for Enhanced Oil Recovery (EOR)”. *OGST* 69.3 (2014), pp. 457–466 (cit. on p. 27).

[2] L. Ducloué. “Comportement rhéologique des fluides à seuil aérés”. PhD thesis. 2014 (cit. on pp. 27, 48, 53, 183).

[3] P. Coussot. *Rheometry of Pastes, Suspensions, and Granular Materials: Applications in Industry and Environment*. Wiley, 2005. ISBN: 9780471720560 (cit. on pp. 27, 48).

[4] T. Brunet, J. Leng, and O. Mondain-Monval. “Soft Acoustic Metamaterials”. *Science* 342.6156 (2013), pp. 323–324 (cit. on p. 27).

[5] G. A. van Aken. “Aeration of emulsions by whipping”. *Colloids Surf, A* 190.3 (2001), pp. 333 –354 (cit. on p. 27).

[6] P. Oswald and M. Saint-Jean. *Rhéophysique: ou comment coule la matière*. Belin, 2005. ISBN: 9782701139692 (cit. on pp. 27, 42–44, 53).

[7] P. Coussot. *Rhéophysique la matière dans tous ses Etats*. EDP Sciences, 2012. ISBN: 9782759808601 (cit. on pp. 27, 42, 44, 73).

[8] J. Goyon et al. “Shear Induced Drainage in Foamy Yield-Stress Fluids”. *Phys. Rev. Lett.* 104.12 (2010), p. 128301 (cit. on p. 27).

[9] L. Ducloué et al. “Coupling of elasticity to capillarity in soft aerated materials”. *Soft Matter* 10 (28 2014), pp. 5093–5098 (cit. on p. 27).

[10] A. Salonen et al. “Dual gas and oil dispersions in water: production and stability of foamulsion”. *Soft Matter* 8.3 (2012), pp. 699–706 (cit. on p. 27).

[11] W. L. Olbricht. “Pore-Scale Prototypes of Multiphase Flow in Porous Media”. *Annu. Rev. Fluid Mech.* 28.1 (1996), pp. 187–213 (cit. on p. 28).

[12] P. S. Hammond. “Nonlinear adjustment of a thin annular film of viscous fluid surrounding a thread of another within a circular cylindrical pipe”. *J. Fluid Mech.* 137 (1983), pp. 363–384 (cit. on p. 28).

[13] P.A Gauglitz and C.J Radke. “The dynamics of liquid film breakup in constricted cylindrical capillaries”. *J. Colloid Interface Sci.* 134.1 (1990), pp. 14 –40 (cit. on p. 28).

[14] P. A. Gauglitz et al. “Foam generation in homogeneous porous media”. *Chem. Eng. Sci.* 57.19 (2002), pp. 4037–4052 (cit. on p. 28).

[15] T. Chevalier. “Ecoulements de fluides a seuil en milieux confines”. PhD thesis. 2013 (cit. on p. 28).

[16] C. N. Baroud, F. Gallaire, and R. Dangla. “Dynamics of microfluidic droplets”. *Lab Chip* 10 (16 2010), pp. 2032–2045 (cit. on pp. 28, 76, 78, 79, 125, 126).

[17] A. Huerre, V. Miralles, and M.-C. Jullien. “Bubbles and foams in microfluidics”. *Soft Matter* 10 (2014), pp. 6888–6902 (cit. on pp. 28, 76, 125).

[18] R. Seemann et al. “Droplet based microfluidics”. *Rep. Prog. Phys.* 75 (2012), p. 016601 (cit. on pp. 28, 76, 78, 125, 126).

[19] E. K. Sackmann, A. L. Fulton, and D. J. Beebe. “The present and future role of microfluidics in biomedical research”. *Nature* 507.7491 (2014), pp. 181–189 (cit. on p. 28).

[20] S.-Y. Teh et al. “Droplet microfluidics”. *Lab Chip* 8 (2008), pp. 198–220 (cit. on pp. 28, 125).

[21] D. Mark et al. “Microfluidic lab-on-a-chip platforms: requirements, characteristics and applications”. *Chem. Soc. Rev.* 39.3 (2010), pp. 1153–1182 (cit. on p. 28).

[22] G. M. Whitesides. “The origins and the future of microfluidics”. *Nature* 442.7101 (2006), pp. 368–373 (cit. on p. 28).

[23] D. Bartolo and D. G. A. L. Aarts. “Microfluidics and soft matter: small is useful”. *Soft Matter* 8 (2012), pp. 10530–10535 (cit. on pp. 28, 125).

[24] T. Nisisako, T. Torii, and T. Higuchi. “Droplet formation in a microchannel network”. *Lab Chip* 2 (2002), pp. 24–26 (cit. on pp. 28, 125).

[25] M. De Menech et al. “Transition from squeezing to dripping in a microfluidic T-shaped junction”. *J. Fluid Mech.* 595 (2008), pp. 141–161 (cit. on pp. 28, 125, 126).

[26] P. Garstecki et al. “Formation of droplets and bubbles in a microfluidic T-junction - scaling and mechanism of break-up”. *Lab Chip* 6 (2006), pp. 437–446 (cit. on pp. 28, 125, 126).

[27] M.-C. Jullien et al. “Droplet breakup in microfluidic T-junctions at small capillary numbers”. *Phys. Fluids* 21 (2009), p. 072001 (cit. on pp. 28, 125).

[28] S.L. Anna, N. Bontoux, and H.A. Stone. “Formation of dispersions using flow focusing in microchannels”. *Appl. Phys. Lett.* 82 (2003), pp. 364–366 (cit. on pp. 28, 125, 126).

[29] A. G. Marin, F. Campo-Cortes, and J. M. Gordillo. “Generation of micron-sized drops and bubbles through viscous coflows”. *COLSUA* 344 (2009), pp. 2–7 (cit. on pp. 28, 125).

[30] Z. Nie et al. “Emulsification in a microfluidic flow-focusing device: effect of the viscosities of the liquids”. *Microfluid. Nanofluidics* 5 (2008), pp. 585–594 (cit. on pp. 28, 125).

[31] P. Garstecki, H. A. Stone, and G. M. Whitesides. “Mechanism for flow-rate controlled breakup in confined geometries: A route to monodisperse emulsions”. *Phys. Rev. Lett.* 94 (2005), p. 164501 (cit. on pp. 28, 30, 125, 126, 135, 136).

[32] B. Dollet et al. “Role of the channel geometry on the bubble pinch-off in flow-focusing devices”. *Phys. Rev. Lett.* 100 (2008), p. 034504 (cit. on pp. 28, 30, 125, 127, 135, 136).

[33] W. van Hoeve et al. “Microbubble formation and pinch-off scaling exponent in flow-focusing devices”. *Phys. Fluids* 23 (2011), p. 092001 (cit. on pp. 28, 125).

[34] R. Suryo and Osman A. Basaran. “Tip streaming from a liquid drop forming from a tube in a co-flowing outer fluid”. *Phys. Fluids* 18 (2006), p. 082102 (cit. on pp. 28, 125).

[35] S. Sugiura et al. “Interfacial tension driven monodispersed droplet formation from microfabricated channel array”. *Langmuir* 17 (2001), pp. 5562–5566 (cit. on pp. 28, 125, 126).

[36] R. Dangla et al. “The physical mechanisms of step emulsification”. *J. Phys. D-Applied Phys.* 46 (2013), p. 114003 (cit. on pp. 28, 125).

[37] R. Dangla, S. C. Kayi, and C. N. Baroud. “Droplet microfluidics driven by gradients of confinement”. *Proc. Natl. Acad. Sci. USA* 110 (2013), pp. 853–858 (cit. on pp. 28, 125).

[38] M. Stoffel et al. “Bubble Production Mechanism in a Microfluidic Foam Generator”. *Phys. Rev. Lett.* 108 (2012), p. 198302 (cit. on pp. 28, 125).

[39] B. Chen et al. “Three-Dimensional Simulation of Bubble Formation Through a Microchannel T-Junction”. *Chemical Engineering & Technology* 36.12 (2013), pp. 2087–2100 (cit. on pp. 28, 151, 205).

[40] A. Duboin et al. “Cusps, spouts and microfiber synthesis with microfluidics”. *Soft Matter* 9 (2013), pp. 3041–3049 (cit. on p. 28).

[41] T. Fu et al. "Breakup dynamics of slender bubbles in non-newtonian fluids in microfluidic flow-focusing devices". *AICHE J.* 58 (2012), pp. 3560–3567 (cit. on pp. 28, 128).

[42] T. Fu et al. "Gas-liquid flow stability and bubble formation in non-Newtonian fluids in microfluidic flow-focusing devices". *Microfluid. Nanofluidics* 10 (2011), pp. 1135–1140 (cit. on pp. 28, 128).

[43] T. Fu et al. "Bubble formation in non-Newtonian fluids in a microfluidic T-junction". *Chem. Eng. Proc.* 50 (2011), pp. 438–442 (cit. on pp. 28, 128).

[44] Ph. Nghe et al. "Microfluidics and complex fluids". *Lab Chip* 11 (2011), pp. 788–794 (cit. on pp. 28, 128).

[45] O. E. Yildirim and O. A. Basaran. "Dynamics of formation and dripping of drops of deformation-rate-thinning and -thickening liquids from capillary tubes". *J. NN Fluid Mech.* 136.1 (2006), pp. 17–37 (cit. on pp. 28, 129).

[46] L. Derzsi et al. "Flow focusing with viscoelastic liquids". *Phys. Fluids* 25.9 (2013) (cit. on p. 28).

[47] Y. Xia and G. M. Whitesides. "Soft lithography". *Annu. Rev. Mater. Sci.* 28.1 (1998), pp. 153–184 (cit. on pp. 28, 62).

[48] J.C. McDonald et al. "Fabrication of microfluidic systems in poly (dimethylsiloxane)". *Electrophoresis* 21.1 (2000), pp. 27–40 (cit. on pp. 28, 62).

[49] S. Takeuchi et al. "An Axisymmetric Flow-Focusing Microfluidic Device". *Advanced materials* 17.8 (2005), pp. 1067–1072 (cit. on pp. 28, 62).

[50] P. F. Jacobs. *Rapid prototyping & manufacturing: fundamentals of stereolithography*. Society of Manufacturing Engineers, 1992 (cit. on pp. 29, 62).

[51] F. P.W. Melchels, J. Feijen, and D. W. Grijpma. "A review on stereolithography and its applications in biomedical engineering". *Biomaterials* 31 (2010), pp. 6121–6130 (cit. on pp. 29, 62).

[52] L.D. Landau et al. *Theory of Elasticity* (cit. on pp. 35, 37).

[53] L.D. Landau and E.M. Lifshits. *Fluid Mechanics*. Teoreticheskaia fizika. Pergamon Press, 1959 (cit. on pp. 38, 41, 84).

[54] E. Guyon, J.P. Hulin, and L. Petit. *Hydrodynamique physique*. EDP Sciences, 2001. ISBN: 9782868835024 (cit. on pp. 39, 41, 48, 51, 52, 66).

[55] National Committee for Fluid Mechanics Films and NCFMF. *Illustrated Experiments in Fluid Mechanics. The NCFMF Book of Film Notes. Based on Material in Films Produced Under Direction of the National Committee for Fluid Mechanics Films, NCFMF*. MIT Press, 1972. ISBN: 9780262140140 (cit. on p. 40).

[56] P.G. de Gennes, F. Brochard-Wyart, and D. Quéré. *Gouttes, bulles, perles et ondes*. Belin, 2002. ISBN: 9782701130248 (cit. on pp. 40–42, 44, 48, 70, 89, 116, 127).

[57] A. W. Adamson, A. P. Gast, et al. *Physical chemistry of surfaces*. Interscience publishers New York, 1967 (cit. on pp. 41, 42, 44, 70).

[58] D.A. Edwards, H. Brenner, and D. T. Wasan. *Interfacial transport processes and rheology*. Elsevier, 2013 (cit. on pp. 41, 42).

[59] V.G. Levich. *Physicochemical hydrodynamics*. Prentice-Hall, 1962 (cit. on pp. 42, 84, 107, 119).

[60] F. Mahaut et al. "Yield stress and elastic modulus of suspensions of noncolloidal particles in yield stress fluids". *J. Rheol.* 52 (2008) (cit. on pp. 44, 47).

[61] T.G. Mason, J. Bibette, and D.A. Weitz. "Yielding and Flow of Monodisperse Emulsions". *J. Colloid Interface Sci.* 179 (1996), pp. 439 –448 (cit. on p. 44).

[62] P. Coussot et al. “Macroscopic vs. local rheology of yield stress fluids”. *J. NN Fluid Mech.* 158 (2009), pp. 85 –90 (cit. on pp. 44, 53).

[63] J.M. Piau. “Carbopol gels: Elastoviscoplastic and slippery glasses made of individual swollen sponges: Meso- and macroscopic properties, constitutive equations and scaling laws”. *J. NN Fluid Mech.* 144 (2007), pp. 1 –29 (cit. on pp. 44, 47, 48).

[64] P. Moller et al. “An attempt to categorize yield stress fluid behaviour”. *Phil. Trans. R. Soc. A* 367 (2009), pp. 5139–5155 (cit. on p. 44).

[65] H.M. Princen. “Rheology of foams and highly concentrated emulsions: I. Elastic properties and yield stress of a cylindrical model system”. *J. Colloid Interface Sci.* 91 (1983), pp. 160 –175 (cit. on pp. 44, 96).

[66] M. P. Aronson. “The role of free surfactant in destabilizing oil-in-water emulsions”. *Langmuir* 5 (1989), pp. 494–501 (cit. on pp. 44, 47).

[67] I. Cantat et al. *Foams: Structure and Dynamics*. OUP Oxford, 2010. ISBN: 9780191505454 (cit. on pp. 45, 183, 219).

[68] G. I. Taylor. “The Formation of Emulsions in Definable Fields of Flow”. *Phil. Trans. R. Soc. A* 146 (1934), pp. 501–523 (cit. on pp. 45, 126).

[69] G. I. Taylor. “The Viscosity of a Fluid Containing Small Drops of Another Fluid”. *Phil. Trans. R. Soc. A* 138 (1932), pp. 41–48 (cit. on p. 45).

[70] H. P. GRACE. “Dispersion phenomena in high viscosity immiscible fluid systems and application of static mixers as dispersion devices in such systems”. *Chem. Eng. Commun.* 14 (1982), pp. 225–277 (cit. on p. 45).

[71] J.M.J. BIBETTE and T. Mason. *Emulsion manufacturing process*. EP Patent App. EP19,970,920,773. 1998 (cit. on p. 45).

[72] C. Mabille et al. “Rheological and shearing conditions for the preparation of monodisperse emulsions”. *Langmuir* 16.2 (2000), pp. 422–429 (cit. on p. 46).

[73] L. Bécu. “Complex fluids under shear: local rheology, inhomogeneous flows ans spatio-temporal dynamics”. PhD thesis. Nov. 2005 (cit. on p. 47).

[74] J. Goyon. “Materiaux amorphes : des solides qui coulent de facon collective”. PhD thesis. 2008 (cit. on pp. 47, 53, 66, 69, 72).

[75] R.J.Jr. Ketz, R.K. Prud’homme, and W.W. Graessley. “Rheology of concentrated microgel solutions”. *Rheol. Acta* 27 (1988), pp. 531–539 (cit. on p. 47).

[76] R. T. Bonnecaze and M. Cloitre. “Micromechanics of soft particle glasses”. *High Solid Dispersions*. Springer, 2010, pp. 117–161 (cit. on pp. 47, 70, 71).

[77] J. Boujlel and P. Coussot. “Measuring the surface tension of yield stress fluids”. *Soft Matter* 9 (25 2013), pp. 5898–5908 (cit. on p. 48).

[78] P. Coussot. “Yield stress fluid flows: A review of experimental data”. *J. NN Fluid Mech.* 211 (2014), pp. 31 –49 (cit. on pp. 48, 53).

[79] B. Geraud et al. “Capillary rise of yield-stress fluids”. *EPL* 107 (2014), p. 58002 (cit. on pp. 48, 128).

[80] C. Gutfinger and J. A. Tallmadge. “Films of non-Newtonian fluids adhering to flat plates”. *AIChE Journal* 11.3 (1965), pp. 403–413 (cit. on pp. 48, 93, 94).

[81] C.W. Macosko. *Rheology: principles, measurements, and applications*. New York: Wiley-VCH, 1994. ISBN: 978-0-471-18575-8 (cit. on pp. 49–51).

[82] B. Geraud, L. Bocquet, and C. Barentin. "Confined flows of a polymer microgel". *Eur. Phys. J. E Soft Matter* 36 (2013) (cit. on pp. 51, 69).

[83] L.-H. Luu and Y. Forterre. "Drop impact of yield-stress fluids". *J. Fluid Mech.* 632 (2009), pp. 301–327 (cit. on p. 51).

[84] I. Cheddadi et al. "Numerical modelling of foam Couette flows". *Eur. Phys. J. E* 27 (2008), pp. 123–133 (cit. on p. 51).

[85] J. R. Seth et al. "A micromechanical model to predict the flow of soft particle glasses". *Nature materials* 10.11 (2011), pp. 838–843 (cit. on pp. 51, 54, 55).

[86] R.G. Larson. "The elastic stress in film fluids". *J. Rheol.* 41.2 (1997), pp. 365–372 (cit. on p. 51).

[87] R. G Larson. *The Structure and Rheology of Complex Fluids (Topics in Chemical Engineering)*. 1998 (cit. on p. 52).

[88] J. Ashmore et al. "Coating flows of non-Newtonian fluids: weakly and strongly elastic limits". *J. Eng. Math.* 60 (2008), pp. 17–41 (cit. on pp. 55, 94).

[89] E. Andres. "Discrete circles, rings and spheres". *Computers & Graphics* 18.5 (1994), pp. 695–706 (cit. on p. 64).

[90] P. Guillot and A. Colin. "Determination of the flow curve of complex fluids using the Rabinowitsch-Mooney equation in sensorless microrheometer". *Microfluid. Nanofluidics* 17 (2014), pp. 605–611 (cit. on p. 66).

[91] G.B. Froishteter and G.V. Vinogradov. "The laminar flow of plastic disperse systems in circular tubes". *Rheol. Acta* 19 (1980), pp. 239–250 (cit. on p. 68).

[92] J. Goyon, A. Colin, and L. Bocquet. "How does a soft glassy material flow: finite size effects, non local rheology, and flow cooperativity". *Soft Matter* 6 (12 2010), pp. 2668–2678 (cit. on p. 69).

[93] P. Jop et al. "Microscale Rheology of a Soft Glassy Material Close to Yielding". *Phys. Rev. Lett.* 108 (14 2012), p. 148301 (cit. on pp. 69, 79, 172).

[94] Y. Yan et al. "The influence of flow confinement on the rheological properties of complex fluids". *Rheol. Acta* 49.3 (2010), pp. 255–266 (cit. on p. 69).

[95] T. Divoux, C. Barentin, and S. Manneville. "From stress-induced fluidization processes to Herschel-Bulkley behaviour in simple yield stress fluids". *Soft Matter* 7 (18 2011), pp. 8409–8418 (cit. on pp. 69, 172).

[96] V. Mansard and A. Colin. "Local and non local rheology of concentrated particles". *Soft Matter* 8 (15 2012), pp. 4025–4043 (cit. on p. 69).

[97] V. Mansard, L. Bocquet, and A. Colin. "Boundary conditions for soft glassy flows: slippage and surface fluidization". *Soft Matter* 10 (36 2014), pp. 6984–6989 (cit. on pp. 69, 72).

[98] H. A. Barnes. "A review of the slip (wall depletion) of polymer solutions, emulsions and particle suspensions in viscometers: its cause, character, and cure". *J. NN Fluid Mech.* 56 (1995), pp. 221 –251 (cit. on pp. 70, 71).

[99] D. Bonn et al. "Yield Stress Materials in Soft Condensed Matter". *ArXiv e-prints* (Feb. 2015). arXiv: `1502.05281` (cit. on pp. 70, 71).

[100] J.N. Israelachvili. *Intermolecular and Surface Forces*. Intermolecular and Surface Forces. Elsevier Science, 2010 (cit. on p. 70).

[101] J. R. Seth et al. "How do soft particle glasses yield and flow near solid surfaces?" *Soft Matter* 8 (1 2012), pp. 140–148 (cit. on pp. 70–72, 74).

[102] J. R. Seth, M. Cloitre, and R. T. Bonnecaze. "Influence of short-range forces on wall-slip in microgel pastes". *J. Rheol.* 52 (2008), pp. 1241–1268 (cit. on pp. 71, 72).

[103] A.-L. Vayssade et al. "Dynamical role of slip heterogeneities in confined flows". *Phys. Rev. E* 89 (5 2014), p. 052309 (cit. on p. 71).

[104] W.B. Horne et al. *Phenomena of pneumatic tire hydroplaning*. NASA technical note vol. 2056. National Aeronautics and Space Administration, 1963 (cit. on p. 71).

[105] H.M. Princen and A.D. Kiss. "Osmotic pressure of foams and highly concentrated emulsions. 2. Determination from the variation in volume fraction with height in an equilibrated column". *Langmuir* 3 (1987), pp. 36–41 (cit. on p. 71).

[106] S. P. Meeker, R. T. Bonnecaze, and M. Cloitre. "Slip and flow in pastes of soft particles: Direct observation and rheology". *J. Rheol.* 48 (2004), pp. 1295–1320 (cit. on pp. 71–73).

[107] S. P. Meeker, R. T. Bonnecaze, and M. Cloitre. "Slip and flow in soft particle pastes". *Phys. Rev. Lett.* 92 (2004), p. 198302 (cit. on pp. 71, 74, 75).

[108] G.V. Vinogradov et al. "The flow of plastic disperse systems in the presence of the wall effect". *Rheol. Acta* 14 (1975), pp. 765–775 (cit. on p. 73).

[109] C. Metivier et al. "Stick-slip control of the Carbopol microgels on polymethyl methacrylate transparent smooth walls". *Soft Matter* 8 (28 2012), pp. 7365–7367 (cit. on p. 73).

[110] T.G. Mason, J. Bibette, and D.A. Weitz. "Elasticity of compressed emulsions". *Phy. Rev. Lett.* 75 (1995), p. 2051 (cit. on p. 74).

[111] G. I. Taylor. "Deposition of a viscous fluid on the wall of a tube". *J. Fluid Mech.* 10 (1961), pp. 161–165 (cit. on pp. 76, 78, 84, 88, 92, 104, 153).

[112] F. P. Bretherton. "The motion of long bubbles in tubes". *J. Fluid Mech.* 10 (1961), pp. 166–188 (cit. on pp. 76–78, 84, 85, 88, 92, 153).

[113] V. S. Ajaev and G.M. Homsy. "Modeling shapes and dynamics of confined bubbles". *Annu. Rev. Fluid Mech.* 38 (2006), pp. 277–307 (cit. on pp. 76, 78).

[114] J.-P. Raven, P. Marmottant, and F. Graner. "Dry microfoams: formation and flow in a confined channel". *Eur. Phys. J. B* 51 (2006), pp. 137–143 (cit. on pp. 76, 142, 162).

[115] M. J. Fuerstman et al. "The pressure drop along rectangular microchannels containing bubbles". *Lab Chip* 7 (2007), pp. 1479–1489 (cit. on p. 77).

[116] S.R. Hodges, O.E. Jensen, and J.M. Rallison. "The motion of a viscous drop through a cylindrical tube". *J. Fluid Mech.* 501 (2004), pp. 279–301 (cit. on p. 78).

[117] L. W. Schwartz, H. M. Princen, and A. D. Kiss. "On the motion of bubbles in capillary tubes". *J. Fluid Mech.* 172 (Nov. 1986), pp. 259–275 (cit. on p. 78).

[118] B.V. Deryagin and S.M. Levi. *Film Coating Theory*. The Focal Press, 1964 (cit. on pp. 84, 94, 95, 119).

[119] W Böhme and A Gädeke. "Zum Gießen photographischer Emulsionen". *Kolloid-Zeitschrift* 116.2 (1950), pp. 99–102 (cit. on p. 84).

[120] P. M. Schweizer and S.F. Kistler. *Liquid Film Coating: Scientific principles and their technological implications*. 2012 (cit. on p. 84).

[121] P. Aussillous and D. Quéré. "Quick deposition of a fluid on the wall of a tube". *Phys. Fluids* 12 (2000), pp. 2367–2371 (cit. on pp. 84, 89, 91, 92, 104).

[122] D. Quéré. "Fluid coating on a fiber". *Annu. Rev. Fluid Mech.* 31 (1999), pp. 347–384 (cit. on pp. 84, 89, 95).

[123] D. A. Reinelt. "The penetration of a finger into a viscous fluid". PhD thesis. California Institute of Technology, 1984 (cit. on pp. 85, 93).

[124] E. J. Hinch. *Perturbation methods*. Cambridge university press, 1991 (cit. on p. 85).

[125] J. Seiwert. "Entraînements visqueux". PhD thesis. Ecole Polytechnique, 2010 (cit. on pp. 89, 96, 115).

[126] D. A. White and J. A. Tallmadge. "A theory of withdrawal of cylinders from liquid baths". *AIChE Journal* 12.2 (1966), pp. 333–339 (cit. on p. 92).

[127] D.A. Reinelt and P.G. Saffman. "The penetration of a finger into a viscous fluid in a channel and tube". *SIAM J. Sci. Comput.* 6.3 (1985), pp. 542–561 (cit. on pp. 92, 93).

[128] Quéré, D. and de Ryck, A. "Le mouillage dynamique des fibres". *Ann. Phys. Fr.* 23.1 (1998), pp. 1–149 (cit. on pp. 93, 110, 118).

[129] A. de Ryck and D. Quéré. "Fluid coating from a polymer solution". *Langmuir* 14.7 (1998), pp. 1911–1914 (cit. on p. 94).

[130] S. J. Weinstein and K. J. Ruschak. "Coating flows". *Annu. Rev. Fluid Mech.* 36 (2004), pp. 29–53 (cit. on p. 94).

[131] F. Kamışlı. "Free coating of a non-Newtonian liquid onto walls of a vertical and inclined tube". *Chem. Eng. Process.* 42.7 (2003), pp. 569–581 (cit. on p. 94).

[132] M. W. Boehm, S. Sarker, and K. Koelling. "An experimental investigation of two-phase coating flow within microchannels: the effect of coating fluid rheology". *Microfluid. Nanofluidics* 10.6 (2011), pp. 1175–1183 (cit. on p. 94).

[133] A. Lindner. "L'instabilité de Saffman-Taylor dans les fluides complexes: relation entre les propriétés rhéologiques et la formation de motifs". PhD thesis. Université Pierre et Marie Curie-Paris VI, 2000 (cit. on p. 94).

[134] P.G. Saffman. "Viscous fingering in Hele-Shaw cells". *J. Fluid Mech.* 173 (1986), pp. 73–94 (cit. on p. 94).

[135] M. Maillard, J. Boujlel, and P. Coussot. "Solid-Solid Transition in Landau-Levich Flow with Soft-Jammed Systems". *Phys. Rev. Lett.* 112 (2014), p. 068304 (cit. on pp. 96, 107, 115, 118, 119, 129).

[136] M. Maillard, J. Boujlel, and P. Coussot. "Flow characteristics around a plate withdrawn from a bath of yield stress fluid". *J. NN Fluid Mech.* (2014) (cit. on pp. 96, 115).

[137] S. Cohen-Addad and R. Höhler. "Rheology of foams and highly concentrated emulsions". *Curr. Opin. Colloid Interface Sci.* 19.6 (2014), pp. 536–548 (cit. on p. 96).

[138] A. Le Goff. "Figures d'impact: tunnels, vases, spirales et bambous". PhD thesis. Université Pierre et Marie Curie-Paris VI, 2009 (cit. on pp. 96, 115).

[139] C.-S. Park et al. "Two-phase flow in a gas-injected capillary tube". *Adv. Polym. Tech.* 22.4 (2003), pp. 320–328 (cit. on p. 97).

[140] T. Gibaud, C. Barentin, and S. Manneville. "Influence of boundary conditions on yielding in a soft glassy material". *Phys. Rev. Lett.* 101.25 (2008), p. 258302 (cit. on p. 114).

[141] Q. Barral. "Superposition d'ecoulements orthogonaux dans des fluides complexes : mise en place de l'experience, application aux suspensions et aux fluides a seuil". PhD thesis. 2011 (cit. on p. 116).

[142] B. Laborie et al. "Bubble Formation in Yield Stress Fluids Using Flow-Focusing and T-Junction Devices". *Phys. Rev. Lett.* 114 (20 2015), p. 204501 (cit. on p. 125).

[143] A.S. Utada et al. “Monodisperse double emulsions generated from a microcapillary device”. *Science* 308 (2005), pp. 537–541 (cit. on p. 125).

[144] E. Lorenceau et al. “Generation of polymerosomes from double-emulsions”. *Langmuir* 21.20 (2005), pp. 9183–9186 (cit. on p. 125).

[145] S. Okushima et al. “Controlled production of monodisperse double emulsions by two-step droplet breakup in microfluidic devices”. *Langmuir* 20 (2004), pp. 9905–9908 (cit. on p. 125).

[146] I. Kobayashi, S. Mukataka, and M. Nakajima. “Novel Asymmetric Through-Hole Array Microfabricated on a Silicon Plate for Formulating Monodisperse Emulsions”. *Langmuir* 21.17 (2005), pp. 7629–7632 (cit. on p. 126).

[147] T. Nisisako and T. Torii. “Microfluidic large-scale integration on a chip for mass production of monodisperse droplets and particles”. *Lab Chip* 8 (2 2008), pp. 287–293 (cit. on p. 126).

[148] M. Hashimoto et al. “Formation of Bubbles and Droplets in Parallel, Coupled Flow-Focusing Geometries”. *Small* 4.10 (2008), pp. 1795–1805 (cit. on p. 126).

[149] E. Amstad, S. S. Datta, and D. A. Weitz. “The microfluidic post-array device: high throughput production of single emulsion drops”. *Lab Chip* 14.4 (Feb. 2014), pp. 705–709 (cit. on p. 126).

[150] G.F. Christopher and S.L. Anna. “Microfluidic methods for generating continuous droplet streams”. *J. Phys. D: Appl. Phys.* 40.19 (2007), p. 319 (cit. on pp. 126, 140, 162, 169).

[151] J. Husny and J. J. Cooper-White. “The effect of elasticity on drop creation in T-shaped microchannels”. *J. NN Fluid Mech.* 137.1 (2006), pp. 121–136 (cit. on p. 126).

[152] J.H. Xu et al. “Experimental and theoretical approaches on droplet formation from a micrometer screen hole”. *J. Membr. Sci.* 266.1 (2005), pp. 121–131 (cit. on p. 126).

[153] P. Garstecki, A.M. Ganan-Calvo, and G.M. Whitesides. “Formation of bubbles and droplets in microfluidic systems”. *Technical sciences* 53.4 (2005) (cit. on p. 126).

[154] P. Garstecki et al. “Formation of monodisperse bubbles in a microfluidic flow-focusing device”. *Appl. Phys. Lett.* 85.13 (2004), pp. 2649–2651 (cit. on pp. 127, 162).

[155] A. M. Gañán-Calvo. “Generation of steady liquid microthreads and micron-sized monodisperse sprays in gas streams”. *Phys. Rev. Lett.* 80.2 (1998), p. 285 (cit. on p. 127).

[156] A. M. Ganán-Calvo. “Perfectly monodisperse microbubbling by capillary flow focusing: An alternate physical description and universal scaling”. *Phys. Rev. E* 69.2 (2004), p. 027301 (cit. on p. 127).

[157] L. Derzsi et al. “Flow focusing with viscoelastic liquids”. *Phys. Fluids* 25.9 (2013), p. 092001 (cit. on p. 128).

[158] Y. Ren, Z. Liu, and H. C. Shum. “Breakup dynamics and dripping-to-jetting transition in a Newtonian/shear-thinning multiphase microsystem”. *Lab Chip* 15.1 (2015), pp. 121–134 (cit. on p. 128).

[159] J. Eggers. “Nonlinear dynamics and breakup of free-surface flows”. *Rev. Mod. Phys.* 69 (1997), pp. 865–929 (cit. on p. 128).

[160] J. Eggers and E. Villermaux. “Physics of liquid jets”. *Rep. Prog. Phys.* 71 (2008), p. 036601 (cit. on p. 128).

[161] P. Doshi et al. “Persistence of memory in drop breakup: The breakdown of universality”. *Science* 302 (2003), pp. 1185–1188 (cit. on p. 128).

[162] N. J. Balmforth, I. A. Frigaard, and G. Ovarlez. “Yielding to Stress: Recent Developments in Viscoplastic Fluid Mechanics”. *Annu. Rev. Fluid Mech.* 46 (2014), pp. 121–146 (cit. on p. 129).

[163] P. Coussot and F. Gaulard. "Gravity flow instability of viscoplastic materials: The ketchup drip". *Phys. Rev. E* 72 (2005), p. 031409 (cit. on p. 129).

[164] G. German and V. Bertola. "Formation of viscoplastic drops by capillary breakup". *Phys. Fluids* 22 (2010), p. 033101 (cit. on p. 129).

[165] A. Lindner, P. Coussot, and D. Bonn. "Viscous Fingering in a Yield Stress Fluid". *Phys. Rev. Lett.* 85 (2000), pp. 314–317 (cit. on p. 129).

[166] N. Louvet, D. Bonn, and H. Kellay. "Nonuniversality in the Pinch-Off of Yield Stress Fluids: Role of Nonlocal Rheology". *Phys. Rev. Lett.* 113.21 (2014), p. 218302 (cit. on p. 129).

[167] J. S. Hong and J. Cooper-White. "Drop formation of Carbopol dispersions displaying yield stress, shear thinning and elastic properties in a flow-focusing microfluidic channel". *Korea-Australia Rheo. J.* 21 (2009), pp. 269–280 (cit. on p. 129).

[168] A.R. Abate et al. "Impact of inlet channel geometry on microfluidic drop formation". *Phys Rev E* 80.2 (2009), p. 026310 (cit. on p. 130).

[169] M. T. Sullivan and H. A. Stone. "The role of feedback in microfluidic flow-focusing devices". *Phil. Trans. R. Soc. A* 366.1873 (2008), pp. 2131–2143 (cit. on pp. 133, 162).

[170] M. Baudoin et al. "Airway reopening through catastrophic events in a hierarchical network". *Proc. Natl. Acad. Sci. USA* 110.3 (2013), pp. 859–864 (cit. on pp. 133, 145, 146, 155, 162).

[171] H. Tavana et al. "Epithelium damage and protection during reopening of occluded airways in a physiologic microfluidic pulmonary airway model". *Biomedical microdevices* 13.4 (2011), pp. 731–742 (cit. on p. 146).

[172] S. Ubal et al. "Stability of the Steady-State Displacement of a Liquid Plug Driven by a Constant Pressure Difference along a Prewetted Capillary Tube". *Ind. Eng. Chem. Res.* 47.16 (2008), pp. 6307–6315 (cit. on p. 146).

[173] H. Fujioka, S. Takayama, and J. B. Grotberg. "Unsteady propagation of a liquid plug in a liquid-lined straight tube". *Phys. Fluids* 20.6 (2008), p. 062104 (cit. on p. 146).

[174] P. Zamankhan et al. "Steady motion of Bingham liquid plugs in two-dimensional channels". *J. Fluid Mech.* 705 (2012), pp. 258–279 (cit. on p. 146).

[175] M. T Sullivan, K. Moore, and H. A. Stone. "Transverse instability of bubbles in viscoelastic channel flows". *Phys. Rev. Lett.* 101.24 (2008), p. 244503 (cit. on p. 151).

[176] J. Ren, B. Ganapathysubramanian, and S. Sundararajan. "Experimental analysis of the surface roughness evolution of etched glass for micro/nanofluidic devices". *J. Micromech. Microeng.* 21.2 (2011), p. 025012 (cit. on p. 157).

[177] T. Ward et al. "Microfluidic flow focusing: Drop size and scaling in pressure versus flow-rate-driven pumping". *Electrophoresis* 26 (2005), pp. 3716–3724 (cit. on p. 162).

[178] D. E. Angelescu. *Highly Integrated Microfluidics Design*. Artech House, 2011. ISBN: 9781596939806 (cit. on p. 162).

[179] D. Liu and S. V. Garimella. "Investigation of liquid flow in microchannels". *J. Thermophys. Heat Tr.* 18.1 (2004), pp. 65–72 (cit. on p. 162).

[180] J.-P. Raven and P. Marmottant. "Periodic microfluidic bubbling oscillator: Insight into the stability of two-phase microflows". *Phys. Rev. Lett.* 97.15 (2006), p. 154501 (cit. on p. 162).

[181] P. Garstecki, M. J. Fuerstman, and G. M. Whitesides. "Oscillations with uniquely long periods in a microfluidic bubble generator". *Nature Physics* 1.3 (2005), pp. 168–171 (cit. on p. 162).

[182] J. Berthier et al. "Highly viscous fluids in pressure actuated flow focusing devices". *Sensors and Actuators A: Physical* 158.1 (2010), pp. 140–148 (cit. on p. 162).

[183] W. Lee, L. M. Walker, and S. L. Anna. "Role of geometry and fluid properties in droplet and thread formation processes in planar flow focusing". *Phys. Fluids* 21.3 (2009), p. 032103 (cit. on p. 162).

[184] H. Willaime et al. "Arnold tongues in a microfluidic drop emitter". *Phys. Rev. Lett.* 96.5 (2006), p. 054501 (cit. on p. 169).

[185] M. A. Unger et al. "Monolithic microfabricated valves and pumps by multilayer soft lithography". *Science* 288.5463 (2000), pp. 113–116 (cit. on pp. 169, 170).

[186] R. Mokso. *The network of plateau borders of wet liquid foam obtained by X-ray tomography at ESRF.* (Cit. on p. 183).

[187] J.-P. Raven. "Generation, flow and manipulation of a microfoam". PhD thesis. Université Joseph-Fourier - Grenoble I, 2007 (cit. on pp. 208, 209).

[188] C. Epstein and M.S. Plesset. "On the Stability of Gas Bubbles in Liquid-Gas Solutions". *J. Chem. Phys.* 18.11 (1950), pp. 1505–1509 (cit. on pp. 219, 220).

[189] W. Kloek, T. van Vliet, and M. Meinders. "Effect of bulk and interfacial rheological properties on bubble dissolution". *J. Colloid Interface Sci.* 237.2 (2001), pp. 158–166 (cit. on p. 221).

[190] A. Arefmanesh and S.G. Advani. "Diffusion-induced growth of a gas bubble in a viscoelastic fluid". *Rheol. Acta* 30.3 (1991), pp. 274–283 (cit. on p. 221).